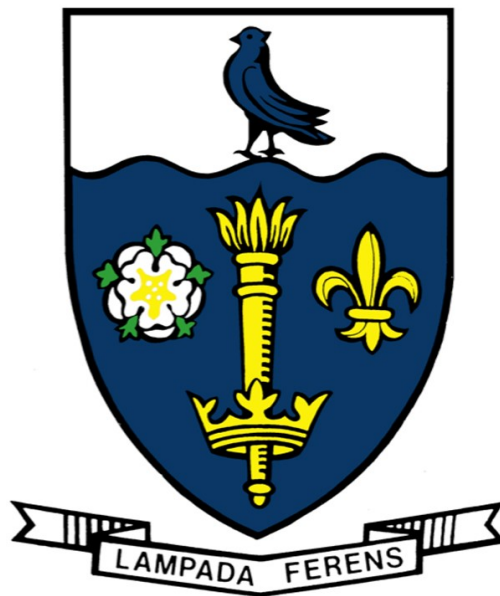


**IN SITU IMAGING AND DIFFRACTION
STUDIES OF THE DEFORMATION OF
METALLIC GLASSES AND
COMPOSITES**

JIA CHUAN KHONG



University of Hull

Jan 2016

**IN SITU IMAGING AND DIFFRACTION
STUDIES OF THE DEFORMATION OF
METALLIC GLASSES AND
COMPOSITES**

JIA CHUAN KHONG

A thesis submitted for the degree of
Doctor of Philosophy at
University of Hull

Jan 2016

Abstract

Three types of experimental studies were done on metallic glass alloys in this PhD project. Firstly, in situ tensile deformation of bulk metallic glass alloy $Zr_{41.2}Ti_{13.8}Cu_{12.5}Ni_{10}Be_{22.5}$ (Vit-1), and a bulk metallic glass matrix composite, $Zr_{39.6}Ti_{33.9}Nb_{7.6}Cu_{6.4}Be_{12.5}$ (ZrTi composite) were studied using in situ scanning electron microscopy (SEM) and in situ synchrotron X-ray diffraction (SXR). It was found that the initiation and propagation of the shear band can be controlled through introduction of notch-type stress concentrator and allow it to be observed under in situ SEM. Using this technique, the local stresses/strains in front of the shear band can be measured using in situ SXR that linked the initiation and propagation of shear band directly to the local stress field.

In Vit-1 sample, the formation of "step" was first observed between 1703MPa and 1992 MPa under in situ SEM imaging after two opposite propagating shear bands met and formed a crossly joined. This then led to formation of stress concentration area at the crossly joined area and led to another bigger "step". In ZrTi composite, the plastic deformation in the dendrite was captured by in situ SEM. Moreover, in situ SXR showed reduced axial strain rate in dendrite and increased axial strain rate in matrix at similar tensile stress. This concluded that load was transferred to matrix when yielding occurred in dendrite.

Secondly, in situ high pressure compression studies of a binary metallic glass alloy, $Cu_{50}Zr_{50}$, and a ternary metallic glass alloy, $Fe_{60}Nb_{15}B_{25}$ composite was done using Diamond Anvil Cell and SXR. $Cu_{50}Zr_{50}$ showed no obvious polyamorphism structural change when pressed until 43.15 GPa but the pair distribution function analysis showed that the 3rd atomic shell started to split into two minor peaks which indicated the atomic coordination number in the 3rd atomic shell start to change. Likewise, $Fe_{60}Nb_{15}B_{25}$ showed no obvious polyamorphism structural change when pressed until 70.64 GPa but pair distribution function analysis showed that the rate of deformation in 2nd atomic shell become 5 times slower at 35.33 GPa. The difference in atomic size ratio between binary and ternary behaved differently during high pressure compression such that $Cu_{50}Zr_{50}$

with 30% difference from bigger atom and same atomic concentration of the two elements showed more fluctuation in atom shell movement compared to $\text{Fe}_{60}\text{Nb}_{15}\text{B}_{25}$ that have 3 different atomic radii with 21% and 56% difference from the bigger atom. The 3rd atomic shell movement fluctuation in $\text{Cu}_{50}\text{Zr}_{50}$ might be due to the rearrangement of Cu and Zr to allow further compression.

Thirdly, studies were carried out to design, make and characterise a series of new Fe-based bulk metallic glass alloys that can achieve sufficient glass forming ability and neutron absorption capability. After 3 rounds of iterative studies, $\text{Fe}_{48}\text{Cr}_{15}\text{Mo}_{14}\text{C}_{15}\text{B}_6\text{Gd}_2$ (Fe-B₆Gd₂) was successfully developed with high glass forming ability of up to $\varnothing 5.8$ mm and highest neutron absorption cross section with 73.64 cm^{-1} at thermal neutron 25.3 meV compared to other existing Fe-based metallic glass.

Acknowledgements

I would like to express my sincere gratitude for the International PhD Studentship awarded by the University of Hull for me to pursue a PhD degree.

I am very grateful for the guidance and encouragement given by my supervisor, Dr Jiawei Mi and Professor Philip Rubini throughout of my PhD study. At the very beginning, research is completely new to me; especially I have little background knowledge in this particular research field. Dr Mi have very patiently educated me and imparted a wide range of knowledge to myself, and provided many valuable resources for me to climb up a very steep learning curves in the first two years and move onto the stage where I can conduct a very advanced research program using the cutting-edge research tools, such as the synchrotron X-ray facilities around the world, including those at the Advanced Photon Source, Argonne National Laboratory, in the US, the Diamond Light Source in the UK and Swiss Light Source in Switzerland, and the ISIS spallation neutron source in the Appleton Rutherford Laboratory, UK. Without these tremendous supports, I cannot go this far in my education and research.

I would like to thank the following scientists who have given their supports for the research I carried out, and their simulating discussions and inputs for a number of publications we jointly published. Through them, I have interacted closely with a wide research community in the field of physics, materials and engineering. They are:

Scientists from Diamond Light Source (DLS): Dr Thomas Connolley (I12), Dr Michael Drakopoulos (I12), Dr Dominik Daisenberger (I15), Dr Andrew Bodey (I13), Dr Christoph Rau (I13) and Professor Chiu Tang (I11). Scientists from ISIS spallation neutron and muon source: Dr Winfried Kockelmann (IMAT), Dr Genoveva Burca (IMAT), Dr Saurabh Kabra (Engin-X) and Dr Joe Kelleher (Engin-X)

Scientists from Advanced Photon Source (APS) and Swiss Light Source (SLS): Dr Kamel Fezza and Dr Alex Derity from beamline 32-ID-B (SLS) and Dr Fife Julie Louise (SLS).

Special thanks also go to the technical support and administration support by the staff in the School of Engineering, University of Hull, and they are: Mr Garry Robinson for helping on sample preparation, and SEM training, Miss Ronnie Hewer for the X-ray diffractometer training, Mr Tony Sinclair for SEM imaging, Professor Michael Fagan and Miss Sue Taft for X-ray imaging and nano-indentation tests, workshop technical supports from Mr John Hebden, Mr Simon Cowell, Mr Stuart Butterick and Mr Mike Jost. Administrative support from Mr David Wright, Miss Joanna Arnett and Miss Fiona Childs.

I also would like to thank Dr Yongjiang Huang, a Royal Society K.C. Wong Postdoctoral Research Fellow in Dr Mi's group during 2012-2014, who taught me a lot of knowledge about bulk metallic glasses, and my fellow PhD classmates, Dr Theerapatt Manuwong, Dr Dongyue Tan, Mr Tung Lik Lee and Mr Wei Zhang for company and help for my research.

Last but not least, I would like to thank my dad Mr Thet Chong Khong, my mum Miss Su Eng Ang, my sisters Miss Jia Hui Khong and Jia Ching Khong for the love and support they have been giving in my whole life. Without those, I would not go this far. Also to my childhood buddy, Lucky, who passed away when I am doing my PhD. I would like to thank my girlfriend, Miss Tsin Shue Koay for all the love she gave me throughout my PhD research. She was always there to share, help and accompany me during some very stressful period of time during my research.

Publications

- T.L. Lee, **J.C. Khong**, K. Fezzaa, and J. Mi, "Ultrafast X-ray Imaging and Modelling of Ultrasonic Cavitations in Liquid Metal", *Material Science Forum*, Vol. 765, pp. 190-194, 2013.
- Y.J. Huang, **J.C. Khong**, T. Connolley, J. Mi, "In situ study of the evolution of atomic strain of bulk metallic glass and its effects on shear band formation", *Scripta Materialia*, Vol 69, Issue 3, pp. 207-210, 2013.
- Y.J. Huang, **J.C. Khong**, T. Connolley, J. Mi, "The onset of plasticity of a Zr-based bulk metallic glass", *International Journal of Plasticity*, Vol 60, pp. 87-100, 2014.
- Y.J. Huang, **J.C. Khong**, T. Connolley, J. Mi, "Understanding the deformation mechanism of individual phases of a ZrTi-based bulk metallic glass matrix composite using in situ diffraction and imaging methods", *Applied Physics Letters*, Vol 104, Issue 3, pp. 031912, 2014.
- D. Tan, T.L. Lee, **J.C. Khong**, T. Connolley, K. Fezzaa, and J. Mi, "High-Speed Synchrotron X-ray Imaging Studies of the Ultrasound Shockwave and Enhanced Flow during Metal Solidification Processes", *Metallurgical and Materials Transactions A*, Vol 46, Issue 7, pp. 2851-2861, 2015.
- **J.C. Khong**, D. Daisenberger, G. Burca, W. Kockelmann, A. S. Tremsin, J. Mi "Design and Characterization of Metallic Glassy Alloys of High Neutron Shielding Capability", (Submitted).
- W. Zhang, **J.C. Khong**, J. Mi, "Study of Local Ordering in Zr-Ti Based Bulk Metallic Glass Matrix Composite Using HRTEM Based Image Processing and Synchrotron X-ray Total Scattering", (Under preparation).
- W. Zhang, **J.C. Khong**, T. Connolley, J. Mi, "Synchrotron X-ray in situ Studies of the Evolution of Atomic Structures of Bulk Metallic Glass during Heating and Cooling", (Under preparation).
- **J.C. Khong**, D. Daisenberger, P. F. McMillan, J. Mi, "The stability of Metallic Glasses atomic structure under Extreme Pressure", (Under preparation).

Table of Contents

Abstract	i
Acknowledgements.....	iii
Publications	v
Table of Contents	vi
Chapter 1 Introduction.....	1
1.1 The background of the research	1
1.2 The objectives of the research	2
1.3 The research funds and synchrotron X-ray beam times	2
1.4 The structure of the thesis.....	5
Chapter 2 Literature reviews	6
2.1 A brief history of the research on metallic glasses	6
2.2 Local atomic structure of metallic glasses.....	13
2.2.1 Short-range order, medium-range order and long-range order.....	16
2.2.2 Synchrotron X-ray diffraction for total and anomalous scatterings studies of metallic glasses	16
2.2.3 Dense random packing model	26
2.2.4 Structure of ETM–LTM metallic glasses.....	26
2.2.5 Structure of LTM + NM metallic glasses.....	28
2.2.6 Quasicrystals in metallic glasses	28
2.3 Design and manufacturing of BMGs and BMG composites	31
2.3.1 Glass forming ability	31
2.3.2 Alloy design and selection principles	32
2.3.3 Manufacturing and applications of BMGs and BMG composites	35
2.4 Mechanical, functional properties and deformation of BMGs	40

2.4.1 Elastic limit, yield strength and nano-indentation.....	41
2.4.2 Shear bands, plastic deformation and fracture toughness.	43
2.4.3 Hardness, wear and corrosion resistances	50
2.4.4 Radiation shielding properties.....	52
2.5 In-situ studies of the deformation of BMGs.....	55
2.5.1 Imaging studies using electron microscopes	56
2.5.2 Digital image correlation.....	58
2.5.3 Diffraction studies using synchrotron X-rays	59
2.5.4 High pressure compression using Diamond Anvil Cell	61
2.6 Summary	62
Chapter 3 Alloy design, sample making and experimental methods	63
3.1 Selection and design of novel metallic glass alloys.....	63
3.2 Manufacturing of the alloys and samples.....	68
3.3 Design and preparation of samples for in situ studies.....	68
3.3.1 Design of the miniature dog-bone tensile test samples	68
3.3.2 Machining, grinding and polishing of samples.....	70
3.3.3 Samples for high pressure compression experiments.....	72
3.4 Nano-indentation experiments	72
3.5 In situ tensile deformation experiments	76
3.5.1 Design and making of new sample clamps.....	76
3.5.2 In situ imaging studies of tensile deformation inside SEM.	78
3.5.3 Synchrotron X-ray diffraction studies and in situ tensile tests.....	82
3.6 The relevant synchrotron X-ray proposals and beam time.....	89
3.7 Summary	91
Chapter 4 In situ tensile deformation studies of bulk metallic glass and composite.....	92
4.1 Hardness and Young's modulus measured by nano-indentation ..	93

4.2	In situ imaging study of tensile deformation of Vit-1	98
4.3	In situ diffraction study of tensile deformation of Vit-1	107
4.4	Finite element modelling of tensile deformation of Vit-1	119
4.5	In situ imaging study of tensile deformation of ZrTi composite .	126
4.6	In situ diffraction study of tensile deformation of ZrTi composite	133
4.6.1	A generic method for decoupling the convoluted diffraction dataset	135
4.7	Finite element modelling of tensile deformation of ZrTi composite	145
4.8	Discussion	150
4.8.1	Shear bands initiation and propagation control	150
4.8.2	Shear band propagation in BMGs	155
4.8.3	Shear band propagation in ZrTi BMGMC	159
4.9	Summary	162
Chapter 5	High pressure compression of metallic glass and anomalous X-ray scattering	163
5.1	High pressure compression experiments	163
5.1.1	Diamond Anvil cell and sample loading	163
5.1.2	Alignment of X-ray beam with DAC and samples	168
5.1.3	DAC pressure control and measurement	173
5.1.4	In situ acquisition of X-ray diffraction patterns	176
5.2	Data processing and analyses	176
5.2.1	Masking of the unwanted diffraction information.....	176
5.2.2	Compensation of X-ray intensity attenuated by diamond anvil and backing plate.....	178
5.2.3	Integration of 2D diffraction pattern into 1D spectra	182
5.3	The experimental results for $\text{Cu}_{50}\text{Zr}_{50}$	184
5.4	The experimental results for $\text{Fe}_{60}\text{Nb}_{15}\text{B}_{25}$	192
5.5	Anomalous X-ray scattering	201

5.5.1	Experiment setup for anomalous X-ray scattering	201
5.5.2	Sample preparation	201
5.5.3	X-ray energy tuning and flatfield correction	202
5.5.4	Experimental results for $\text{Cu}_{50}\text{Zr}_{50}$ and $\text{Fe}_{60}\text{Nb}_{15}\text{B}_{25}$	203
5.6	Discussion	214
5.6.1	Atomic structure evolution under high pressure.....	214
5.6.2	The effect of atomic ratio.....	215
5.6.3	The advantage of anomalous scattering	215
5.7	Summary	217
Chapter 6	Novel metallic glass alloys for neutron absorption studies	218
6.1	Design, making and characterisation of new glassy alloys.....	218
6.1.1	The 1 st round alloy design: selection of basic alloy systems	222
6.1.2	The 2 nd round alloy design: improving glass forming ability	223
6.1.3	The 3 rd round alloy design: improving neutron shield capacity	230
6.2	Effect of cooling rates on glass forming of the designed alloys ..	230
6.3	Hardness and Young's modulus of the designed alloys	235
6.4	Neutron absorption measurement.....	239
6.4.1	Sample preparation for neutron absorption measurement	239
6.4.2	Neutron source, detector, experiment setup	241
6.4.3	Data acquisition and analyses	243
6.5	Discussion	250
6.5.1	Composition design for Fe-based metallic glassy alloys ..	250
6.5.2	Effect of cooling rates on glass forming ability	251
6.5.3	Improvement in mechanical properties	253
6.5.4	Improvement in neutron shielding capability	255

6.6 Summary	258
Chapter 7 Conclusions and future work.....	259
7.1 Conclusions.....	259
7.2 Future work	261
References	262
Appendix	281

Chapter 1 Introduction

1.1 The background of the research

Metallic glasses (MGs) and bulk metallic glasses (BMGs) are amorphous alloys formed under rapid solidification from the melt. The alloys often have superior strength and hardness, excellent corrosion and wear resistance, as compare to their crystalline counterpart [1]. It was first reported by Klement, *et al* in 1960 at Caltech through rapid solidification from the melt [2]. Since the introduction of the first MG, in the past 60 years, many BMG systems were developed [3]. The excellent material properties of the BMGs enable it to be widely explored as advance engineering materials [4].

However, monolithic BMGs have a major drawback. At temperature $1/2$ of its glass transition temperature, T_g , typically around 400°C , it exhibit near zero plasticity strain [5]. It is because of the inhomogeneous deformation of BMG with localised plastic deformation in the narrow shear bands [6]. Alternatively, crystalline phases were introduced into the monolithic BMG to form the bulk metallic matrix composite (BMGMC), with the purpose to enhance its plasticity strain. For example, Hofmann reported the in situ formed crystalline dendrites in the amorphous matrix which exhibit equal to surpass those achievable in the toughest titanium or steel alloys, placing the BMGMC among the toughest known materials [7].

The crystalline dendrites in the amorphous matrix were reported with ability intercept the shear bands propagation in the amorphous matrix [8]. In the past, the shear bands formation and propagation in the BMGs and BMGMCs were widely investigated, especially under in situ observation using the electron microscopy [9] and synchrotron X-ray diffraction [10]. However, the combination of both techniques to correlate the surface deformation was not widely reported. Recently, together with Dr Yongjiang Huang and Dr Jiawei Mi, we reported the shear bands formation in the monolithic BMG [11, 12] and BMGMC [13] under tensile deformation by combining the in situ SEM, in situ Synchrotron X-ray diffraction and total scattering techniques. The reported works were part of my PhD research and will be discussed in details in Chapter 4.

1.2 The objectives of the research

The tensile deformation and high pressure compression of the metallic glasses and its composite were investigated in the research project. Using the in situ scanning electron microscopy (SEM), in situ synchrotron X-ray diffraction (SXR), Diamond Anvil Cell (DAC) and pulsed-neutron time-of-flight (TOF) imaging to study:

- The atomic structure changes during the shear bands initiation and propagation in the monolithic bulk metallic glass and bulk metallic glass matrix composite using the in situ SEM and in situ SXR.
- The changes of the atomic pair distances in the binary and ternary metallic glasses under high pressure compression using the Diamond Anvil and in situ SXR.
- New BMG alloy systems with high neutron shielding capability that can be target to use as a coating material in nuclear waste repository.

1.3 The research funds and synchrotron X-ray beam times

The research presented in this thesis is supported by three funded projects:

- Hull University PhD Scholarship – “*Synthesis of novel bulk metallic glasses coatings for offshore renewable energy infrastructure (£43 k, 01/10/2011 - 25/09/2015)*”. It provides the international student bursary to cover the tuition fee for my PhD study.
- The Royal Society K.C. Wong Postdoctoral Fellowship (for Dr Yongjiang Huang from Professor Jun Shen’s group in Harbin Institute of Technology, China) – “*Synthesis and in situ study of deformation mechanism of ductile Ti-based bulk metallic glasses (£66k, 31/03/2012-30/03/2014)*”. It funds partially the manufacturing of the alloys and samples, design and making of the in situ tensile test rigs, and the use of electron microscopes.

- The EPSRC feasibility studies project funded via the EPSRC Centre for Innovative Manufacturing in Liquid Metal Engineering – “*Studies of nucleation controlled carbide morphology during the solidification of cast Ni superalloys (£24 k, 01/06/2014 - 31/12/2014)*”. It partially funds the living expense for my PhD study in 2014, and the consumables for machining and polishing samples.

My supervisor, Dr Jiawei Mi is the UK academic host for the Royal Society K. C. Wong Postdoctoral Fellow and the principal investigator for the EPSRC project. Directly relevant to those research projects, he authored four successful proposals, winning 33 shifts (1 shift = 8 hours) of synchrotron X-ray beam time from the Diamond Light Source (DLS) in year 2012 - 2015 as detailed in Table 1.1. Using those beam times, tensile deformation of a Ti-based and Zr-based metallic glass and a ZrTi-based metallic glass composite, and high pressure compression of a Fe-based, Cu-based and a Ti-based metallic glasses were studied in situ. In addition, X-ray diffraction patterns of the many newly designed alloys (detailed in Table 3.2 and Table 3.3 in Chapter 3) were acquired at ambient condition, allowing the correlation between the atomic structures and chemical compositions to be studied in great details.

I have played a leading role in the four experiments during my PhD study in terms of designing, making and commissioning the in situ test rigs, preparation of the samples and conducting the experiments. More importantly, I have analysed the huge amount of data sets obtained from those experiments in order to extract the new scientific findings.

Table 1.1 The synchrotron X-ray proposals and experiments that produced the results presented in this thesis.

Proposal code	Proposal title	Beamline of DLS	Dates to do the experiment
EE7665-1	In-situ study of deformation mechanism of ductile bulk metallic glasses composites	I12	03-05 May 2012 (48 hrs =6 shifts)
EE8858-1	Study of the evolution of atomic structure of Fe-based metallic glasses	I15	10-13 July 2013 (72 hrs =9 shifts)
EE9902-1	In-situ study of the evolution of atomic structure of metallic glasses under extreme pressure	I15	18-21 April 2014 (72 hrs =9 shifts)
EE11525-1	Resolving the convoluted atomic structures of metallic glasses using anomalous X-ray scattering and pair distribution function	I11	22-25 April 2015 (72 hrs =9 shifts)

Throughout my PhD study, I also participated and supported 7 other synchrotron X-ray and 3 neutron experiments which were led by Dr Mi or my colleagues in Dr Mi's group. Those experiments were conducted at (1) the Advanced Photon Source (2 experiments in 29 Feb to 03 Mar 2012 and 01 to 05 Mar 2013), (2) the Diamond Light Source (4 experiments in 20 to 25 Jun 2013, 11 to 14 Oct 2013, 9 to 13 Oct 2014 and 4 to 7 Feb 2015), (3) the Swiss Light Source (1 experiment in 31 Oct 2014), and ISIS (2 experiments in 22-25 Feb 2014 and 04-07 Jun 2015). I have accumulated a total of 944 hours of hand-on experiences on operating many sophisticated instruments and in situ test rigs in those national laboratories, and mastered the corresponding software for processing the data and images.

1.4 The structure of the thesis

The thesis consists of 7 chapters as detailed below.

Chapter 1 introduces briefly the research background, the objectives, the relevant research funds and awarded synchrotron X-ray beam times, and the structure of the thesis.

Chapter 2 reviews the literatures that are directly relevant to the research, and they are grouped into 7 sections.

Chapter 3 summarises the designed alloys, sample manufacturing and preparation, and lastly, the experiments design and procedure.

Chapter 4 contains the experiment setup, results and discussion for the in situ tensile test under SEM and synchrotron X-ray diffraction and finite element modelling.

Chapter 5 covers the high pressure experiment setup, results and discussion for the in situ high pressure compression using the Diamond Anvil Cell for the binary and ternary alloys. The chapter also include the anomalous X-ray scattering experiment.

Chapter 6 includes the alloys design results and discussion for the neutron shielding application. The chapter also include the TOF neutron imaging experiment.

Chapter 7 contains the summary and future development of the thesis.

Chapter 2 Literature reviews

2.1 A brief history of the research on metallic glasses

Natural metals and glasses are very common materials on earth, and have been used, exploited and developed for many thousand years by human society. Metals are made of metallic elements via metallic bonding, and atoms in metals form periodical crystalline structure (or lattice) with long-range translational order [14]. Glasses are solids (frozen liquids), and atoms in glasses exhibit a random (or disordered) three dimensional (3D) structure held together by covalent and ionic bonds, or Van der Waals force [15]. Metallic glasses (MGs), as a relatively new class of materials firstly synthesised in 1960, overlap these two categories of materials. MGs consist of predominantly metallic elements and metallic bonds, but have an amorphous atomic structure. Such a combination of “metal” and “glass” leads to many unique functional and mechanical properties, and huge application potentials.

The first reported metallic glass was a binary alloy ($\text{Au}_{75}\text{Si}_{25}$) that was produced at Caltech by Klement, Willens and Duwez in 1960 [2] using a gun quenching technique to quench a molten $\text{Au}_{75}\text{Si}_{25}$ from $\sim 1300^\circ\text{C}$ to room temperature. The cooling rate used in the experiment was $\sim 10^7$ K/s, and it “freezes” the liquid structure into solid state directly without any crystallisation occurring during the cooling [2].

This and other early glass-forming alloys had to be cooled extremely fast (10^6 to 10^7 K/s) to avoid crystallisation. Hence, they could only be produced in forms of very thin thickness (typically ribbons, foils, or wires) which allows heat to be extracted quickly enough to achieve the necessary cooling rate. As a result, metallic glass specimens (with a few exceptions) were limited to thicknesses of less than one hundred micrometres [16, 17].

In 1969, Chen and Turnbull from Harvard University formed amorphous spheres from the Pd–Si–M alloy (where M = Ag, Cu, or Au) [18]. The alloy $\text{Pd}_{77.5}\text{Cu}_6\text{Si}_{16.5}$ could be made into glassy solid with a diameter of 0.5 mm and existence of a glass transition temperature, T_g was demonstrated.

In 1976, (based on the concept of the melt spinner developed by Pond and Maddin in 1969 [19]), Liebermann and Graham developed a new method of manufacturing thin ribbons of amorphous metal on a supercooled fast-spinning wheel. This was an alloy of iron, nickel, phosphorus and boron [20]. The material, known as Metglas, was commercialized in 1980s and used for low-loss power distribution transformers (amorphous metal transformer). In the 1982, Drehman, Greer and Turnbull produced glassy ingots of $\text{Pd}_{40}\text{Ni}_{40}\text{P}_{20}$ with a diameter of 5 mm using surface etching followed by heating and cooling cycles [21]. In 1984, they reported the possible of extending the critical casting thickness to 1 cm by processing the alloy in boron oxide flux [22].

During the late 1980s, Inoue, *et al* at Tohoku University succeeded in finding multicomponent alloy systems consisting mainly of common metallic elements with lower cooling rates [23], and followed by investigated the rare earth material La, successfully in making the $\text{Al}_{20}\text{La}_{55}\text{Cu}_{25}$ [24] and $\text{Al}_{25}\text{La}_{55}\text{Ni}_{20}$ [25] alloys with exceptional glass-forming ability and wide supercooled liquid region. By casting the alloy melt in water-cooling copper mould, they obtained fully glassy rods and bars with thicknesses of several millimetres.

In the 1990s, however, new alloys were developed that form glasses at cooling rates as low as 1 K/s. These cooling rates can be achieved by casting using metallic moulds. These "bulk" amorphous alloys can be cast into parts of up to several centimetres in thickness (the maximum thickness is dependent on the alloy) while retaining an amorphous structure. The best glass-forming alloys are based on zirconium and palladium, but alloys based on iron, titanium, copper, magnesium, and other metals are also known [5]. Many amorphous alloys are developed by exploiting the so called "confusion" effect [26]. Such alloys contain so many different elements (often four or more) that when cooled at sufficiently fast rates, the constituent atoms simply cannot coordinate themselves into the equilibrium crystalline state before their mobility is stopped. In this way, the random disordered state of the atoms is "locked in".

In 1992, the first commercial amorphous alloy, Vitreloy 1 – Vit-1 ($Zr_{41.2}Ti_{13.8}Cu_{12.5}Ni_{10}Be_{22.5}$), was developed Peker and Johnson at Caltech, as a part of Department of Energy and NASA research of new aerospace materials [27]. In 1997, Inoue, *et al* re-visited the $Pd_{40}Ni_{40}P_{20}$ alloy and replaced the 30% of Ni with Cu. As a result, they developed the $Pd_{40}Cu_{30}Ni_{10}P_{20}$ alloy with glass forming ability up to 72mm [28], and remained the highest glass-forming ability alloy up to date.

In 2004, two research groups succeeded in producing bulk amorphous steels [29], one at Oak Ridge National Laboratory, the other at University of Virginia. The product is non-magnetic at room temperature and significantly stronger than conventional steel, though a further research and development process remains secret.

In 2008, Byrne and Eldrup from Risø DTU National Laboratory for Sustainable Energy compared the strength and fracture toughness of few selected BMGs with some crystalline metals and plastics [30]. Showing an improving universal description of structure and behaviour of BMGs should lead to better predictive tools for their design and thus a greater propensity for commercialization. In 2011, Demetrious, *et al* from California Institute of Technology, Lawrence Berkeley National Laboratory and University of California [31] demonstrate that the level of damage tolerance (combination of toughness and strength) of $Pd_{79}Ag_{3.5}P_6Si_{9.5}Ge_2$ glassy alloy extends beyond the traditional limiting ranges towards levels previously inaccessible to any material as show in Figure 2.1. In 2011, Axinte from Gheorghe Asachi Technical University of Iași reviewed the BMGs as engineering materials, some strategic lines of glass usage in industry and estimations about the future of glass development [32].

Table 2.1 summarises the most important metallic glassy alloy systems discovered or developed since 1960.

The typical constituent elements used for BMGs can be grouped as: alkali and alkaline earth metals (AM), semi- or simple metals (SM) in IIIA and IVA groups neighbouring the semiconductors, transition metals (TM), including early transition metals (ETM) and late transition metals (LTM), rare earth metals (RE), and non-metals (NM) [33]. The simple classification of

commonly used constituent elements for BMGs and the typical MGs based on the binary prototypes are listed in Table 2.2.

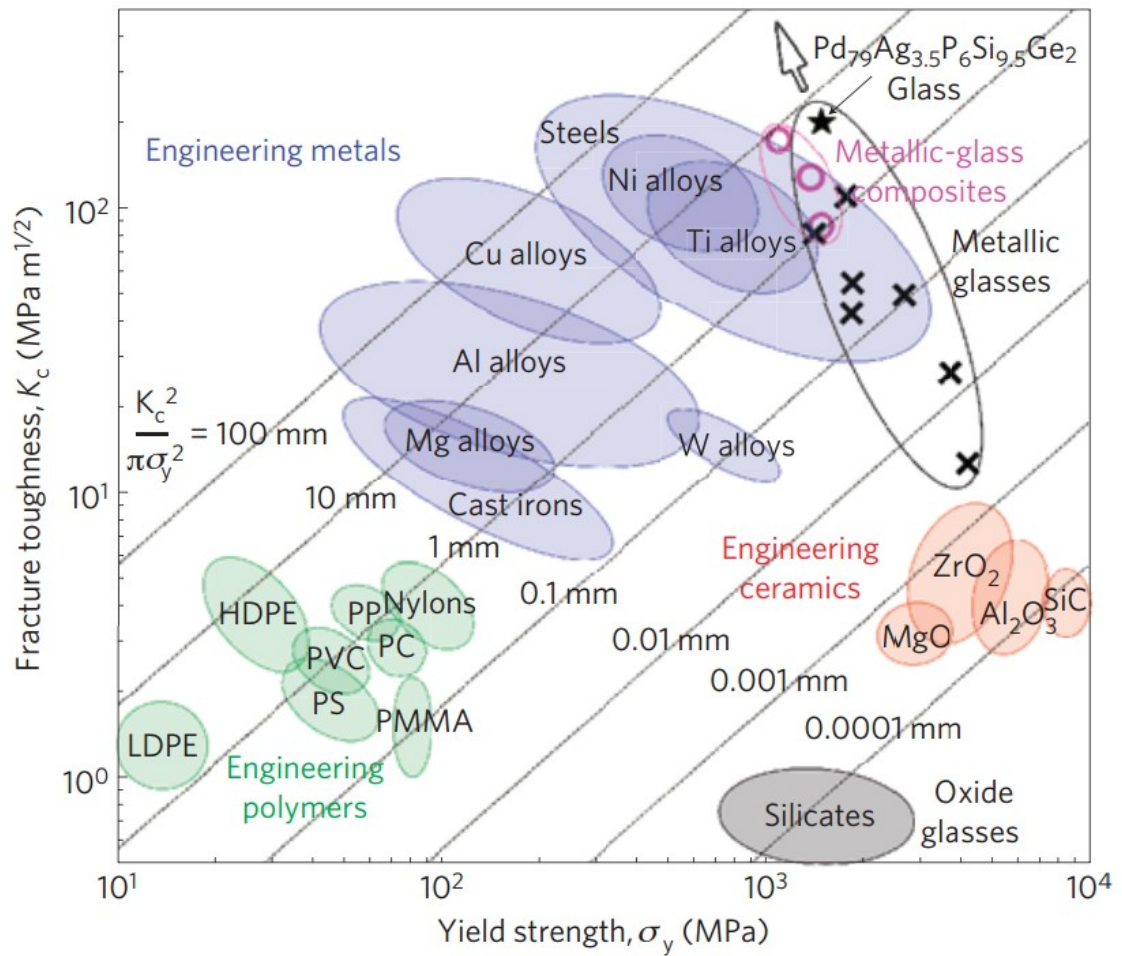


Figure 2.1 Ashby map of the damage tolerance (toughness versus strength) of materials [31].

Table 2.1 Summary of the important metallic glassy alloys discovered since 1960.

Year	MGs/BMGs composition (commercial name)	Authors	MGs/BMGs place of birth
1960	Au ₇₅ Si ₂₅ [2]	Klement, Willens and Duwez	Caltech
1969	Pd-Si-M (M=Ag, Cu or Au) [18]	Chen and Turnbull	Harvard University
1976	Fe ₄₀ Ni ₄₀ B ₂₀ (MetGlass) [19]	Liebermann and Graham	University of Pennsylvania
1992	Zr _{41.2} Ti _{13.8} Cu _{12.5} Ni ₁₀ Be _{22.5} (Vitreloy 1, Vit-1) [27]	Peker and Johnson	Caltech
1997	Pd ₄₀ Cu ₃₀ Ni ₁₀ P ₂₀ [28]	Inoue, Nishiyama and Kimura	Tohoku University
2004	Fe _{44.3} Cr ₅ Co ₅ Mo _{12.8} Mn _{11.2} C _{15.8} B _{5.9} , (Fe _{44.3} Cr ₅ Co ₅ Mo _{12.8} Mn _{11.2} C _{15.8} B _{5.9}) _{98.5} Y _{1.5} , (Fe _{44.3} Cr ₁₀ Mo _{13.8} Mn _{11.2} C _{15.8} B _{5.9}) _{98.5} Y _{1.5} [29]	Lu, Liu, Thompson and Porter	Oak Ridge National Laboratory University of Virginia
2011	Pd ₇₉ Ag _{3.5} P ₆ Si _{9.5} Ge ₂ [31]	Demetriou, Launey, Garrett, Schramm, Hofmann, Johnson and Ritchie	California Institute of Technology Lawrence Berkeley National Laboratory University of California

Table 2.2 The classification of common constituent elements of BMGs and typical MGs based on the binary prototypes [33].

Abbreviation	Description	Examples
AM	Alkaline earth metals group IA and IIA metals	Mg, Ca, Be
SM	Semi- or simple metals, metals in groups III A and IVA	Al, Ga
TM, ETM	Transition metals TM , including early transition metals (ETM) – metals in groups VIII B, IB, IIB	Ti, Zr, Hf, Nb, Ta, Cr, Mo, Mn
LTM	Late transition metals, metals in groups VIII B, IB, IIB	Fe, Co, Ni, Cu, Pd, Pt, Ag, Au, Zn
RE	Sc, Y, lanthanides (Ln)	Sc, Y, La, Ce, Nd, Gd
NM	Nonmetals and metalloids	B, C, P, Si, Ge

Prototype	Base metal	Examples
LTM + NM	LTM	Ni-P, Pd-Si, Au-Si-Ge, Pd-Ni-Cu-P, Fe-Cr-Mo-P-C-B
ETM + LTM	ETM/LTM	Zr-Cu, Zr-Ni, Ti-Ni, Zr-Cu-Ni-Al, Zr-Ti-Cu-Ni-Be
SM + RE	SM/RE	Al-La, Ce-Al, Al-La-Ni-Co, La-(Al/Ga)-Cu-Ni
AM + LTM	AM	Mg-Cu, Ca-Mg-Zn, Ca-Mg-Cu

In 1998, Dandliker, *et al* from Caltech developed alternative way to enhance the mechanical properties of the BMGs [34]. Using the $Zr_{41.2}Ti_{13.8}Cu_{12.5}Ni_{10}Be_{22.5}$ (Vit-1) as the matrix material, they reinforce with continuous metal wires, tungsten powder, or silicon carbide particulate preforms. Especially for the sample reinforced with 60 vol% tungsten wires, it was reported that it exhibited 16% plastic strain in compression. Since then, the reinforced second crystalline phase into the glassy matrix was widely studied [35]. The volume fraction of this secondary phase can be tailored to achieve high plasticity. For example, Xue, *et al* developed the BMGMC using the $Zr_{38}Ti_{17}Cu_{10.5}Co_{12}Be_{22.5}$ as matrix and adding in 80 vol-% of porous tungsten powder thorough powder infiltration, which shows extremely large fracture strain up to 82% in compression [36]. Choi-Yim, *et al* reported the $Zr_{57}Nb_5Al_{10}Cu_{15.4}Ni_{12.6}$ (Vitreyloy 106) reinforced with 80 vol-% 0.25mm Mo or Ta wire exhibited 20% plasticity strain in compression [37].

The BMG composites can be classified as in situ [7, 8, 38-40] or ex situ [34, 36, 37, 41, 42] composites, depends on whether the second phase is grown out of the glassy matrix in situ during forming, or is added from outside in an ex-situ manner. It was reported by Hays that the interface of the in situ composite between the glassy matrix and the crystalline dendrites is very strong [8]. For example, the $Zr_{36.6}Ti_{31.4}Nb_7Cu_{5.9}Be_{19.1}$ (DH1) and $Zr_{39.6}Ti_{33.9}Nb_{7.6}Cu_{6.4}Be_{12.5}$ (DH3) alloys reported by Hofmann, *et al* [7] are in situ composite alloys formed during solidification process as show in Figure 2.2a and Figure 2.2b, correspondingly. The DH3 composite is used in my PhD research as detailed in Chapter 4. For the ex-situ made composites, the reinforcement phase is added separately during the processing of the alloy. Consequently, the interface between the matrix and the secondary phase may not be very strong.

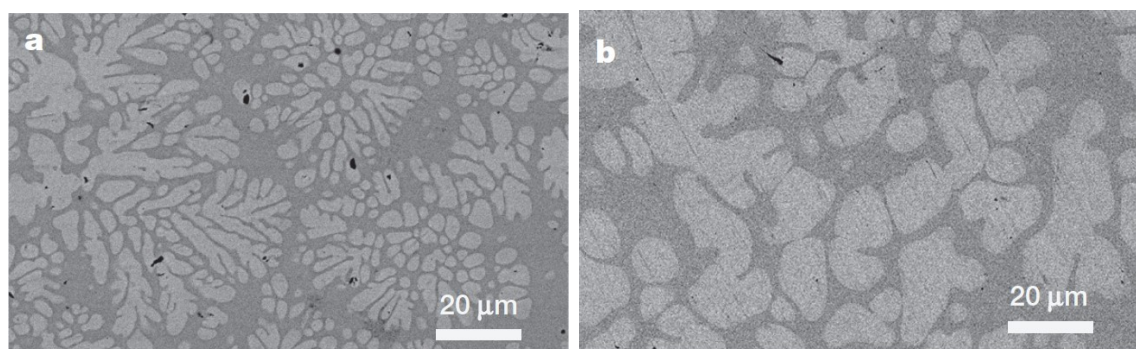


Figure 2.2 The SEM images of the in situ formed composite (a) DH1 (b) DH3 [7].

2.2 Local atomic structure of metallic glasses

Since the discovery of the first MG ($\text{Au}_{75}\text{Si}_{25}$) in 1960, there has been an increasing interest in developing and understanding this new family of materials. Among the many unresolved scientific questions and puzzles, the atomic-level structure and structure–property relationship [26] are one of the central topics concerning researchers in physics, materials and engineering communities. The important publications, methods, theories, models, and development in this field, especially those directly relevant to the research of my PhD study are reviewed below.

Hirata, *et al* [43] made direct observations of the local atomic order of bulk metallic glasses (BMGs) and concluded that: “Amorphous materials do not have any translational and rotational symmetry down to the sub-nanoscale because of their disordered atomic arrangement. Thus, it is quite difficult to experimentally characterise their atomic structure by conventional diffraction, spectroscopic and imaging techniques. Various structural models, such as Bernal’s ‘dense random packing’, Gaskell’s ‘short-range order’ and the recent ‘solute-centred quasi-equivalent cluster models’, have been proposed in the past 50 years” [43].

According to Cheng [33], Hirata [43] and Egami [44] there are two major challenges in the study of BMGs structures: how to construct a realistic 3D amorphous structure, using experimental and/or computational tools and how to effectively characterise a given amorphous structure and extract the key structural features relevant to the fundamentals of glass formation and properties, using appropriate structural parameters.

Table 2.3 lists a wide range of structure parameters that have been proposed and used by numerous researchers [33] in the past for interpreting and understanding the local atomic structures of BMGs.

Table 2.3 Structure parameters for atomic structure of BMGs [33].

Structure parameter	Abbreviations	Definition – characterization
Pair distribution function	PDF	Pair correlation representing the probability of finding atoms as a function of distance r from an average centre atom
Structure factor	$S(Q)$	The partial PDFs are directly related to partial structure factors in reciprocal space via Fourier transformation
Coordination number	CN	The number of atoms that are in the nearest-neighbour shell of a given centre atom
Chemical short-range order	SRO	For a structure with more than one species, it is useful to analyse the chemical make-up of the nearest-neighbour atoms, and compare with the composition of the alloy. This reflects how far the local chemistry deviates from the expectation of a random solution, i.e., the degree of chemical SRO
Bond angle distribution	BAD (θ)	Bond angle distribution is a three-body correlation describing the spatial relations of three neighbouring atoms. One first determines the nearest-neighbour atoms that are “bonded” with the centre atom. Then the angles between each and every two bonds are calculated. The same is repeated for all atoms in the system to obtain the distribution
Bond orientational order	BOO	The BOO is a many-body correlation and is a quantitative description of the bond orientational symmetry around the centre atom, which concerns multiple bond angles and their spatial relationship. The normalized parameter W_i evaluates the bond orientational order, and differentiates the various local environments
Common neighbour analysis	CAN	CNA is a multi-body correlation between neighbouring atoms. In CNA, each pair of nearest-neighbour atoms is given in a three-number index, $ijkl$. j is the number of nearest neighbours common to both atoms in the pair. k is the number of bonds between the j atoms themselves. l is the number of bonds in the longest continuous chain formed by the k bonds. CNA can detect various local atomic arrangements. Example: CNA index of 555 corresponds to a pentagonal bipyramid, which is the building block of an icosahedron
Voronoi tessellation	VT	VT is a scheme to divide the 3-D space into cells centred by each atom. A plane is drawn to bisect each line connecting the centre atom and one of the neighbouring atoms, and the cell enclosed by all the inner planes is called a Voronoi cell, or Dirichlet cell, or Wigner-Seitz primitive cell

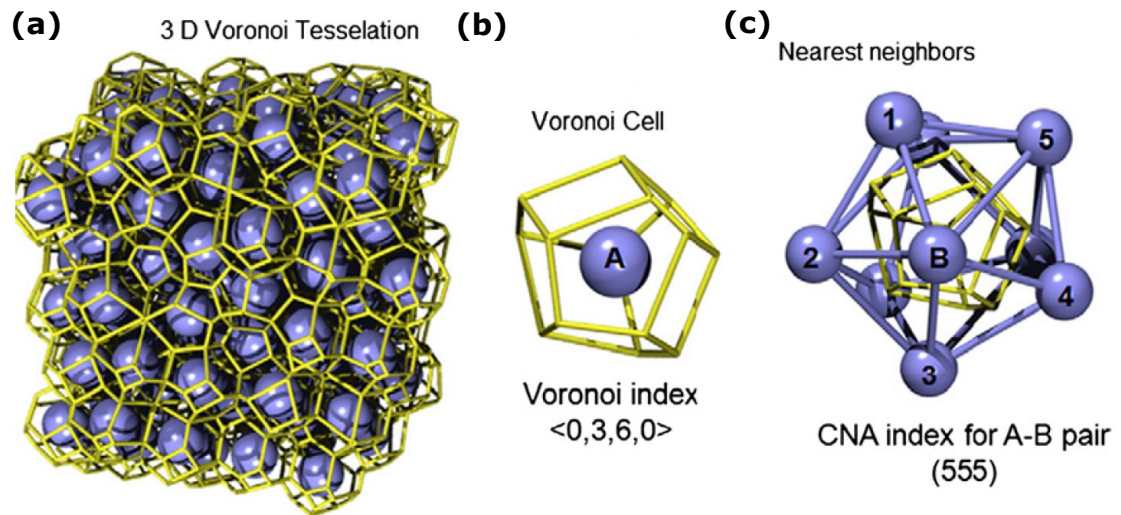


Figure 2.3 (a) 3D Voronoi tessellation (b) Voronoi cell (c) the nearest neighbours of A.

For example, Figure 2.3a shows an example of using Voronoi tessellation (named after Russian–Ukrainian scientist G.F. Voronoi 1868–1908) method to represent the 3D configuration of an amorphous structure [33] that is constructed by space tiling of Voronoi cells, while the motif of each cell (the centre atom) is determined by the spatial arrangement of the nearest neighbours. The example Voronoi cell in (Figure 2.3b) has three quadrangular faces and five pentagonal faces, and thus has a Voronoi index of $\langle 0, 3, 6, 0 \rangle$. The A–B pair forms a 5-fold bond, and the example in (Figure 2.3c) has five common neighbours (1–5) forming a loop, with a CNA index of 555.

However, for BMGs, direct reconstruction of the local 3-D structure is very difficult. Cheng and Ma, in review paper [33] says: “Some experimental techniques can be used to extract statistical information about the average glass structure, but the data usually cannot provide a complete picture. Nevertheless, the experimental results still serve as a yardstick against which any hypothetical structural model should be verified.” Structural studies have been transformed in recent years by acceleration in the acquisition of X-ray and neutron scattering data, and by improved computational methods, including the reverse Monte-Carlo method to fit measured data, and molecular-dynamic simulations [44]. A summary of the experimental and computational methods used in studying local atomic structure of BMGs is presented in Table 2.4.

Table 2.4 Experimental and computational methods for studying local atomic structure of BMGs [26].

Experimental techniques	Computational methods
X-ray/neutron diffraction (XRD)	Reverse Monte Carlo modelling (RMC)
X-ray absorption fine structure (XAFS)	Molecular dynamics simulation (MD)
Fluctuation electron microscopy (FEM)	Quantum molecular dynamic
Transmission electron microscopy (TEM)	Classical molecular dynamics
Nuclear magnetic resonance (NMR)	(classical MD)

2.2.1 Short-range order, medium-range order and long-range order

A solid is a crystalline if it has long-range order (LRO). The LRO is describing as the range above 20 Å of atomic distance. If the positions of an atom and its neighbours are known, the place of each atom can be identified throughout the crystal. On the other hand, most liquids only have the short-range order (SRO), and lack of the long-range order. Short range is defined as the first- or second-nearest neighbours of an atom, usually within 5 Å of atomic distance. In many liquids the first-neighbour atoms are arranged in the same structure as in the corresponding solid phase. However, at distances that are many atoms away, the positions of the atoms become uncorrelated. The medium-range order (MRO) can be defined as the next-level structural organization beyond the SRO [45] and is describe as the range between 5 Å and 20 Å of atomic distance. The atomic packing of metallic glasses was particular in the short-range order (SRO) and medium-range order (MRO) [46, 47].

2.2.2 Synchrotron X-ray diffraction for total and anomalous scatterings studies of metallic glasses

X-ray is an electromagnetic radiation that widely used in material characterisation because the short wavelength (0.01Å to 100Å) and highly penetrability. Three different techniques are often used: X-ray imaging, X-ray scattering and X-ray spectroscopy [48].

X-ray images are formed when X-ray passing through a sample and projecting onto an X-ray detector. The images will have different contrast depending on the elements of the sample which attenuate the incident X-ray beam.

X-ray scattering works by measuring the intensity and directions of the scattered X-ray exited from the sample. The scattering patterns contain the structure information of the samples.

X-ray spectroscopy measures the different energies that are absorbed when an incident beam passing through the sample. It provides information that identifies specific atoms in the sample.

In this project, synchrotron X-rays and the scattering technique was used primarily to study the structures of MGs, BMGs and their composites.

Synchrotrons are large research facilities that capable to produce intense and high energy X-rays than a laboratory X-ray sources [49]. Figure 2.4 shows a schematic diagram of a synchrotron light source. All synchrotron facilities use the same principle [50] to generate electrons to circulate inside the storage ring with a speed near the speed of light. The information of how electrons are generated can be easily found in the website of any synchrotron facility, and therefore not repeat here.

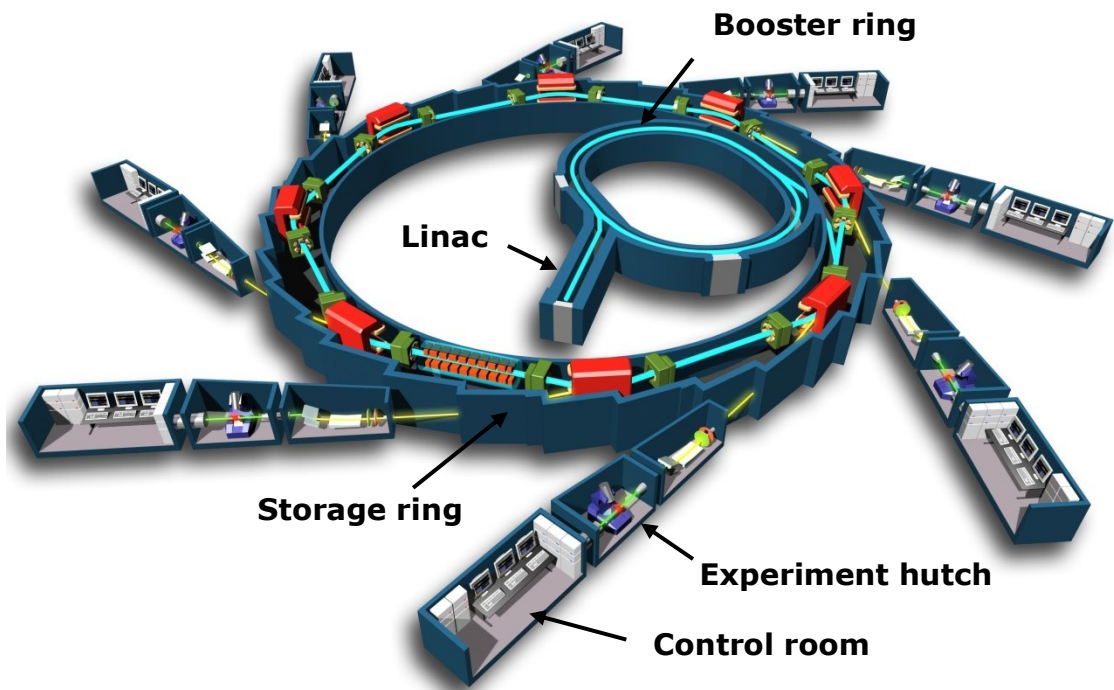


Figure 2.4 Schematic of Synchrotron light source [51].

When the circulating electrons are deflected from their straight path by a bending magnet (Figure 2.31b), or any insertion devices (normally wiggler and undulator) X-rays are generated and emitted tangentially from the

storage ring. The synchrotron light from a bending magnet covers a wide and continuous spectrum, from microwaves to hard X-rays [50]. However it is much less focused and less brilliant than the X-rays generated by the insertion devices which are placed at the straight section of storage ring for increasing significantly the brilliance of the X-rays generated. An insertion device is made up of a complex array of small magnets that are used to force the electrons to follow an undulating or wavy trajectory [52]. At each bend, X-rays are generated, overlapping and interfering with other bends, resulting in more focussed and brilliant X-ray beam than that from a single bending magnet. There are two types of insertion devices: multipole wiggler and undulator which provide different wavelength profiles. Figure 2.31c shows the schematic diagram of the multipole wiggler. It produces a cone of X-rays which emitted at each bend in the 'wiggle' and superimpose on each other. The multipole wiggler produces a broader spectrum of wavelengths as compared to an undulator insertion device. Figure 2.31d shows the schematic diagram of the undulator. It uses less powerful magnets than the multipole wiggler to produce a gentler undulation of the beam. The X-rays produce at each bend overlap and interface with each other, so that at certain wavelength of X-rays will be enhanced by 10,000 times [53]. These specific wavelengths can be changed by altering the gap between the component magnets. Figure 2.31a shows the brilliance of X-rays produced by different insertion devices.

X-ray crystallography (X-ray diffraction from crystal) was widely used to determine the crystal structure of crystalline materials [54]. As shows in Figure 2.6a, when an incident X-ray beam hits onto an array of atoms, X-rays are diffracted into specific directions and if the material exhibits a long-range, periodic atomic order, such as a crystal, a diffraction pattern with numerous sharp spots, called Bragg diffraction peaks are generated as shows in the 1D spectrum of bulk metallic matrix composite which consists of crystalline phase (Figure 2.6c). The spacing between crystals can be calculated by the Bragg's law:

$$n\lambda = 2d \sin\theta$$

Where λ is the X-ray wavelength, d is the spacing between the crystal, θ is the scattering angle (half of 2θ). The structure of the crystals can be identified by comparing with the well-established lattice patterns [54].

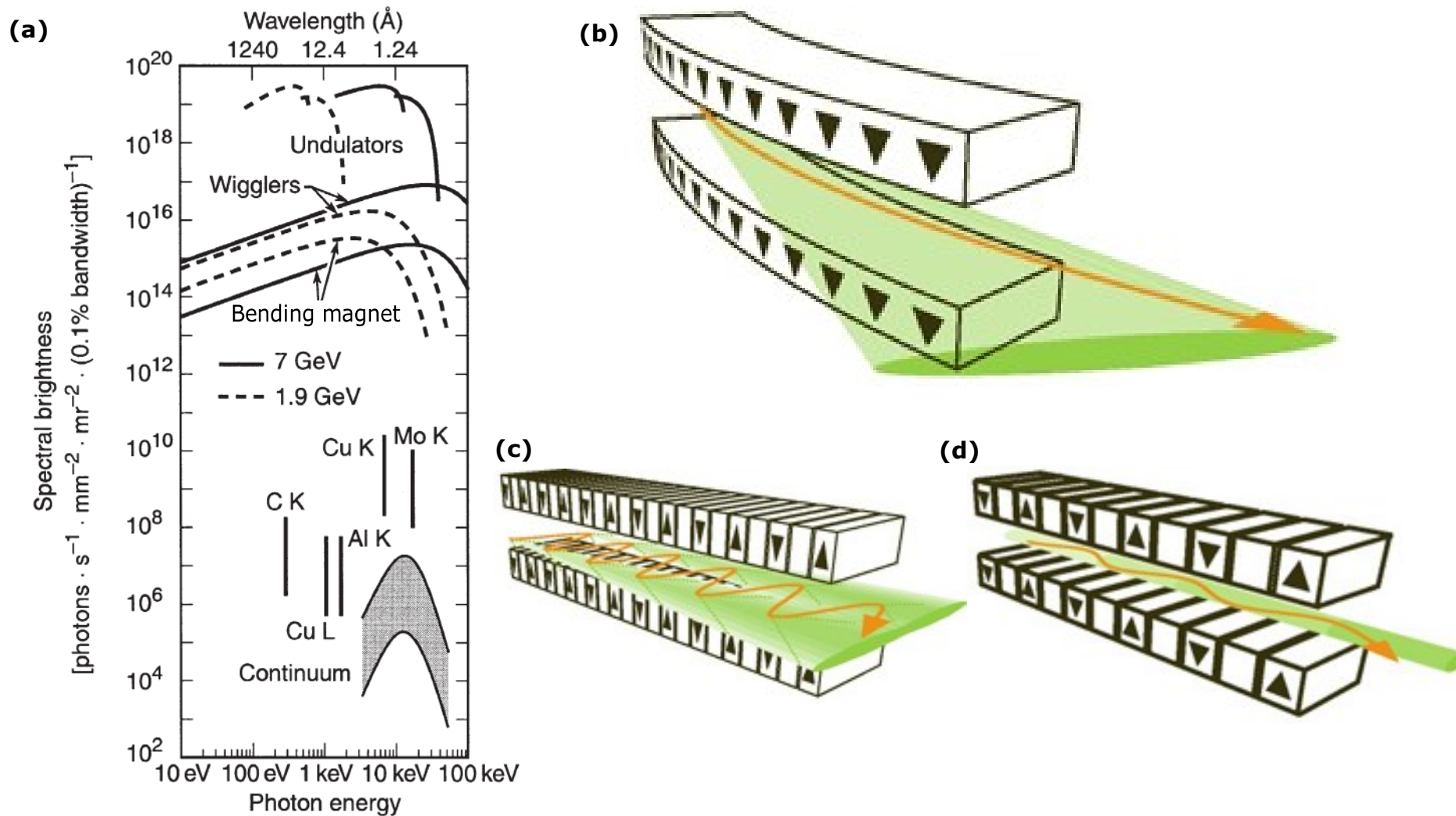


Figure 2.5 (a) X-ray brilliantness against the photon energy, showing the significant increase in brilliantness for different X-ray sources [50] and schematic diagrams of electromagnets (b) bending magnet (c) multipole wiggler insertion device (d) undulator insertion device [53].

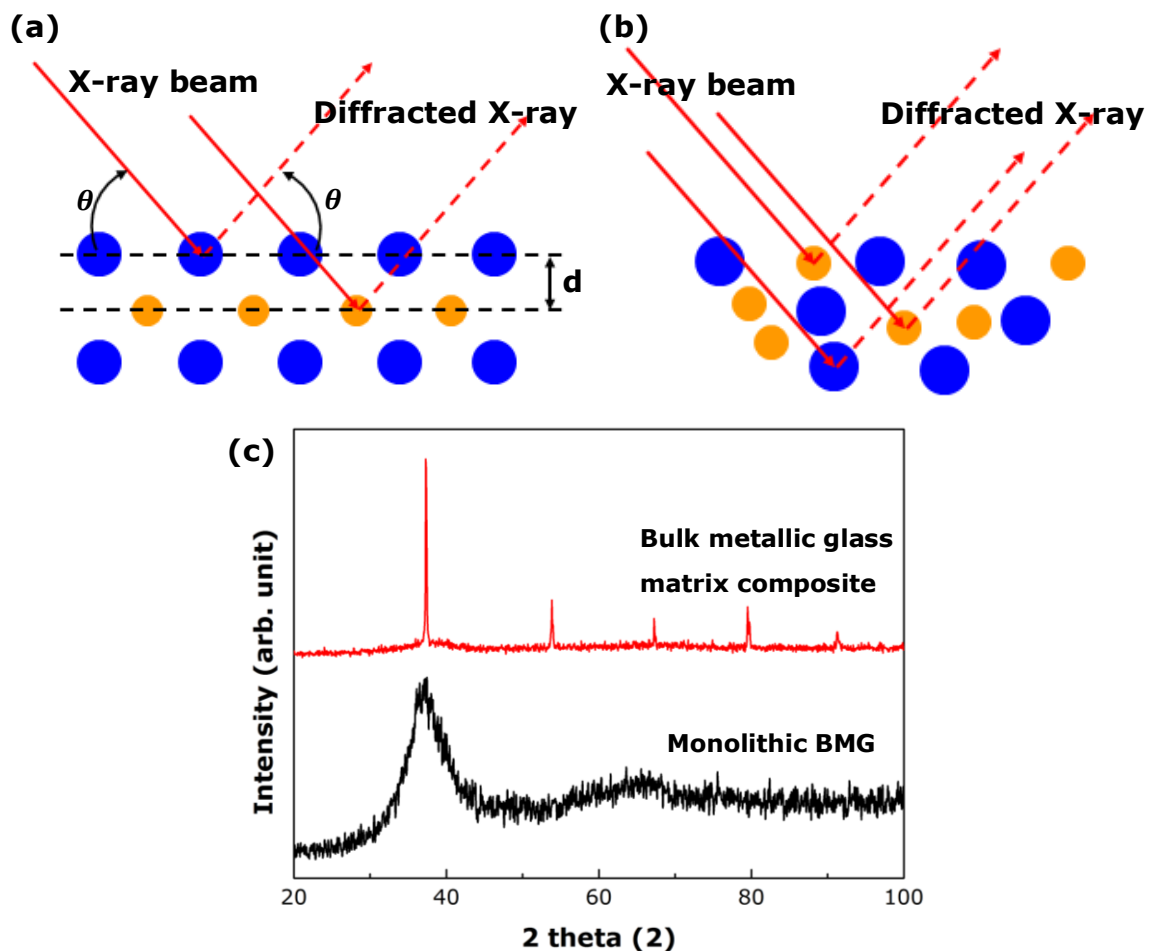


Figure 2.6 Schematic diagram of X-ray diffraction on a crystalline plane (a) and on amorphous (b) and (c) 1D spectra of X-ray diffraction on BMGMC and monolithic BMG.

X-ray scattering on amorphous materials and total scattering/pair distribution function techniques

When X-rays shine on materials that exhibit short range, non-periodic and disordered atomic structure such as a glass or a liquid, it produces an X-ray pattern that are very diffuse in nature as shows in black profile Figure 2.6b. It feature a first sharp diffraction peak (FSDP) follow by several broad and low intensity peaks. To study the atomic structure, one can utilise the total scattering technique which not only take account of the Bragg's scattering but also the diffuse scattering [55].

As shows in Figure 2.6c, the 1D spectrum of a monolithic BMG, the intensity of the diffuse scattering is relatively weak compared to the sharp Bragg's peak, therefore it is usually covered by the background scattering noise generated by the instrument and environment. Hence, total scattering

experiments are usually carried out using synchrotron X-ray source which has a very “clean” background.

The total intensity of the scattered X-rays, I_T are composed of several parts:

$$I_T = I_C + I_{IC} + I_{MC} + I_{BG}$$

Where I_C is the coherent scattering intensity, I_{IC} is the incoherent scattering intensity, I_{MC} is the multiple-scattering intensity, and I_{BG} is the background intensity.

The total scattering intensity I_T is measured as a function of the scattering angle, 2θ , and the wavelength of the probe, λ . For elastic scattering, the diffraction vector, Q , defined as below:

$$Q = \frac{4\pi \sin\theta}{\lambda}$$

Where λ is the wavelength of the scattered particle and $\theta = 2\theta/2$, where 2θ is the angle between the incident and diffracted beams. In the case of powder measurements, the only relevant quality is the magnitude of the diffraction vector, Q . We note that since $\sin\theta \leq 1$, the experimentally accessible range for Q is limited to less than $4\pi/\lambda$. For instance, Cu K_α radiation, which is most widely used in laboratory X-ray facilities, has a wavelength of 1.54\AA . This mean the range of Q is limited to about 8\AA^{-1} . In general, for the total scattering study, the Q range of $\sim 20\text{-}40\text{\AA}^{-1}$ is preferred [55].

Figure 2.7 shows the interaction of the X-ray with atom. X-ray photons are scattered by atom through interaction with electrons. The electron is accelerated by the electromagnetic field of the incident photon which induces oscillation of the electron and result in scattered photon. If the energy (wavelength) of the photon remains unchanged the process is called elastic or coherent scattering (case 3). Weakly bound electrons can recoil upon interaction with a photon and absorb some energy. In this case the X-

ray photon loses energy (shift to longer wavelength). This is incoherent (inelastic) or Compton scattering (case 4). As for the multiple scattering, it occurs mainly within the sample that the scattering event occurs more than 1 time. The background intensity here includes scattering without the sample, due to the air, optical system (lenses, slit), and etc.

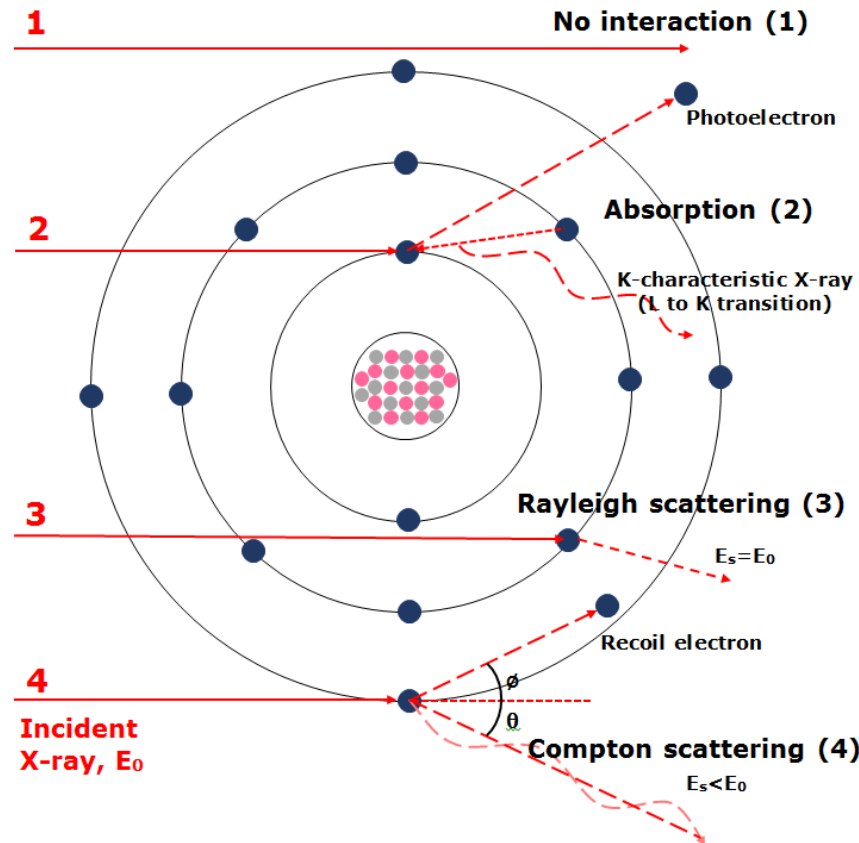


Figure 2.7 Schematic diagram of X-ray interaction with a Si atom.

Structure factor $S(Q)$

The basis of the total-scattering method is the normalized, measured, scattering intensity from a sample, the total-scattering structure function, $S(Q)$ [44]. This intensity distribution is a continuous function of the wave vector, Q , and, in general, contains both Bragg and diffuse intensity. It is the theoretically normalized scattering intensity from the atom and can be experimentally measured and corrected using following equation:

$$S(Q) = 1 + \frac{I_e(Q) - [\sum_{i=1}^n c_i f_i^2(Q)]}{[\sum_{i=1}^n c_i f_i^2(Q)]^2}$$

Where $I_e(Q)$ is the normalized elastically scattered intensity, and c_i and $f_i(Q)$ are the atomic concentration and the scattering factor of the i atom in the alloy, respectively.

Reduced pair distribution function $G(r)$

The pair distribution function is a correlation function of the distribution between particle pairs within a given volume. Mathematically, if a and b are two particles in a fluid, the PDF of b with respect to a denoted by $G_{ab}(r)$ and it is the probability of finding the particle b at the distance r from a.

The microscopic real-space structure of a material can be obtained by Fourier transform the $S(Q)$ into the reduced pair distribution function, $G(r)$ with following equation [44], where r is distance between the pair atoms in Angstroms unit:

$$G(r) = \frac{2}{\pi} \int_0^{Q_{max}} Q(S(Q) - 1) \sin(rQ) dQ$$

The scattering factor of an atom is nearly independent of the energy of X-rays except in the vicinity of the absorption edge of the atom where it depends rather strongly on the X-ray energy E ,

$$f(Q, E) = f_0(Q) + f'(E) + if''(E)$$

Where $f'(E)$ and $f''(E)$ are the anomalous scattering dependent on X-ray energy [56]. The $f'(E)$ is the real part which related to the scattering of the atom and $f''(E)$ is the imaginary part which related to the absorption of the atom.

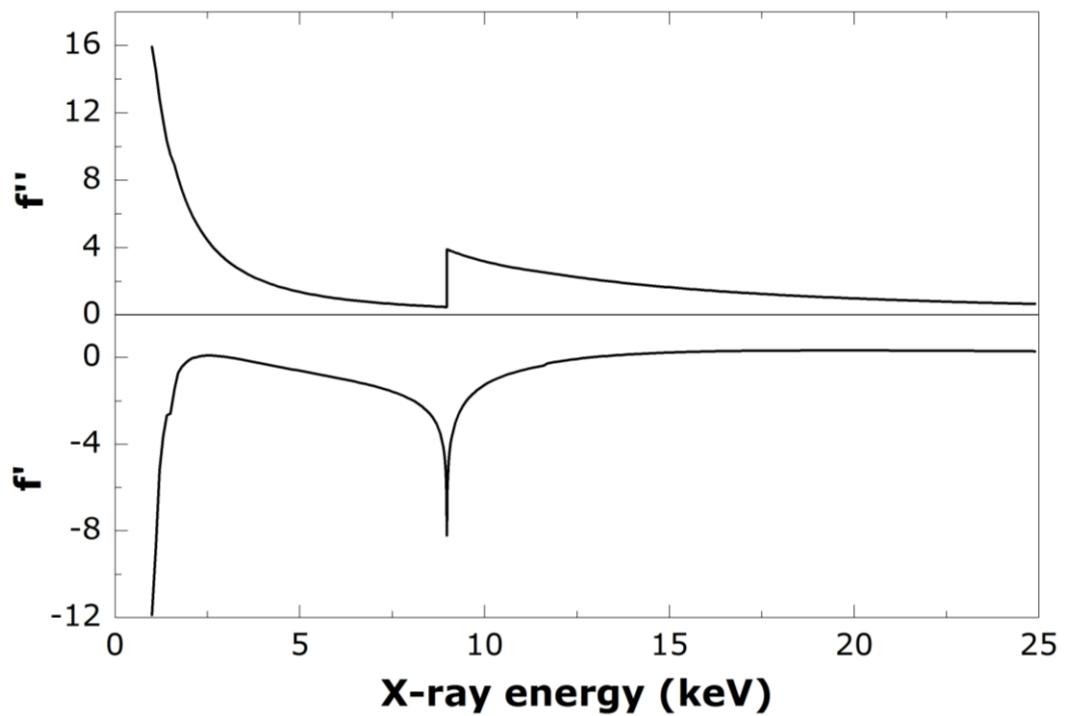


Figure 2.8 The intensity of f' and f'' for Cu element against the X-ray energy extracted from the NIST database [56].

Figure 2.8 shows an example of the energy dependence of f' . This energy dependence is known as anomalous dispersion and originates from the resonance of the X-ray with the excitation of electrons in the core of an atom. Thus, if one tunes the X-ray energy to the edge of an element, the scattering power from the particular element varies strongly with energy, while the scattering from other elements remain more or less constant. We can take advantage of this special nature of interaction between an atom and X-ray to determine the differential and partial PDF. By carrying out the measurement at two or more energies in the vicinity of the edge of the element α , the scattering power $f_{\alpha}(Q)$ if the α atoms change but those of the other constituent ions do not. By taking the derivative of $S(Q)$ with respect to $f_{\alpha}(Q)$, by repeating on other element in the system it is possible to obtain the partial pair distribution function [44].

Currently the most possible resolvable case is a ternary alloy because more than three elements, there are too many measurement required. For example, Hosokawa, *et al* used the anomalous X-ray scattering to resolve the partial PDF of the $\text{Pd}_{40}\text{Ni}_{40}\text{P}_{20}$ and $\text{Zr}_{63}\text{Ni}_{25}\text{Al}_{12}$ BMGs [57, 58].

2.2.3 Dense random packing model

In 1960, Bernal [59, 60], Scott [61] and Finney [62, 63] as the pioneers in this field, proposed the dense random packing (DRP) model for modelling the structure of monatomic metallic liquids. The atoms in metals are approximated using hard spheres. Using this idea, the hard spheres should be packed in such a manner that there exists no one hole (empty space) in 3D space that is sufficiently large to accommodate one more identical sphere without adjusting its neighbours [33]. Based on this principle, Bernal proposed that five types of holes with edges of equal length (i.e., equilateral triangle faces) are likely the basic structural units of monatomic liquids. Figure 2.9 presents the Bernal's canonical holes. In each panel, the left figure shows the hard sphere packing surrounding the hole, and the right figure shows the hole in the centre (the radius of the pink sphere is the size of the hole). Over six decades of MGs research has approved that the trend to achieve the densest packing is a key factor in governing the structure of metallic liquids and glasses [26].

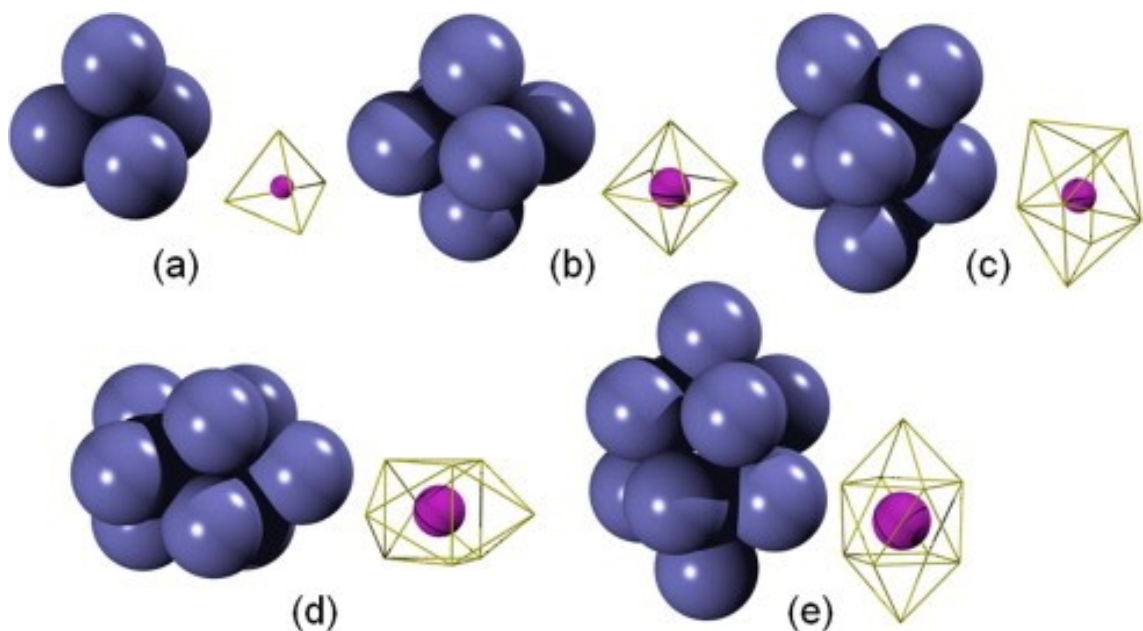


Figure 2.9 Bernal's canonical holes. (a) tetrahedron (b) octahedron (c) tetragonal dodecahedron (d) trigonal prism capped with three half octahedra (e) Archimedean antiprism capped with two half octahedra [33].

2.2.4 Structure of ETM–LTM metallic glasses

ETM–LTM are the most common metallic glasses, many ETM–LTM-based compositions can be made into BMGs of relatively large sizes, with

properties that are currently being intensively studied. The most popular metallic glasses from this category are: Cu–Zr binary metallic glasses [64, 65], Cu–Zr–Al metallic glasses [66], Cu–Zr–Ag metallic glasses [67], (Ti, Zr, Nb, Hf, Ta)–(Ni, Cu, Pd, Ag)–(Al)–(Be) metallic glasses [68].

Typically 3D configurations of the $\text{Cu}_{46}\text{Zr}_{54}$ and $\text{Cu}_{46}\text{Zr}_{47}\text{Al}_7$ BMGs samples obtained in MD simulation are presented in Figure 2.10 [66]. Apparently, the population and degree of connectivity are higher in $\text{Cu}_{46}\text{Zr}_{47}\text{Al}_7$ (Figure 2.10d) than those in $\text{Cu}_{46}\text{Zr}_{54}$ (Figure 2.10c).

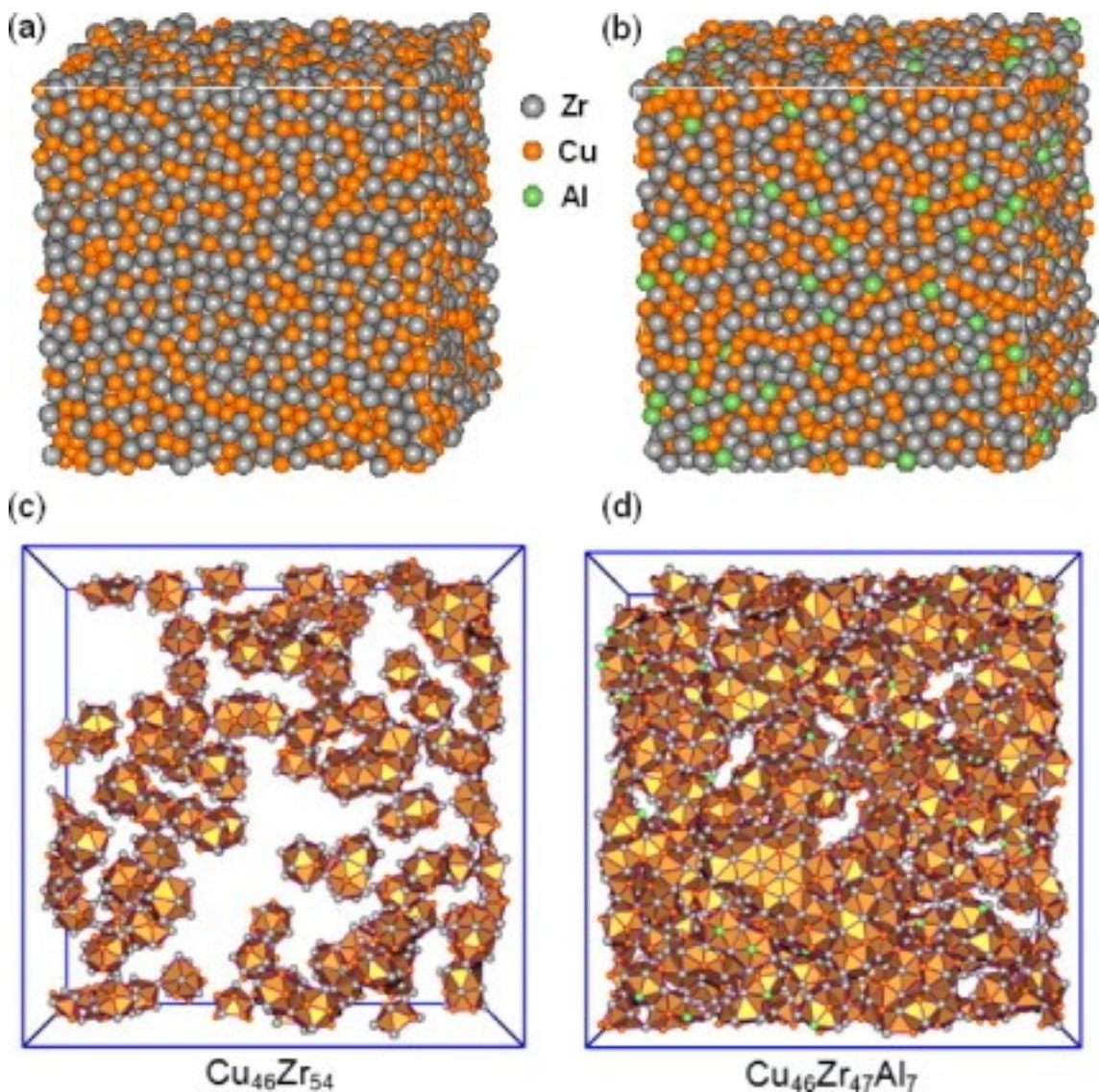


Figure 2.10 3D configuration of the MG samples obtained in MD simulation for (a) $\text{Cu}_{46}\text{Zr}_{54}$ (b) $\text{Cu}_{46}\text{Zr}_{47}\text{Al}_7$ and the corresponding population and degree of connectivity for each case (c) and (d) [66].

2.2.5 Structure of LTM + NM metallic glasses

These MGs are from the category of binary prototype (Ni-P, Pd-Si, Au-Si-Ge, Pd-Ni-Cu-P, Fe-Cr-Mo-P-C-B). Among them, the Palladium based metallic glasses, owing to their superior damage-tolerance capacity, were considered as a superior alternative to conventional palladium dental alloys [31]. A typical simulated structure for a binary Ni₈₁B₁₉ alloy is presented in Figure 2.11. The chemical ordering is very interesting in that the solute boron atoms are fully coordinated by solvent nickel atoms and do not make contact with each other [46].

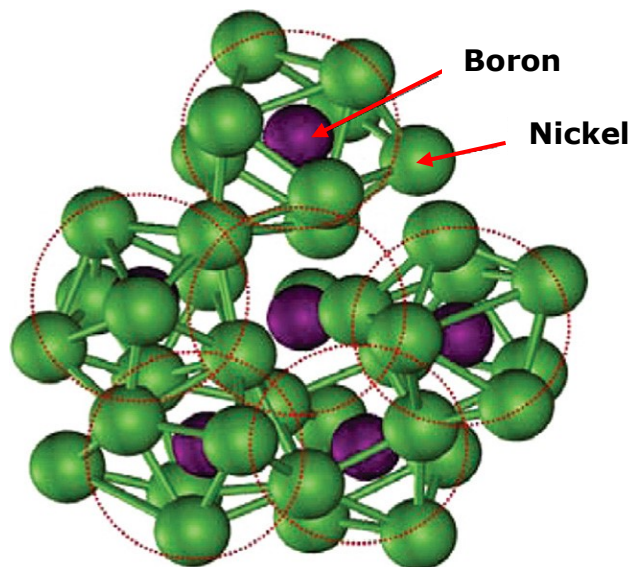


Figure 2.11 Structure of Ni₈₁B₁₉ metallic glass obtained from ab initio MD simulation [46].

2.2.6 Quasicrystals in metallic glasses

Quasicrystals are ordered structures, predictable but not periodic crystals. The Bragg diffraction pattern of quasicrystals shows sharp peaks with other symmetry orders, for instance 5-fold, rather than the 2, 3, 4, and 6-fold rotational symmetries commonly found in ordinary crystals [69]. Quasicrystals was firstly reported by Shechtman *et al* in 1984 [70]. Since Shechtman's discovery, hundreds of quasicrystals were reported in Aluminium alloys (Al-Li-Cu, Al-Mn-Si, Al-Ni-Co, Al-Pd-Mn, Al-Cu-Fe, Al-Cu-V) and in other compositions (Cd-Yb, Ti-Zr-Ni, Zn-Mg-Ho, Zn-Mg-Sc, In-Ag-Yb, Pd-U-Si [71]).

There are two types of quasicrystals [69]: The first is polygonal (dihedral) quasicrystals which have an axis of 8, 10, or 12-fold local symmetry (octagonal, decagonal, or dodecagonal quasicrystals, respectively). They are periodic along this axis and quasiperiodic in planes normal to it. The second is icosahedral quasicrystals that are aperiodic in all directions. Regarding thermal stability, there are three types of quasicrystals: (1) stable quasicrystals grown by slow cooling or casting with subsequent annealing, (2) metastable quasicrystals prepared by melt-spinning, and (3) metastable quasicrystals formed by the crystallization of the amorphous phase [72]. Figure 2.12 shows an atomic model for the 5-fold Al-Pd-Mn quasicrystal and a scanning tunnelling microscopy image of a $8.6 \times 8.6 \text{ nm}^2$ area [73].

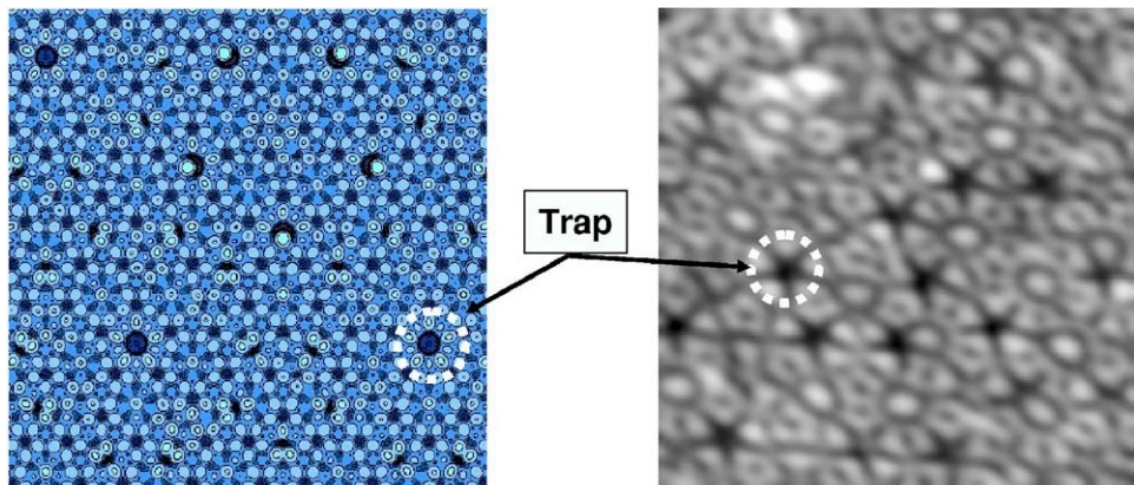


Figure 2.12 (a) An atomic model for 5-fold Al-Pd-Mn quasicrystal, and (b) a scanning tunnelling microscopy image of an $8.6 \times 8.6 \text{ nm}^2$ area [73].

Structure of 5-fold symmetry is common in liquids and BMGs and structural similarities between quasicrystals and metallic glasses certainly exists [26]. The icosahedral quasicrystals were founded in many metallic glass alloys, for example, in Cu-rich alloys and Cu-Zr systems. A summary of the structural models for MGs is presented in Table 2.5 [33].

Table 2.5 Summary of structural models for MGs [33].

Structural model	Symbol	Descriptors
Densest packing with identical hard spheres [74]	DRPHS	Starting from a single sphere, Bernal's holes including the tetrahedron, essentially a frustrated polytetrahedral packing.
Polytetrahedral packing model [75, 76]	PPM	Triangulated coordination shells surrounding the centre atom with nearly equal edges. The polytetrahedral model describes the SRO only.
Stereochemical model [77]	SM	The nearest-neighbour interaction is the strongest of all; the SRO in MGs is the same as that in the corresponding crystals, while the differences lie in the MRO (Gaskell). Available for a particularly a group of LTM-NM MGs.
Efficient cluster [78]	ECP	To achieve stable solute-centred clusters by selecting the size ratio R between centre solute and surrounding solvent and how these clusters are connected and arranged in medium range.

2.3 Design and manufacturing of BMGs and BMG composites

2.3.1 Glass forming ability

The concept of critical cooling rate can be easily understood by referring to the time-temperature-transformation (T-T-T) diagram. Figure 2.13 shows the schematic diagram of T-T-T for a hypothetical alloy. The transformation curve, which has a C-shape, represents, at any given temperature, the time required to start the formation of stable (crystalline) solid phase. If the alloy is cooled from the liquid state under equilibrium condition, for example in case 1, solidification will require a very long time and the solidified product will be crystalline. If the alloy is solidified at a higher rate, for example in case 2, which represents a tangent to the C-curve at its nose, then crystal formation will not take place. The cooling rate represented by curve of case 2 is "referred" as critical cooling rate, R_c . The significance of this value is that if the liquid alloy is cooled above this rate, then it is possible to form a completely glass. If the solidified alloy is heated above the T_g , for example in case 3, it will remain in the supercooled liquid region as long as it away from the crystallization curve. Whereas, in case 4, once the solidified touches the crystallization curve, crystals will start to form within the supercooled liquid and the temperature for the crystallization is defined as T_x .

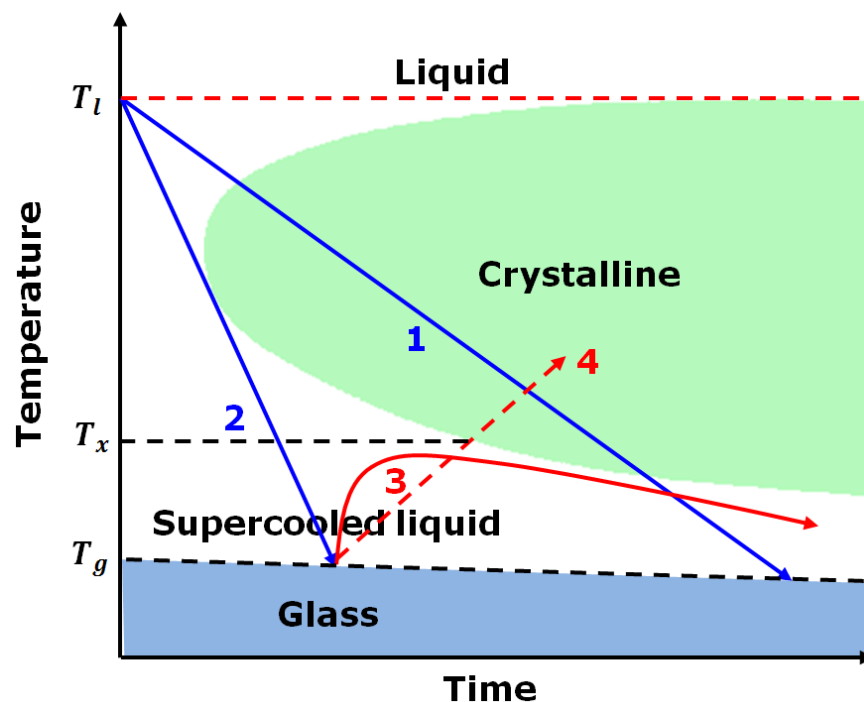


Figure 2.13 Schematic diagram of time-temperature-transformation (T-T-T) for a hypothetical alloy.

Glass forming ability (GFA) is the key parameter in characterising the ability of glass forming for MGs. Until now, there is no standard definition for GFA, and many indicators have been proposed to either link with or measure GFA. Although the direct and quantifiable GFA indicator of an alloy could be the critical cooling rate, R_c , and the maximum section of thickness, t_{\max} or diameter, d_{\max} , it is very difficult to obtain experimentally [23, 79, 80]. Thus, significant efforts have been devoted on searching for the GFA criteria or parameter. Table 2.6 summarised the proposed criteria and parameter with the year and authors in determined the GFA.

2.3.2 Alloy design and selection principles

BMGs are multi-component metallic alloy systems. Although exponential number of publications have touched or discussed in one way or another on developing guidelines or principles for alloys design, unfortunately, until now, there are no universal alloy design rules that work for all alloy systems [81]. Many alloy development efforts in the past had used three empirical rules proposed by Inoue [82]:

1. Multi-component, consisting of three elements or more,
2. Significant atomic size mismatch $>12\%$ among the three main constituent elements, and
3. Negative heats of mixing among the three main elements.

Cai *et al* [81] gave a comprehensive review on the methods used for designing and developing multi-component bulk metallic glasses as listed in Table 2.7.

The similitude principle is actually very effective. In this research, we primarily used this method and the above empirical rules to develop successfully a new system of bulk metallic glass alloys with high glass forming and high neutron absorption capability as detailed in Chapter 6.

Table 2.6 GFA criteria and parameter.

Year	Criteria/Parameter	Authors	Equation
1969	Reduced glass transition temperature, T_{rg}	Turnbull [83]	$T_{rg} = \frac{T_g}{T_l}$
1972	K_{gl} parameter	Hrubý [84]	$K_{gl} = \frac{T_x - T_g}{T_m - T_x}$
1995	Supercooled liquid region, ΔT_x parameter	Inoue [85]	$\Delta T_x = T_x - T_g$
2002	γ parameter	Lu and Liu [86, 87]	$\gamma = \frac{T_x}{T_g + T_l}$
2005	α parameter	Mondal and Murty [88]	$\alpha = \frac{T_x}{T_l}$
2005	β parameter	Mondal and Murty [88]	$\beta = 1 + \frac{T_x}{T_l} = 1 + \alpha$
2005	T_{rx} parameter	Kim, <i>et al</i> [89]	$T_{rx} = \frac{T_x}{T_s}$
2006	δ parameter	Chen, <i>et al</i> [90]	$\delta = \frac{T_x}{T_l - T_g}$
2007	γ_m parameter	Du, <i>et al</i> [91]	$\gamma_m = \frac{2T_x - T_g}{T_l}$
2007	ϕ parameter	Fan, <i>et al</i> [92]	$\phi = T_{rg} \left(\frac{\Delta T_x}{T_g} \right)^{0.143}$
2008	New β_1 parameter	Yuan, <i>et al</i> [93]	$\beta_1 = \frac{T_x \times T_g}{(T_l - T_x)^2}$
2009	ω parameter	Long, <i>et al</i> [94, 95]	$\omega = \frac{T_g}{T_x} - \frac{2T_g}{T_g + T_l}$
2010	Q parameter	Suo, <i>et al</i> [96]	$Q = \frac{T_g + T_x}{T_l} \times \frac{\Delta E}{\Delta H}$ where ΔE and ΔH the crystalline enthalpy and the fusion enthalpy
2011	β' parameter	Dong, <i>et al</i> [97]	$\beta' = \frac{T_g}{T_x} - \frac{T_g}{T_l \eta}$ where η has been optimally selected as 1.30

Table 2.7 The design methods for multi-component BMGs [81].

Design method	Description
Trial and error method [98, 99]	It is primarily a main method. It is applied to design the component of the BMG on the basis of existing phase diagrams, thermodynamic parameters, physical and chemical parameters and the component of the developed BMGs. The components are experimented one by one.
Nearly-free-electron method [100]	The method was proposed by Nagel and Tauc in 1975, that treats the alloy as a nearly-free-electron gas and employs many of the concepts used in Ziman's theory of liquid metals to describe the system. And then, are calculated the parameters relating to GFA such as energy levels, density states, fermi momentum, pseudo potential and structure factor by perturbation theory, and then, designing the component. This method can predict the correct composition range of metallic glasses.
Valence electron concentration method [101]	The method is to calculate chemical bond length, overlapping population and binding energy by using quantum chemistry on the basis of the cluster model, predicting the GFA and designing the component of metallic glasses.
Discrete variational method [102]	The method is a molecular orbital method titled by numerical self-consistent field method based on the density function theory. It is suitable for the macromolecules, macro-clusters and solid system, especially the system with heavy-atoms.
Thermodynamic and dynamic methods [103]	The method is to establish the thermodynamic or dynamic model for the alloys and calculate the thermodynamic and dynamic parameters, predicting the GFA or designing the component of the alloy.
Similitude principle and artificial neural network method (SPANNM) [104]	This method is to model based on similitude principle and artificial neural network because of the similarity between all kinds of the metallic glasses. In addition, the artificial neural network can extract usable information from large quantity of discrete data with noise and is usable for resolving the highly non-linear and uncertain problems.

2.3.3 Manufacturing and applications of BMGs and BMG composites

2.3.3.1 Melt spinning for manufacturing MG ribbons

The melt spinning is the most commonly used method for producing long and continuous rapidly solidified ribbons, wires and filaments [105, 106]. Figure 2.14 shows schematically the production of ribbons using melt spinning technique. The molten alloy melted in an induction coil is ejected through a nozzle onto a rotating copper wheel on which the heat from the molten alloy is extracted very quickly (cooling rate $> 10^5$ K/s) and solidified into continuous ribbons [107] with a typical thickness of 20-50 μ m and 2-5mm in width. The copper wheel rotation speed and the nozzle width are the important parameters in determining the thickness and width of the ribbon [107].

2.3.3.2 Copper mould casting for manufacturing BMGs

The most economical way to produce BMGs is using casting method, which is possible for BMGs (glass forming ability > 1 mm [108]). In 1974, Chen, *et al* firstly produced a BMG using water-quenching mould [108]. Since then, numerous casting techniques have been developed to manufacture BMG. This included high-pressure die casting [109, 110], copper mould casting [111-113], cap-cast technique [114], suction-casting method [115], squeeze-casting method [116, 117], and very recently continuous casting [118]. Among them, copper mould casting is still the widely used conventional casting method. Figure 2.15 shows a schematic diagram of the copper mould casting technique used in manufacturing the BMGs in this research. The master ingot alloy is melted by arc and then is poured into the water-cooled copper mould to form rod bar with stepped diameters. To avoid oxidation, the casting process is usually carried out under low vacuum or filled with inert gas such as argon or helium.

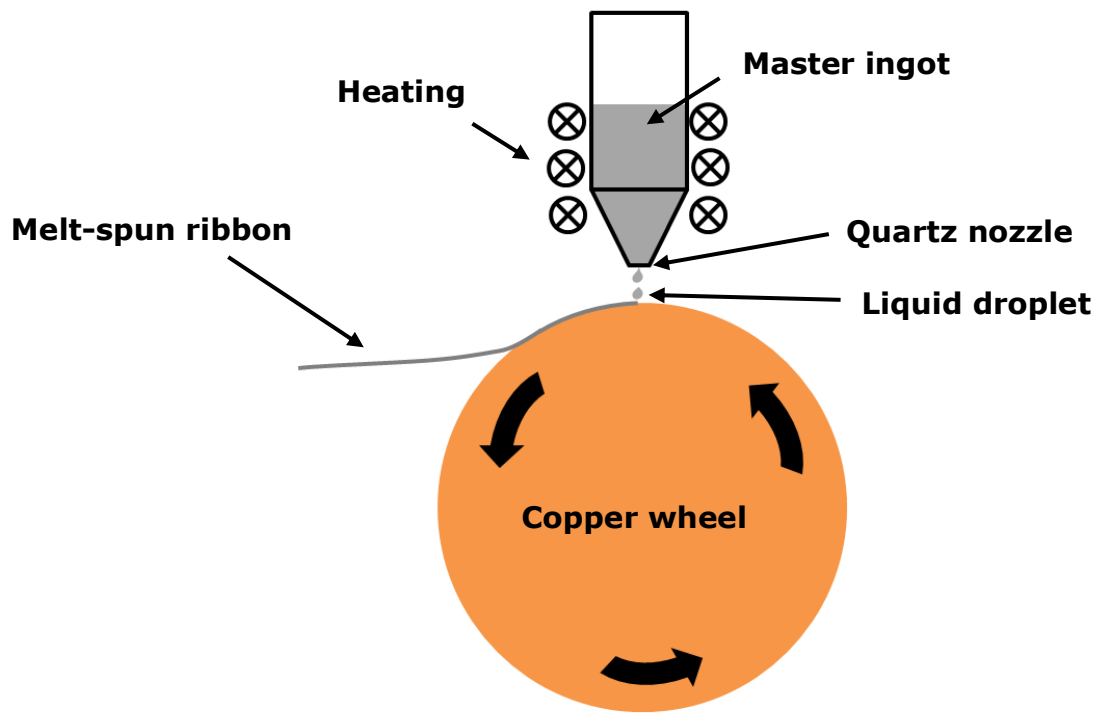


Figure 2.14 Schematic diagram of melting spinning process.

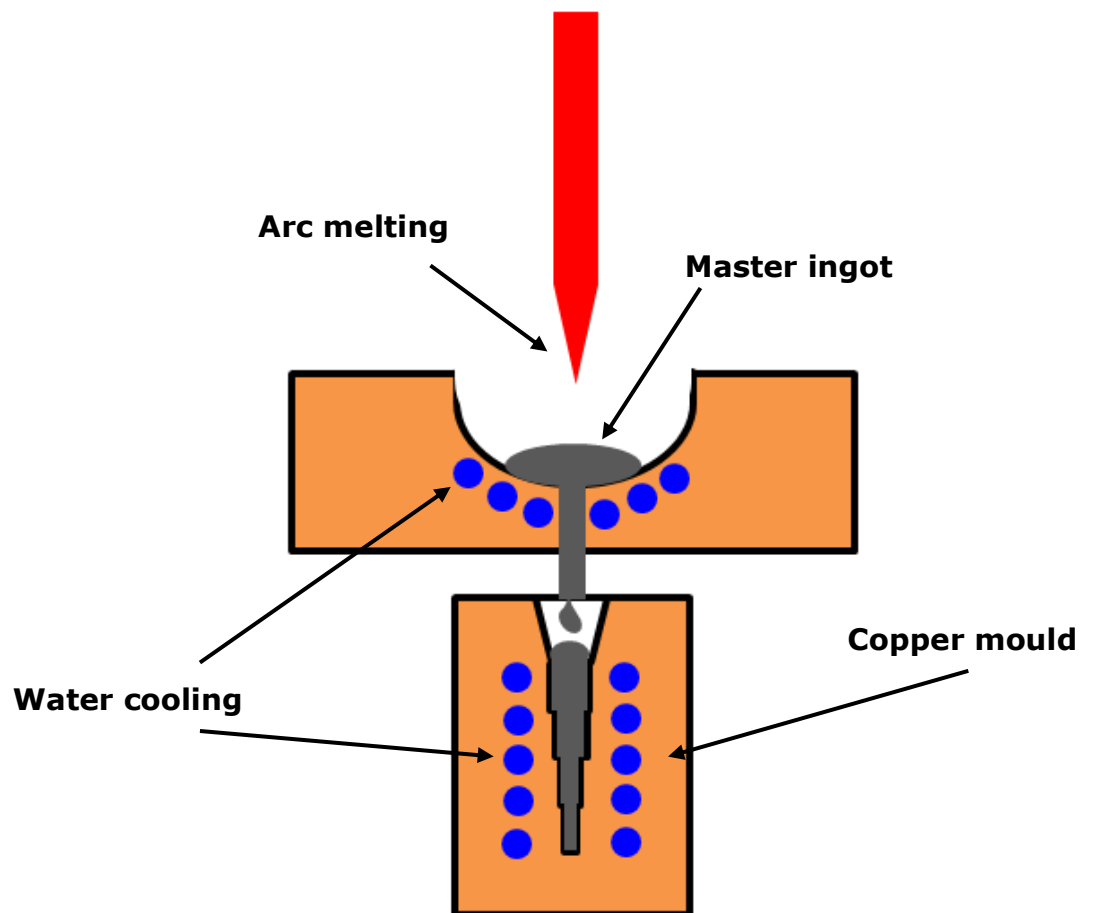
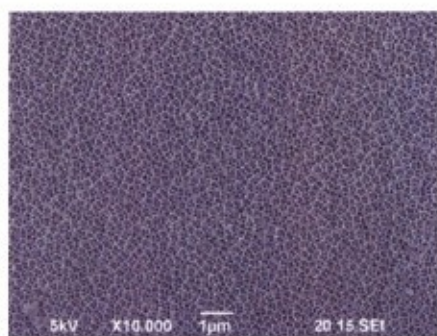


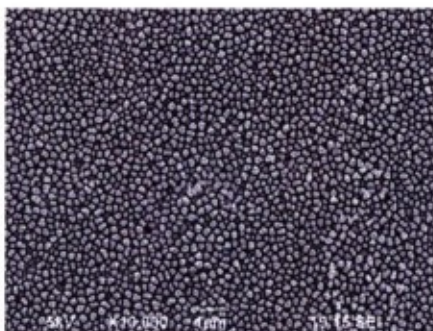
Figure 2.15 Schematic diagram of copper mould casting.

2.3.3.3 Thermoplastic processing and nano-imprinting

BMGs exhibit an excellent superplastic behaviour in the supercooled liquid region. This excellent forming ability have been explored to produce very fine patterns in nanometre scale [119]. For example, Saotome, *et al* demonstrated that, using Pt–Pd–Cu–P glassy alloys, imprinted patterns with intervals of 800 nm and 400 nm can be produced by die-forging the supercooled liquid against the nanometre patterns in a die machined by focus ion beam [120]. While nano-pillars with a diameter of 200 nm and length $\sim 5 \mu\text{m}$ were also reported by pressing the glassy alloy into porous alumina in the supercooled liquid region (Figure 2.16) The nano-pillars were tested for commercialization as anti-reflection material cell culture medium for bio-chips, and electrode material [5].



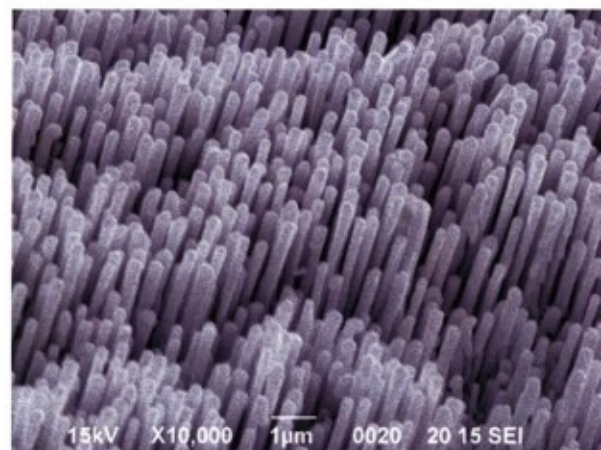
Die surface of porous alumina



Topview of nanoimprinted Pt-BMG



Anti-reflection surface



Nano-pillars of 200 nm in diameter

Figure 2.16 Imprinted BMG nano-pillars obtained by pressing the glassy alloy into porous alumina [5].

Such good superplastic behaviour also open a huge opportunity for using thermoplastic based processing to make net shape components from BMGs, and Schroers, *et al* [121] gave a comprehensive review on this aspect which

is not repeated here because forming is not the main research objective of this research.

2.3.3.4 Applications of BMGs and BMG composites

Currently, BMGs are practically used in the fields summarised in Figure 2.17, and as a relative new class of metallic materials with many unique mechanical and functional properties, the near future applications which already show very promising step change performances are in the field of:

1. Bio-medicine applications

Using a new generation of biocompatible and/or biodegradable BMG-based implants for repairing broken bones.

For example, $\text{Ti}_{40}\text{Cu}_{36}\text{Pd}_{14}\text{Zr}_{10}$ is believed to be noncarcinogenic, is about three times stronger than titanium, and its elastic modulus nearly matches bones. It has a high wear resistance and does not produce abrasion powder. The alloy does not undergo shrinkage on solidification. A surface structure can be generated that is biologically attachable by surface modification using laser pulses, allowing better joining with bone [122, 123].

$\text{Mg}_{60}\text{Zn}_{35}\text{Ca}_5$, rapidly cooled to achieve amorphous structure, is being investigated as a biomaterial for implantation into bones as screws, pins, or plates, to fix fractures. Unlike traditional steel or titanium, this material dissolves in organisms at a rate of roughly 1 millimetre per month and is replaced with bone tissue. This speed can be adjusted by varying the content of zinc [124].

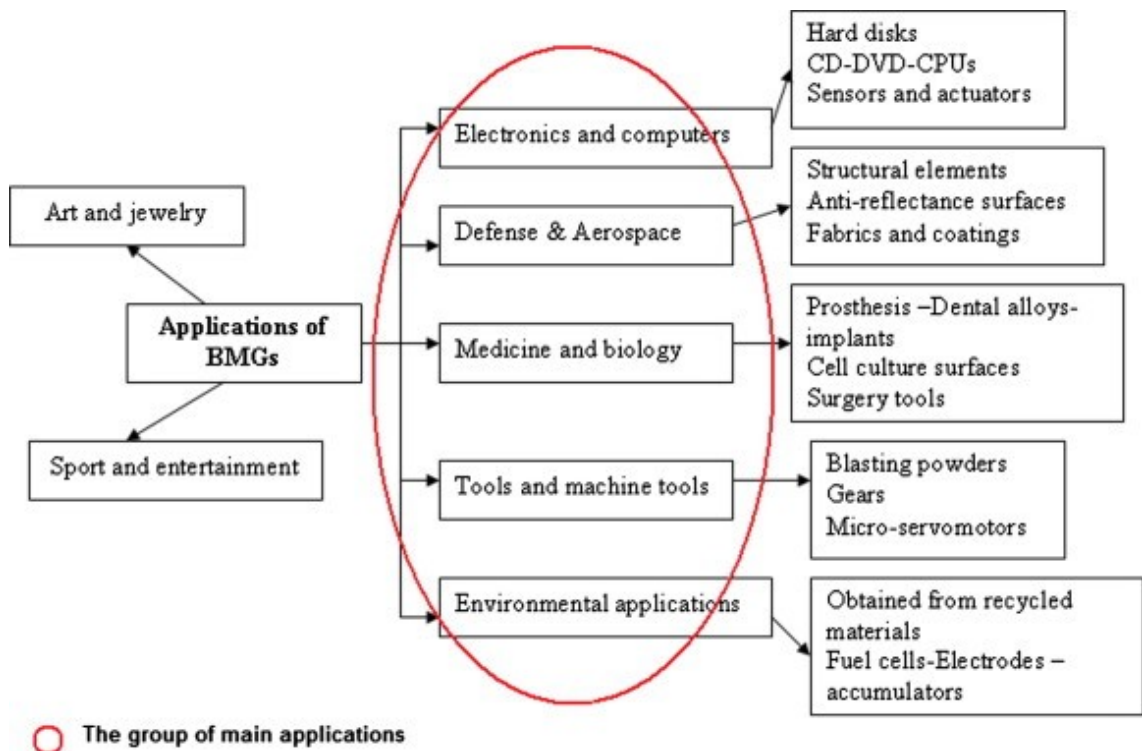


Figure 2.17 Applications of BMGs in 21st century [26].

2. Engineering applications

BMGs exhibit unique softening behaviour between the T_g and T_x , and this softening has been increasingly explored for thermoplastic forming of metallic glasses [125, 126]. It has been shown that metallic glasses can be patterned on extremely small length scales ranging from 10 nm to several millimetres [127]. It has been suggested that this may solve the problems of nano-imprint lithography where expensive nano-molds made of silicon break easily. Nano-moulds made from metallic glasses are easy to fabricate and more durable than silicon moulds. The uses of BMGs in micro-electro-mechanical systems (MEMS) have great potential; many examples have showed that metallic glasses are used for fabrication of micro-gears, micro-springs, micro-motors, spring actuator and some other engineering parts at small scale [128, 129].

At engineering scale, Yokoyama, *et al* [114] succeed in the development of cap casting and enveloped casting technique to accomplish the fabrication of centimetre sized BMGs. The former has an advantage to increase cooling rate and the later has an advantage to joint another materials instead of welding. The glassy $Zr_{55}Cu_{30}Ni_5Al_{10}$ alloy rod with a diameter of 32mm was

formed using cap casting and joined with other materials for industrial applications [130].

Fe based glassy alloy powders $(\text{Fe,Co,Ni})_{75}\text{Si}_8\text{B}_{14}\text{Mo}_3$ produced by water atomization are commercialized under the commercial name "AMO-beads" [131]. The "AMO-beads" have the advantage of much longer endurance times; with service life has been prolonged for 4 to 10 times compared with the conventional high hardness blasting materials. By use of the high hardness (900-950 HV) in conjunction with high corrosion resistance and a smooth outer surface, the peening shot treatment using "AMO beads" can generate a higher level of residual compressive stress on the surface of high class alloy steel vehicle gears with high Vickers hardness of 750 achieved by carburization treatment. As a result, fatigue strength increase by 50–80% compared with the steel gear subjected to peening shot using high-speed steel balls. This causes a significant reduction in the weight of alloy steel vehicle gear by ~45% [5].

Developing novel Fe based glassy alloy with high neutron absorption capability is one of the main target of my research which is described in Chapter 6.

2.4 Mechanical, functional properties and deformation of BMGs

Bulk metallic glasses (BMGs) often have superior strength and hardness, excellent corrosion and wear resistance, but inability to undergo homogeneous plastic deformation [1]. The mechanical and functional properties of BMGs have been a subject of intensive research for over 60 years. In summary, all studies point that BMGs have much higher tensile strengths but much lower Young's modulus. The difference in these values between the BMGs and crystalline alloys is as large as 60%. The significant difference in the mechanical properties is due to the difference in the deformation and fracture mechanisms between BMGs and crystalline alloys.

In a comprehensive review paper about mechanical properties of BMGs [132], Trexler and Thadhani pointed out that (quote): "The scientific interest stems from the unconventional deformation and failure initiation

mechanisms in this class of materials in which the typical carriers of plastic flow (dislocations) are absent. Metallic glasses undergo highly localized, heterogeneous deformation by formation of shear bands, a particular mode of deformation of interest for certain applications, but which also causes them to fail catastrophically due to uninhibited shear band propagation. Varying degrees of brittle and plastic failure creating intricate fracture patterns are observed in metallic glasses, quite different from those observed in crystalline solids. The tension–compression anisotropy, strain-rate sensitivity, thermal stability, stress-induced crystallization and polyamorphism transformations, are some of the attributes that have sparked engineering studies on bulk metallic glasses. Understanding of the glass-forming ability and the deformation and failure mechanisms of bulk metallic glasses, has given insight into alloy compositions and intrinsically-forming or extrinsically-added reinforcement phases for creating composite structures, to attain the combination of high strength, tensile ductility, and fracture toughness needed for use in advanced structural applications”.

2.4.1 Elastic limit, yield strength and nano-indentation

BMGs often have high elastic limits (or yield stresses), much closer to the theoretical limit than their crystalline counterparts due to the absence of dislocation and crystallographic defined slip-systems. For example, Ashby and Greer assessed the material properties of the BMGs and BMGMC with conventional engineering materials, showing the metallic glass have some outstanding properties, including high strength, approaching the theoretical limit; uniquely high capacity for elastic energy storage per unit volume or mass; low damping; and in some cases very high toughness [133]. Figure 2.18 shows the comparison made for 1507 different metallic glasses, metals, alloys, and metal–matrix composites materials; and BMG group materials have higher elastic limits than almost any other existing engineering metal alloys.

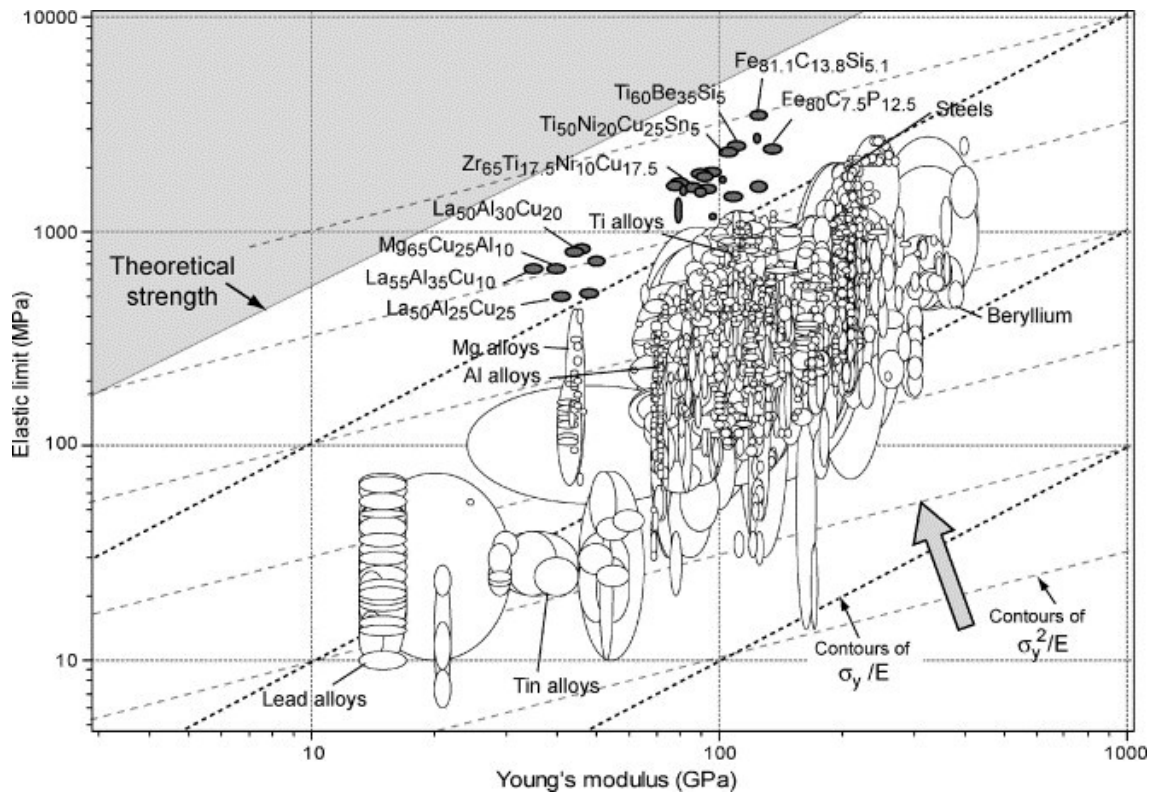


Figure 2.18 Elastic limit (yield stress), σ_y plotted against the Young modulus, E for 1507 metals, alloys, metal–matrix composites, and metallic glasses [133].

The elastic constants bulk modulus (K), shear modulus (G), and Young modulus (E) and Poisson's ratio can be measured by mechanical tests or ultrasonic-wave propagation method [3]. The tensile and compression strengths were mostly evaluated using uniaxial tensile and compressive tests [134]. The load-displacement curves recorded by the load cell and strain gauge are routinely used to calculate the yield strength and fracture strength.

Nano-indentation test [135] is also used to measure mechanical properties such as hardness or Young's modulus based on the Oliver and Pharr method [136], especially when sample size is small, and not suitable for standard mechanical tests. The depth of the indents made by nano-indentation is normally a few hundred of nanometres. With such high spatial and temporal resolution, the loading discontinuities in the form of displacement bursts can be linked directly with the nucleation of individual shear bands, allowing the fundamental deformation mechanism of MGs to be studied [137]. For example, Schuh and Nieh investigated the serrated flow in load-

displacement curve for the Pd-based and Zr-based BMGs using nano-indentation [138], and the serrated flow was correlated to the shear bands formation and the strain rate.

2.4.2 Shear bands, plastic deformation and fracture toughness

BMGs normally have very low plasticity (<2% in compression and near zero in tension), when are subject a mechanical load at temperature lower than $T_g/2$ [5]. Figure 2.19 shows a typical specimen (Vitreloy 1 alloy, short for Vit-1 hereafter) fractured under a compression load, and the corresponding engineering stress-strain curves for the Vit-1 specimen and other three BMG composites specimens (DH1, DH2, and DH3 [7]). DH3 is the ZrTi-based BMG composite with nominal composition of $Zr_{39.6}Ti_{33.9}Nb_{7.6}Cu_{6.4}Be_{12.5}$ [7], and it was used in this research as the model alloy to study the tensile deformation behaviour of BMG composites in situ using scanning electron microscopy and synchrotron X-ray diffractions. A part of this study has already been reported in [13]. More detail work is described in Chapter 4 of this thesis.

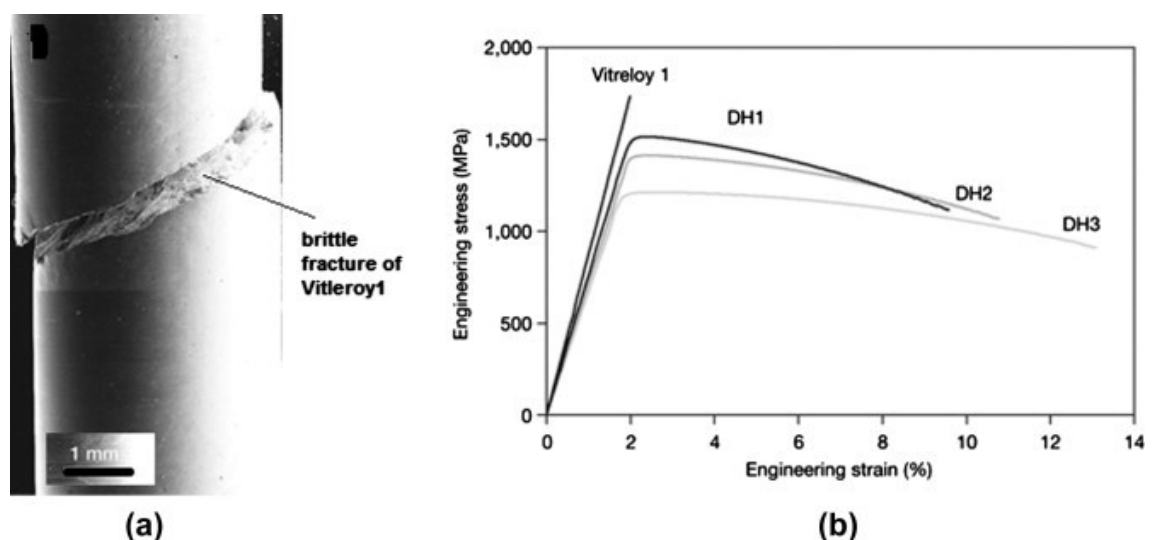


Figure 2.19 (a) The fractured Vit-1 sample under a compression load (b) the corresponding stress-strain curves for Vit-11 and other three BMG matrix composites specimens [7].

Zhang, *et al* studied the fracture mechanisms under compressive and tensile loads respectively using a $Zr_{59}Cu_{20}Al_{10}Ni_8Ti_3$ BMG [134]. Figure 2.20 and Figure 2.21 show schematically the directions of the normal and shear

stress components for compression and tension deformation respectively. In compression, shear stresses are the mainly drivers for deformation to proceed, resulting in vein-like patterns on the fractured surface as shows in Figure 2.20b. While in tension, initial fractures are nucleated under the action of normal stresses, creating voids or cores first (Figure 2.21a), followed by propagation mainly driven by shear stresses, leading to the combined fracture feature as shows in Figure 2.21c. Figure 2.22 shows two typical SEM images of the fractured surfaces of the specimens, one for compressive tests (a), and the other (b) is for tensile tests [134].

The plastic deformation in the MGs is inhomogeneous and localised within the narrow shear bands. Figure 2.23a and Figure 2.23b shows typical shear bands observed by Conner, *et al* from a 0.5mm and a 0.58 mm thick melt-spun ribbons of $Zr_{57}Nb_5Cu_{15.4}Ni_{12.6}Al_{10}$ BMG (Vitreloy 106) that were bent over a mandrel with a radius of 1 mm [139]. The images show that the shear bands formed under tension (blue arrow) and compression stresses (red arrow) are different. Those on the tensile side are tended to be longer and more uniformly spaced as compared to the compression side. It was reported later by the same group [140], that there are differences in secondary and tertiary shear bands formed on the tensile and compression side. On the tensile side, secondary shear bands are form along the length of the primary shear bands, particularly below the area of the shear offset. Tertiary shear bands are formed within the secondary shear bands. On the other hand, secondary and tertiary shear bands formed on the compression side have numerous branches but do not generated as evenly spaced secondary and tertiary shear bands on the tensile side.

After shear bands are nucleated (or initiated), they propagate very rapidly in a very narrow region, leading to a very sudden failure of the materials. This phenomenon is also called strain softening in contrast to the very common strain hardening phenomenon found in most crystalline materials [1, 6]. An individual shear band has a thickness of 10–20 nm [6]. It has been generally accepted that shear band formation is attributed to a local decrease in viscosity of the glass with two possible hypotheses: free volume formation (structural change) and local heating (temperature rise) within the shear bands.

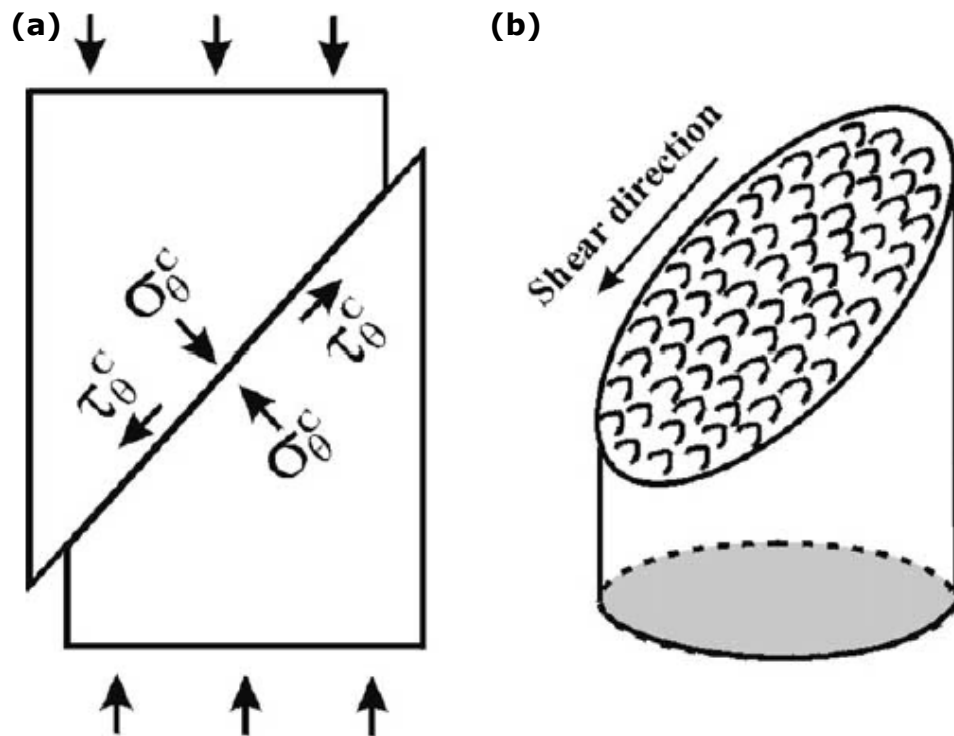


Figure 2.20 Schematic diagram of BMG compression fracture process (a) shear fracture process (b) vein-like structure [134].

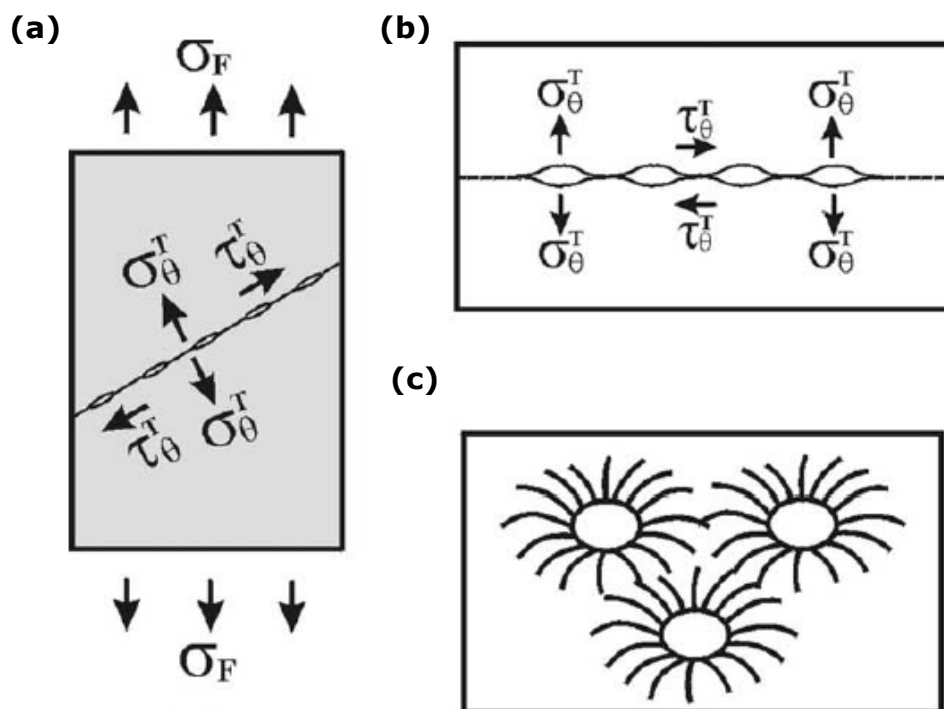


Figure 2.21 Schematic diagram of BMG tensile fracture process (a) nucleation of the cores (b) propagation of the cores (reoriented) (c) cores and vein-like structure [134].

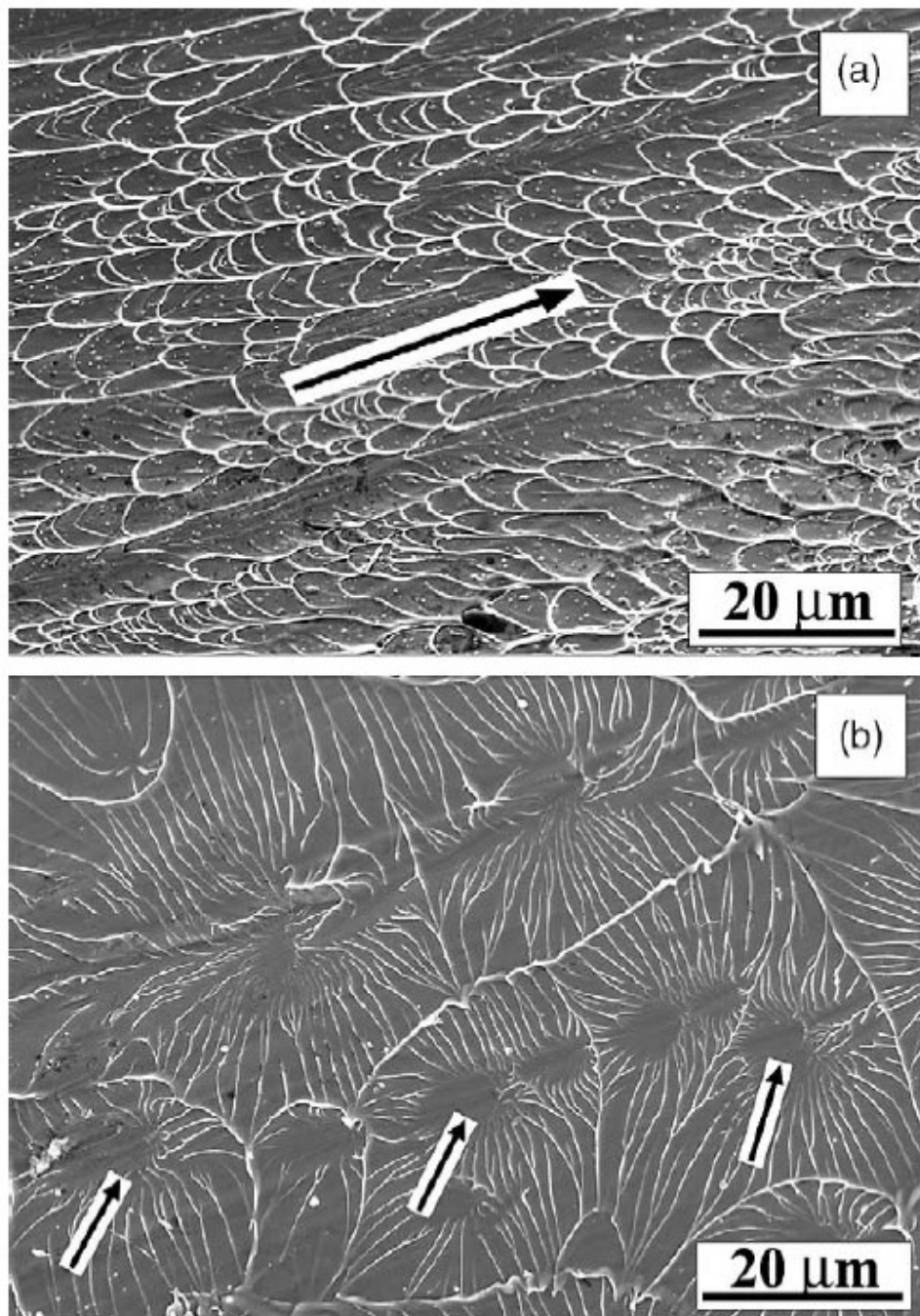


Figure 2.22 Fractured surfaces SEM images of $Zr_{59}Cu_{20}Al_{10}Ni_8Ti_3$ BMG (a) compressive test (b) tensile test [134].

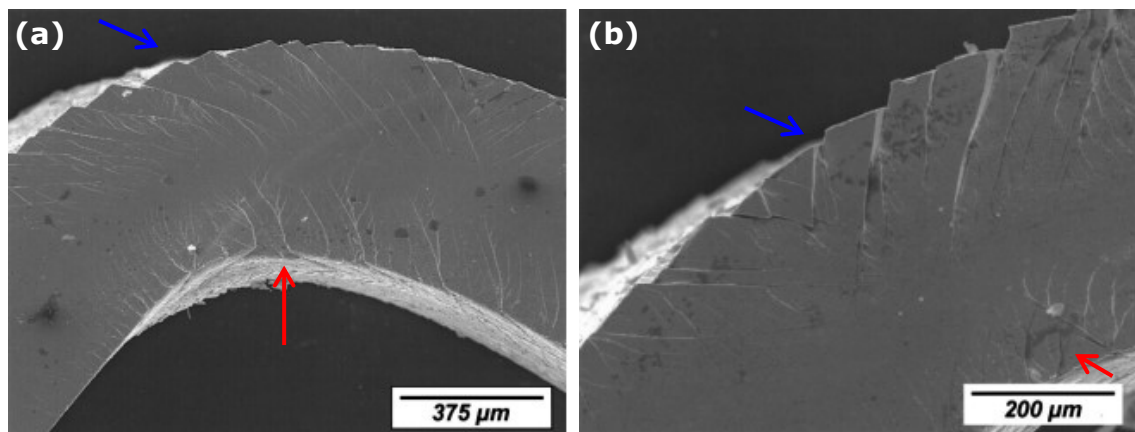


Figure 2.23 Shear bands observed on the (a) 0.5mm and (b) 0.58mm thick melt-spun ribbons of Vitreloy 106 that bend over a mandrel with a radius of 1mm [139].

The first hypothesis suggests that the viscosity in shear bands decreases during deformation due to formation of free volume. This results in decreases in material density and subsequently leads to reduce in its resistance to deformation [141].

Spaepen derived an expression for steady-state inhomogeneous flow in metallic glasses on the basis of a competition between the stress-driven creation and the diffusional annihilation of free volume [141]. Argon demonstrated the flow localization occurs in a shear band in which the strain rate has been perturbed due to the creation of the free volume [142]. Steif, *et al* derived an expression for the stress at which catastrophic softening due to free volume creation occurring during uniform shearing of a homogeneous body under constant applied strain rate [143].

The second hypothesis suggests that local adiabatic heating occurs in the shear bands [144], which leads to a decrease in the viscosity of the metallic glass by several orders of magnitude [145]. This adiabatic heating could lead to a substantial increase in the temperature to a level above the glass transition temperature or even beyond the melting temperature of the alloy. Temperature rise at the shear bands have been reported using infrared imaging [146, 147] and fusible coating on the BMG [148].

Spaepen's free volume model is also a widely used microscopic model to explain shear band propagation. Equally important for explaining shear propagation is the shear transformation zone (STZ) model proposed by

Argon [142]. Both models are based on the assumption that the fundamental unit process of deformation is a local rearrangement of atoms which accommodates the local shear strain [149]. These processes are schematically represented in Figure 2.24. A group of atoms change its configuration under a shear stress from one relatively low energy configuration to a next such configuration by thermal activation, leading to the propagation of shear bands, hence a local plastic flow of materials.

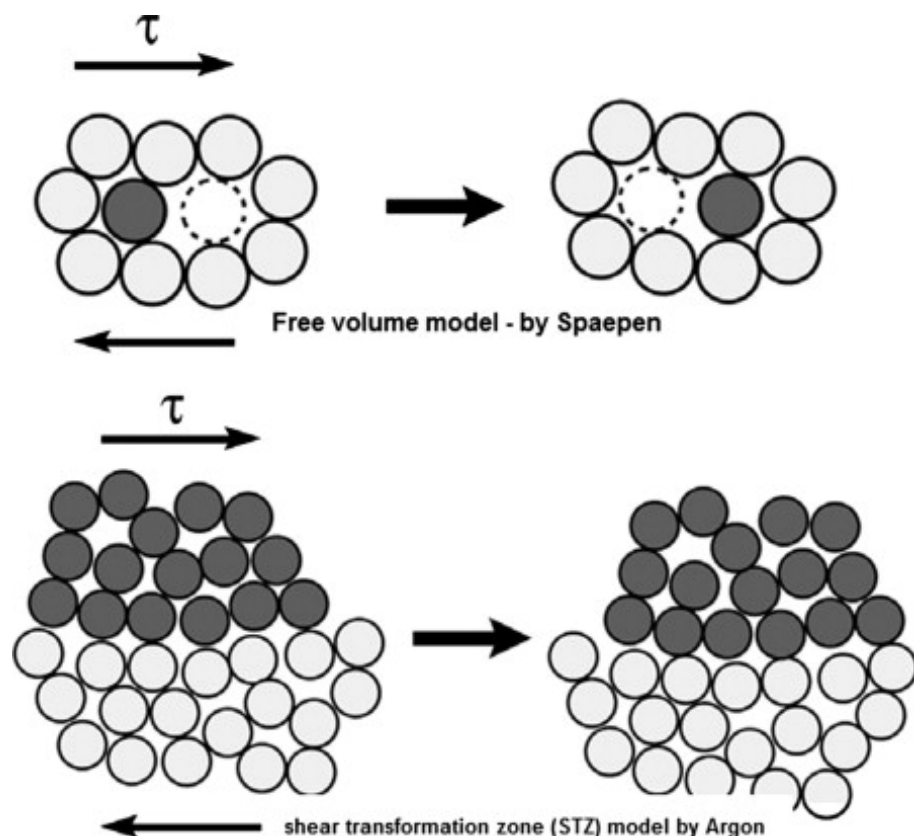


Figure 2.24 Spaepen's free volume model and Argon's shear transformation zone (STZ) model for the deformation of MGs [149].

Argon's STZ model was recently developed further into a two-state STZ models by Falk and Langer by assuming that the STZs are intrinsically two-state systems [150].

To improve the ductility of monolithic BMG, a secondary reinforced crystalline phase was introduced to the amorphous matrix. The secondary phases influence the shear bands formation through 4 possible mechanisms: (1) residual stresses created during solidification, (2)

difference in elasticity between the amorphous matrix and reinforced crystalline phases, (3) stress concentration from the plastic misfit strain between the amorphous matrix and reinforced crystalline phases, and (4) “obstacles” for the shear band propagation that eventually lead to crack.

Dragoi, *et al* reported that thermal residual stress up to 480MPa existed within amorphous matrix of the W fibre reinforced $Zr_{41.2}Ti_{13.8}Cu_{12.5}Ni_{10}Be_{22.5}$ BMG using neutron powder diffraction [151]. The residual stress is generated due to the different coefficient of thermal expansion between the amorphous matrix and reinforced crystalline phase. This high residual stress is expected to influence the mechanical behaviour of the BMGMC.

Balch, *et al* reported tensile deformation behaviour of W and Ta reinforced $Zr_{57}Nb_5Al_{10}Cu_{15.4}Ni_{12.6}$ BMGs using in situ synchrotron X-ray diffraction [152]. W and Ta are stiffer than the amorphous matrix, thus considerable load transfer is expected during the deformation with the particle carry higher stress than the matrix. At low applied stresses, elastic loading was found being well transferred between two well-bonded elastic phases. At higher stresses, onset of plasticity was found in the crystalline particles followed by strain hardening, thus reducing the load transfer efficiency, resulting in increased stress in the matrix followed by shear banding in matrix and fracture.

Hays, *et al* reported that the matrix-dendrite interface is atomically sharp, intimate and apparently strong and allow effective transfer of stress from the β crystalline phase to the amorphous matrix when yielding occurs initially in the β crystalline phase and may play a key role in seeding the formation of multiple shear bands [8].

Hoffmann, *et al* reported high toughness and ductility of ZrTi-based BMGMC with different volume fraction of the crystalline phases [7]. The principle of the alloy design is to introduce reinforced crystalline phase with ‘soft’ elastic/plastic inhomogeneities in a metallic glass matrix to initiate local shear banding around the inhomogeneity; and matching of microstructural length scales to the characteristic length scale RP (for plastic shielding of an

opening crack tip) to limit shear band extension, suppress shear band opening, and avoid crack development.

2.4.3 Hardness, wear and corrosion resistances

Hardness is the mechanical property that controls dominantly the wear resistance capabilities of a material. It also correlates linearly with the material yield strength [153, 154]. BMGs, in general, exhibit higher hardness than their crystalline counterpart [155]. It is because the densely packed and randomly distributed atomic structures of BMGs do not have grains and defects which significantly affect hardness [156]. Since early 1980s, the wear and scratch resistance of various BMG systems have been widely reported [157-161]. Among the BMGs of higher wear and scratch resistance, the Fe-based BMGs [162] also have exceptional high fracture strength ($> 4000\text{MPa}$ for the $[(\text{Fe}_{1-x}\text{Co}_x)_{0.75}\text{B}_{0.2}\text{Si}_{0.05}]_{96}\text{Nb}_4$ BMG) [163], making them a promising engineering coating materials. A number of techniques, including laser sintering [162, 164], high velocity oxygen fuel (HVOF) [165, 166] and plasma [167, 168] spraying have been used to make full amorphous Fe-based BMG coatings, and the corresponding wear/scratch resistance were characterised as well.

Figure 2.25 shows the result reported by Zhang, *et al* regarding the wear resistance of an AISI 1045 mild steel substrate and the $\text{Fe}_{48}\text{Cr}_{15}\text{Mo}_{14}\text{C}_{15}\text{B}_6\text{Y}_2$ BMG coating made by HVOF technique [165].

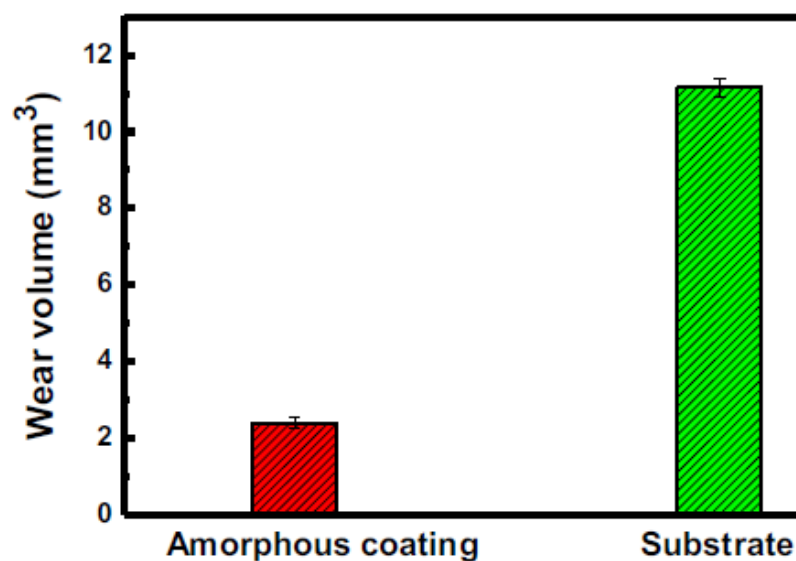


Figure 2.25 The volume of wear on the Fe-based BMG coating and the AISI 1045 mild steel substrate under the 32N load and 0.1m/s sliding test [165].

MGs and BMGs also exhibit superior corrosion resistance compared to their crystalline counterparts because of the absence of defects common to crystalline alloys, such as grain boundaries, dislocations and secondary phases, which could act as galvanic cells to initiate localised corrosion [1].

The corrosion resistance of MGs was first reported 1974 by Naka, *et al* after adding Cr into the $\text{Fe}_{80-x}\text{Cr}_x\text{P}_{13}\text{C}_7$ MG ribbon [169, 170]. The result showed that the MG ribbons had no significant measurable corrosion rate under the exposure in 1 moles NaCl solution at 30°C. However, the crystalline Fe-Cr alloys corroded at 0.5-1mm per year. Since the first reported corrosion resistance enhancement in the Fe-Cr-P-C system in 1974, other MGs [171, 172] and BMGs [173, 174] with high corrosion resistance were also developed and widely reported.

For Fe-based BMGs, all reported alloy systems generally exhibit good corrosion resistance [1]. Adding B [175], Cr [175], Mo [176], Y [177] and N [178] elements were reported to have significant improvement in the resistance of the alloys in corrosive medias. For example, Pang, *et al* reported that increasing B concentration in the $\text{Fe}_{50-x}\text{Cr}_{16}\text{Mo}_{15}\text{C}_{18}\text{B}_x$ significantly improved the corrosion resistivity in 1, 6 and 12 moles of HCl solution by immersion and electrochemical tests [175]. Figure 2.26 shows the reduction in corrosion rate with higher B concentration. It was also reported that the 6 and 8% B samples do not exhibit any pitting corrosion from the sample surface observation using SEM.

The high corrosion resistance of Fe-based BMGs were also explored when used as coating materials [166, 179-182]. For example, Zhang, *et al* prepared the $\text{Fe}_{48}\text{Cr}_{15}\text{Mo}_{14}\text{C}_{15}\text{B}_6\text{Y}_2$ BMG coating onto a mild steel (AISI 1045) substrate using the HVOF method. The coated material was submerged into the NaCl solution and the pitting initiation in the coating was investigated using TEM and nanobeam EDX [182]. On the similar BMG, Ni, *at el* coated the material using HVOF onto a stainless steel substrate and the corrosion resistance was evaluated using the electrochemical measurement [183].

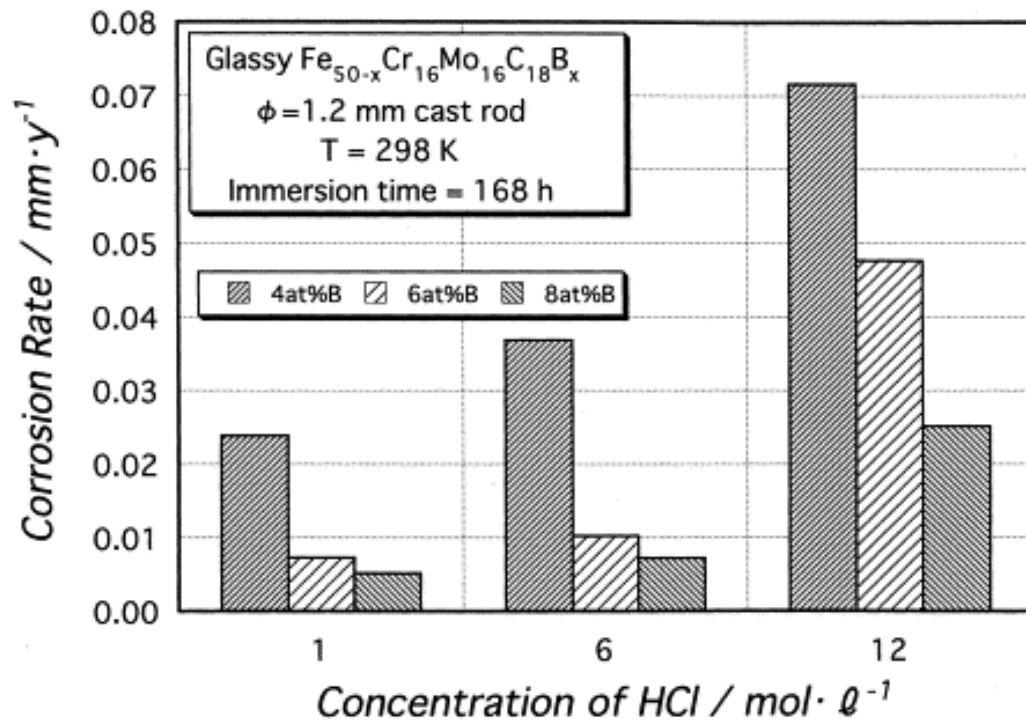


Figure 2.26 The influence of B concentration in the $\phi 1.2$ mm Fe-Cr-Mo-C-B BMG cast rod in HCl solution at 298K for 168 hours immersion time [175].

2.4.4 Radiation shielding properties

BMGs with exceptionally high strength, elastic limit, hardness and corrosion resistance can be made into bulk metallic glass matrix composites (BMGMC) by adding soft crystalline reinforced phases in the matrix to increase their ductility and fracture toughness. Recently, Davison, *et al* have investigated the BMG and its composites (for example, Zr_{36.6}Ti_{31.4}Nb₇Cu_{5.9}Be_{19.1} BMGMC) with the aim of using them as shielding materials for spacecraft [4]. The shielding is for the outer layer of a satellite or spacecraft, protecting the impact of possible micrometeorite and orbital debris (MMOD), radiation damage by cosmic rays and high temperatures during re-entry.

In addition to radiation shielding of cosmic rays from outer space, BMGs were also evaluated as the radiation shielding coating materials in nuclear industry, particularly for nuclear waste containers. The remaining spent fuels from nuclear reactors are a high level nuclear waste containing long half-life isotopes such as neptunium, americium and curium which must be kept isolated in a safe repository [184]. According to the Net Enabled Waste Management Database 2013, the cumulative disposal for high level waste until 2013 was estimated up to 72000 cubic metres [184] and is increasing.

A long-term solution to store nuclear waste is to bury it in geologically stable repositories for naturally decay [184]. During decay, ionizing radiation including alpha, beta, gamma, X-ray and neutrons will be emitted from the nuclear waste, therefore radiation shielding is required. Other than containing these harmful radiations, the shielding material must be able to withstand the possible corrosion and oxidation caused by the storage environment. Materials that are often selected for making nuclear waste containers are copper, iron, stainless steels, titanium alloys and nickel-based alloys [185]. Bulk metallic glasses (BMGs) are amorphous metals that have exceptionally high corrosion and wear resistance properties compared to their crystalline counterparts [30], might a solution to the problem.

Farmer, *et al* investigated $\text{Fe}_{49.7}\text{Cr}_{17.7}\text{Mn}_{1.9}\text{Mo}_{7.4}\text{W}_{1.6}\text{B}_{15.2}\text{C}_{3.8}\text{Si}_{2.4}$ (SAM2X5) BMG that containing Cr, Mo and W elements and have significantly enhanced corrosion resistance. The B element in the alloy provided the glass forming ability and neutron absorption capability [186]. The BMG was used as a coating material and applied onto a 316 stainless steel cylinder using HVOF for the potential application as a nuclear waste container. The HVOF SAM2X5 coatings have significant higher neutron absorption cross section as compared to 316L stainless steel, nickel based alloy C-22, borated stainless steel, Ni-Cr-Mo-Gd alloy as shows in Figure 2.27.

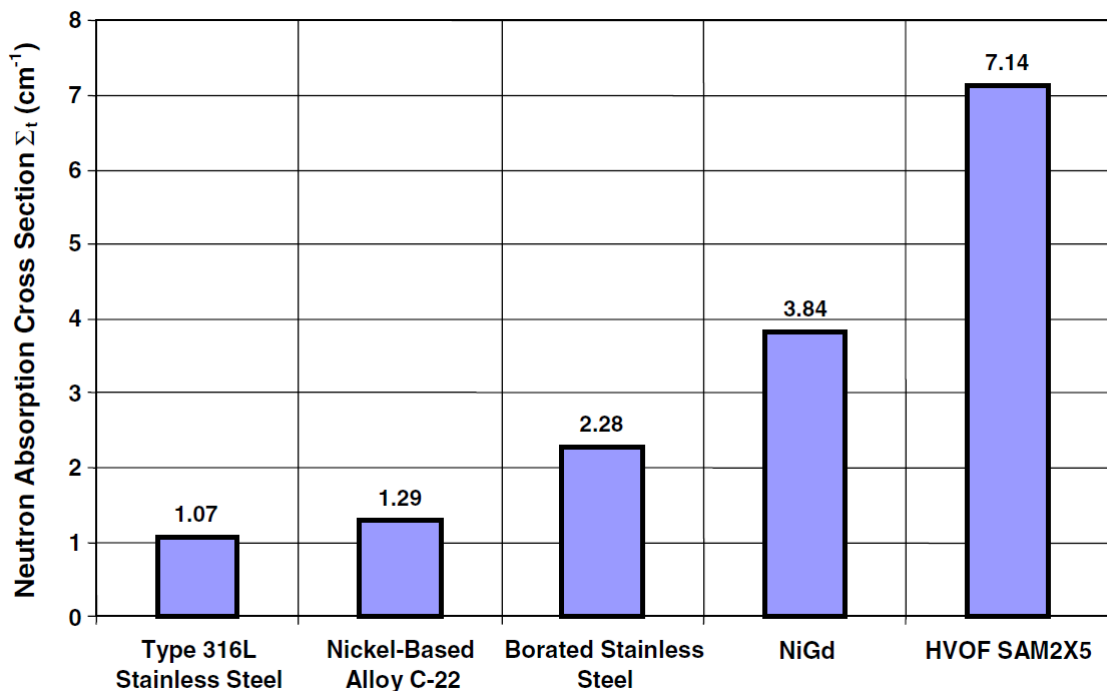


Figure 2.27 Neutron absorption cross section of HVOF SAM2X5 BMG as compare to other crystalline alloys [186].

2.4.4.1 Neutron scattering and total cross section

When neutrons pass through a material, there is a probability of an interaction event occurring between the incident neutrons and the nuclei of the material [187]. Figure 2.28 shows the possible interactions between the neutrons and the nuclei.

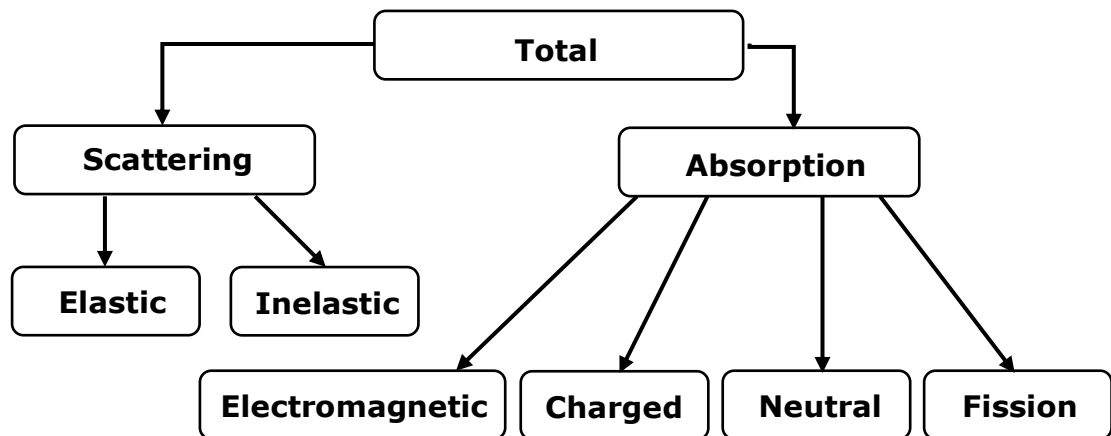


Figure 2.28 Neutron interaction with nucleus.

The interactions are grouped into two categories: scattering and absorption. When neutron is scattered by a nucleus, its speed and direction change without affecting the nucleus (number of protons and neutrons remained the same). After the scattering event, the nucleus will have some recoil velocity which might be in an excited state that will lead to release of radiation. On the other hand, when neutron is absorbed by the nucleus, a wide range of radiations can be emitted or fission can be induced. The probability of a particular scattering event occurs when neutrons passing through a thin material is expressed by the concept of microscopic cross section, σ . For example, the larger, the cross section, the higher probability, the event occurs. The standard unit for cross section is "barn" (10^{-28} m^2 or 10^{-24} cm^2). The total cross section σ_t is expressed as the probability of all interactions occurs, and it is different for different elements and also energy dependent parameter [187].

Figure 2.29 shows the interaction of the neutrons after passing through a thick material. The interaction can be viewed as neutrons passing a series

of atomic layers, each with a microscopic cross section. The probability of the total interactions can be defined as the total macroscopic cross section or macroscopic attenuation coefficient, Σ_t . Therefore the intensity of the uncollided neutrons beam, I_x after passing through the thick sample can be calculated similarly as the linear attenuation coefficients of X-rays:

$$\Sigma_t = N\sigma_t$$

$$I_x = I_0 e^{-N\sigma_t x}$$

Where I_0 is the incoming neutron beam intensity, x is the thickness of the material, σ_t is the total cross section of the material, and N is the atomic number density.

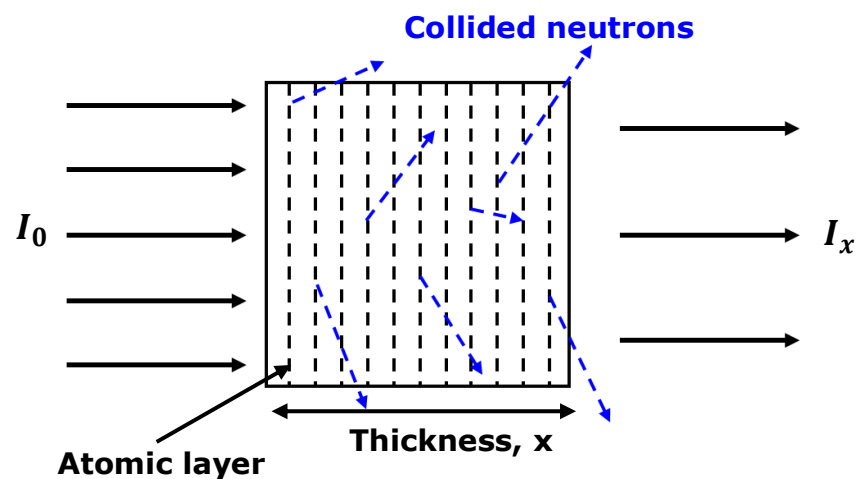


Figure 2.29 The intensity of neutron after passing through the material.

2.5 In-situ studies of the deformation of BMGs

At low temperatures, usually lower than half of T_g , where T_g is the glass transition temperature, the plastic deformation is "inhomogeneous" and concentrated in a few thin "shear bands" that form approximately on the planes of maximum resolved shear stress. These planes are inclined close to 45° to the loading axis. The inhomogeneous deformation in the metallic glass, results in mechanically unstable at high stresses, and consequently into catastrophically failure.

At high temperature, usually higher than 70% of T_g , and in the supercooled liquid state which is the temperature between T_x (crystallization temperature) and T_g , the metallic glass under homogeneous deformation. This deformation was also considered to be the viscous flow of the supercooled liquid. The plastic deformation of various BMG systems in the supercooled liquid region was widely reported [188, 189]. Therefore, by deforming the metallic glasses in the supercooled liquid region, it is possible to achieve net-shape forming capability as reported in many cases [190-192].

The inhomogeneous plastic deformations in the metallic glass begin with shear band initiation, propagation and followed by sudden fracture. The very fast propagation of shear bands on the sample during deformation makes it very difficult to be observed during experiments. Especially for the monolithic bulk metallic glasses under tension, which have near-zero plasticity, making it very difficult to capture the moment when shear bands is nucleated and the subsequent propagation of the shear bands, and the evolution of the local stress/strain ahead of the shear band propagation path [11].

2.5.1 Imaging studies using electron microscopes

The in situ study of the nucleation and propagation of the shear bands were reported using the transmission electron microscopy (TEM) [193-196] and scanning electron microscopy (SEM) [9]. Chen, *et al* reported the intrinsic size effects on the deformation mode of taper-free $\text{Cu}_{47}\text{Ti}_{33}\text{Zr}_{11}\text{Ni}_6\text{Sn}_2\text{Si}_1$. It was reported that with different diameter of glassy pillar gradually decrease from 640nm to 70nm, the deformation mode observed under in situ TEM exhibit four scenarios [195]:

1. highly localized and catastrophic shear bands
2. initially non-localized deformation follow by stop-and-go shear bands accompanied by softening
3. homogeneous and banding-less deformation with intermittent shear events
4. fully homogeneous and smooth plastic flow

Matthews, *et al* [193] reported an in situ TEM study of the primary shear band propagation and formation of the secondary shear bands on the 3 BMGs; $\text{Cu}_{47}\text{Ti}_{33}\text{Zr}_{11}\text{Ni}_6\text{Sn}_2\text{Si}_1$, $\text{Zr}_{50}\text{Cu}_{30}\text{Ni}_{10}\text{Al}_{10}$ and $\text{Zr}_{52.5}\text{Cu}_{17.9}\text{Ni}_{14.6}\text{Al}_{10}\text{Ti}_5$. Yang, *et al* [197] performed the micro-compression experiments on 6 micro-pillars BMGs as shows in Figure 2.30. They demonstrated that the stable shear banding behaviour could exhibit dual characteristics; (1) stochastic propagation, which is found insensitive to sample sizes, (2) deterministic propagation, which display a clear trend of sample size effect. Bouzakher, *et al* [9] reported different in the shear bands formation at the tip of the artificial mode I crack for the 3 BMGs; $\text{Cu}_{60}\text{Zr}_{30}\text{Ti}_{10}$, $\text{Zr}_{65}\text{Ni}_{10}\text{Cu}_{15}\text{Al}_{10}$ and $\text{Pd}_{42.5}\text{Cu}_{30}\text{Ni}_{7.5}\text{P}_{20}$.

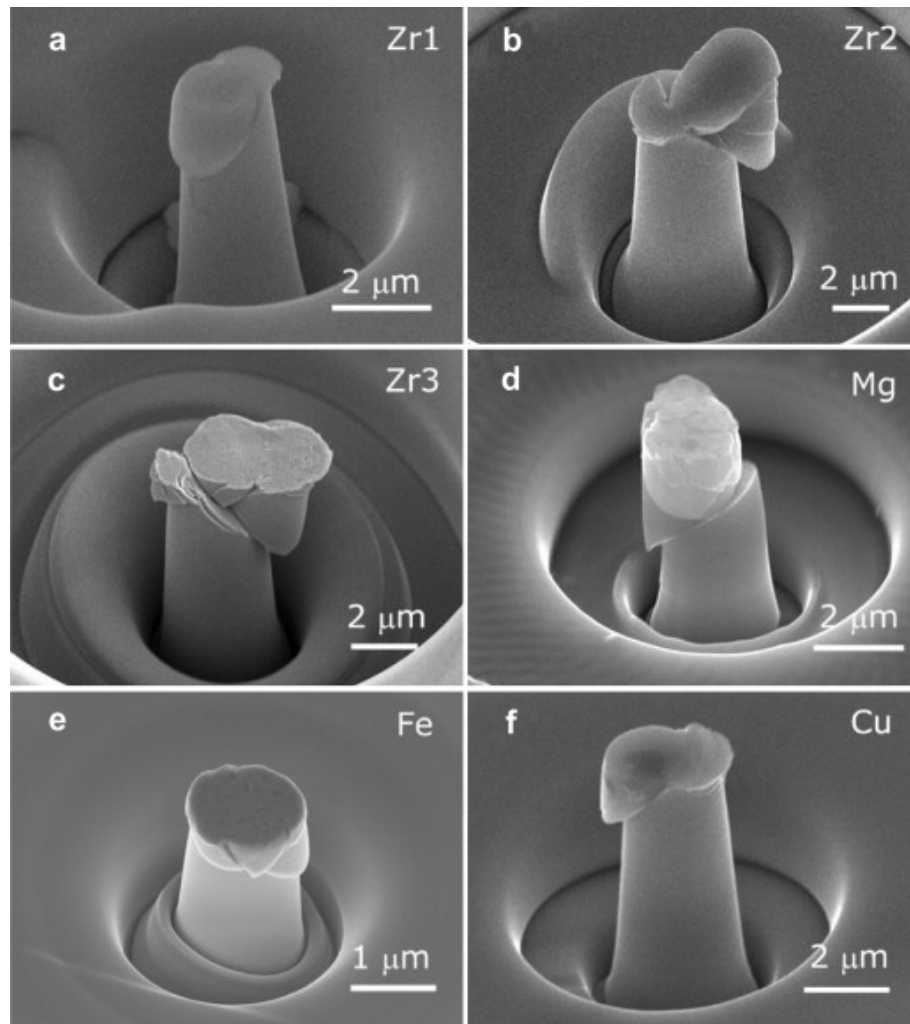


Figure 2.30 The typical morphologies of the shear banding mediated plasticity in the micro-compressed micro-pillars for (a) $\text{Zr}_{50}\text{Cu}_{37}\text{Al}_{10}\text{Pd}_3$ (Zr1), (b) $\text{Zr}_{55}\text{Cu}_{30}\text{Ni}_5\text{Al}_{10}$ (Zr2), (c) $\text{Zr}_{55}\text{Cu}_{23}\text{Ni}_5\text{Al}_{10}\text{Nb}_2$ (Zr3), (d) $\text{Mg}_{58}\text{Cu}_{31}\text{Nd}_5\text{Y}_6$ (Mg), (e) $(\text{Fe}_{44.3}\text{Cr}_5\text{Co}_5\text{Mo}_{12.8}\text{Mn}_{11.2}\text{C}_{15.8}\text{B}_{5.9})_{98.5}\text{Y}_{1.5}$ (Fe) and (f) $\text{Cu}_{46.25}\text{Zr}_{44.25}\text{Al}_{7.5}\text{Er}_2$ (Cu) BMGs [197].

2.5.2 Digital image correlation

Digital Image Correlation (DIC) [198] is an innovative non-contact optical technique for measuring strain and displacement under loading [199]. DIC works by comparing digital photographs of a component test piece at different stages of deformation. It tracks the blocks of pixels pattern to measure surface displacement and build up full field 2D and 3D deformation vector fields and strain maps. To allow the DIC work efficiently, the pixels pattern need to be random and unique with a range of contrast and intensity levels.

Zhang, *et al* [200] used the DIC technique to study the $Zr_{62}Cu_{15.5}Ni_{12.5}Al_{10}$ under in situ uniaxial compression to observe the deformation mechanism. The reported observations, which come from the unique combination of fast IR images, DIC of photographic images and SEM scans, show that the shear failure of BMGs is more complex than anticipated in terms of geometry and sequence of localized strain regions. The multiplicity of different slip surfaces being activated at different times and the roughness of these surfaces provide a possible mechanism for the arrest of slip, and hence the large apparent strain to failure that was observed for this material.

Whereas, Song, *et al* [201] used a high-speed camera combining with the DIC technique to observe the shear band propagation in $Zr_{55}Al_{10}Ni_5Cu_{30}$ metallic glass under in situ uniaxial compression. The shear velocity was calculated and further compared with that measured from using strain gages. The images also showed that localized shear occurs in a simultaneous fashion, the shear band was found operates simultaneously across the entire shear plane, rather than in a progressive manner.

The DIC technique is not use in this thesis mainly because of the purpose of this research is to observe the differences in the shear bands formation in the monolithic metallic glasses and composites, whereas the DIC require a random pixel pattern on the sample surface which will eventually obscure the shear bands feature. Indeed, we tried to introduce cross lines pattern into the sample surface using the focussed ion beam with tungsten deposition for the DIC, however, it did not success due to non-randomise pattern.

2.5.3 Diffraction studies using synchrotron X-rays

In situ study of the deformation of BMGs and its composites were reported using Synchrotron X-ray diffraction (SXRD) and total scattering methods [10, 202, 203]. Poulsen, *et al* [10] demonstrated that SXRD is a suitable technique for characterizing the stress/strain fields in the amorphous materials. The strain evolution of the $\text{Mg}_{60}\text{Cu}_{30}\text{Y}_{10}$ BMG under compression test was studied using the Q-space and real space methods. For the Q-space method, the strain was measured using the shift on the first sharp diffraction peak (FSDP) in the 1D spectra (X-ray intensity against the scattering vector curves), whereas, for the real space, it was measured using the shift in the atomic shells on the pair distribution function [10]. Ott, *et al* [202] evaluated the different concentration of the Ta particle in the $(\text{Zr}_{70}\text{Cu}_{20}\text{Ni}_{10})_{90-x}\text{Ta}_x\text{Al}_{10}$ BMG composite under in situ compression test. The different deformation behaviour for the Zr-based amorphous matrix and Ta crystalline particle were reported [202]. Wang, *et al* [203] evaluated the atomic structure evolution of $\text{Cu}_{64.5}\text{Zr}_{35.5}$ BMG under in situ compression test. It was reported that the atomic bond reorientations were accompanied by directionally dependent changes in the chemical and topological within the short-range order (SRO) structure, whereas, the medium-range order (MRO) structure reflects the macroscopic strain of the sample.

However, combining both in situ electron microscopy and in situ SXRD to investigate the correlation between local atomic rearrangements and shear band formation has not been reported so far.

Led by Dr Y. Huang and Dr J. Mi, we reported the tensile deformation of the $\text{Ti}_{40}\text{Zr}_{25}\text{Ni}_{12}\text{Cu}_3\text{Be}_{20}$ [11] and $\text{Zr}_{41.2}\text{Ti}_{13.8}\text{Cu}_{12.5}\text{Ni}_{10}\text{Be}_{22.5}$ (Vit-1) [12] BMG, and $\text{Zr}_{39.6}\text{Ti}_{33.9}\text{Nb}_{7.6}\text{Cu}_{6.4}\text{Be}_{12.5}$ [13] BMGMC (DH3 from Hoffmann, *et al* [7]) using in situ Synchrotron X-ray diffraction and in situ scanning electron microscopy. Figure 2.31 shows the generic procedure was developed to separate the diffraction information of the crystalline phases away from the amorphous matrix, to precisely calculate the microscopic strains of the two phases during the shear bands initiation in the dendrites and matrix as shows in Figure 2.32 [13]. The detail of the finding will be discussed later in Chapter 4.

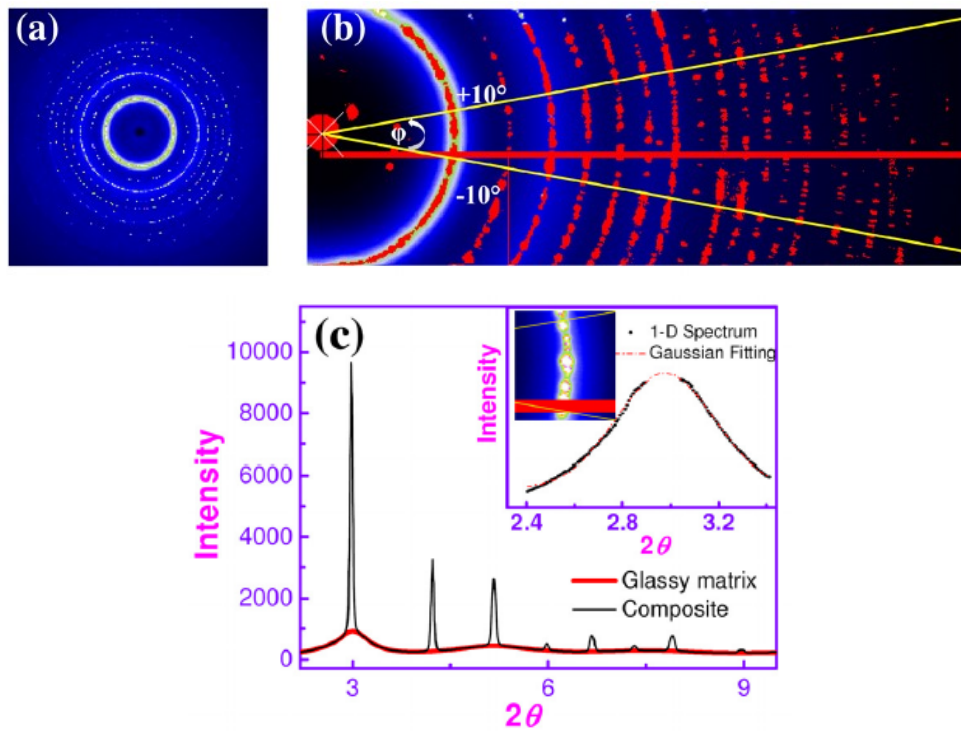


Figure 2.31 (a) typical X-ray diffraction pattern for the as-cast ZrTi composite, (b) an enlarged section of the composite diffraction pattern, highlighting the diffraction rings and the spots, (c) the 1D X-ray intensity curve of the composite and that of the matrix separated [13].

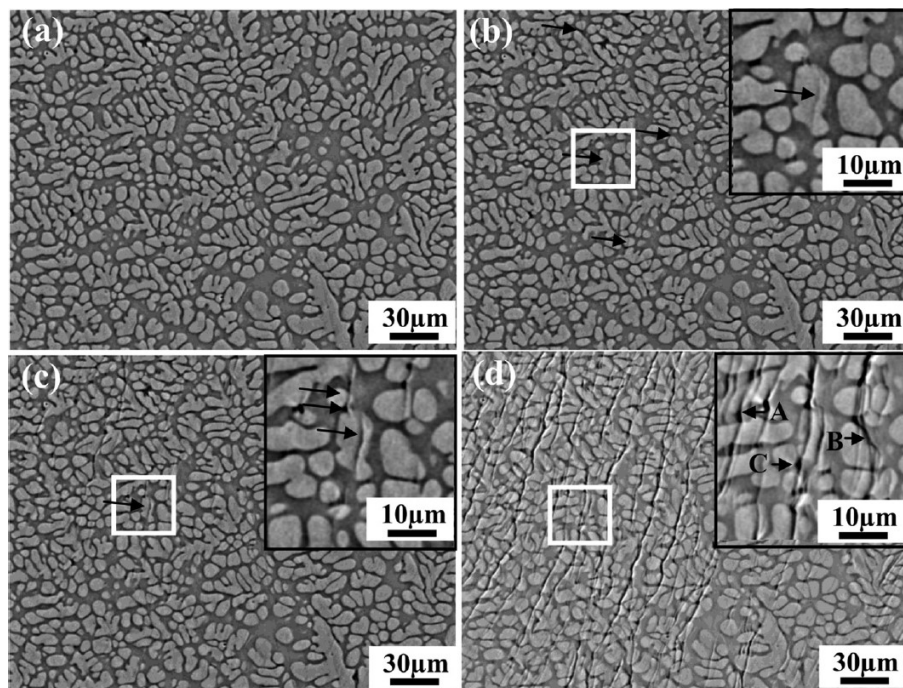


Figure 2.32 The backscattered scanning electron images, showing the microstructure at the location where the diffraction patterns are acquired. (a) No shear bands found in the composite (b) shear band nucleation in the dendrites, (b) shear band nucleation in the matrix and (d) shear band propagation in the composite [13].

2.5.4 High pressure compression using Diamond Anvil Cell

In situ study of the metallic glasses under near isotropic compression or high pressure was conducted using the Diamond Anvil Cell [204] under SXRD illumination [205]. Under high pressure compression, the density of some amorphous increase with pressure, resulting in polyamorphism that is a transition from a low-density amorphous (LDA) state to a high-density amorphous (HDA) state. Such phenomenon often results in the increase in atomic coordination from low coordination number $N_1 \leq 6$ such as amorphous ice [206] and silicon [207] to higher atomic coordination number (12-14). $\text{Cu}_{55}\text{Al}_{45}$ [205] was the first MG system reported for polyamorphism. Figure 2.33a shows the synchrotron XRD patterns of the $\text{Cu}_{55}\text{Al}_{45}$ during the compression cycle. The FSDP shifts toward higher Q with increase pressure and were found proceeds at a relatively fast pace over the pressure range of 2-13 GPa. Throughout the pressure cycle the diffraction intensity maxima between 3 and 4 \AA^{-1} were diminished, whereas those between 4 and 5.5 intensified. The XRD pattern at final pressure step 30 GPa was found different from those at ambient pressure and show sign of different amorphous phase. The transition was found in the pressure range of 2-13.5 GPa as shows in the specific volume versus the pressure in Figure 2.33b. The density difference between the two amorphous states is attributed to the difference in electronic and atomic structures, and particularly to the bond shortening as confirmed by *ab initio* modelling of the delocalization of f-electron similar to that found in the γ to α phase transformation in crystalline cerium [208, 209]. Similar transition was also reported later in other MG system that contain Ce element such as $\text{Ce}_{75}\text{Al}_{25}$ [210, 211], and BMG system $\text{Ce}_{70}\text{Al}_{10}\text{Ni}_{10}\text{Cu}_{10}$ [212] and $\text{La}_{32}\text{Ce}_{32}\text{Al}_{16}\text{Ni}_5\text{Cu}_{15}$ [213]. In addition to the Ce contained MGs and BMGs, atomic structure changes under high pressure were also reported for BMG system $\text{Zr}_{60}\text{Ni}_{21}\text{Al}_{19}$ [214] and $\text{Zr}_{57}\text{Nb}_5\text{Cu}_{15.4}\text{Ni}_{12.6}\text{Al}_{10}$ [215]. So far, to the best of our knowledge, polyamorphism in MG and BMG have been only reported for alloy systems containing Ce element. So whether polyamorphism occur in other non Ce contained system is not clear.

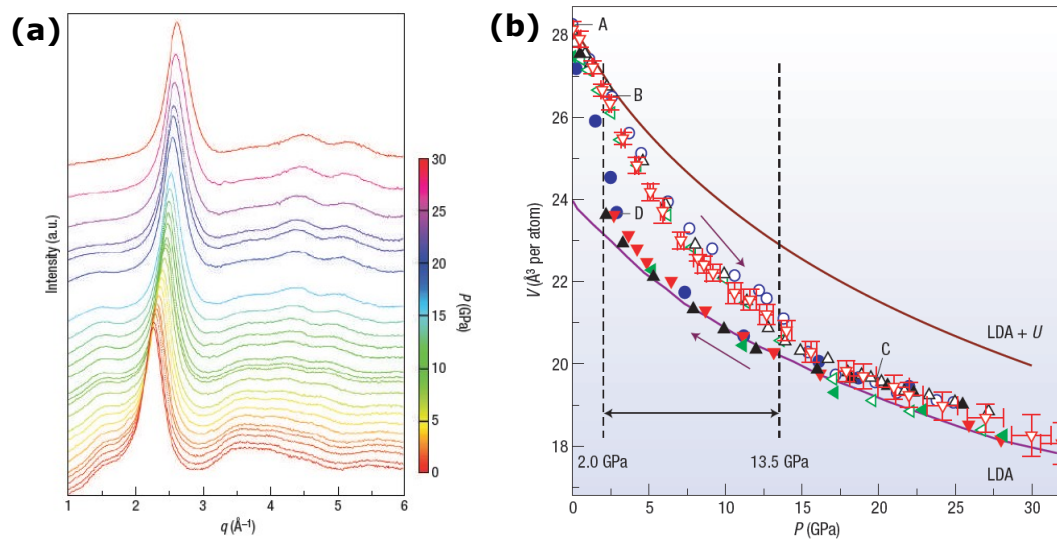


Figure 2.33 DAC high pressure compression of $\text{Cu}_{55}\text{Al}_{45}$ MG. (a) XRD patterns acquired at different pressure step during the compression cycle, (b) specific volume versus pressure for the amorphous $\text{Ce}_{55}\text{Al}_{45}$ obtained from the in situ SXR of 4 samples in DAC [205].

2.6 Summary

This chapter give a comprehensive review on the historical and recent development on metallic glasses, bulk metallic glasses and composites including their existing and future applications. The experimental and modelling methods and techniques developed to design bulk metallic glass alloys, and to study and characterise the atomic structures, and mechanical properties are also discussed in details.

Chapter 3 Alloy design, sample making and experimental methods

This chapter describes systematically the alloys, samples and experimental methods used in this project. Sections are grouped into (1) selection and design of novel metallic glass alloys, (2) manufacturing of alloys and samples for different experiments, (3) preparation of special samples and in situ experiments for tensile deformation studies of bulk metallic glasses and composites, (4) nano-indentation experiments, and (5) summary of the awarded synchrotron X-ray proposals and beam time that are directly relevant to my PhD project. The materials and information described here are linked directly to the results described in chapter 4, 5 and 6. In addition to the experimental methods described in this chapter, the methods used in the high pressure compression experiments (using Diamond Anvil Cell) plus anomalous scattering experiments, and neutron absorption measurement are described in details in Chapter 5 and 6 respectively, so as to construct a more logically linked individual document for Chapter 5 and Chapter 6.

3.1 Selection and design of novel metallic glass alloys

Four different types of samples were made and used in this project for different experimental purposes as summarised in Table 3.1. The ribbon alloys and samples (Table 3.2) used in the project were made by using a single-roller melt-spinning method. The stepped rod bars (Table 3.3) with different diameters, and the plates (Table 3.4) were cast using water cooled copper mould. The button-shaped ingots (Table 3.5) were melted and then solidified inside the copper crucible of the arc remelting furnace. The alloys with the chemical compositions marked by asterisk * are the systems chosen from open literatures with the aims of using them as the baseline alloys to benchmark the newly designed alloys for the targeted mechanical and functional properties. All new alloys were designed by my supervisor (Dr Jiawei Mi) and myself, and then manufactured at Prof Jun Shen's group in Harbin Institute of Technology (HIT), China via the research collaboration supported by the Royal Society K. C. Wong Postdoctoral Fellowship from April 2012 to March 2014. The alloys used in the high pressure compression experiments (EE8858-1 and EE9902-1 in Table 1.1) were jointly designed

by my supervisor, and Dr Qiang Luo of Tong Ji University who is also in Prof Jun Shen's group (Prof Shen moved to Tong Ji University in 2013), and made by Dr Luo. The two high pressure compression experiments are actually the joint research effort among my supervisor, Dr Mi, Prof Shen and Professor Paul McMillan of University College London.

Table 3.1 The types of samples and their dimensions used in this project.

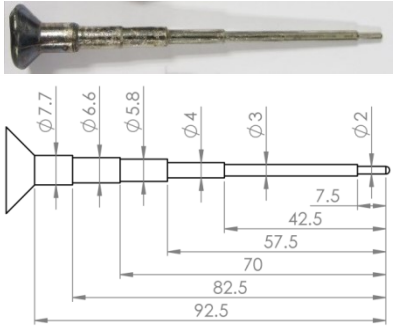
Sample, dimension and image	Cooling rate(K/s)	Aims of the samples and research
Ribbon: 7-14 mm (wide) X 30-40 μm (thick) 	$\sim 10^6 - 10^7$	Ribbons were used for testing the newly designed binary and ternary alloy systems to determine whether they can be made into amorphous state or not. In addition, the sample thickness fits well to the Diamond Anvil Cell
Stepped rod bar: All dimensions are in [mm] 	$10^2 - 10^3$	The stepped rod bar has different diameter sections that are subject to different cooling rates. Such sample is often used to determine the glass forming ability at different cooling rates for new alloys.
Plate: 60 (long) X 30 (wide) X 3(thick) [mm] 	$\sim 10^3$	It has a consistent cooling rate throughout the length of the sample, which is ideal for being machined into the dog-bone shaped tensile test samples
Button ingot: $\sim \text{Ø}39 \times 10$ (high) [mm] 	$1 - 10^3$	This is for the ZrTi based bulk metallic glass composites, because it is too viscous to be cast into plates. Button ingots were used for making the miniature dog-bone shaped tensile test samples as well

Table 3.2 The alloys and ribbon samples made by melt-spinning method

Alloy matrix	Code	Nominal composition (atomic %)	The objectives of the designed alloys	
Fe-based	Fe ₉₀ Zr ₁₀	Fe ₉₀ Zr ₁₀	High pressure compression experiments using Diamond Anvil Cell	
	Fe ₇₅ B ₂₅	Fe ₇₅ B ₂₅		
	Fe ₆₀ Nb ₁₅ B ₂₅	Fe ₆₀ Nb ₁₅ B ₂₅		
				Others
	Fe-B ₆ Y ₂	Fe ₄₈ Cr ₁₅ Mo ₁₄ C ₁₅ B ₆ Y ₂ *[216]		
	Fe-B ₆ Y ₂ Co ₃	Fe ₄₅ Cr ₁₅ Mo ₁₄ C ₁₅ B ₆ Y ₂ Co ₃		
	Fe-B ₆ Y ₂ Co ₅	Fe ₄₃ Cr ₁₅ Mo ₁₄ C ₁₅ B ₆ Y ₂ Co ₅		
Fe-B ₆ Y ₂ Co ₇	Fe ₄₁ Cr ₁₅ Mo ₁₄ C ₁₅ B ₆ Y ₂ Co ₇			
Fe-B ₆ Y ₂ Co ₉	Fe ₃₉ Cr ₁₅ Mo ₁₄ C ₁₅ B ₆ Y ₂ Co ₉			
Fe-B ₆ Er ₁	Fe ₄₉ Cr ₅ Mo ₁₄ C ₁₅ B ₆ Er ₁			
Cu-based	Cu ₅₀ Zr ₅₀	Cu ₅₀ Zr ₅₀	High pressure compression experiments using Diamond Anvil Cell	
	Cu ₅₇ Zr ₄₃	Cu ₅₇ Zr ₄₃		
	Cu _{64.5} Zr _{35.5}	Cu _{64.5} Zr _{35.5}		
	Cu ₅₀ Ni ₅₀	Cu ₅₀ Ni ₅₀		
	Cu ₅₅ Zr ₄₀ Al ₅	Cu ₅₅ Zr ₄₀ Al ₅		
Ti-based	Cu ₅₀ Ti ₅₀	Cu ₅₀ Ti ₅₀	High pressure compression experiments using Diamond Anvil Cell	
	Ti ₅₄ Cu ₄₆	Ti ₅₄ Cu ₄₆		
	Ti ₅₅ Cu ₄₅	Ti ₅₅ Cu ₄₅		
	Ti ₅₇ Cu ₄₃	Ti ₅₇ Cu ₄₃		
	Ti ₆₀ Cu ₄₀	Ti ₆₀ Cu ₄₀		
	Ti ₅₅ Cu ₄₂ Ni ₃	Ti ₅₅ Cu ₄₂ Ni ₃		
	Ti ₅₅ Cu ₃₈ Ni ₇	Ti ₅₅ Cu ₃₈ Ni ₇		
			High pressure compression experiments using Diamond Anvil Cell	
	Ti ₆₅ Ni ₃₅	Ti ₆₅ Ni ₃₅		
	Ti ₇₀ Ni ₃₀	Ti ₇₀ Ni ₃₀		
	Ti ₇₅ Ni ₂₅	Ti ₇₅ Ni ₂₅		
			Others	
	Vit-1	Ti ₄₀ Zr ₂₅ Ni ₁₂ Cu ₃ Be ₂₀		
	Vit-1-V ₄	Ti ₄₀ Zr ₂₅ Ni ₈ Cu ₃ Be ₂₀ V ₄		
Vit-1-V ₈	Ti ₄₀ Zr ₂₅ Ni ₄ Cu ₃ Be ₂₀ V ₈			
Vit-1-V ₁₂	Ti ₄₀ Zr ₂₅ Cu ₃ Be ₂₀ V ₁₂			
Vit-1-Nb ₄	Ti ₄₀ Zr ₂₅ Ni ₈ Cu ₃ Be ₂₀ Nb ₄			
Vit-1-Nb ₈	Ti ₄₀ Zr ₂₅ Ni ₄ Cu ₃ Be ₂₀ Nb ₈			
Vit-1-Nb ₁₂	Ti ₄₀ Zr ₂₅ Cu ₃ Be ₂₀ Nb ₁₂			
Al-based	Al ₉₂ Ce ₈	Al ₉₂ Ce ₈	High pressure	

Table 3.3 The alloys and stepped rod bars cast by copper mould

Alloy matrix	Alloy code	Nominal composition (atomic %)	The objectives of the designed alloys
Fe-based	Fe ₇₅ B ₂₅	Fe ₇₅ B ₂₅	Neutron absorption experiment alloy design (1 st batch)
	Fe ₆₆ Nb ₄ B ₃₀	Fe ₆₆ Nb ₄ B ₃₀	
	FeNb-Si ₅	Fe ₅₀ Cr ₂₅ Nb ₄ Si ₅ B ₁₆	
	Fe-Si ₃ B ₃	Fe ₅₀ Cr ₂₄ Mo ₂₀ Si ₃ B ₃	
	Fe-Si ₆	Fe ₅₀ Cr ₂₄ Mo ₂₀ Si ₆	
	Fe-B ₅	Fe ₄₅ Cr ₁₆ Mo ₁₆ C ₁₈ B ₅	Neutron absorption experiment alloy design (2 nd batch)
	Fe-B ₆ Sn ₂	Fe ₄₈ Cr ₁₅ Mo ₁₄ C ₁₅ B ₆ Sn ₂	
	Fe-B ₆ Zr ₂	Fe ₄₈ Cr ₁₅ Mo ₁₄ C ₁₅ B ₆ Zr ₂	
	Fe-B ₆ Zr ₁ Sn ₁	Fe ₄₈ Cr ₁₅ Mo ₁₄ C ₁₅ B ₆ Zr ₁ Sn ₁	
	Fe-B ₆ Y ₂	Fe ₄₈ Cr ₁₅ Mo ₁₄ C ₁₅ B ₆ Y ₂ *[216]	
	Fe-B ₁₆	Fe ₅₂ Cr ₁₉ Mn ₂ Nb _{4.5} B ₁₆ C ₄ Si _{2.5}	Neutron absorption experiment alloy design (3 rd batch)
	FeNb-Si ₅ Gd ₃	Fe ₅₀ Cr ₂₂ Nb ₄ B ₁₆ Si ₅ Gd ₃	
	FeMn-B ₆ Gd ₂	Fe ₄₈ Cr ₁₅ Mn ₁₄ C ₁₅ B ₆ Gd ₂	
	Fe-B ₁₅ Gd ₂	Fe ₄₈ Cr ₁₅ Mo ₁₄ C ₆ B ₁₅ Gd ₂	
	Fe-B ₆ Gd ₂	Fe ₄₈ Cr ₁₅ Mo ₁₄ C ₁₅ B ₆ Gd ₂	
	Fe-B ₆ Y ₂ Co ₇	Fe ₄₇ Cr ₁₅ Mo ₁₄ C ₁₅ Y ₂ Co ₇	Others
Ti-based	TiZr-W ₄	(Ti ₄₅ Zr ₁₆ Be ₂₀ Cu ₁₀ Ni ₉) ₉₆ W ₄	BMGMC alloy design
	TiZr-W ₁₂	(Ti ₄₅ Zr ₁₆ Be ₂₀ Cu ₁₀ Ni ₉) ₈₈ W ₁₂	

Table 3.4 The alloys and plates cast by copper mould

Alloy matrix	Alloy code	Nominal composition (atomic %)	The objectives of the designed alloys
Ti-based	TiZr	Ti ₄₀ Zr ₂₅ Ni ₁₂ Cu ₃ Be ₂₀ *[217]	In situ tensile test
Zr-based	Vit-1	Zr _{41.2} Ti _{13.8} Cu _{12.5} Ni ₁₀ Be _{22.5} (Vit-1)*[27]	In situ tensile test

Table 3.5 The alloy and ingot cast by copper mould

Alloy matrix	Alloy code	Nominal composition (atomic %)	The objectives of the designed alloys
Zr-based	ZrTi	Zr _{39.6} Ti _{33.9} Nb _{7.6} Cu _{6.4} Be _{12.5} [7]	In situ tensile test

3.2 Manufacturing of the alloys and samples

The arc remelting furnace (FD-1200H, KYKY Technology Development Ltd) housed at Harbin Institute of Technology, China was used to make the alloys. The arc melting furnace was first pumped into low vacuum (~ 0.06 Pa) followed by circulating with argon gas. Next, pure Ti was first heated up into liquid to absorb the residual oxygen inside the chamber and discarded before melting the master alloys. The master alloys for each chemical composition were first made by arc melting a mixture of the corresponding elemental button ingots with the purity of $> 99.9\%$. The master alloys were then remelted at least four times to ensure chemistry homogeneity before melt-spinning into ribbons or cast into the copper mould to form stepped rod bars or plates.

3.3 Design and preparation of samples for in situ studies

3.3.1 Design of the miniature dog-bone tensile test samples

For in situ tensile tests, dog-bone shaped samples with the dimensions show in Figure 3.1a and Appendix 1 were designed according to British Standard (BS EN 10002-1:2001) [218] for non-proportional test pieces. In addition to the samples with parallel gauge length, for some other samples, either a notch on the edge (Figure 3.1b) or a hole in the centre (Figure 3.1d) of the gauge length is introduced as a local stress concentrator for tensile tests. In addition, micro-indentation marks were placed on the gauge length to measure the strain as shown in Figure 3.1c and Figure 3.1e.

Electric discharging machining (EDM) was used to machine the dog-bone shaped samples from as cast plates and button ingots. EDM was chosen because firstly, it provides a smooth cutting edge which was critical for the tensile test as rough edge might cause undesired stress concentration, secondly, EDM cutting is carried out in a water jet cooled environment, avoiding any possible undesired mechanical or heating damages to the samples. The typical dog-bone samples and the left-over pieces cut off by EDM are shown in Figure 3.2. The hole in the middle of the gauge length was drilled using a bench top driller with $\varnothing 0.4$ mm tungsten carbide drill bit.

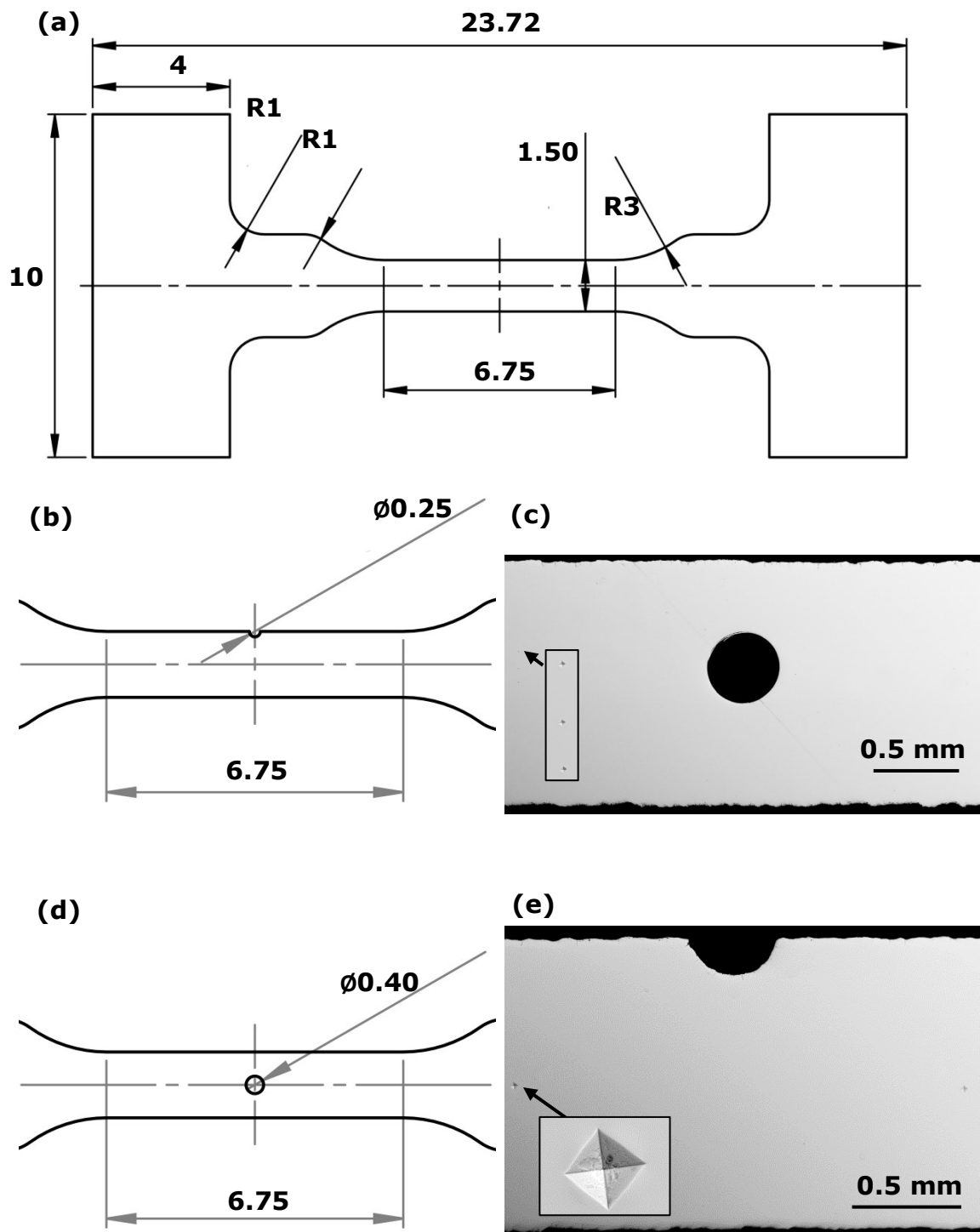


Figure 3.1 A CAD drawing of dog-bone shaped sample designed for the in situ tensile tests. (a) The dimension of the sample with a uniform thickness of 0.8 (all dimensions are in mm). (b) The gauge length section with either a notch or (d) a hole introduced as the stress concentrator and their corresponding SEM images (c) and (e) with insert image showing the micro-indentation marks.

3.3.2 Machining, grinding and polishing of samples

Lab-based X-ray radiography with a copper target (HMX-160, X-TEK) was used to examine whether there are any detectable porosity or defects. The typical micro-crack and porosity found by lab X-ray radiography is shown in Figure 3.3. The samples without any detectable defects will proceed to a very delicate grinding and polishing process. The samples need to have a very high quality surface for “visualising” the initiation and propagation of shear bands under electron microscopy during in situ tensile tests, and for the nano-indentation tests as well. In addition, maintaining a parallel and constant thickness for the whole gauge length is also very important to minimise any uncertainty or error in measuring and calculating the strains and stresses during the tensile tests.



Figure 3.2 The dog-bone shape samples and other pieces cut from a button ingot using EDM.

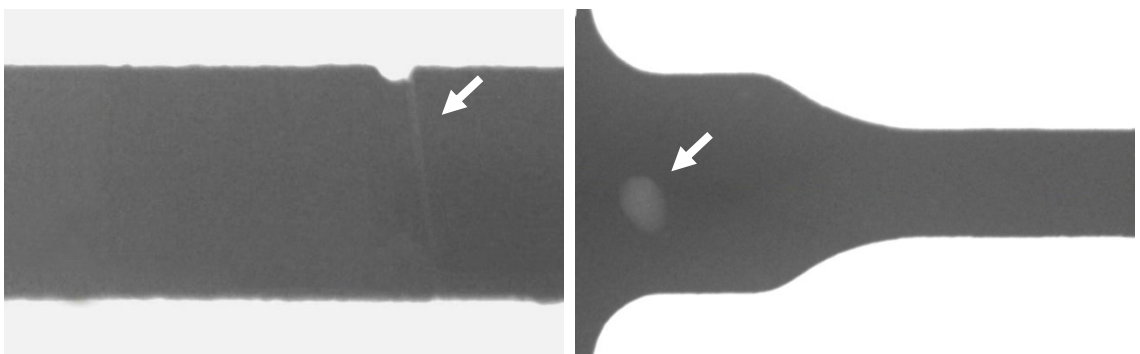


Figure 3.3 Lab-based X-ray radiography images, showing (a) a crack and (b) a pore found in the dog-bone sample.

For grinding and polishing normal samples (non dog-bone shaped samples, including some of the samples for nano-indentation experiments), the samples were mounted on conductive Bakelite using the 38 mm Buehler hot

mounting press operated at $\sim 200^{\circ}\text{C}$ with 4800 PSI pressure. Conductive Bakelite was used for facilitating SEM observation. For grinding and polishing dog-bone shaped samples and thin disk samples for neutron absorption measurement, special sample holders were designed and made using brass and aluminium rods as shows in Figure 3.4. The CAD drawing of such sample holder is also listed in Appendix 2 and Appendix 3. It was designed to retain the sharp edge of the samples and achieve a parallel and constant thickness for the whole sample length, while at the same time to realise a high quality polished surface.

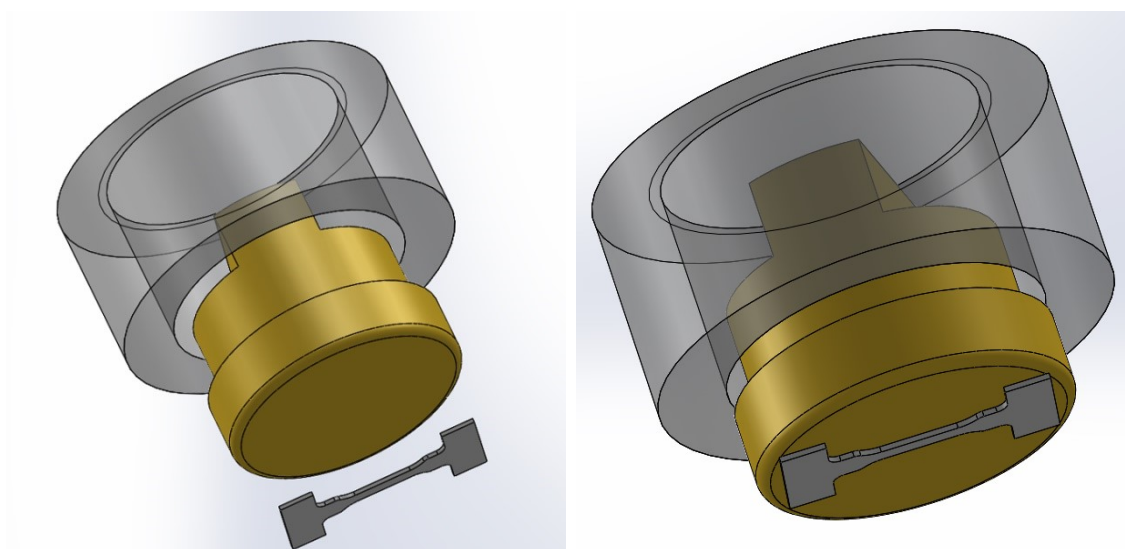


Figure 3.4 CAD drawing of the sample holder that was designed to hold the dog-bone shape and thin disk samples during the grinding and polishing process.

The samples were first ground using different grades of SiC papers (P400, P800 and P1200) and then polished using diamond suspensions of 6, 3 and 1 μm . The final surface finishing was carried out using 0.06 μm colloidal silica suspension (Kemet). All grinding and polishing were carried out using a semi-automatic polishing machine, Buehler Motopol 12. After polishing, the samples were cleaned inside an ultrasonic bath (Gem 3D, Kemet) using firstly acetone, secondly methanol and finally isopropanol (each for 5 minutes). The samples were than taken out of the ultrasound bath and flushed with isopropanol thoroughly before dried up using a hair dryer. For the whole cleaning process, the samples were handled using a bamboo tweezers to prevent any scratches on the surface. For the samples mount on the conductive Bakelite, one side surface was polished. While for the dog bone samples and thin disks for neutron transmission measurement, both

side surfaces were polished to remove any surface imperfection that might cause undesired local shear band nucleation during the tensile tests and affect the neutron transmission measurement.

3.3.3 Samples for high pressure compression experiments

For the in situ high pressure experiments, a sample was placed inside the Diamond Anvil Cell (DAC) that was used to create high pressure surround the sample. To reach the target pressure for the experiments, the space in the sample chamber has to be confined to a very small volume and this restricts the sample size to 50~70 μm in diameter with the thickness of ~50 μm . Hence, ribbon samples which usually have thickness of 30~50 μm were used in the high pressure experiments. Because of the limited beam times awarded, only 3 alloys ($\text{Zr}_{50}\text{Cu}_{50}$, $\text{Ti}_{60}\text{Cu}_{40}$ and $\text{Fe}_{60}\text{Nb}_{15}\text{B}_{25}$) were selected for the experiments. The training of loading a sample into a DAC was given by the senior support beamline scientist, Dr Dominik Daisenbeger during the visit to beamline I15 of DLS on 20th March 2013. During the actual experiments on 10-13 July 2013 (EE8858-1) and 18-21 April 2014 (EE9902-1), all samples and their loadings into the DAC were carried out by Dr Dominik Daisenbeger in order to reduce the chances of failure during the experiments. Normally, it needs years of training and experience for being able to prepare a high quality sample, and load it properly into the DAC for the acquisition of high quality diffraction data. The details of the high pressure experiments, including sample preparation and loading are described in Chapter 5.

3.4 Nano-indentation experiments

The nano-indentation experiments were carried out to obtain nano hardness and Young's modulus of the samples studied, to complement the results from other experiments and provide essential data needed for finite element modelling. Table 3.6 lists the nano-indentation experiments performed, samples and the parameters used. The CSM nano-indenter (CSM Instruments, Switzerland) housed at the School of Engineering, University of Hull was used for the experiments with the support from a dedicated technician, Ms Sue Taft. To minimise the vibration on the samples during

the tests, the indenter is seated on a vibration-free station (Kinetic Systems Inc. MA, USA). The indentation marks were done at room temperature using the Berkovich diamond tip onto the polished samples that were mounted on conductive Bakelite. To obtain sufficient statistical data, array of indents were made for each sample as typically shows in Figure 3.5. A larger indent was firstly made alongside with those small indents as a marker for easy tracking of those indents under microscopes. The indents were then observed and imaged using a Zeiss Evo 60 environmental SEM.

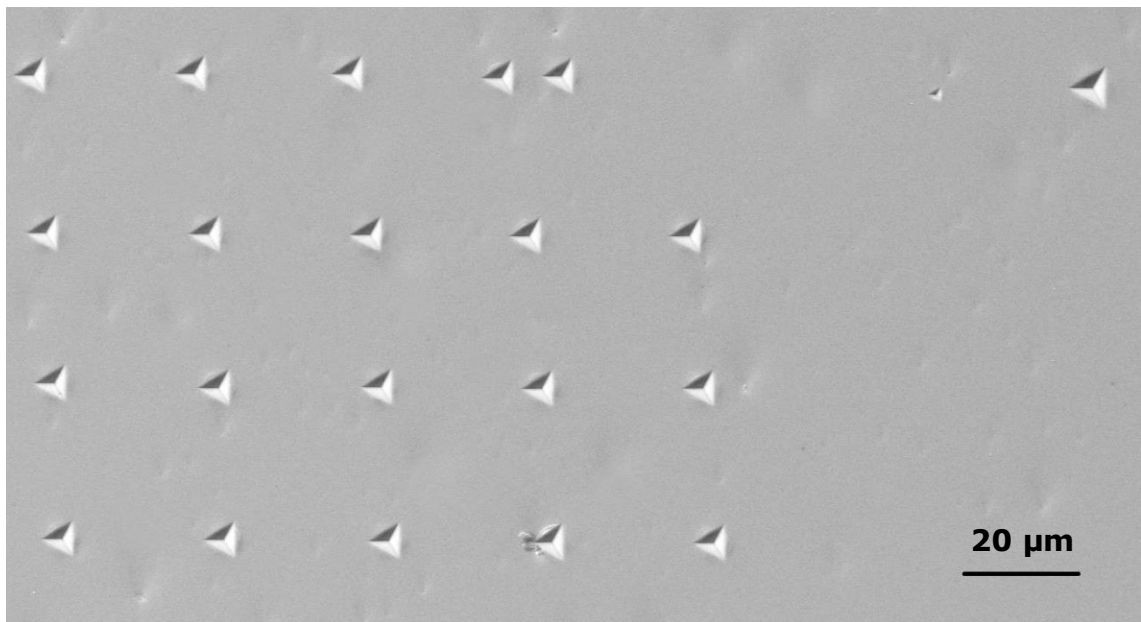


Figure 3.5 A secondary electron image, showing an array of indents made on the Fe-B₆Y₂ Ø5.8 mm step-bar alloy sample using the displacement mode with a maximum depth of 1000 nm and loading and unloading rate of 1000 nm/min.

The nano hardness H_{it} and the Young's Modulus, E is calculated using Eq. (1) and Eq. (2), correspondingly.

$$H_{it} = \frac{P_{max}}{A_C} \quad (1)$$

$$E = \frac{\sqrt{\pi}}{2} \times \frac{S}{\sqrt{A_C}} \quad (2)$$

Where A_C is the contract area, calibrated using a silica block, the P_{max} and S is obtained from the nano-indentation graph as illustrated in Figure 3.6.

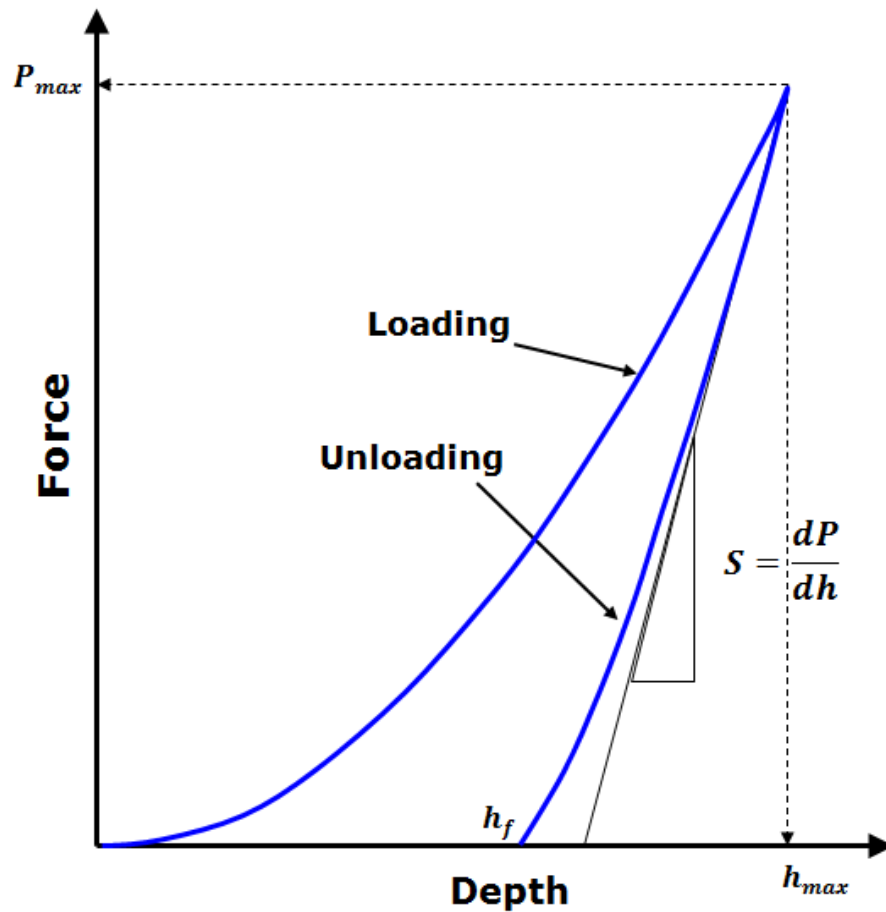


Figure 3.6 A schematic of load versus indentation depth curve of nano-indentation test, showing important measured parameters.

Table 3.6 The nano-indentation experiments, samples and parameters.

Alloy and samples	Test mode and the parameters used	
Monolithic bulk metallic glass alloys: 1. TiZr: $\text{Ti}_{40}\text{Zr}_{25}\text{Ni}_{12}\text{Cu}_3\text{Be}_{20}$ 2. Vit-1: $\text{Zr}_{41.2}\text{Ti}_{13.8}\text{Cu}_{12.5}\text{Ni}_{10}\text{Be}_{22.5}$	Control mode	Displacement
	Maximum depth	200 nm
	Loading rate	500 nm/min
	Unloading rate	500 nm/min
	No of indentation	30
Monolithic bulk metallic glass alloys: $\text{Fe-B}_6\text{Y}_2$: $\text{Fe}_{48}\text{Cr}_{15}\text{Mo}_{14}\text{C}_{15}\text{B}_6\text{Y}_2$ 3 separate nano-indentation tests were carried on $\varnothing 4$, $\varnothing 5.8$ and $\varnothing 6.6$ mm stepped rod bar samples, respectively	Control mode	Displacement
	Maximum depth	1000 nm
	Loading rate	1000 nm/min
	Unloading rate	1000 nm/min
	No of indentation	30

Monolithic bulk metallic glass alloys: Fe-B ₆ Gd ₂ : Fe ₄₈ Cr ₁₅ Mo ₁₄ C ₁₅ B ₆ Gd ₂ 4 separate nano-indentation tests were carried on Ø3, Ø4, Ø5.8 and Ø7.6 mm stepped rod bar samples, respectively	Control mode	Displacement
	Maximum depth	1000 nm
	Loading rate	1000 nm/min
	Unloading rate	1000 nm/min
	No of indentation	30
Bulk metallic glass composite: ZrTi: Zr _{39.6} Ti _{33.9} Nb _{7.6} Cu _{6.4} Be _{12.5}	Control mode	Displacement
	Maximum depth	200 nm
	Loading rate	100 mN/min
	Unloading rate	100 mN/min
	No of indentation	50
Bulk metallic glass composite: ZrTi: Zr _{39.6} Ti _{33.9} Nb _{7.6} Cu _{6.4} Be _{12.5}	Control mode	Displacement
	Maximum depth	200 nm
	Loading rate	500 mN/min
	Unloading rate	500 mN/min
	No of indentation	100
Bulk metallic glass composite: ZrTi: Zr _{39.6} Ti _{33.9} Nb _{7.6} Cu _{6.4} Be _{12.5}	Control mode	Load
	Maximum load	5 mN
	Loading rate	10 mN/min
	Unloading rate	10 mN/min
	No of indentation	30
Mild steel: as the first training material	Control mode	Load
	Maximum load	250 mN
	Loading rate	500 mN/min
	Unloading rate	500 mN/min
	No of indentation	30

3.5 In situ tensile deformation experiments

3.5.1 Design and making of new sample clamps

The tensile deformation behaviours of monolithic bulk metallic glasses and bulk metallic glass composites were studied in situ using imaging method inside scanning electron microscopy and diffraction method at synchrotron X-ray beamline. A Deban micromechanical test module (model 2000 as showed in Figure 3.7) with a 2 kN load capacity was used for such studies.

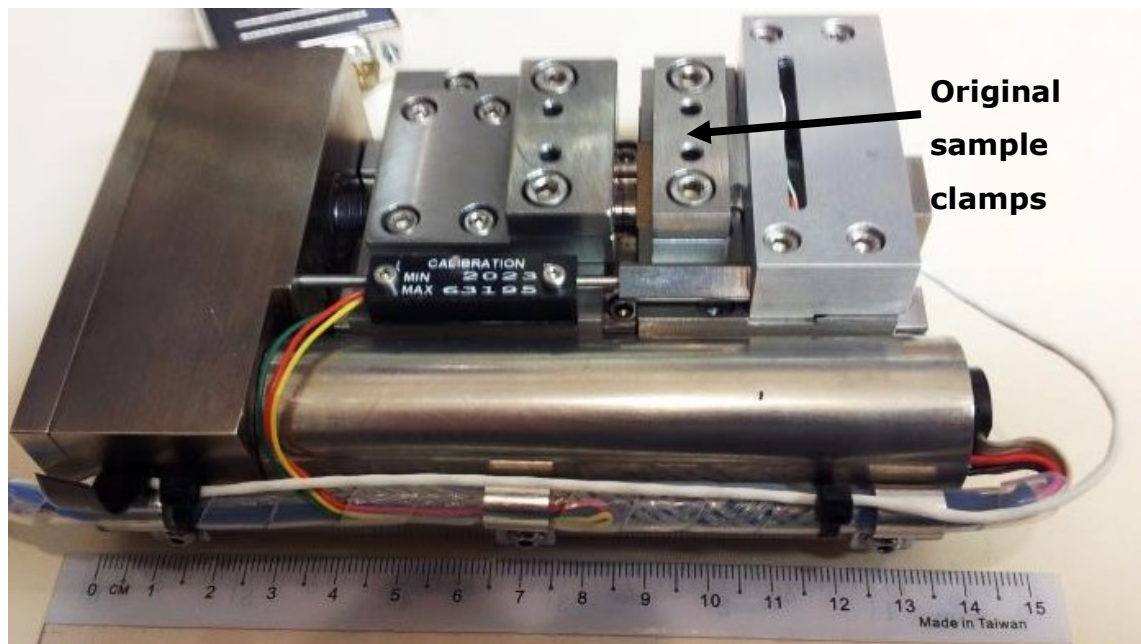


Figure 3.7 Deban Microtest module 2000 used in the in situ tensile test.

The original sample clamps are not suitable for the brittle BMG samples because the pressure and friction force transferred from the clamps often fracture the dog-bone samples. In addition, there is no clear pathway for X-ray to transmit through the dog-bone sample without avoid hitting on the rig body. Therefore, a special sample clamp was designed (Figure 3.8a and Appendix 4-6) and made for the in situ tensile tests. A dog-bone shaped recess (a slightly bigger profile than the sample profile) was machined into the clamp at both sides (Figure 3.8), allowing the dog-bone sample to sink into the recess and held there firmly without subject to any bigger friction force. For SEM experiments, the dog-bone sample is clamped inside the top recess (Figure 3.8a and Figure 3.8b), while for the X-ray experiments, the

sample is clamped inside the side recess to give a clear X-ray pathway as illustrated in Figure 3.8a.

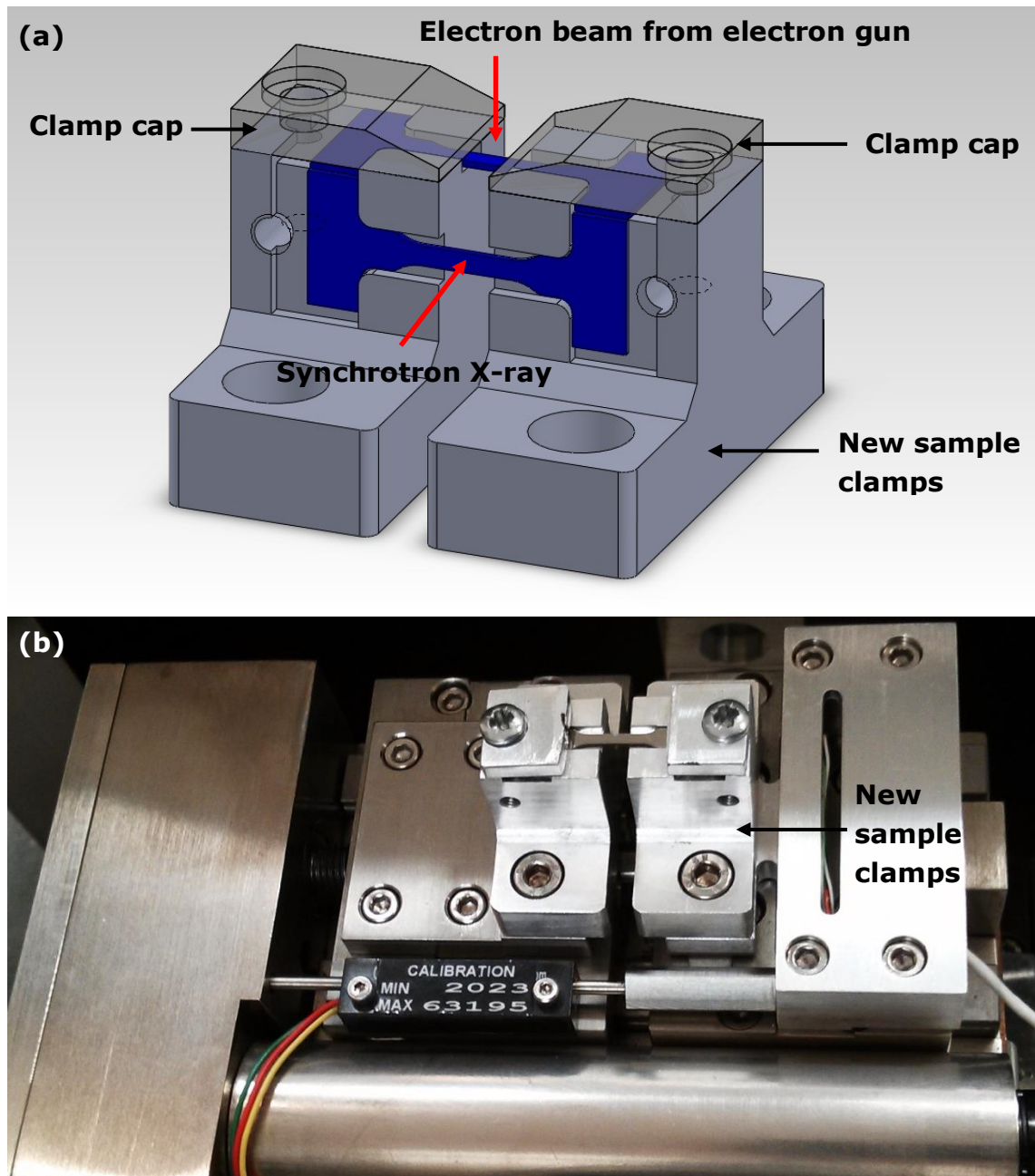


Figure 3.8 The newly designed tensile test sample clamps for the in situ tensile tests. (a) A CAD model of sample clamps, showing the dog-bone sample positions for in situ SEM and SXR experiments. (b) The mounting of the new sample clamps onto the Deban 2000 micromechanical test module with a dog-bone sample clamped into the top recess of the new clamps.

3.5.2 In situ imaging studies of tensile deformation inside SEM

A Zeiss Evo 60 environmental scanning electron microscope (SEM) equipped with a LaB₆ filament was used in this project for routine imaging of polished or fractured samples. This SEM has a big vacuum chamber to accommodate the Deben microtest module. Therefore in situ mechanical tests can be performed inside the chamber as well. Sample loading onto the microtester was carried out using the following procedure. Firstly, a dog-bone sample was placed into the top clamp recess using a tweezers, and a 20 N preload was given to hold the sample temporarily in place. Then, two “caps” (Figure 3.8a) were screwed gradually on top of the sample and pressed the sample onto the bottom of the recess and held it firmly in place after the screw was tight enough (just stop any possible vertical movement of the dog-bone sample during the subsequent test, therefore no big force is needed). Then the whole test module was placed inside the SEM chamber followed by routine gun alignment and imaging parameter adjustment, i.e. adjustment of gun voltage, sample work distance, imaging astigmatism, etc. Figure 3.9 shows a typical image of the microtester inside the SEM chamber, and Figure 3.10 shows, using a schematic, more clearly the relative positions of the sample, new clamps, microtester and the detectors within the SEM chamber during the in situ tensile tests.

Before the tests, a series of images at different magnifications were taken to record the characteristics of the sample, the areas of interest for subsequent studies, especially at the nearby regions of either the notch or the hole. The X, Y coordinates of those areas of interest were also recorded for a quick and convenient come back later at higher tensile loads.

The tensile loads can be applied and controlled using either a load step control (in a range of from 0.1 N to 200 N) mode or displacement control (in a range of from 0.01 mm to 1 mm) model using the Microtest software Ver5.3.41. Figure 4.5b shows a typical load-displacement curve recorded using the software.

In addition to the load-displacement curve recorded, the extension of the gauge length at different load steps were also recorded by imaging the

move of the indents marked on the sample gauge length (Figure 3.1c and Figure 3.1d).

Normally, at the beginning of the tensile test and when the sample is in the elastic region, load step control mode was used. While when approaching to the plasticity region, displacement step control mode can be used to have more precise control on any further extension of the sample at next step. At each load or displacement step, the test was paused (holding the load at that step) and painstaking imaging observation was made to investigate any changes of features on the sample surface at that load, and took necessary images before moving onto the next load or displacement step. The SEM was operated at 20 kV, and the work distance was set at 7.5 mm. Backscattered imaging mode was used in most cases because the secondary electron detector is placed at the left corner as shows in Figure 3.10, and shadowing effect was caused by the clamp cap on the acquired secondary electron images. The line integration imaging mode (scanning 12 times on each scanned line) was used to improve significantly the quality of the backscattered images.

Table 3.7 summarises the samples that were in situ tensile tested for the Royal Society K.C. Wong project, my PhD project and two final year undergraduate and master student projects during 2012~2014. Two types of BMG samples were studied: monolithic BMG and BMGMC. On average, each in situ test took around 7 hours, as images needed to be taken at each load/displacement step to investigate any possible nucleation and propagation of shear bands, and other interesting deformation behaviours as well. After the sample was fractured, it was carefully preserved and labelled, and their fracture surfaces were studied again using SEM later.

I am one of the key researchers in preparing at least 80% of those samples and carried out most of the in situ tests during that period. The results and the analyses of two samples are presented in Chapter 4 as one of the important parts of my PhD thesis.

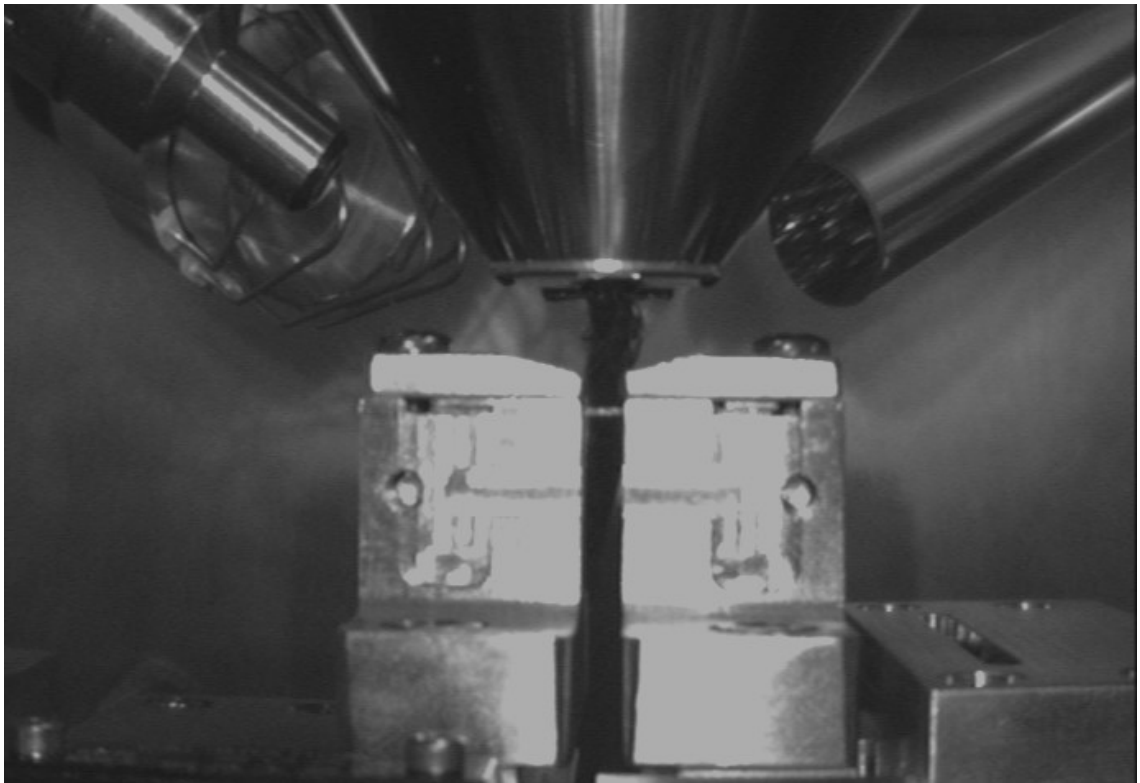


Figure 3.9 An image taken by the infrared camera inside the SEM, showing the dog-bone sample and the new clamps under the electron gun and detectors during the in situ tensile tests.

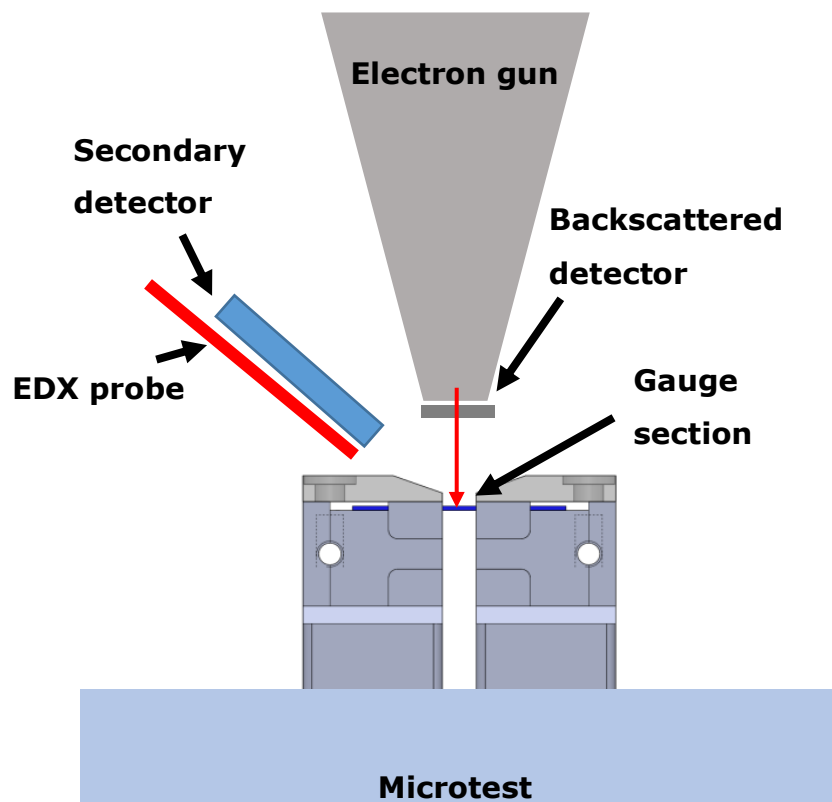


Figure 3.10 A schematic diagram, showing the sample, microtester and detectors.

Table 3.7 The alloys and samples studied by in situ tensile tests inside SEM.

Type of samples	Alloy	Gauge length section width and thickness (mm)	Local stress concentrator (* Result present in Chapter 4)
Monolithic BMG	TiZr: Ti ₄₀ Zr ₂₅ Ni ₁₂ Cu ₃ Be ₂₀	1.46 X 0.46	No
		1.58 X 0.40	No
		1.56 X 0.38	No
		1.49 X 0.29	Ø0.4 mm hole
	Vit-1: Zr _{41.2} Ti _{13.8} Cu _{12.5} Ni ₁₀ Be _{22.5}	1.40 X 0.57	No
		1.40 X 0.43	No
		1.42 X 0.39	R0.15 notch
		1.44 X 0.41	R0.15 notch
		1.42 X 0.27	R0.125 notch
		1.40 X 0.38	R0.125 notch
		1.38 X 0.46	R0.125 notch *
		1.40 X 0.23	Ø0.4 mm hole
	1.44 X 0.44	Ø0.4 mm hole	
	BMGMC	ZrTi: Zr _{39.6} Ti _{33.9} Nb _{7.6} Cu _{6.4} Be _{12.5}	1.42 X 0.41
1.43 X 0.39			R0.125 notch *
1.42 X 0.44			R0.125 notch and FIB pattern
1.42 X 0.35			R0.125 notch and FIB pattern

3.5.3 Synchrotron X-ray diffraction studies and in situ tensile tests

The in situ studies performed inside SEM have generated very rich information concerning the elastic and plastic deformation behaviours of the BMG and BMGMC samples studied. Using the samples with a stress concentrator, i.e. either a notch on the edge, or a hole in the centre of the gauge length of the sample, the nucleation and propagation of shear bands were successfully captured in situ; and the corresponding loads applied via the microtester were recorded as well. However, from the recorded load-displacement curve such as that in Figure 4.9 only the averaged stresses applied onto the whole sample can be obtained, the local strains/stresses near the shear bands and their propagation paths cannot be obtained by such averaged measurement. Hence, in this study, in situ synchrotron diffraction method [10] was used to make such measurements from the particular local areas of interest on the sample. The data obtained from diffraction studies provide the local strains/stress information that, together with the imaging data obtained from SEM studies, helps to understand more thoroughly the tensile deformation behaviour of BMGs and BMGMCs.

Compared to the in situ tensile tests inside SEM, the general experimental setup for in situ tensile tests in a synchrotron X-ray beamline is relative simple. Figure 3.11 shows a typical arrangement for such setup. Basically the microtester is mounted on a sample stage that can be moved in 3 directions with micrometre precision. A monochromatic synchrotron X-ray beam generated by the bending magnets or insertion devices (wiggler or undulator) from the storage ring [219] is transmitting through the sample via an area of interest. Then, the diffracted X-rays by the sample are detected by an X-ray detector, either a 1D diffractometer or a 2D area detector dependent on the primary design purpose the beamlines [219].

Figure 3.13 shows the actual experimental setup at the Joint Engineering, Environmental and Processing beamline (I12) at DLS. Similar to the in situ tests inside SEM. Sample alignment with X-ray, and selection of the local areas of interest for the X-ray to focus onto is paramount important for such studies, especially for the samples with notch on the edge or hole in the middle of the gauge length as showed in Figure 3.12.

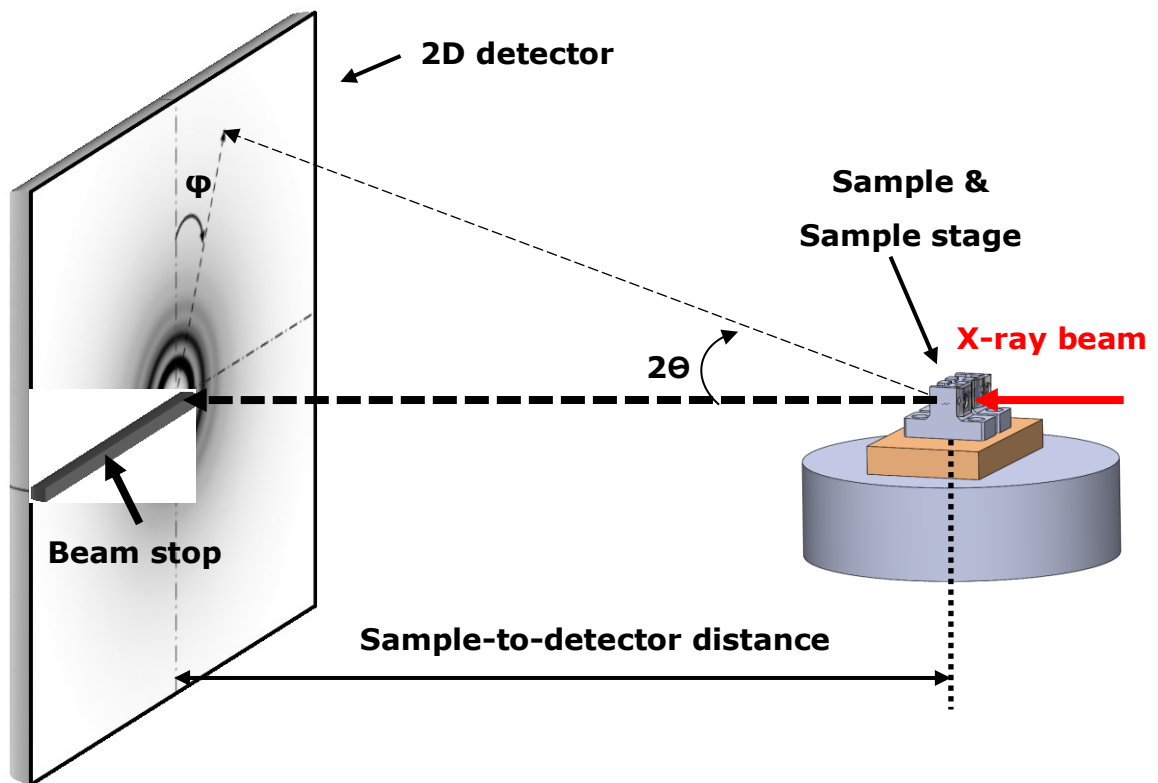


Figure 3.11 A schematic diagram, showing the general experimental setup for in situ synchrotron X-ray diffraction (using an area detector) tests under tensile load.

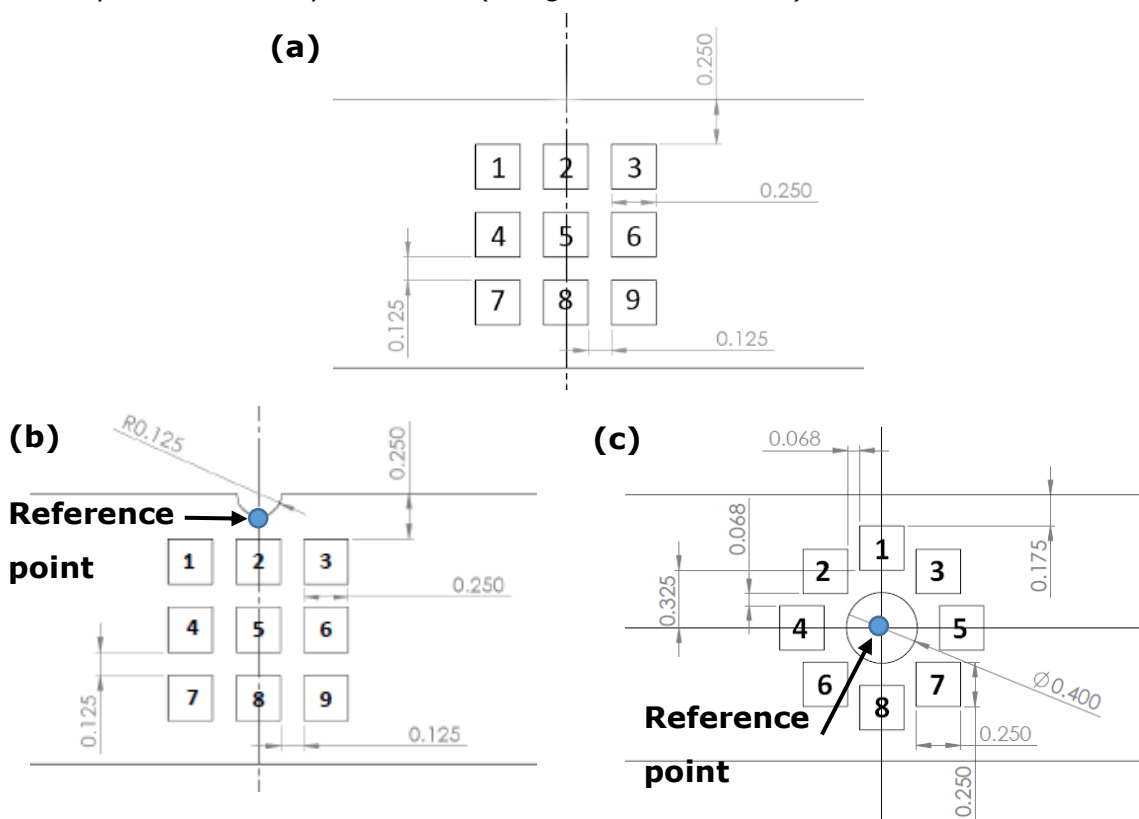


Figure 3.12 The drawings, showing the gauge sections of the samples with (a) no stress concentrator, (b) a notch (ϕ 0.25 mm) on edge, (c) a hole (ϕ 0.4 mm) in the middle, and nine marked local areas where diffraction patterns were acquired at different load steps during the in situ tensile tests.

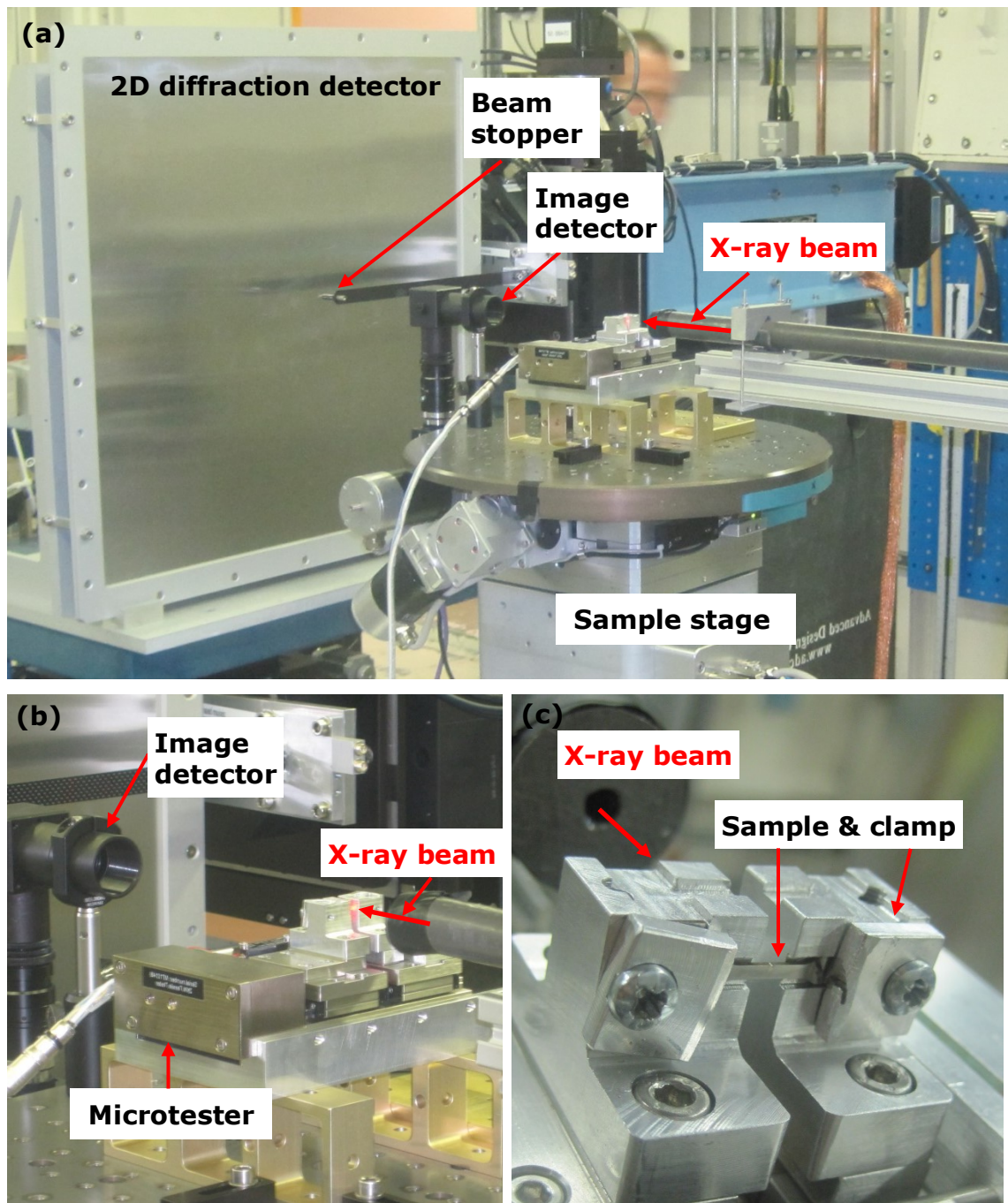


Figure 3.13 The actual experiment setup for in situ diffraction tensile tests at I12 of DLS: (a) an overview of the experiment setup, (b) a zoom-in photo, showing the microtester and X-ray image detector, (c) a close-up photo (facing the X-ray beam guide), showing the incoming X-ray, and the dog-bone shaped sample held in place by the new clamps.

The alignment of X-ray beam onto the areas of interest was carried out using an X-ray image detector (Figure 3.13b) placed behind the sample. For example, the procedure used to find the nine measurement points on the notch sample (Figure 3.12b) is as below.

1. Mount the microtester clamped with a dog-bone notch sample onto the sample stage (Figure 3.13a).
2. Move the sample stage until the alignment laser (a laser that mimic the X-ray beam) in the hutch was focused onto the bottom edge of the notch, i.e. the reference point for the notch as showed in Figure 3.12b.
3. Remove the laser and switch on X-ray beam and firstly set the beam size to 1x1 mm to illuminate the notch area of the sample.
4. Use the X-ray image detector to guide the move of sample stage and position the X-ray beam onto the reference point as shows in Figure 3.12b.
5. Reduce the beam size to 0.25 x 0.25 mm, which was the beam size used to acquire diffraction patterns.
6. Move the X-ray beam downwards to find the 2nd measurement points.
7. Move the X-ray beam to all measurement points one by one, and use the X-ray image detector to confirm a correct movement was made.
8. Record all the coordinates of the measurement points and program the coordinates and stage movement paths into a script in the diamond Generic Data Acquisition (GDA) software that was used later to find the measurement points automatically for acquiring diffraction patterns at those points.

For the sample with a $\varnothing 0.4$ mm hole (Figure 3.1c), similar procedure was used to find the eight measurement points using the centre of the hole as the reference point (Figure 3.12c). The X-ray image detector is so important

for the initial alignment, and also very useful to check any possible deviation from the initial alignment for the sample at different load steps during the test. After a new load was applied during the test, and before taking any new diffraction patterns, the image detector was put back on and used to check the initial reference point. If any deviation occurred, correction was made to find the initial reference point, and then used the script to acquire diffraction patterns. Such operation ensures that diffraction data are acquired from the same measurement points at different load steps. In addition, when a fracture appeared near the edge of the notch or the hole, the X-ray images taken from those areas also provide complementary information to help understanding the initiation and/or propagation of the fracture at that particular load, especially for the BMGMC samples.

After sample alignment, and before applying any load, the tilt and yaw of the 2D area diffraction detector, and sample-to-detector distances were well calibrated using the diffraction patterns collected using Ce_2O and calculated using Fit2D software [220].

During the actual tensile tests, for each measurement point (nine points for notch sample and eight points for hole sample), 30 diffraction patterns were acquired with each having 4 s exposure time. In addition, background and dark frame diffraction patterns were also collected before (15 patterns) and after (15 patterns) collecting the diffraction patterns from the sample. On average, ~18 minutes were needed to complete the diffraction acquisition at each load step.

Five BMG and three BMGMC samples were in situ tensile tested at I12 as summarised in Table 3.8. The fractured samples were carefully labelled and the shear bands formed at the sample surface were studied using SEM after the tests.

Table 3.8 Summary of the dog-bone shape sample tested during the beamtime.

Type of samples	Alloy	Gauge length section width and thickness (mm)	Local stress concentrator (* Result present in Chapter 4)
Monolithic BMG	TiZr: $Ti_{40}Zr_{25}Ni_{12}Cu_3Be_{20}$	1.46 X 0.19	No
		1.49 X 0.32	R0.125 notch
		1.47 X 0.22	Ø0.4 mm hole
	Vit-1: $Zr_{41.2}Ti_{13.8}Cu_{12.5}Ni_{10}Be_{22.5}$	1.46 X 0.36	R0.125 notch *
		1.46 X 0.25	Ø0.4 mm hole
BMGMC	ZrTi: $Zr_{39.6}Ti_{33.9}Nb_{7.6}Cu_{6.4}Be_{12.5}$	1.55 X 0.51	No
		1.55 X 0.47	R0.125 notch *
		1.55 X 0.55	R0.125 notch

In addition to the diffraction measurements carried out during in situ tensile tests, the X-ray beam time available between the gaps in preparing and loading samples were used to collect diffraction data (using the same X-ray parameters and detector set up) for a number of alloys showed in Table 3.2 and Table 3.3, especially during the high pressure experiments at I15 (detailed in Chapter 5) where the loading of a sample and gas into a Diamond Anvil Cell normally take a few hours.

Figure 3.14 shows the set up and alignment for collecting diffraction data at I15, which is different to the X-ray image detector used during alignment at I12. Samples were firstly glued using Blu Tack onto a glass slide that was then clamped onto the sample stage as shows in Figure 3.14a. The sample stage was moved to find the areas of interest on the sample using the "superhead" equipped with an objective lens, which has been calibrated to align with the X-ray beam centre. Once the areas of interest were selected, the sample stage was rotated towards the X-ray beam to acquire diffraction patterns as shows in Figure 3.14b.

For a new alloy sample, 10 s exposure times was used to collect the diffraction pattern which was then immediately integrated into 1D spectrum using Fit2D. If the pattern appeared to be an amorphous feature, another

acquisition was made using 20 s to improve the data quality. Background diffraction patterns were also collected by removing the sample from the sample holder, and the background collection was repeated after every 5 samples' diffraction acquisitions so as to record any possible changes in the background. Darkframe patterns (the noise signals generated from detector without X-ray beam) were collected automatically by the control from the GDA software.

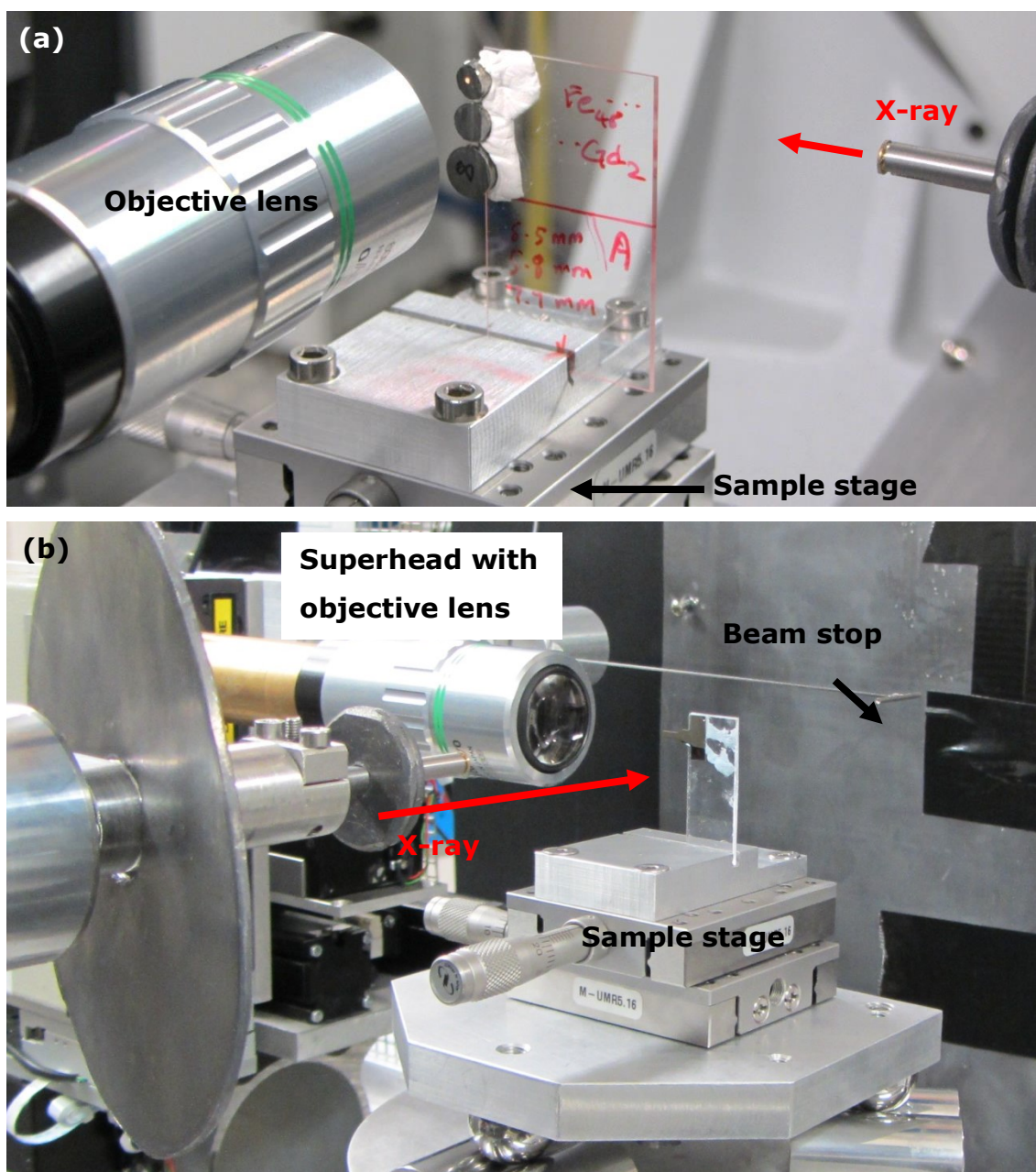


Figure 3.14 Diffraction measurement at beamline I15, (a) sample alignment using the superhead equipped with an objective lens, (b) sample facing the X-ray beam for acquiring diffraction patterns.

3.6 The relevant synchrotron X-ray proposals and beam time

In the period of 2012~2015, four synchrotron X-ray proposals and a total of 17 days beam times (as detailed in Table 1.1) were awarded to the research group led by my supervisor, Dr J. Mi for the research directly relevant to my PhD study and other projects.

The experiments were primarily carried out at three beamlines of Diamond Light Source, i.e. the High Resolution Powder Diffraction (I11), the Joint Engineering, Environmental, and Processing (I12), and the Extreme Conditions (I15). The characteristics of each beamline and the key parameters used in those synchrotron X-ray experiments are summarised in Table 3.6.

In summary, beamline I12 and I15 produce X-rays in a wide range of energy. Using the high energy monochromatic X-ray beams together with a short sample-to-detector distance, diffraction patterns of high scattering vector ($> 20\text{\AA}^{-1}$) can be acquired, which is very important for the total scattering studies described later in Chapter 4 and 5.

Beamline I11 operates in the range of 6-25 keV, and the k-edge energies of most elements in the alloys studied fall into this X-ray energy range. So, I11 was selected for doing the anomalous X-ray scattering experiments as described systematically in Chapter 6. In addition, the PSD arc detector (diffractometer) was used to scan bigger 2θ range (1° to 141°) in order to compensate the lost in high scattering vector due to low X-ray energy.

I am one of the key researchers and played a leading role in preparing samples and carrying out the four experiments above. Typical data from those experiments were selected, analysed and presented in Chapter 4, 5 and 6 to form the essential parts of my PhD thesis.

Table 3.9 Synchrotron X-ray beamline parameters.

Proposal code	Beamline	Insertion Device & energy range	Experiment & samples	X-ray energy & wavelength	Beam size	Detector	SD (mm)	Calibrant
EE7665-1	I12	Wiggler 53-150keV	In situ tensile test: TiZr, Vit-1, ZrTi alloy sample	98.856keV, 0.12541874Å	0.25 X 0.25 and 1 X 1 mm	Thales Pixium RF4343 2D detector 2880 X 2881 pixels 148 X 148 µm pixel size	472.85	CeO ₂
EE8858-1	I15	Undulator 20-80keV	Ambient samples: Table 3.2, Table 3.3	76keV, 0.163137Å	Ø70µm	Perkin Elmer 1621EN 2-D detector 2048 X 2048 pixels 200 X 200 µm pixel size	265.37	Silicon
			High pressure: Cu ₅₀ Zr ₅₀ , Fe ₆₀ Nb ₁₅ B ₂₅ and Ti ₅₅ Cu ₄₅					Silicon in DAC
EE9902-1	I15		Ambient samples: Table 3.2, Table 3.3	72keV, 0.1722Å			327.65	Silicon
			High pressure: Cu ₅₀ Zr ₅₀ , Fe ₆₀ Nb ₁₅ B ₂₅ and Ti ₅₅ Cu ₄₅					Silicon in DAC
EE11525-1	I11	Undulator 6-25keV	Ambient sample: Cu ₅₀ Zr ₅₀ , Fe ₆₀ Nb ₁₅ B ₂₅ and Ti ₅₅ Cu ₄₅	8.337keV, 1.4898Å, 8.984keV, 1.3824Å, 17.983keV, 0.6900Å, 18.963keV, 0.6538Å, 25keV, 0.4952Å	2.5 (width) X 0.6 (height) mm	Position- sensitive detector (PSD) Mythen-II arc detector	N/A	Silicon (for 25keV)

3.7 Summary

This chapter describe the alloy design and sample making and experiments carried out in the thesis. The entire designed alloys were summarised in this chapter with their corresponding designed purposes. This chapter also give details information for the sample preparation for the nano-indentation test, in situ scanning electron microscopy (SEM) and in situ Synchrotron X-ray diffraction experiment, which included sample manufacturing, machining, polishing, and tensile sample clamp designed.

Chapter 4 In situ tensile deformation studies of bulk metallic glass and composite

This chapter presents the in situ tensile test results for a Zr-based monolithic bulk metallic glass, Vit-1, and a ZrTi-based bulk metallic glass matrix composite (named ZrTi composite hereafter) sample (the alloy compositions are showed in Table 3.4 and Table 3.5). The aims of the research are to investigate the underlying relationship between (1) shear band initiation and local atomic strains/stresses; and (2) the local strain/stress field that either drives or prevents the propagation of the shear bands for Vit-1 and ZrTi composite samples.

The tensile test procedures are described in section 3.5.2 (for the imaging method using SEM) and section 3.5.3 (for the diffraction method using Synchrotron X-rays) of Chapter 3 respectively. In addition to the experimental results, finite element method (FEM) was also used to simulate the evolution of local strains/stresses of the samples to complement the experiments for interpreting the tested results.

Table 3.7 lists all samples tested inside SEM, while Table 3.8 lists those tested using Synchrotron X-ray diffraction (SXRD). The results from the sample, TiZr, Vit-1 and ZrTi have already been published in Scripta Materialia [11] , Applied Physics Letters [13] and International Journal of plasticity [12] respectively supported by the Royal Society K.C. Wong Postdoctoral Fellowship project (Dr Y.J. Huang, now back to Harbin Institute of Technology, China).

In this chapter, the results of four samples (sample marked with * in Table 3.7 and Table 3.8) with a notch ($\varnothing 0.25$ mm semi-circular notch) on the edge of the gauge length were presented. The notch is introduced as a local stress concentrator, facilitating the initiation of shear bands in the notched area. One Vit-1 and one ZrTi composite sample were tested in situ inside SEM first, and then the similar load step and procedure was used for the 2nd Vit-1 and 2nd ZrTi composite sample in the SXRD experiments.

4.1 Hardness and Young's modulus measured by nano-indentation

The hardness and Young's modulus of the Vit-1 and ZrTi composite were measured by nano-indentation using the procedure described in section 3.4 of Chapter 3.

Figure 4.1a and Figure 4.1b show the typical SEM images and the corresponding arrays of 30 indents marked on the Vit-1 and ZrTi composite sample. The measured load-depth curves for the two alloys are shown in Figure 4.3.

The hardness and Young's modulus for each alloy were calculated using the formula proposed by Oliver and Pharr as discussed in section 3.4 of Chapter 3, based on the above load-depth curves, and summarised in Table 4.1. Vit-1 has a homogenous amorphous structure, so the result for Vit-1 was obtained by averaging the measured data from all indents. However, the ZrTi composite has two phases – amorphous matrix and crystalline dendrite, SEM was used to carefully examine all indents, and identify the indents marked on the amorphous matrix (Figure 4.2a), the crystalline dendrites (Figure 4.2b), and near or across the amorphous-crystalline interface (Figure 4.2c). Then, their corresponding load-depth curves were also identified as shown in Figure 4.3b where the 5 mN load applied made different depths on the amorphous matrix (black curve), the dendrite (red curve), and near the interface (blue curve). By avoiding the data obtained from the interface region, the hardness and Young's modulus of the amorphous matrix and the crystalline dendrites were calculated by averaging the data measured from the matrix (4 data points) and the dendrites (13 data points), respectively and also listed in Table 4.1.

Table 4.1 Material properties obtained from the Nano-indentation test.

Material Properties	Vit-1	ZrTi composite		
		Matrix	Dendrites	Composite
Young's Modulus (GPa)	124.79	117.77	103.03	109.00
Nano hardness (GPa)	6.60	7.12	3.23	4.81

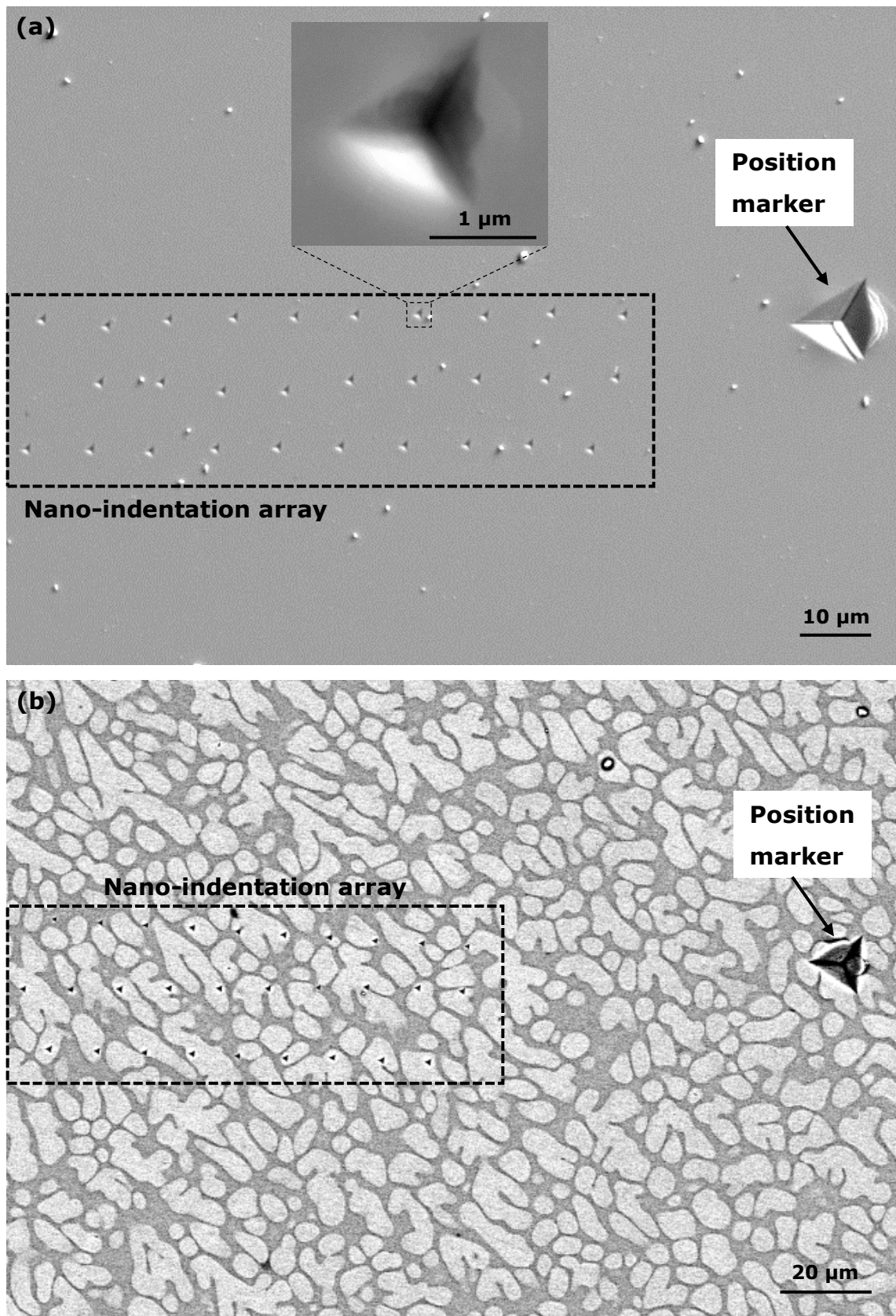


Figure 4.1 SEM images, showing the typical microstructures of (a) Vit-1 and (b) ZrTi composite together with the nano-indentation arrays and the big position marker made on each sample.

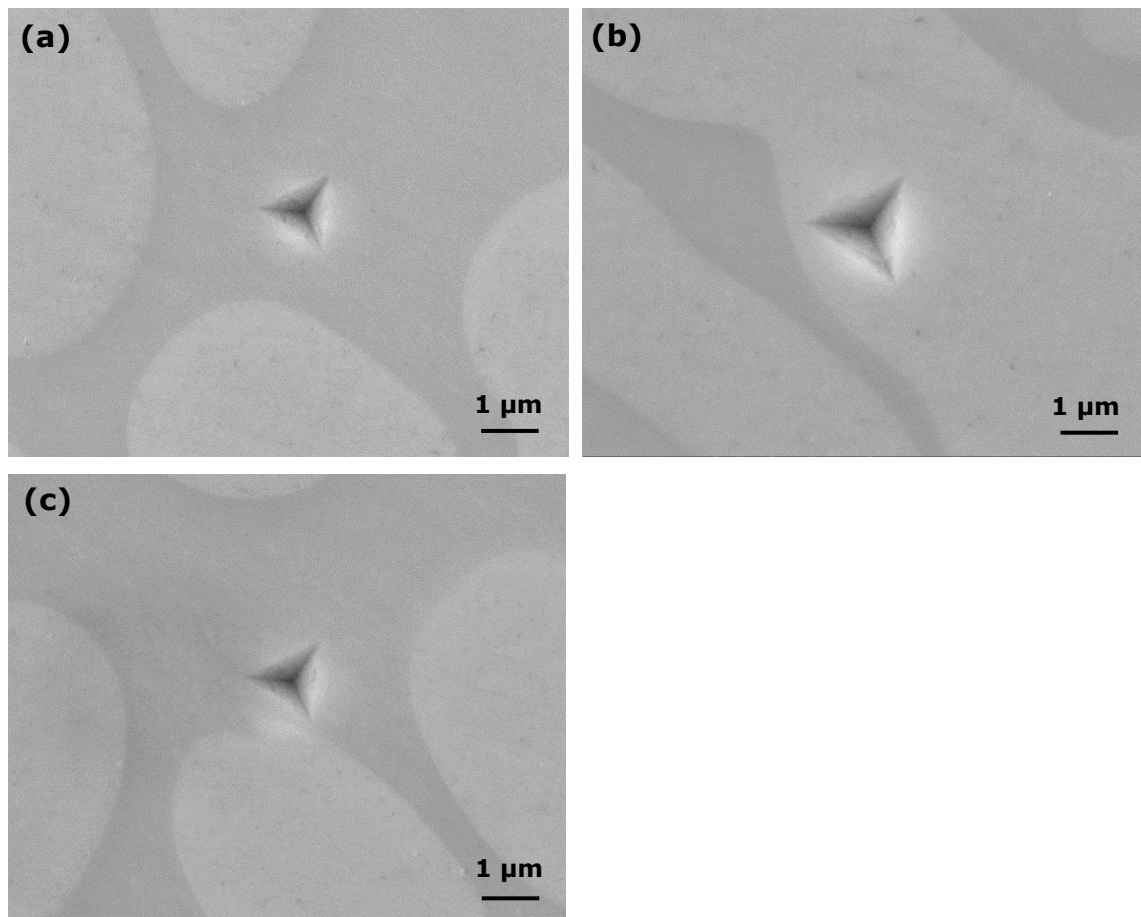


Figure 4.2 SEM images, showing the typical nano-indentations made on ZrTi composite (a) the amorphous matrix, (b) the crystalline dendrite, and (c) near the amorphous-crystalline interface of the ZrTi composite.

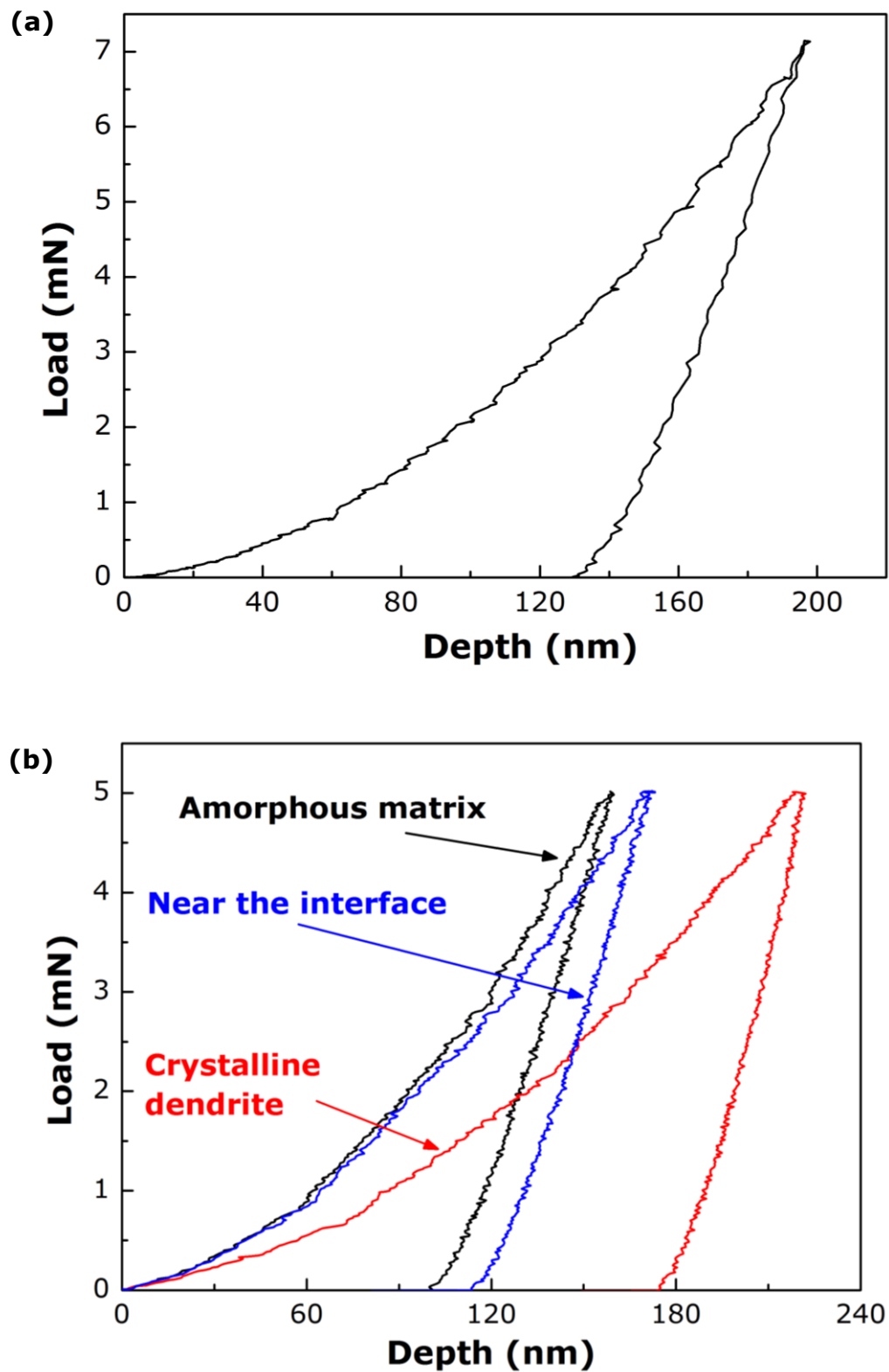


Figure 4.3 Typical nano-indentation load-depth curves measured for (a) Vit-1 and (b) the amorphous matrix, the crystalline dendrite, and near amorphous-crystalline interface region in the ZrTi composite sample.

The average hardness and Young's modulus of the ZrTi composite can be calculated using the rule of mixtures by taking the volume fraction of the amorphous matrix and crystalline dendrites into account. The volume fraction of the crystalline dendrites was calculated and averaged over 17 SEM images. Figure 4.4a shows one of the 17 backscattered SEM images. To enhance the contrast between the matrix and dendrites, the FFT bandpass built-in filter in ImageJ [221] was used to process all images (Figure 4.4b), and then all images were binarised (Figure 4.4c) to differentiate the matrix (white) and dendrites (black). Next, the dendrites were selected (Figure 4.4d) as particles, and the total area of the dendrites was calculated using the software. Finally the volume fraction of the dendrites was obtained by dividing the total area of the dendrites with the area of the image. The calculated dendrite and amorphous matrix volume fraction are 0.595 and 0.405, respectively.

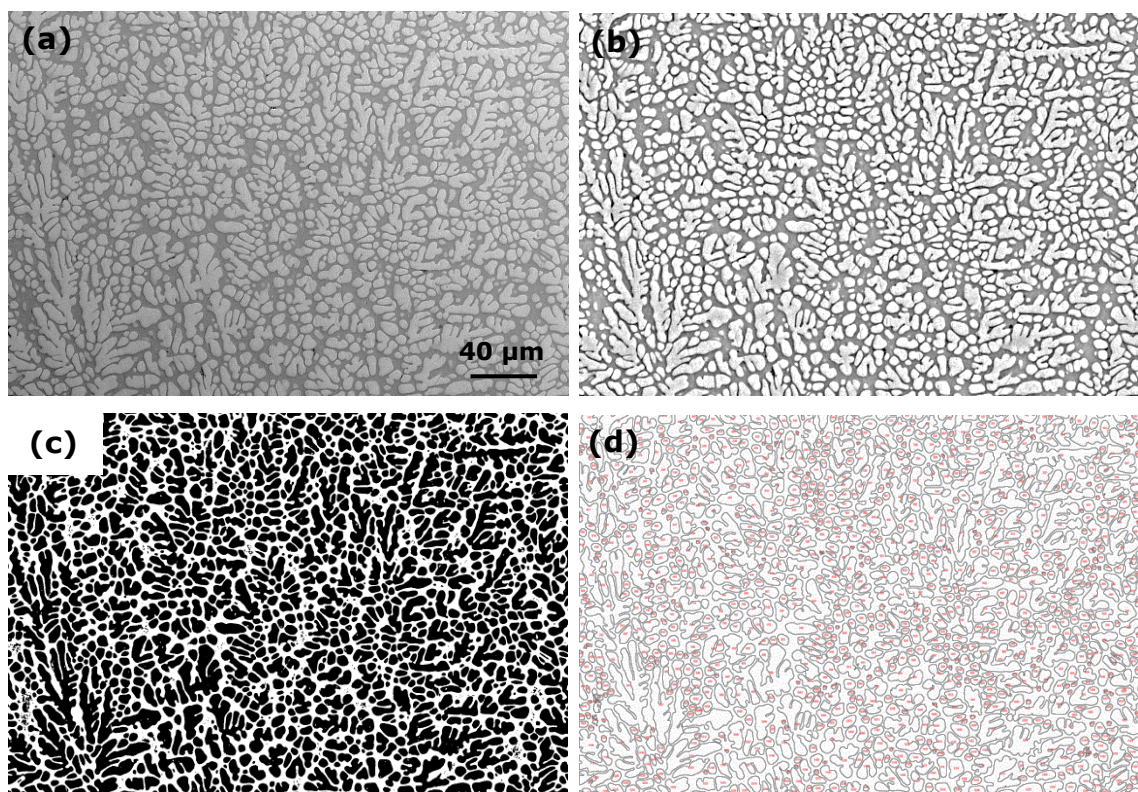


Figure 4.4 One example from the 17 SEM images that was used to analyse the volume fraction of the dendrites (a) as captured SEM image (b) FFT bandpass filter applied (c) binary image (d) identified dendrites.

4.2 In situ imaging study of tensile deformation of Vit-1

Figure 4.5a shows, before the tensile test, the notch and part of the gauge length section of the Vit-1 sample. Two micro-indentation marks with a distance of 2.11 mm apart were made on the gauge length, and they were used as the markers for measuring the extension between them at different load steps to complement the displacement data measured for the whole sample length from the extensometer of the microtester.

Figure 4.5b shows the load-displacement curve recorded by the control software of the microtester, together with the extension measured between the two micro-indentation markers (using the SEM images acquired at each load step). The test was carried out using load step control with a constant speed of 0.05 mm/min. At the predefined target load steps (where the micro-indentations extension was measured) show in Figure 4.5b, the test was paused and painstaking imaging observations were made to investigate and feature changes on the polished surface with a focus on identifying and then recording any initiation of shear band at a particular load step, or the propagation if shear band had already existed.

At each load step, the corresponding average tensile stress is calculated using Eq. (3), and the semi-circular notch is taken into account.

$$\sigma = \frac{F}{t(w - n_r)} \quad (3)$$

Where σ is the tensile stress, F is the applied force, and w is the width and t is the thickness at the centre of the gauge section, and n_r is the radius of the notch.

The tensile strain at each load step is calculated using Eq. (4).

$$\varepsilon_\sigma = \frac{l_\sigma - l_0}{l_0} \quad (4)$$

Where ε is the tensile strain, l_0 is the original distance between the indentation marks and l_σ is the measured distance at the stress level of σ .

Because the distance between the two indentation markers cannot be measured after the sample fractured, the tensile strain at the final fracture point is estimated using Eq. (5) using tensile strain and tensile stress rig extension of the last two data points before the sample fracture.

$$\varepsilon_{frac} = \varepsilon_1 + \left[\frac{\varepsilon_1 - \varepsilon_2}{R_1 - R_2} \times (R_{frac} - R_1) \right] \quad (5)$$

Where ε_{frac} and R_{frac} are the fracture strain and tensile rig extension, ε_2 and R_2 is the 2nd to the last step stain and tensile stress rig extension, ε_1 and R_1 is the last step stain and tensile stress rig extension.

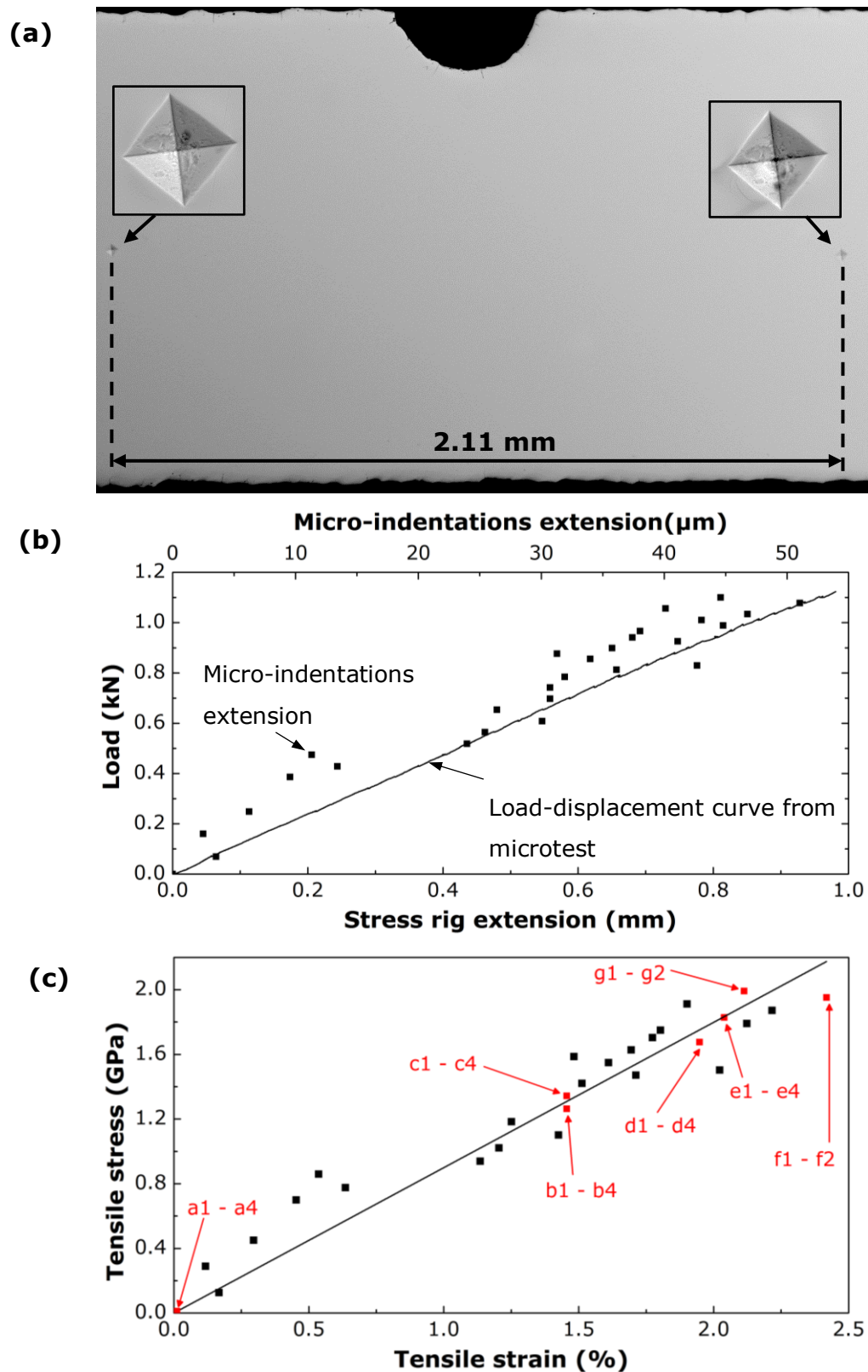
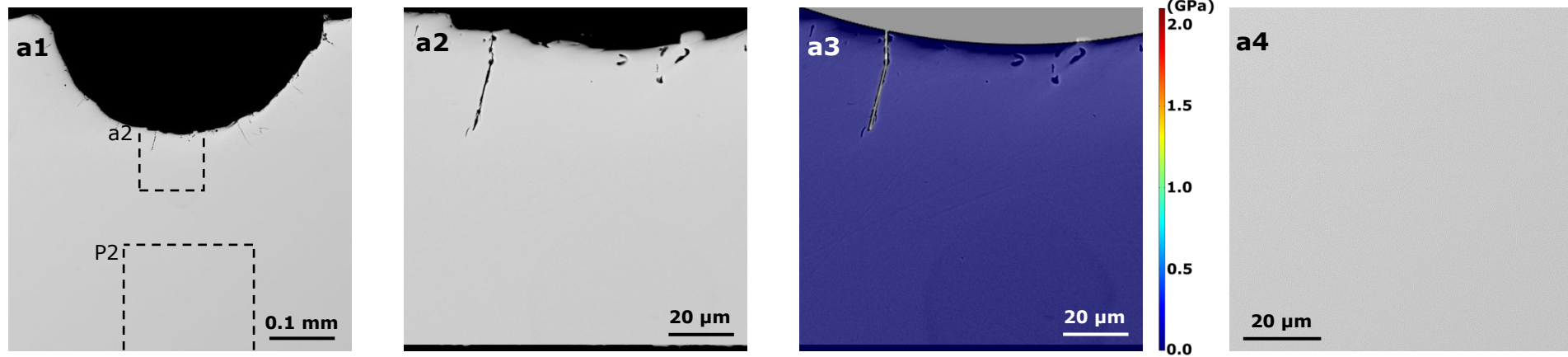


Figure 4.5 (a) A SEM image at the centre of the gauge section of the Vit-1 sample, showing the \varnothing 0.25 mm semi-circular notch and two indentation marks as the physical markers to measure materials extension under different load steps, (b) the load-displacement (bottom-X) curve recorded by the microtester and measured from the two indentation marks (top-X), and (c) the calculated tensile stress versus tensile strain using the measured extension from the two micro-indentation.

Figure 4.6 shows a series of SEM images taken at different critical load steps (the loads were converted into the corresponding average stresses and showed in Figure 4.5c using red squares) where initial crack in the sample surface and/or any shear band initiation and propagation were observed. The initial 20 N was considered as zero stress.

The Vit-1 sample fractured at 2032 MPa with strain of $\sim 2.2\%$. Each fractured half sample was imaged separately and then put together as showed in Figure 4.8a. The fracture stress and strain are very close to the reported tensile strength (1.9 GPa) and strain (2.0 %) of Vit-1 in open literature [156]. Figure 4.8b shows the sample fractured during the in situ SXR experiment with fracture strength of 1962 MPa. Both samples have very similar fracture characteristics.

Tensile stress: 0MPa, Tensile strain: 0%



Tensile stress: 1263MPa, Tensile strain: 1.46%

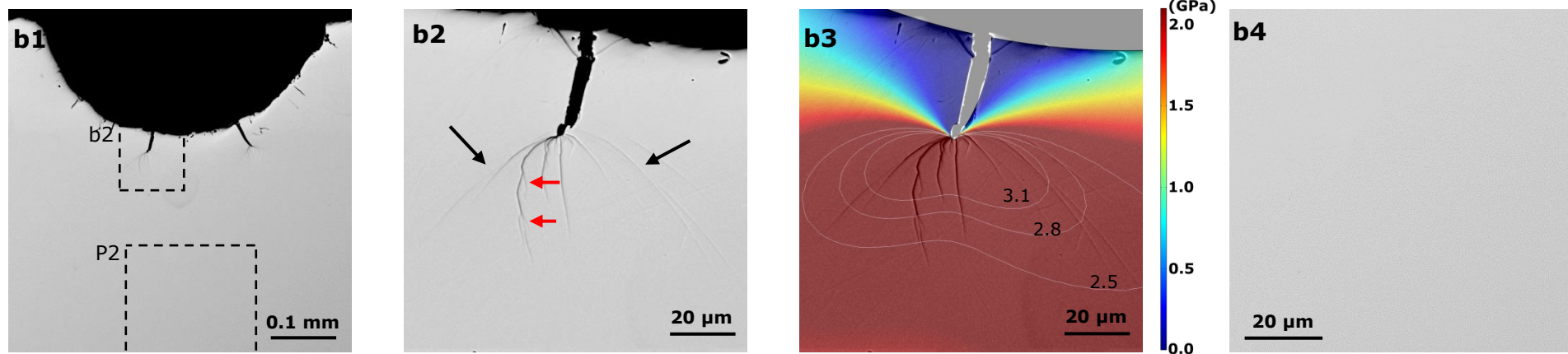
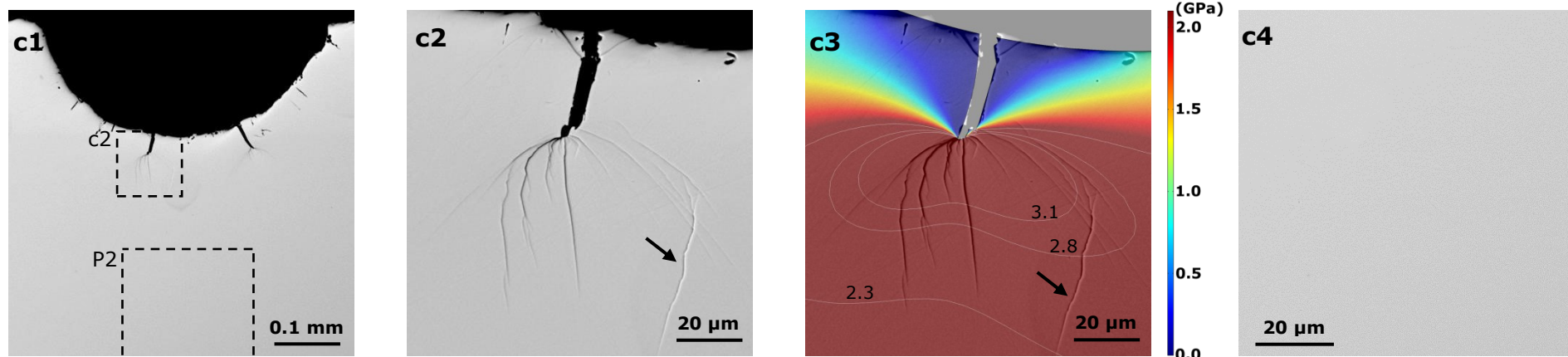


Figure 4.6 (a1) a SEM image of Vit-1 sample near the notch at 0 MPa, (a2) an enlarged image of the framed "a2" area in a1, (a3) the simulated axial stress for a2 area (superimposed with the a2 image), (a4) the image for the marked P2 area in a1. (b1 - b4) are for those at 1263 MPa.

Tensile stress: 1343MPa, Tensile strain: 1.46%



Tensile stress: 1676MPa, Tensile strain: 1.95%

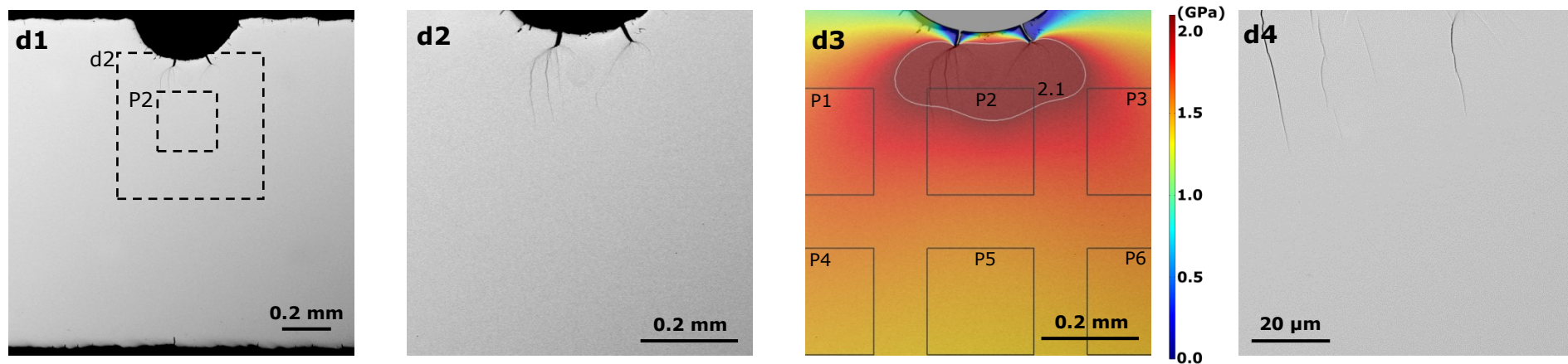
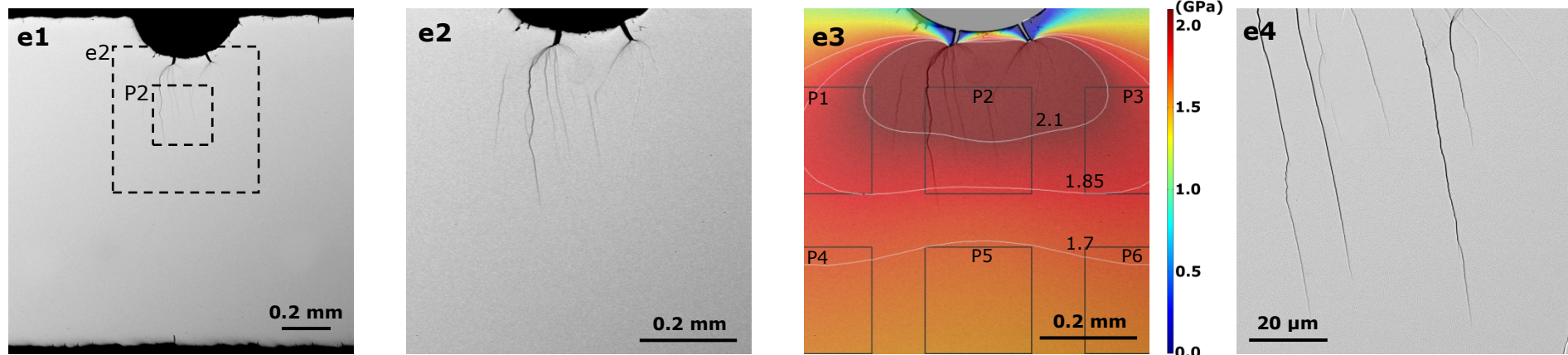


Figure 4.6 continue. (c1 - c4) are for those at 1343 MPa, (d1 - d4) are for those at 1676 MPa.

Tensile stress: 1829MPa, Tensile strain: 2.04%



Tensile stress: 1952MPa, Tensile strain: 2.42%

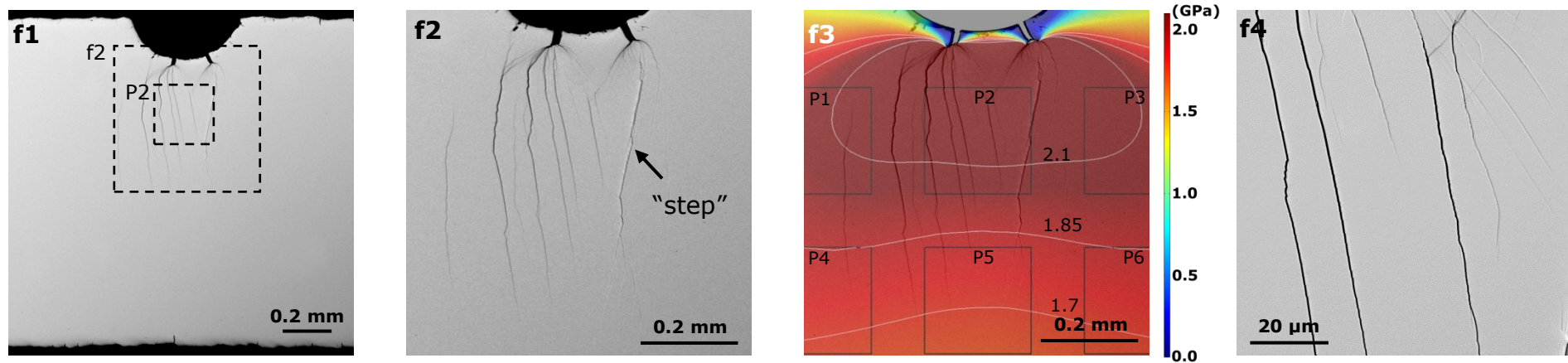


Figure 4.6 continue. (e1 - e4) are for those at 1829 MPa, and (f1 - f4) are those for 1952 MPa.

Tensile stress: 1991MPa, Tensile strain: 2.11%

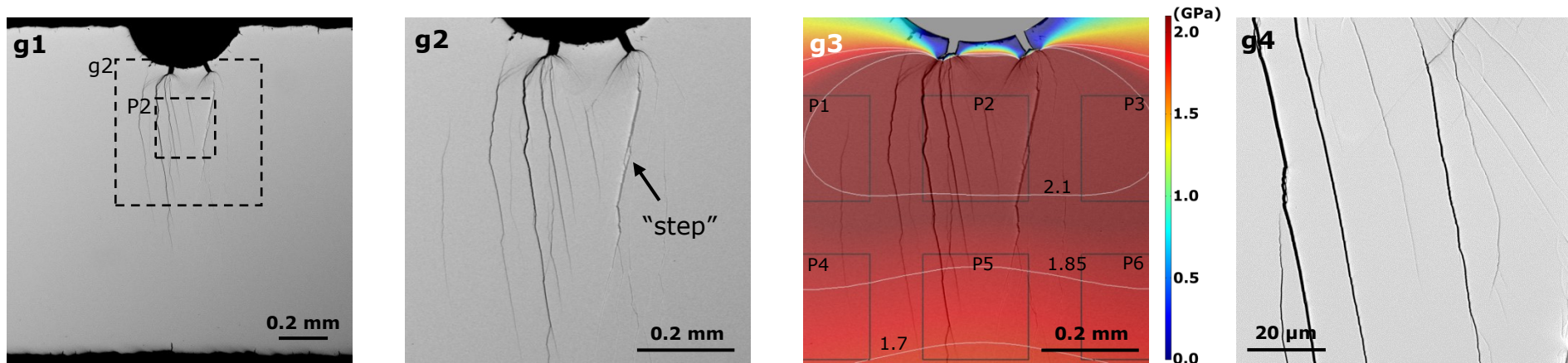


Figure 4.6 continue. (g1 - g4) are for those at 1991 MPa.

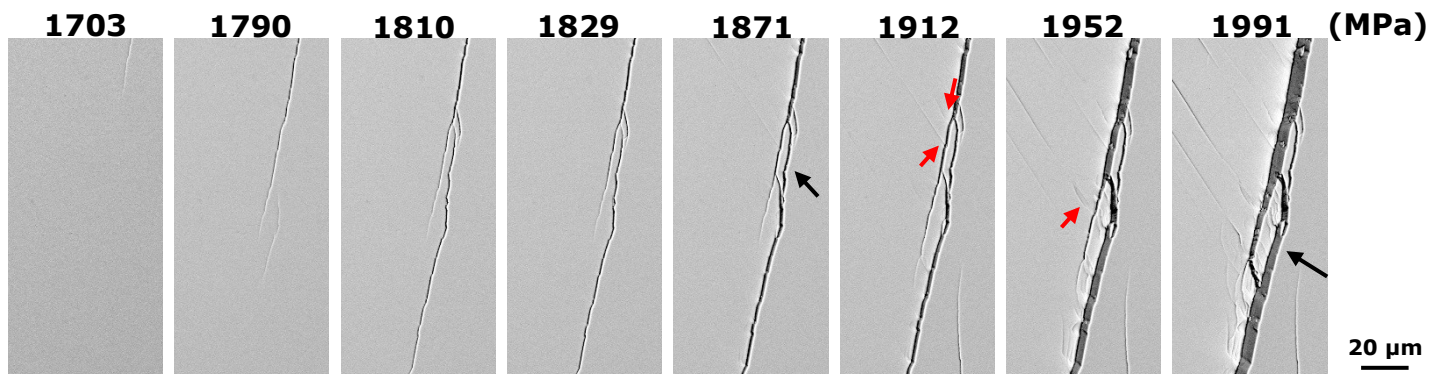


Figure 4.7 The enlarged SEM images at the location marked by "step" in f2 and g2 of Figure 4.6 for different load steps (some of the images showed here are not showed in Figure 4.6), showing the formation of "step" near P2 area at different load steps.

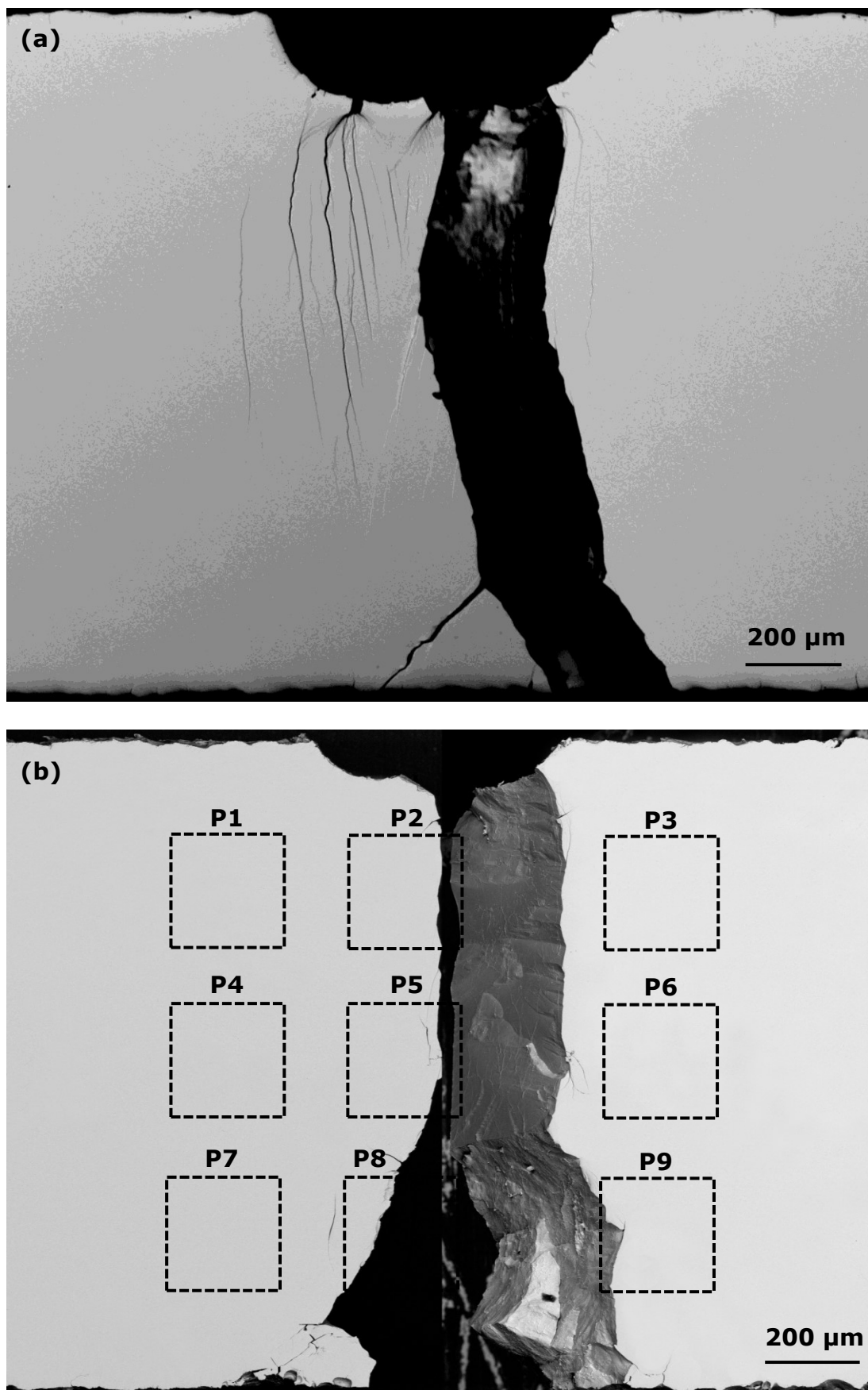


Figure 4.8 SEM images of the Vit-1 tensile tested samples fractured during (a) in situ SEM test (b) in situ SXR D test. The dotted line squares labelled by P1-P9 are the locations where the SXR D patterns were acquired during the in situ tensile diffraction test at I12 of Diamond Light Source.

4.3 In situ diffraction study of tensile deformation of Vit-1

In order to investigate the underlying relationship between local atomic rearrangements and shear band formation, another Vit-1 sample was in situ tensile tested at I12 of DLS where synchrotron X-ray diffraction (SXR) patterns were acquired at the positions marked P1-P9 as showed in Figure 4.8b. Similar tensile stress condition as that used in the in situ SEM test was used in the in situ SXR test. Figure 4.9 shows the tensile stress and load versus stress rig extension recorded from the microtester for the in situ tensile tested Vit-1 sample at I12 of DLS together with the SXR patterns acquired at the predefined load steps. Unlike the in situ SEM, we are not able to obtain the tensile strain of the material by measuring the changes in distance of the indentation marks. As shows in the curve, there is an obvious relaxation of load when paused for taking diffraction patterns (18 minutes holding time is required to collect the SXR patterns for the 9 locations). Whereas this relaxation is not that obvious in the in situ SEM test due to shorter holding time ($\sim 2-5$ mins) used to capture the SEM images as shows in Figure 4.5b.

Figure 4.10c and Figure 4.10d show that when a uniaxial tensile stress was applied on the sample, the concentric diffraction rings obtained at 0 stress become elliptical, reflecting the changes of strains in the axial and transverse directions. The diffraction information in the $\pm 10^\circ$ sector in the axial direction and that in the transverse direction as show in Figure 4.10a and Figure 4.10b were then integrated into 1D spectra as show in Figure 4.10e and Figure 4.10f. The 1D spectra clearly show that when tensile load was applied, the peak according the to axial and transverse direction will be shifted. Before the intergration, beamstop and dead pixels were masked out using the Fit2D software, and the background information was substrate using the background diffraction patterns [11]. Figure 4.11 shows all the 1D spectra obtained for all load steps. The positions of the first sharp diffraction peak (FSDP) in 1D spectra at different stress levels are fitted using Gaussian fitting function and showed in Figure 4.12.

Then, the shift of the position of FSDP at different stress level was used to calculated the strain at that particular stress using Eq. (6):

$$\varepsilon_Q(\varepsilon_a, \sigma) = \frac{Q(\varepsilon_a, 0) - Q(\varepsilon_a, \sigma)}{Q(\varepsilon_a, 0)} \quad (6)$$

Where $\varepsilon_Q(\varepsilon_a, \sigma)$ is the tensile axial strain ($\varepsilon_i(\varepsilon_t, \sigma)$ for transverse strain), $Q(\varepsilon_a, 0)$ and $Q(\varepsilon_a, \sigma)$ represent the position of the FSDP in the 1-D spectra at zero stress and σ respectively.

Using this method, the axial and transverse strains for all nine locations where diffraction patterns were acquired at each load step were calculated and showed in Figure 4.13 for the axial direction and Figure 4.14 for transverse direction.

To understand the strain evolution at atomic level, the information from location P2 (directly below the artificial notch) was selected to calculate the total structure factor $S(Q)$ from the 1D spectra using the Egami-Bilinge procedures [55]. Figure 4.15 shows a stack of $S(Q)$ curves at different stress levels for location P2 in the axial direction. The $S(Q)$ curves were then Fourier transformed into reduce pair distribution functions (PDFs), $G(r)$ as shows in Figure 4.16. Both $S(Q)$ and $G(r)$ calculations were carried out using the PDFgetX2 software [222].

The PDFs in Figure 4.16 clearly show the 3 different atomic shells (the first 3 peaks in the PDFs) in the SRO and MRO region. The positions of the maxima of the 3 peaks are identified, and the shifts of the positions are converted into the atomic strain using Eq. (7):

$$\varepsilon_i(\varepsilon_a, \sigma) = \frac{G_i(\varepsilon_a, \sigma) - G_i(\varepsilon_a, 0)}{G_i(\varepsilon_a, 0)} \quad (7)$$

Where $\varepsilon_i(\varepsilon_a, \sigma)$ is the tensile axial strain [$\varepsilon_i(\varepsilon_t, \sigma)$ for tangential strain], i is the number of the atomic shell, $G_i(\varepsilon_a, 0)$ and $G_i(\varepsilon_a, \sigma)$ represent the position of the atomic shell at zero stress and σ respectively.

Figure 4.17a and Figure 4.17b show the atomic shells strains against the average tensile stresses in the axial and transverse directions, respectively. The 3 atomic shells strains fluctuate as the tensile stress increases. The

data were fitted using linear function for each atomic shell strain, and the standard errors (SE) were also labelled in the figures.

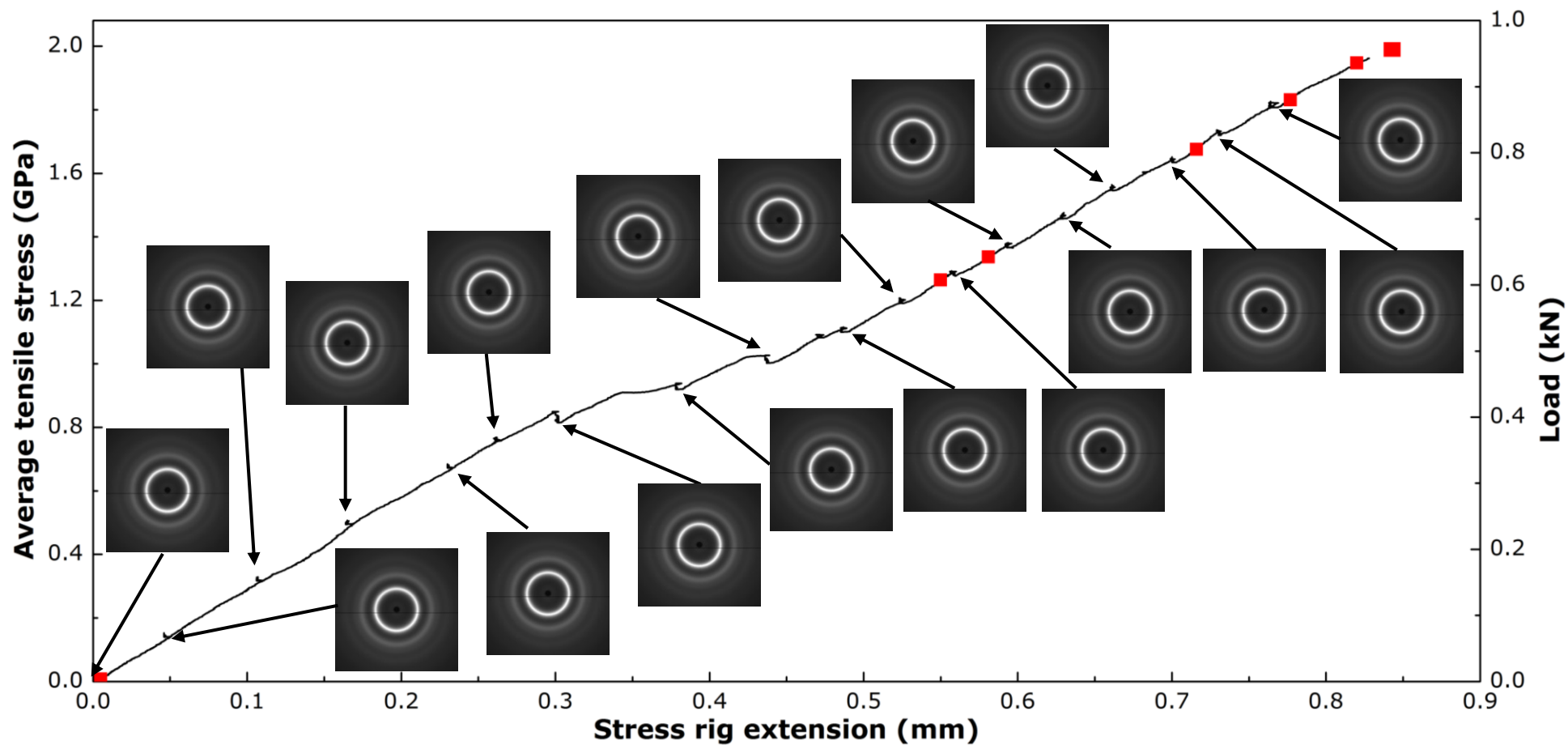


Figure 4.9 The average tensile stress and load versus stress rig extension recorded by the microtester for the Vit-1 sample in situ tensile tested at I12 of DLS. The arrows pointed where the SXR patterns were collected. The red squares show the stress where the SEM images showed in Figure 4.6c were taken.

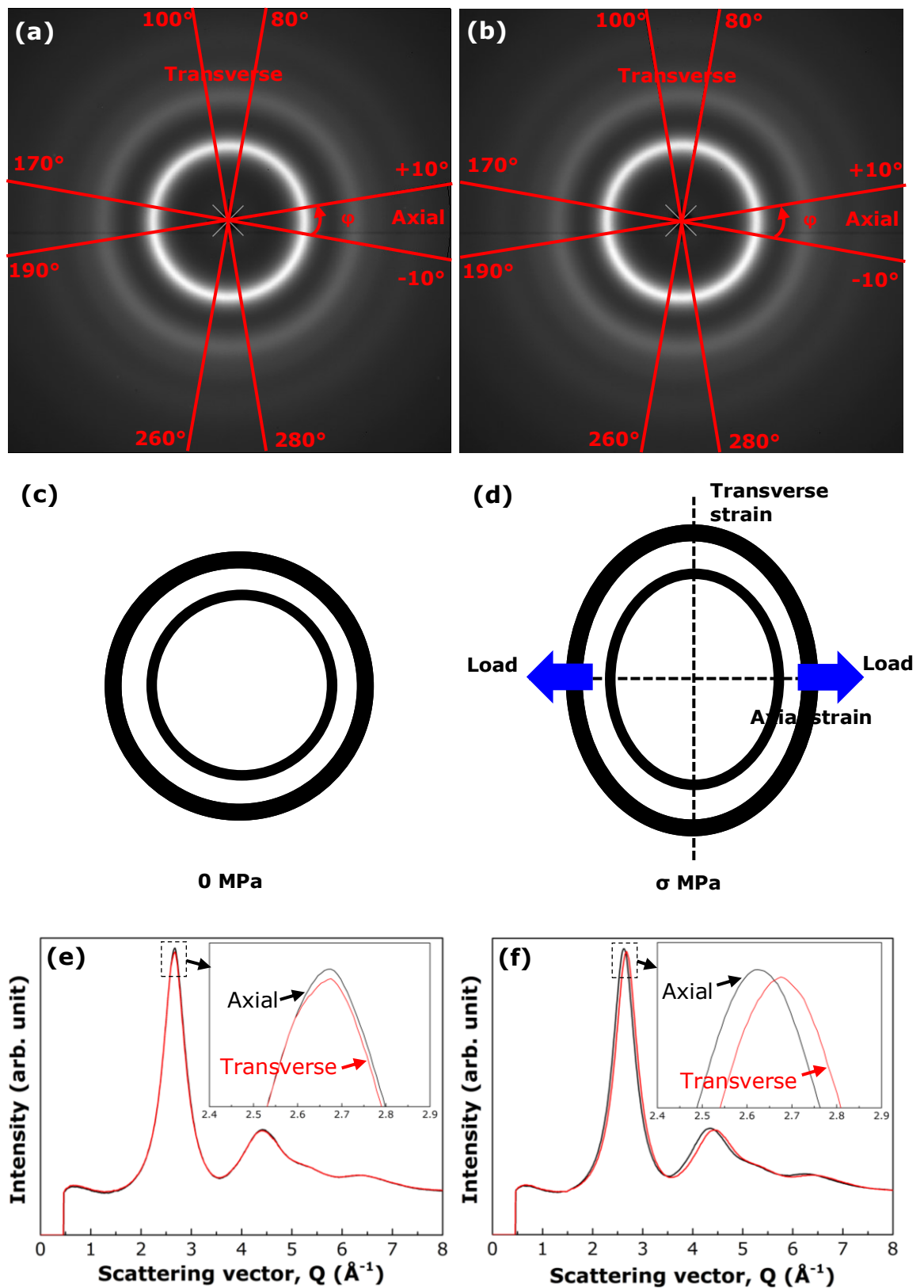


Figure 4.10 Typical SXR D patterns of Vit-1 sample acquired at (a) 0 MPa and (b) 1821 MPa. (c) A schematic diagram, showing the concentric ring, while (d) showing the elliptical ring (magnified) caused by the tensile stress. (e) 1D spectra integrated from the 20° sectors in the axial and transverse directions from a, and (f) are those from b.

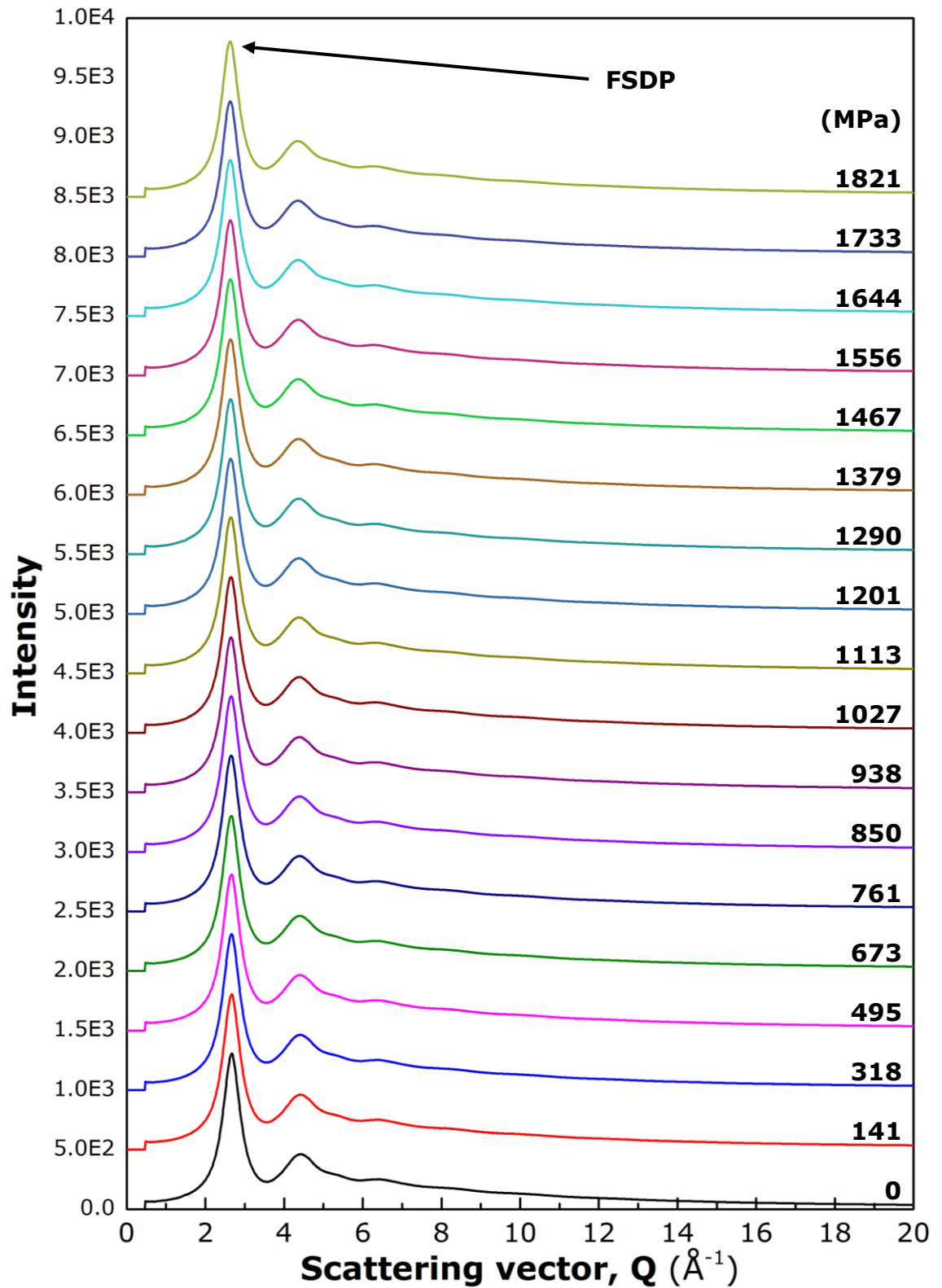


Figure 4.11 The stack of 1-D spectra for the location P2 of Vit-1 sample in the axial direction at different stress levels.

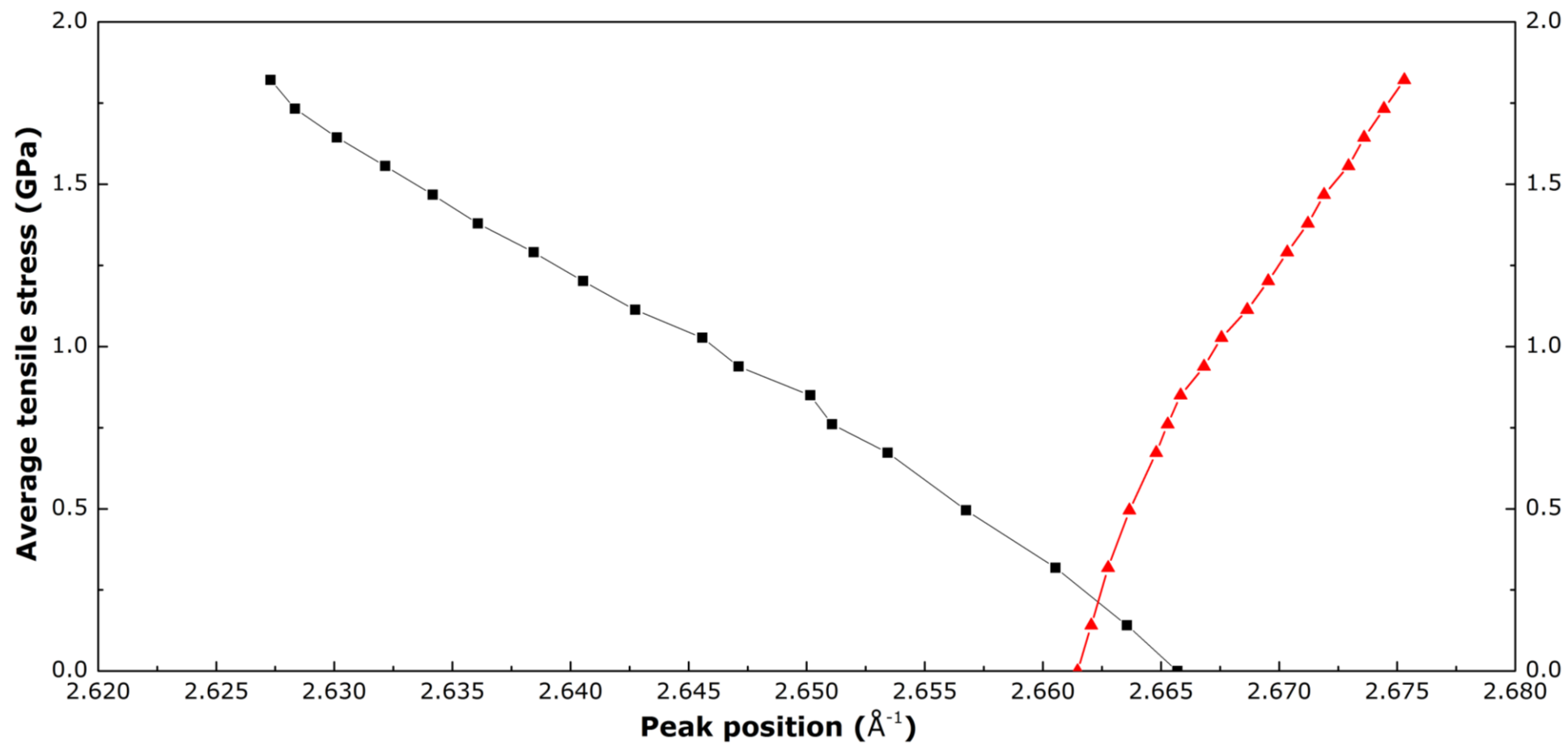


Figure 4.12 The shift of the positions of the FSDP of the 1D spectra acquired at P2 position at different stress level. The black line is for axial direction, while red line is for the transverse direction.

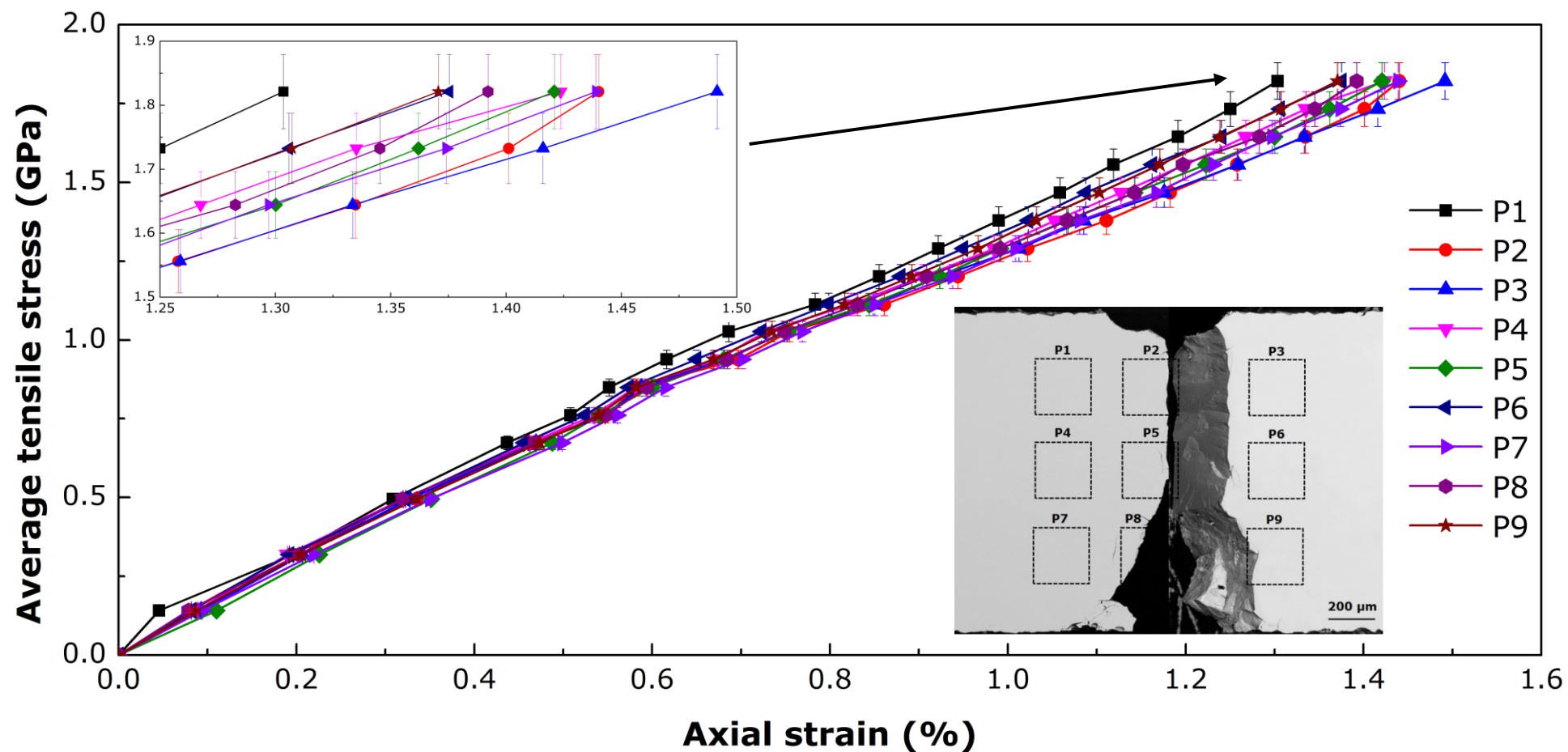


Figure 4.13 The axial strains calculated from the shift of the FSDP of the 1D spectra for all 9 locations shows in the insert SEM image at different stress levels.

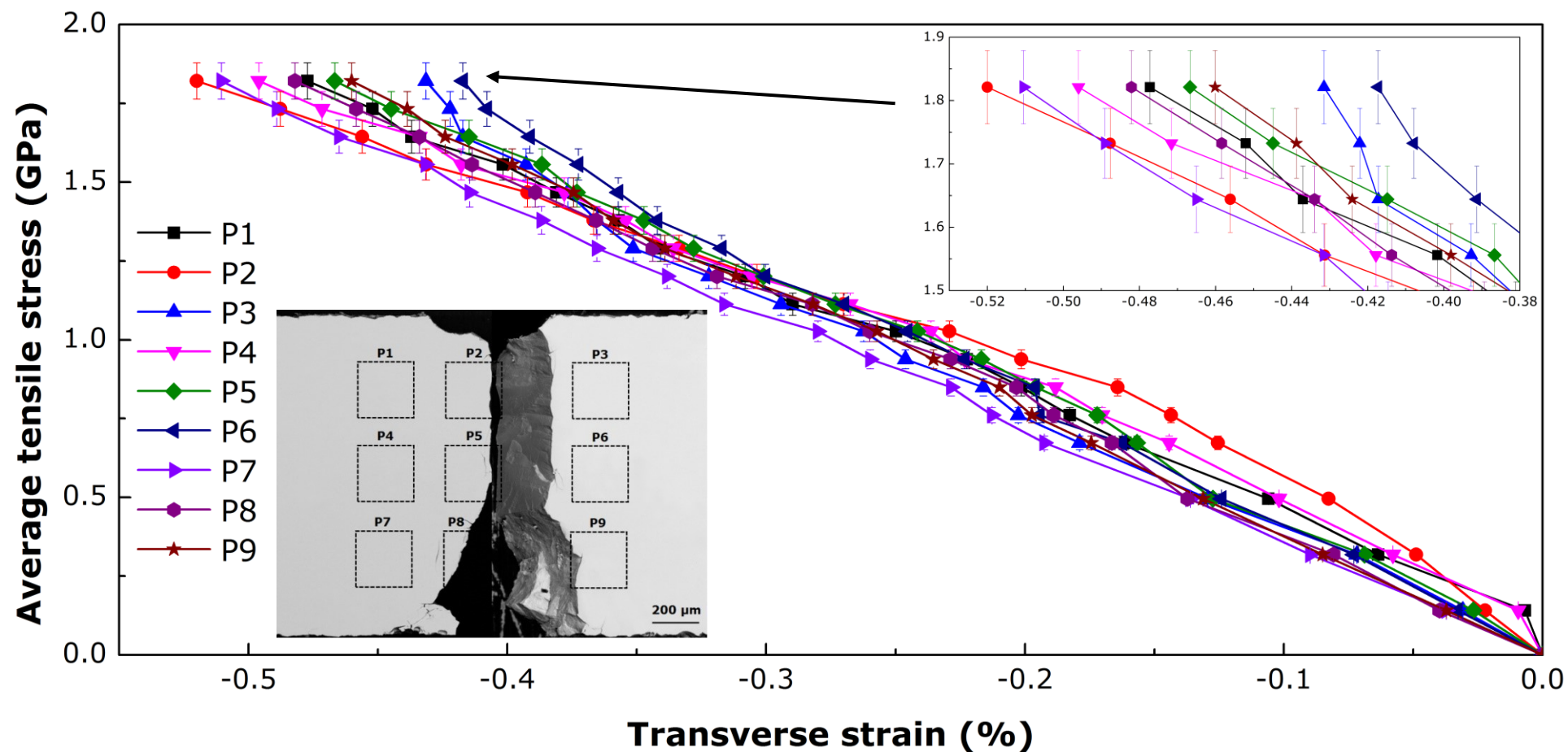


Figure 4.14 The transverse strain calculated from the shift of FSDP of the 1D spectra for all 9 locations shows in the insert SEM image.

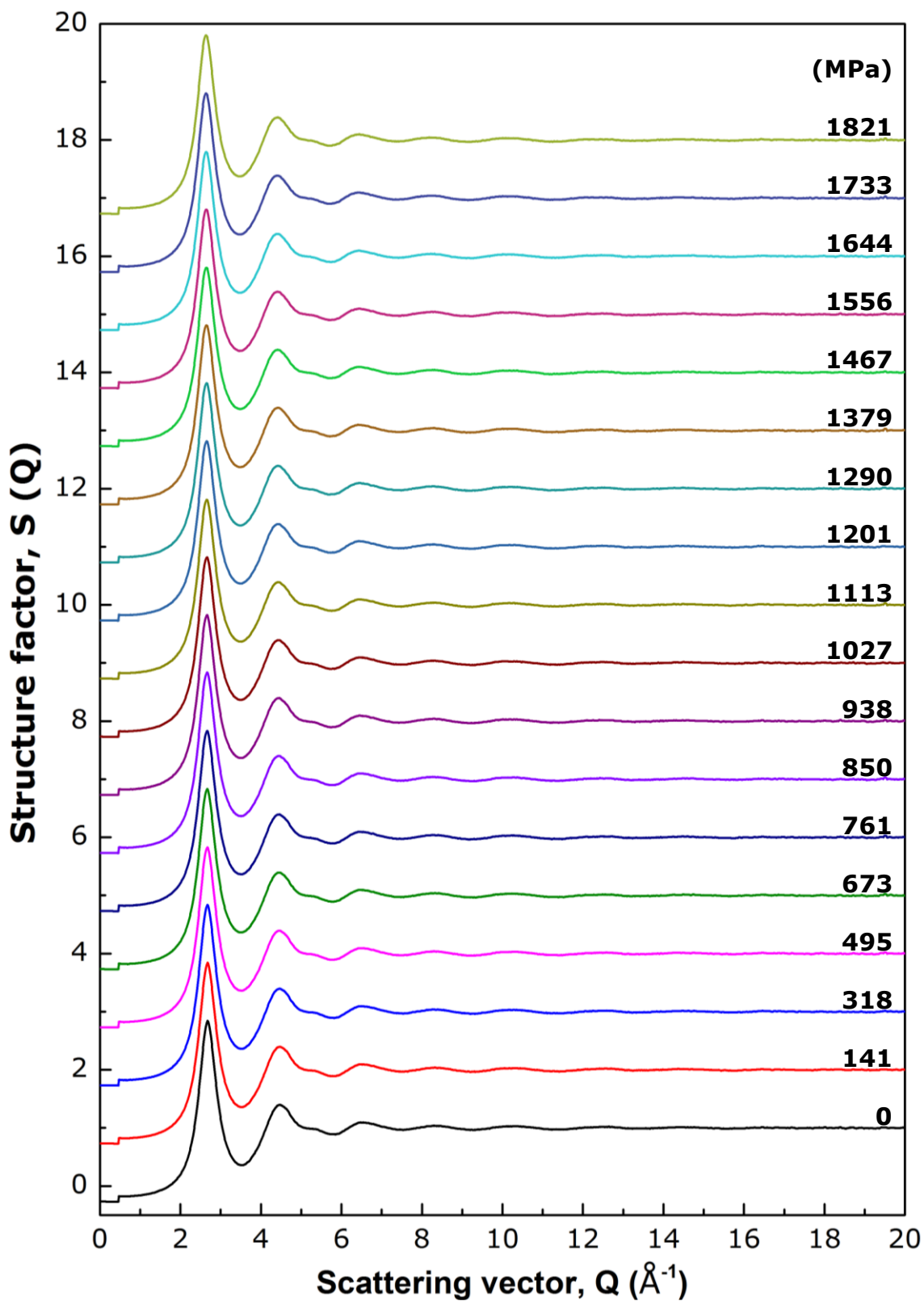


Figure 4.15 The structure factor, $S(Q)$, for location P2 of Vit-1 sample in the axial direction at different tensile stress level.

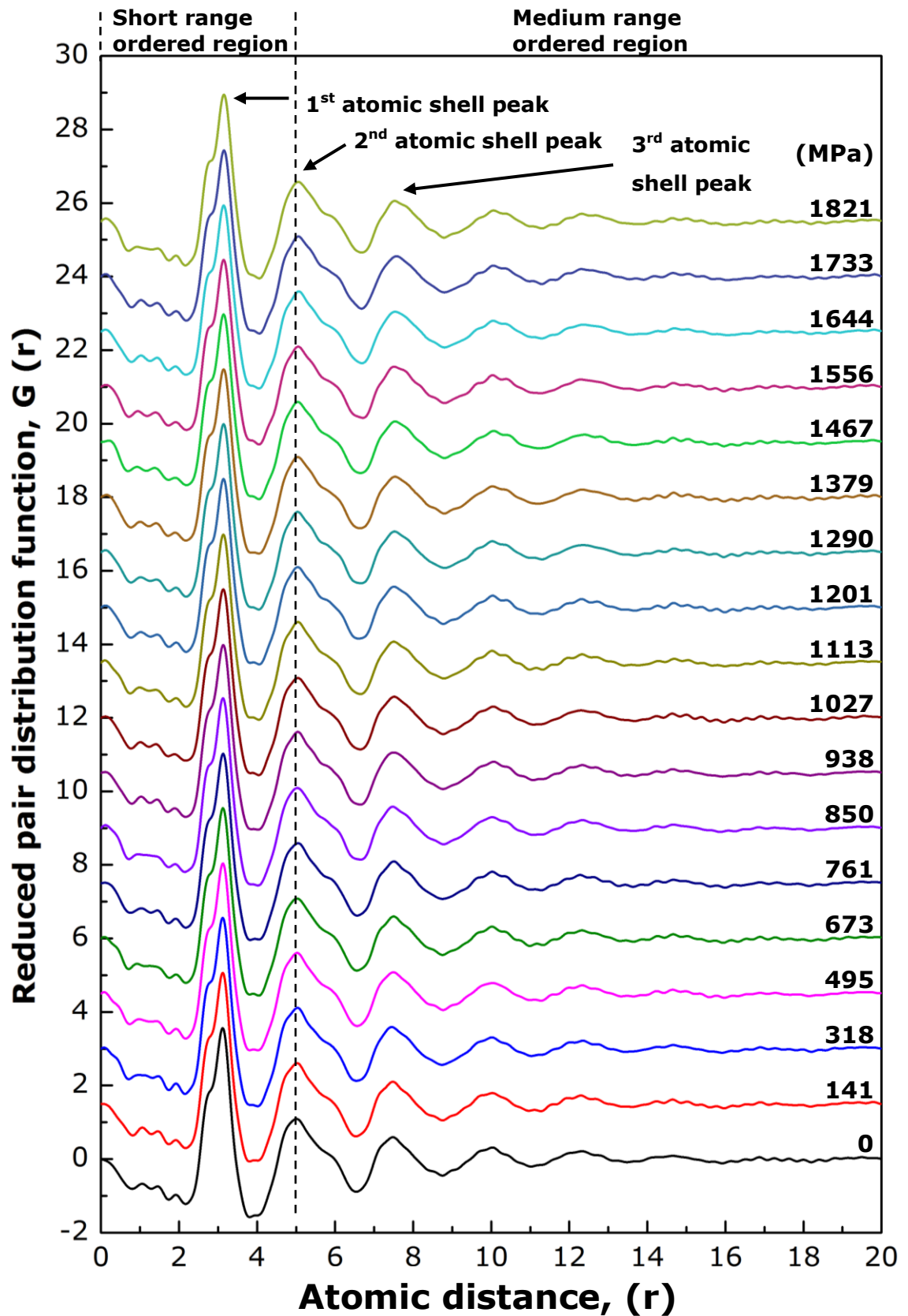


Figure 4.16 The reduced pair distribution function, $G(r)$, for the location P2 of Vit-1 sample in the axial direction at different tensile stress levels.

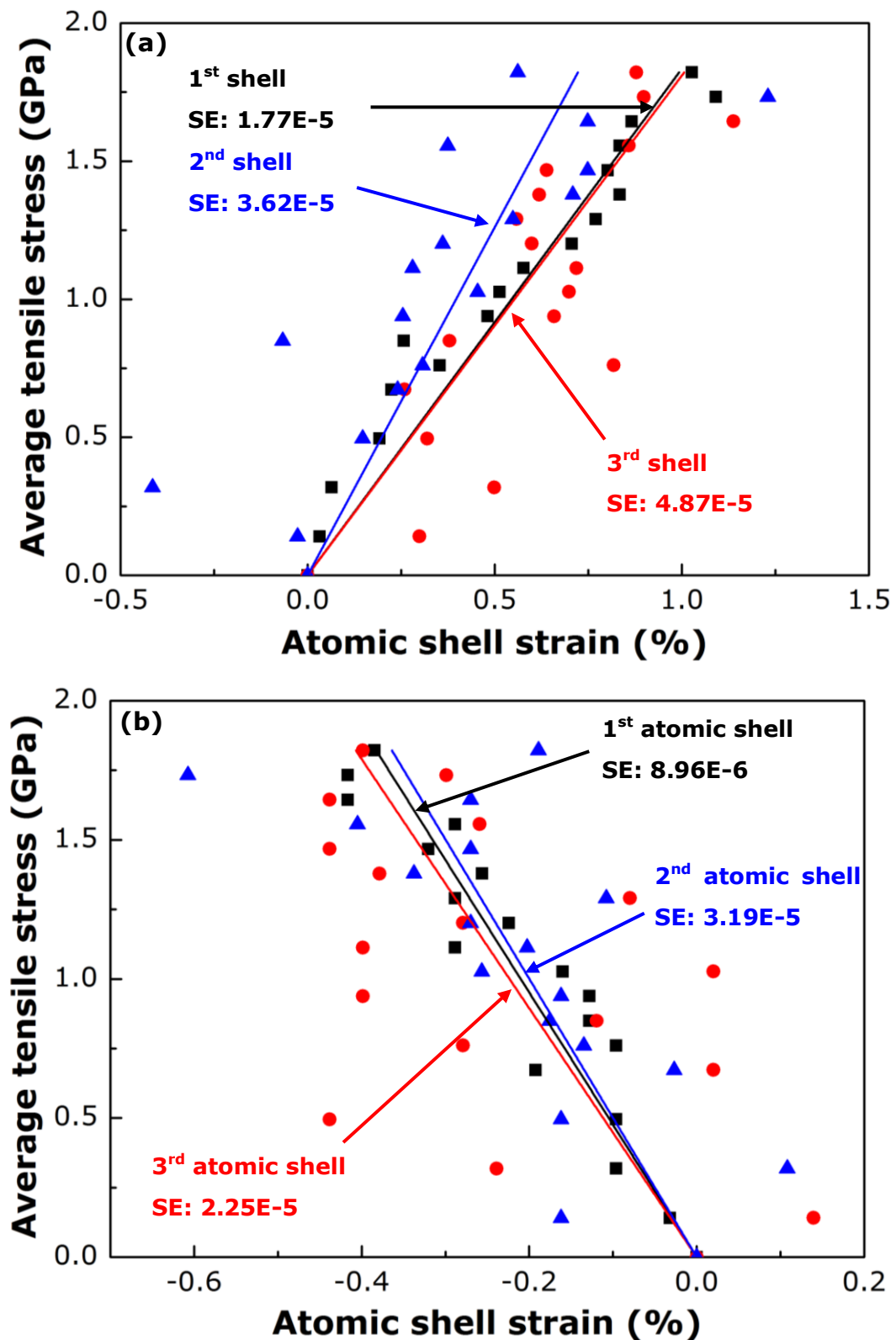


Figure 4.17 The atomic shells strain against the increase in tensile stress for location P2 in the (a) axial and (b) transverse directions. The results are fitted using linear curves and the standard errors (SE) are labelled as well.

4.4 Finite element modelling of tensile deformation of Vit-1

To further investigate the local stress field around the stress concentrator (the $\varnothing 0.25$ mm semi-circular notch) especially, when the shear band nucleation and propagation, 2D finite element models (FEM) were created using COMSOL Multiphysics software (V 4.3). The dog bone sample geometry model was created as shows in Figure 4.18 and a linear elastic model was used for the simulation. The tensile load is applied onto the 4 edges of the dog-bone shoulder with the width of 2.25 mm according to the newly designed tensile sample clamps as shows in Figure 3.8. Figure 4.18 shows that the model is meshed using the built-in "free triangular" mesh function and Figure 4.18a shows the enlarged view at the centre of the gauge section and the mesh around the initial cracks. The model includes two initial cracks formed on the sample during the EDM cutting, and the notch and crack opening resulted from the increase in tensile stress at each load step was updated in the model by tracking the changes observed from the SEM images. Figure 4.18b shows the mesh around the two cracks at 1991 MPa. The model also includes the 9 locations where the SXR patterns were acquired.

Table 4.2 summarises the sample geometries and material properties used in the model. The sample width and notch sizes were measured using the SEM and the thickness was measured using a vernier calliper. The Young's modulus and yield strength used in the model are obtained from the nano-indentation test and in situ SEM tensile test. The Poisson's ratio and density of the material are based on the published data for Vit-1 [7, 156].

Table 4.2 Material properties of Vit-1 and ZrTi composite obtained from the nano-indentation, in situ tensile test and open literatures [7, 156].

Parameter	Vit-1	ZrTi BMGMC
Young's modulus (GPa)	124.80	109 (composite)
		103.03 (dendrites)
		117.77 (matrix)
Yield strength (MPa)	2032	1786.41
Thickness (mm)	0.46	0.39
Width (mm)	1.38	1.43
Actual notch radius (mm)	0.18	0.15
Density (g/cm ³)	6.1	5.8

Poisson's ratio	0.335	0.376
-----------------	-------	-------

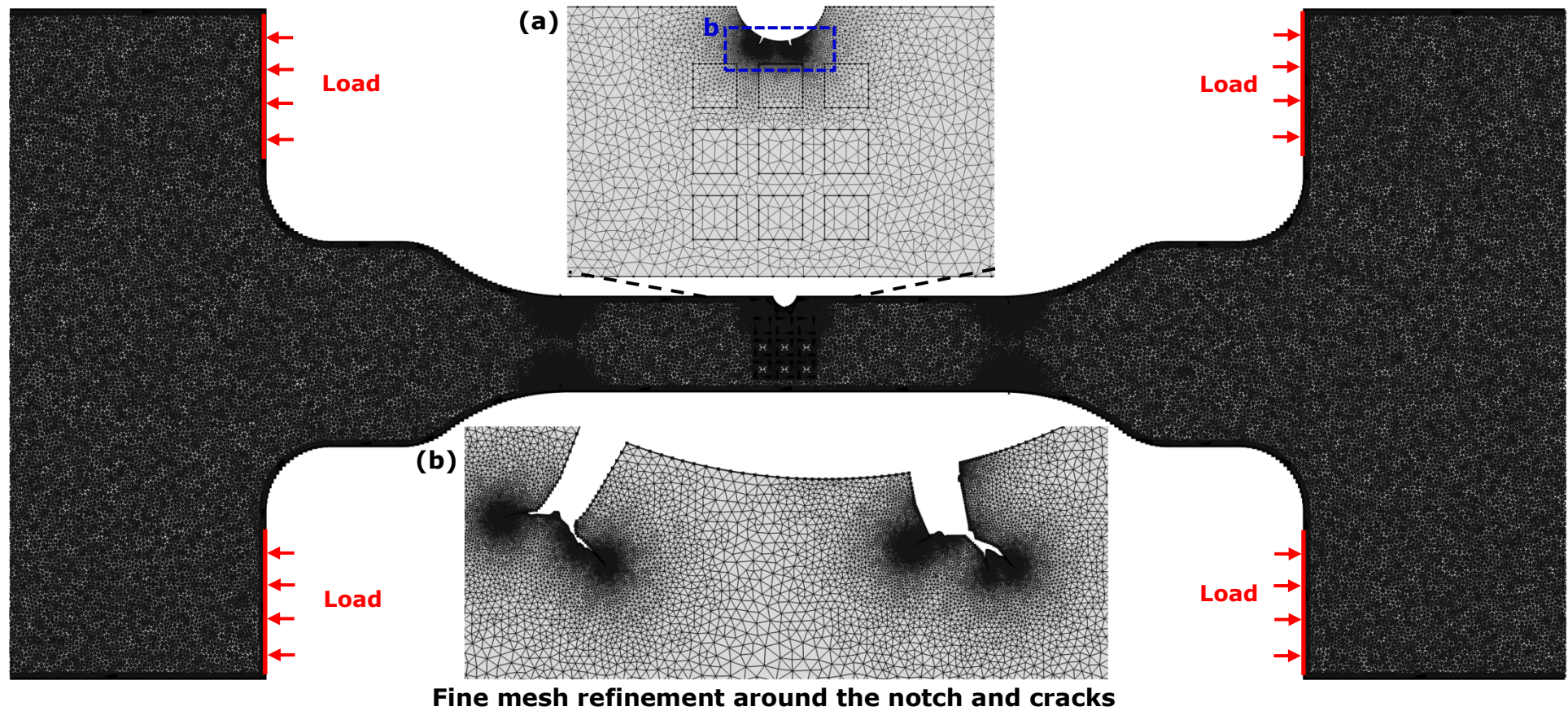


Figure 4.18 The dog-bone sample meshed using “free triangular” mesh at 1991 MPa. (a) An enlarged image at the centre of the gauge section, showing the mesh around the notch. (b) An enlarged image from the framed area in a, showing the mesh around the two cracks.

Figure 4.19a and Figure 4.19b the axial and transverse stress field simulated for the fracture stress at 2032 MPa. The enlarged images at the centre of the gauge section are shown in Figure 4.20a and Figure 4.20b, respectively. In order to visualise the stress fields around notch area with the shear bands, the simulated axial stress fields were superimposed into the SEM images. Figure 4.6 shows the changes in the stress field versus the surface changes. Figure 4.21 and Figure 4.22 show the average axial and transverse strains respectively, extracted from the FEM simulation (solid line) at the 9 position versus the applied tensile stress and the FEM results are plotted together with the in situ SXR results (markers).

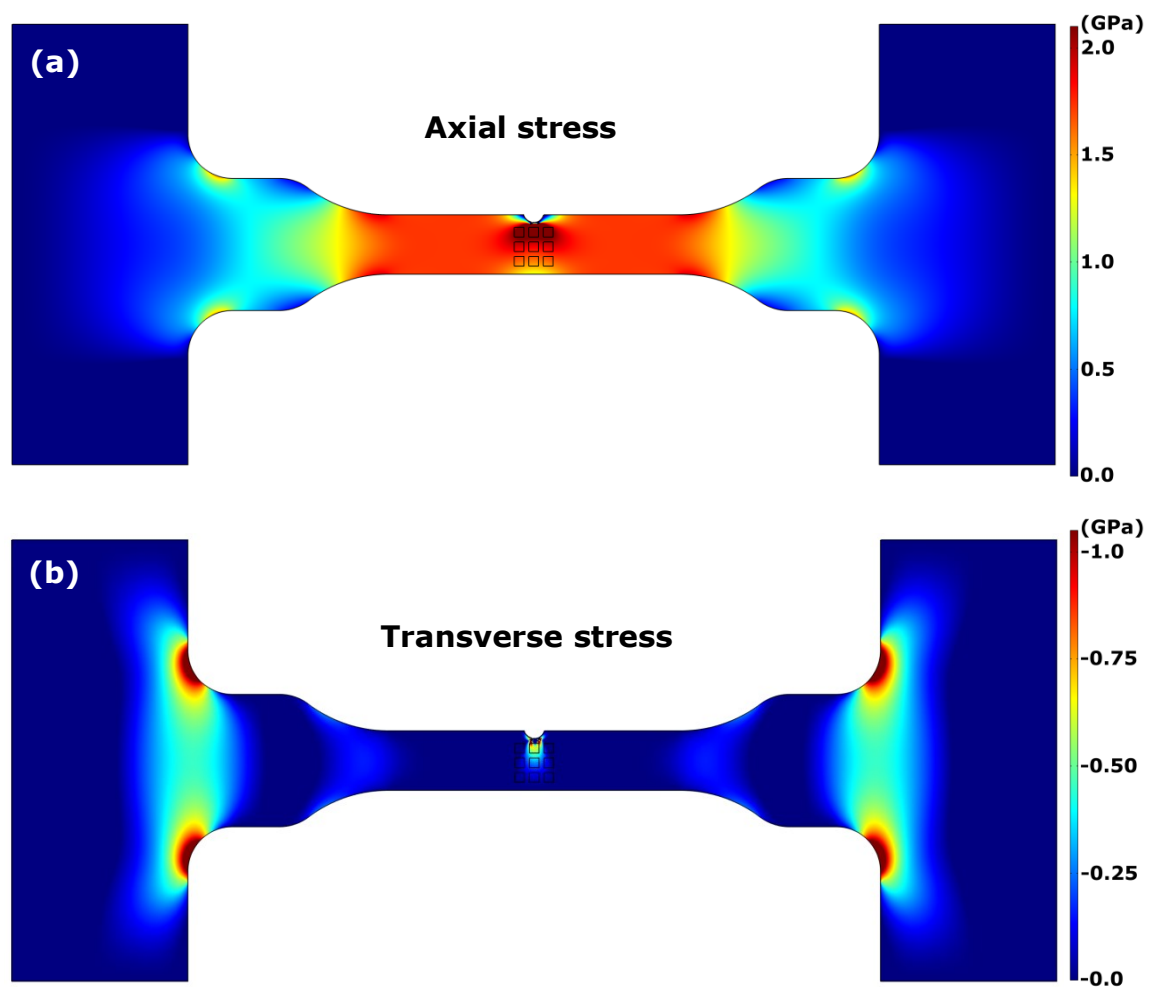


Figure 4.19 The simulated stress fields at the fracture stress of 2032 MPa in (a) axial and (b) transverse direction.

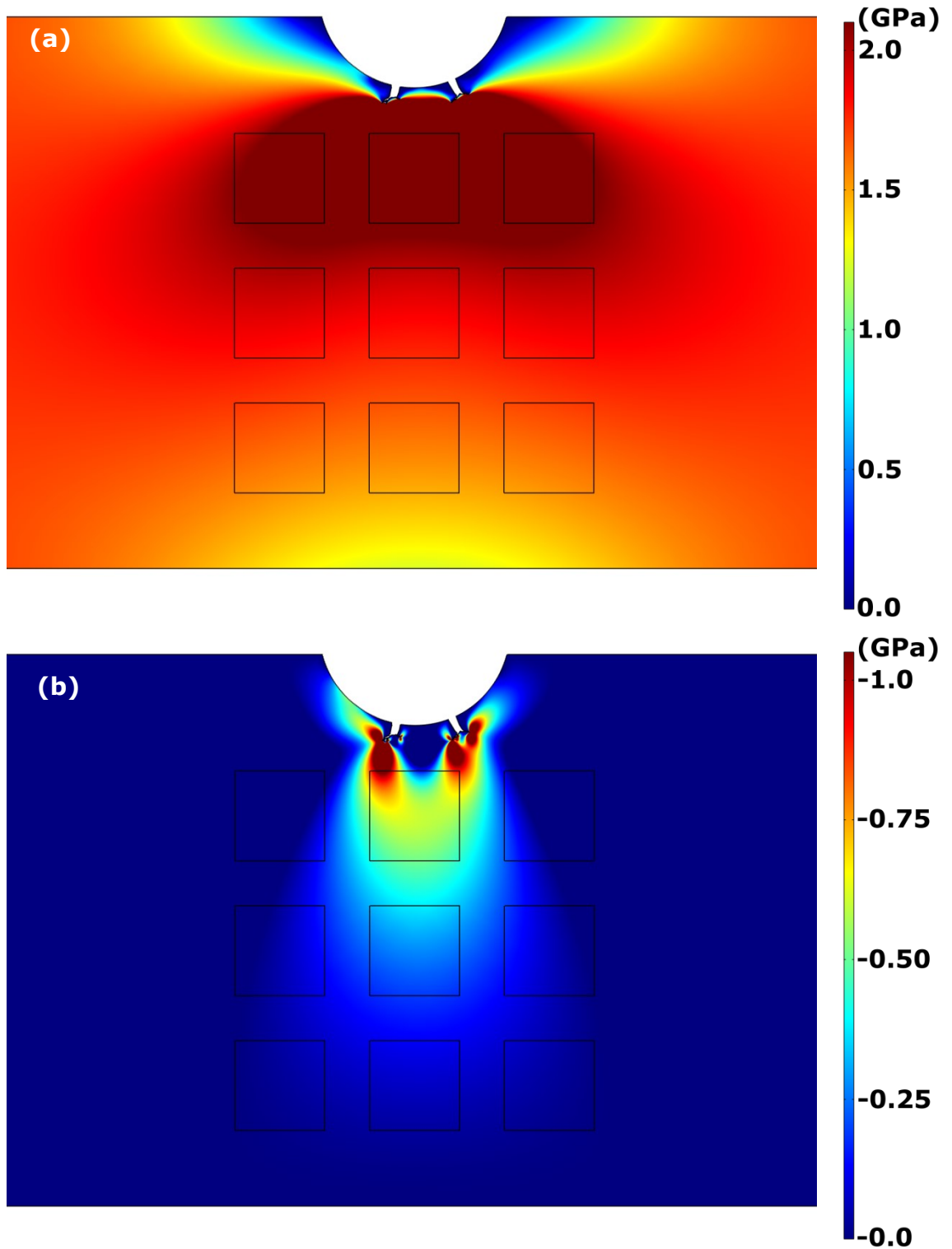


Figure 4.20 The enlarged images at the centre of the gauge section in Figure 4.19, showing the (a) axial and (b) transverse stress around the notch and the 9 locations.

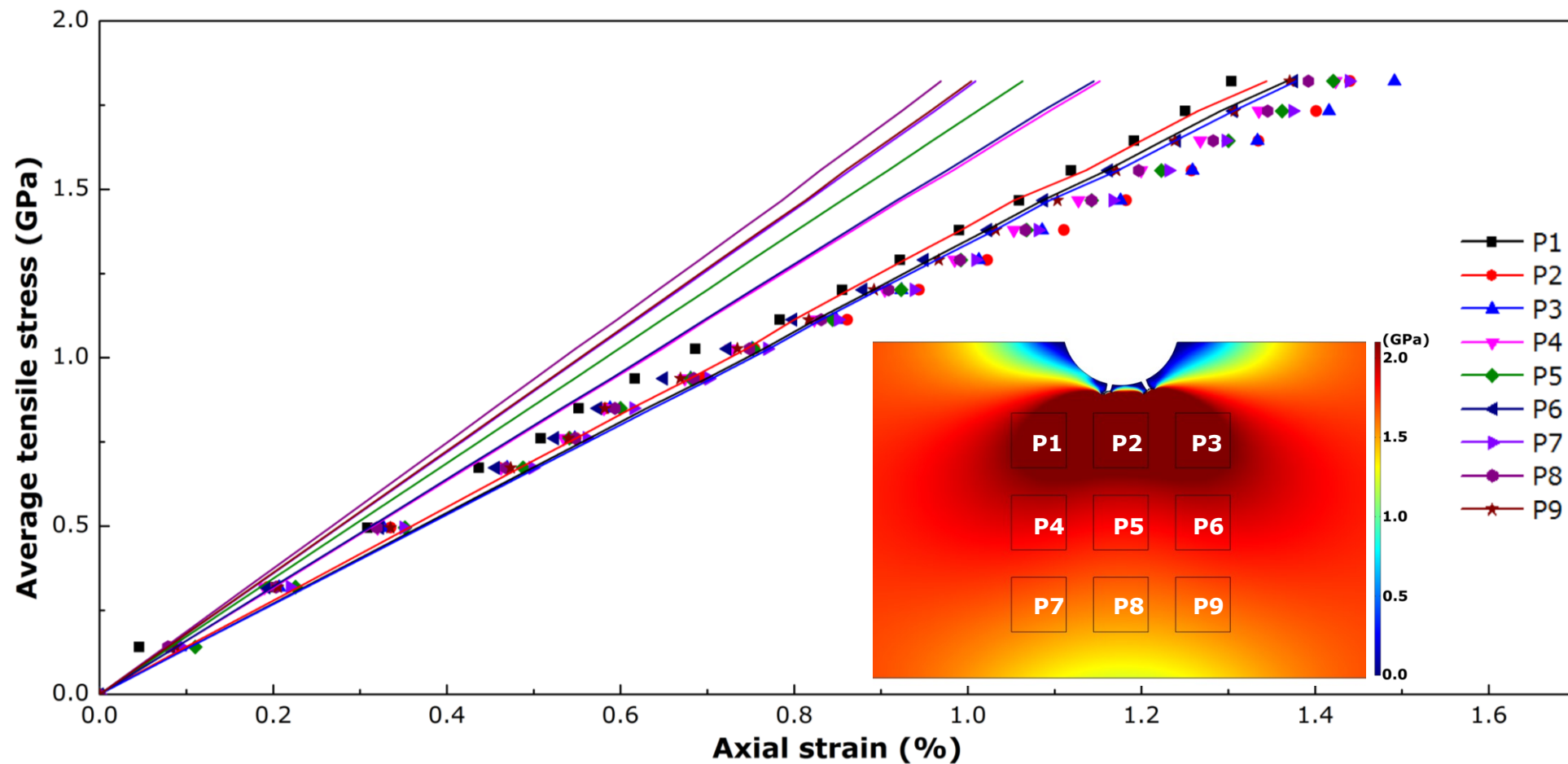


Figure 4.21 The average axial strain obtained from the FEM simulation (solid line) are plotted against the measurement from the SXRD (markers) for the 9 locations (insert figure).

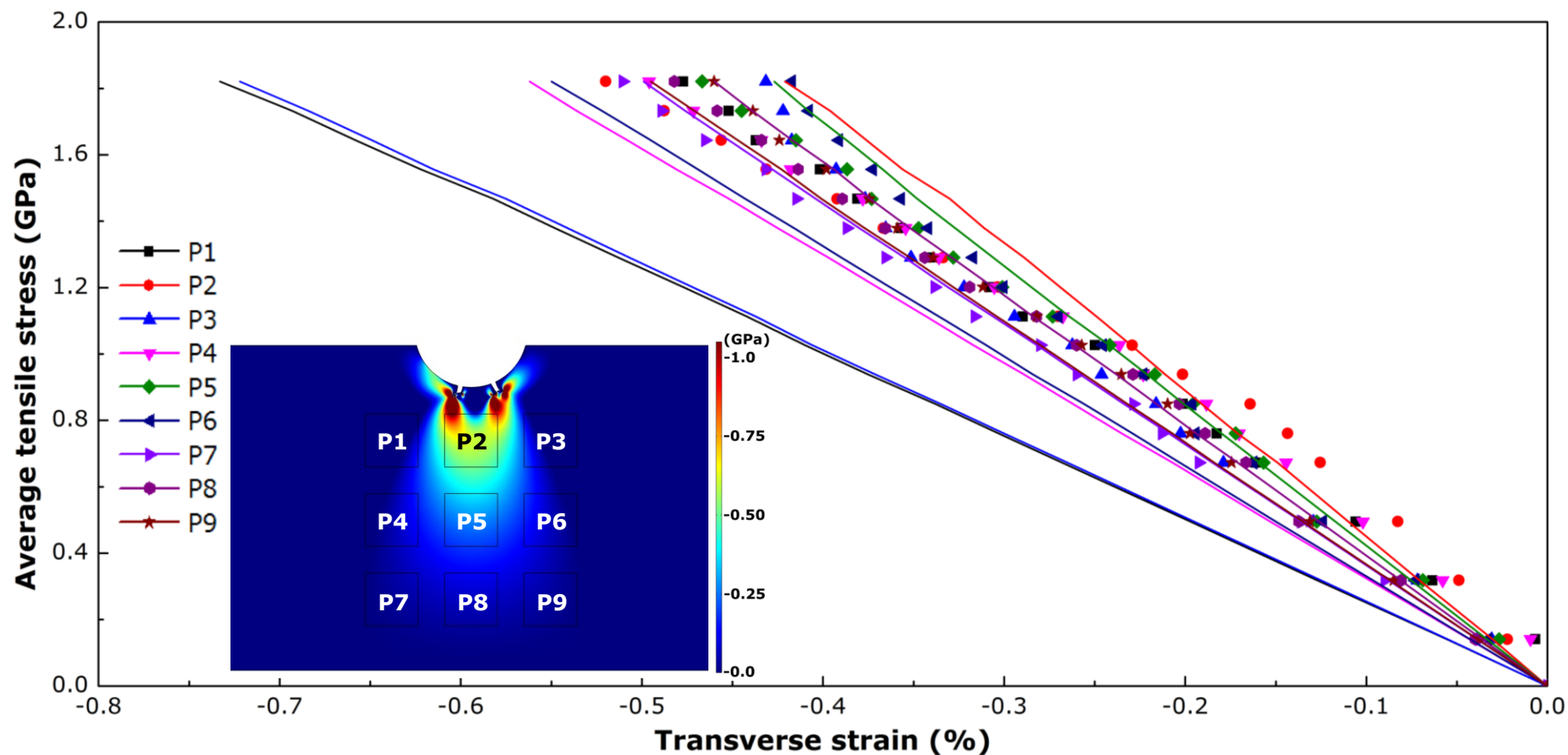


Figure 4.22 The average transverse strain obtained from the FEM simulation (solid line) are plotted against the measurement from the SXR (markers) for to the 9 locations (insert figure).

4.5 In situ imaging study of tensile deformation of ZrTi composite

Figure 4.23a shows part of the gauge length and the notch of the ZrTi composite sample before the tensile test. Two micro-indentation marks with a distance of 2.08mm apart were placed onto the gauge length and used for measuring the extension between the two indentations at different load step.

Figure 4.23b shows the load-displacement curve recorded by the control software of the microtester, and plotted together with the extension between the two micro-indentation markers (top-x), which measured using the SEM images acquired at each load step. The test was carried out using load step control with a constant speed of 0.05 mm/min in the elastic region with the predefined target load steps. However, displacement step control was used in the plasticity region.

The stress, strain and the fracture strain for the ZrTi composite in situ SEM tensile tested sample were calculated based on Eq. (3), (4) and (5), similar to the Vit-1 in situ SEM tensile tested sample.

Figure 4.23c shows the calculated stress-strain curve for sample. The curve was fitted using the 5th order polynomial equation intercept at 0. The Young's modulus calculated from the tensile stress versus tensile strain curve in the elastic region is 89.72 GPa.

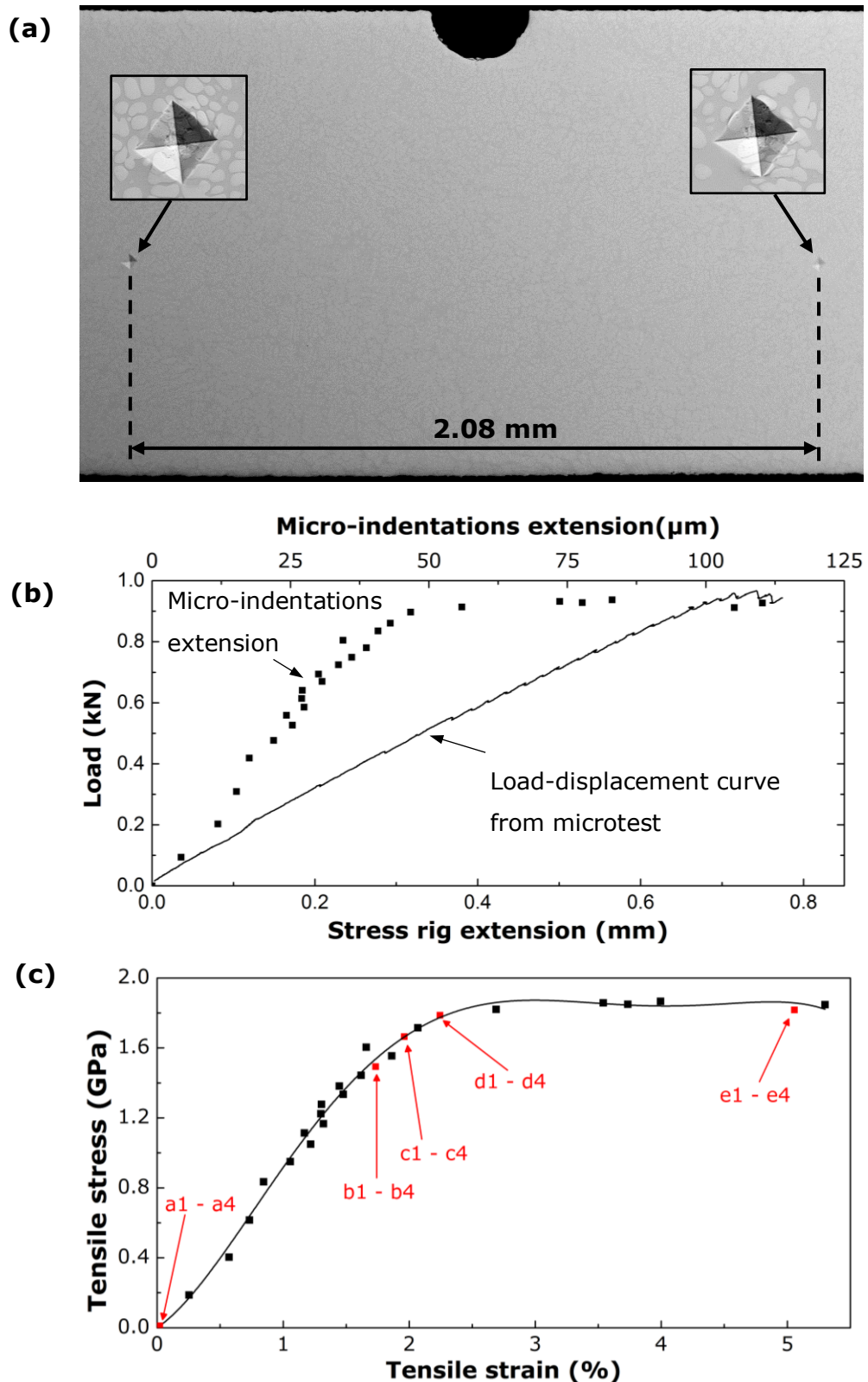


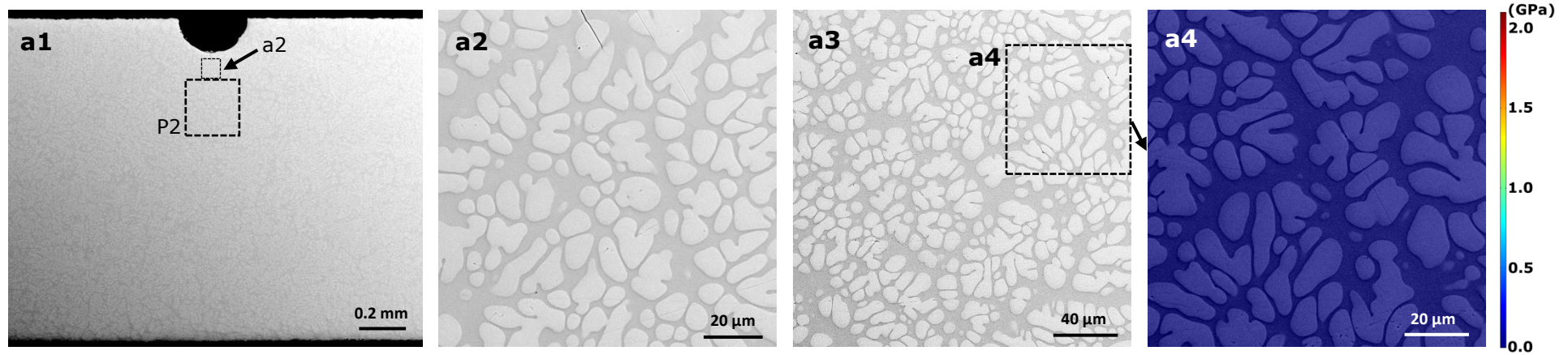
Figure 4.23 (a) SEM image taken at the centre of the gauge section of the ZrTi composite sample, showing the $\varnothing 0.25$ mm semi-circular notch and two indentation marks as the physical markers to measure materials extension under different load steps, (b) the load-displacement (bottom-X) curve recorded by the microtester and measured from the two indentation marks (top-X), and (c) the tested tensile stress

versus tensile strain curve and the red squares corresponding to the SEM images in Figure 4.24.

Figure 4.24 shows a series of SEM images taken at different load steps (the loads were converted into the corresponding average stresses and showed in Figure 4.23c using red squares) where initial crack in the sample surface and/or any shear band initiation and propagation were observed. The initial 20 N was considered as zero stress.

Figure 4.25a shows the in situ SEM sample fractured surface which fractured at a tensile stress of 1847MPa and the strain is estimated to be 5.3%. Figure 4.25b shows in situ SXRD sample fractured surface which the sample fracture at a tensile stress of 1790MPa. Both samples fractured at the similar location.

Tensile stress: 0 MPa, Tensile strain: 0 %



Tensile stress: 1492 MPa, Tensile strain: 1.74 %

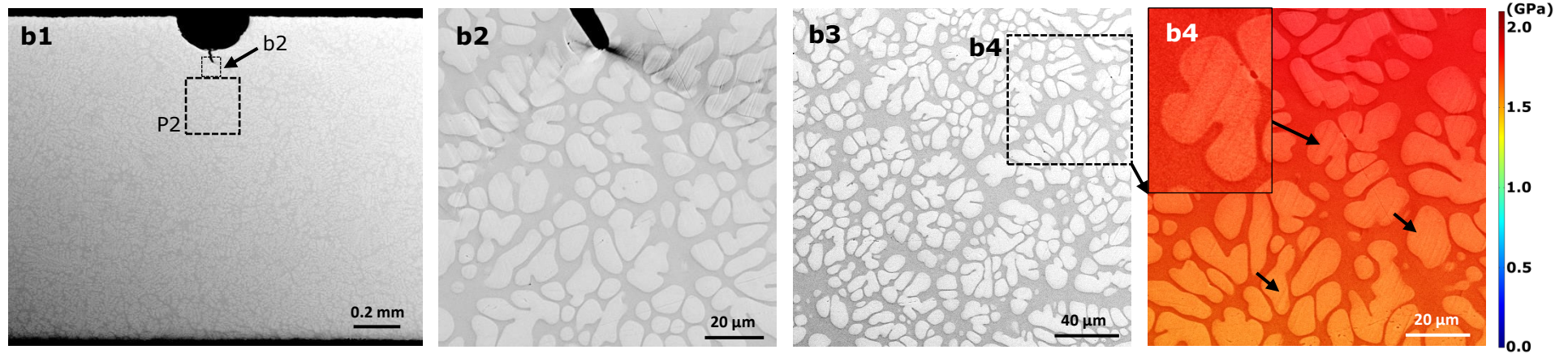
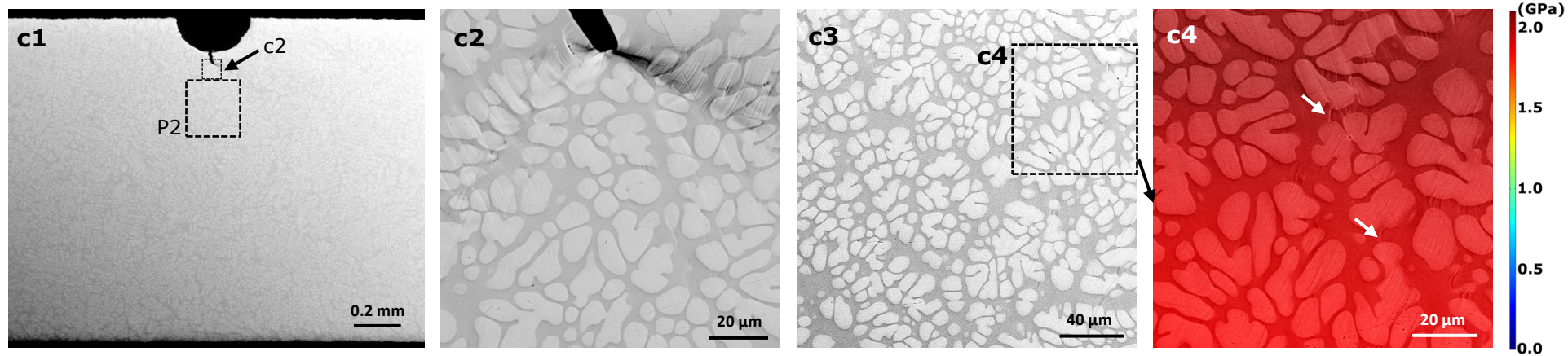


Figure 4.24 (a1) a SEM image of ZrTi composite sample near the notch at 0 MPa, (a2) an enlarged image of the framed "a2" area in a1, (a3) the image for the marked P2 area in a1, (a4) the simulated axial stress for the enlarged area in a3. (b1 - b4) are for those at 1492 MPa.

Tensile stress: 1663 MPa, Tensile strain: 1.96 %



Tensile stress: 1787 MPa, Tensile strain: 2.25 %

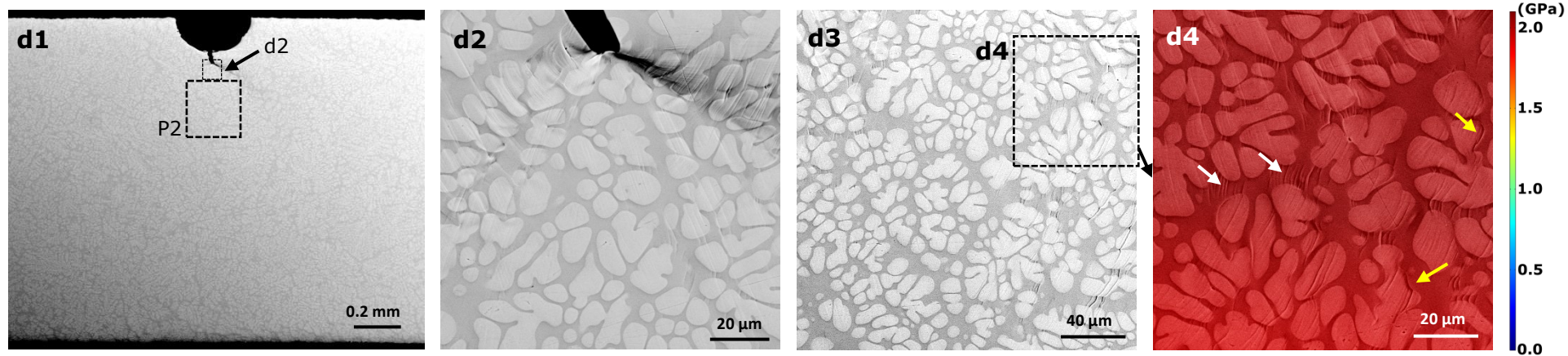


Figure 4.24 continue. (c1 - c4) are for those at 1663 MPa, and (d1 - d4) are for those at 1787 MPa.

Tensile stress: 1817 MPa, Tensile strain: 5.06 %

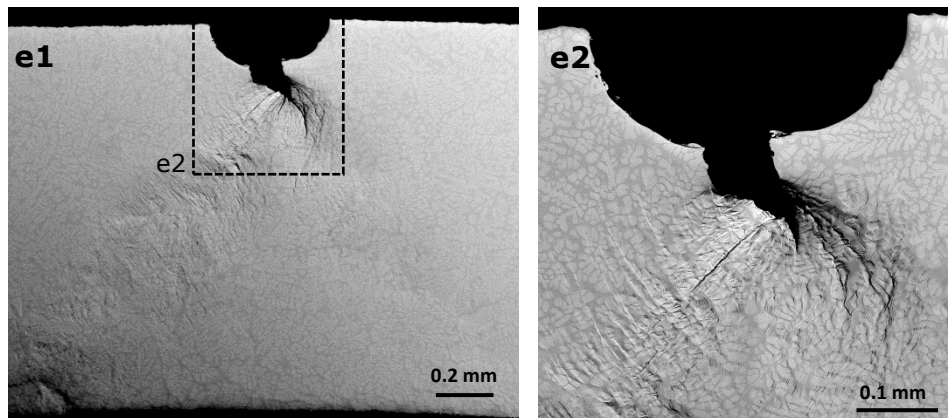


Figure 4.24 continue. (e1) a SEM image of ZrTi composite sample near the notch at 1817 MPa, (e2) an enlarged image of the framed area in a1.

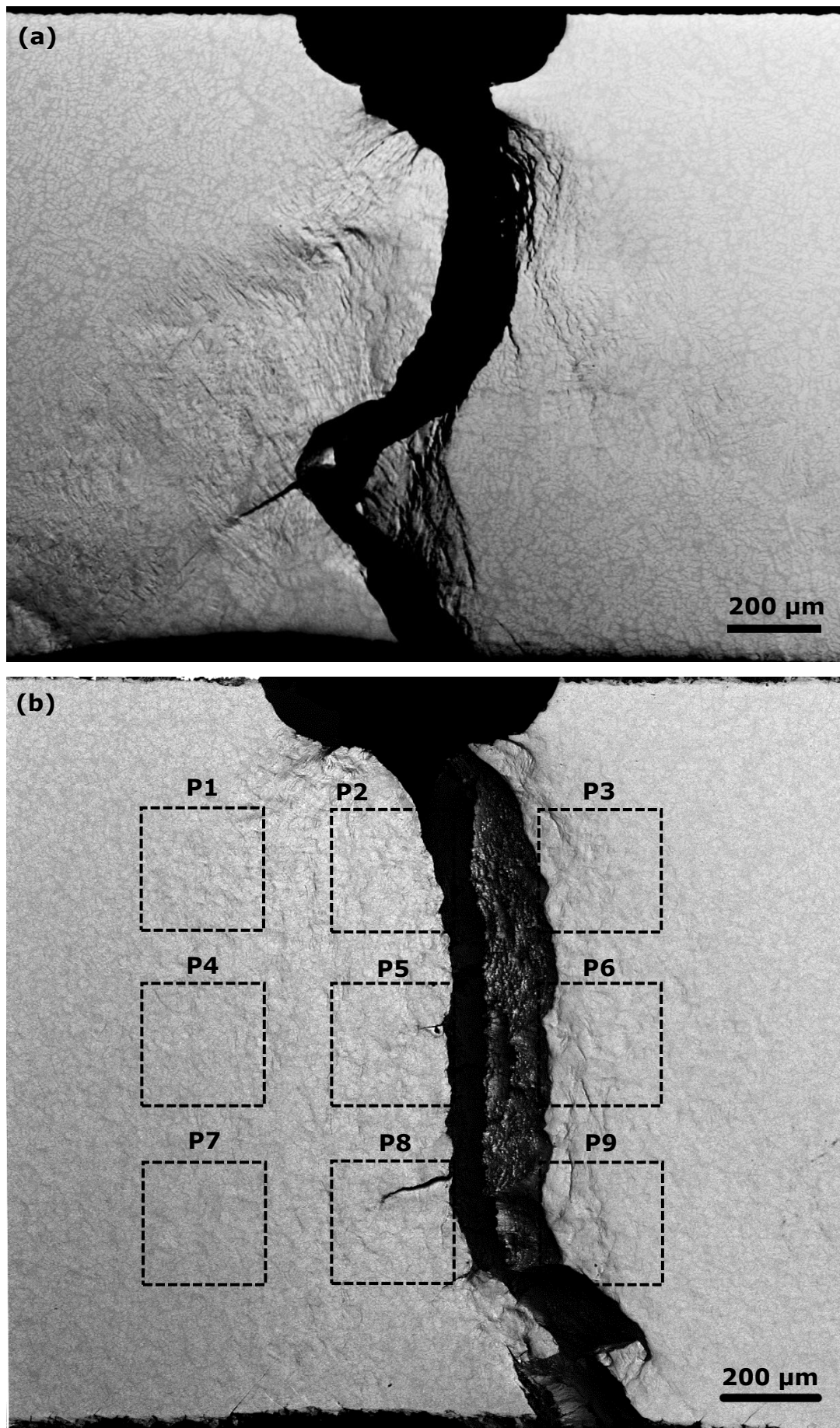


Figure 4.25 SEM images of ZrTi composite tensile tested samples fractured during (a) in situ SEM test (b) in situ SXR test.

4.6 In situ diffraction study of tensile deformation of ZrTi composite

The atomic structure evolution of the ZrTi composite under tensile loading were investigated using in situ SXRD experiment. The in situ study is to investigate the changes in atomic structures during shear bands initiation and propagation, in amorphous matrix and crystalline dendrites as show in the in situ SEM results. Figure 4.26a shows a 2D SXRD pattern obtained for the ZrTi composite sample during the preload state at location P2. Figure 4.26b shows the magnified image at the centre of the 2D pattern where it clearly shows the intensive Bragg spots and the faded halo rings in the background which contains the scattering information from both crystalline dendrites and amorphous matrix. Similar to the Vit-1 sample, to extract the axial and transverse sample information, a sector ($\pm 10^\circ$) at the correponding strain direction as shows in Figure 4.26b was intergraded into 1D spectrum after subtacting the background diffraction pattern using ImageJ. Figure 4.26 shows the 1D spectrum intergraded from the 2D pattern. However, as shows in the 1D spectrum, the crytalline peaks are formed on top of the amorphous profile. Hence the scattering information from the amorphous matrix and crystalline dendrites are coupled together. This causes great diffucties to extract the strain information seperately the amorphous matrix and crystalline dendrites.

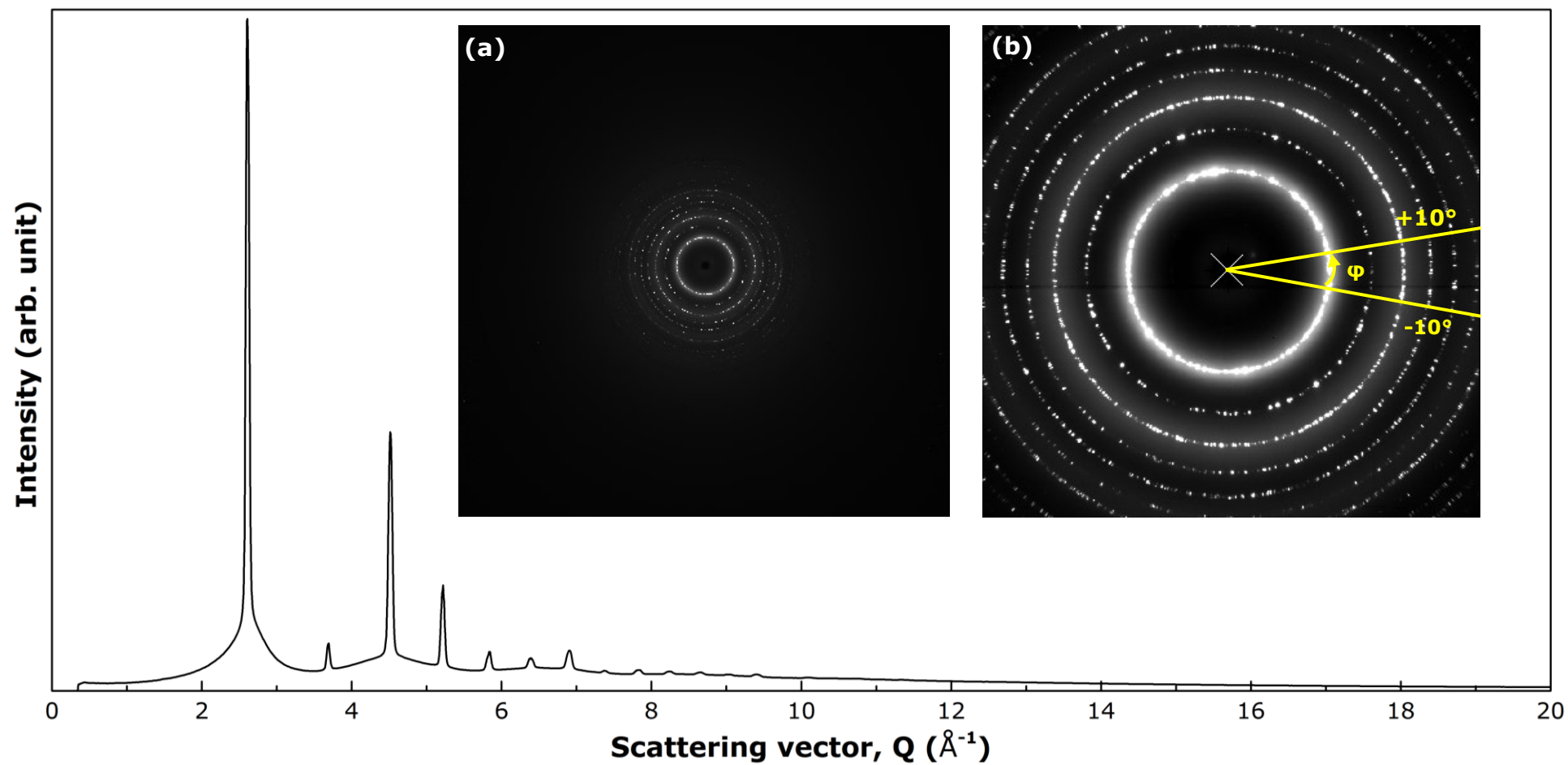


Figure 4.26 1D diffraction spectrum of ZrTi composite sample integrated from $\varphi = -10^\circ$ to 10° showed in (b). The inserts are: (a) 2D SXR pattern, a close-up view of the centre of the SXR pattern.

4.6.1 A generic method for decoupling the convoluted diffraction dataset

In order to separate the coupled scattering information, a generic procedure (algorithm) to separate the diffraction data of the crystalline phases away from the diffraction data of the amorphous matrix was developed. It is an iterative and generic procedure to completely mask out the Bragg's spots from the crystalline phases (Figure 4.27a) using Fit2D software of the 2D pattern into a 1D spectrum [13], and the procedure during the integration includes the following steps:

1. The 2D pattern of the ZrTi composite sample was first subtracted from the background pattern collected without the sample in place on the microtester.
2. The diffraction rings in the 2D pattern were segmented anticlockwise into 4 parts; at (1) 0° and (2) 180° to obtain axial strain information and (3) 90° and (4) 270° to obtain transverse strain information. Each part is integrated with $\pm 10^\circ$ in both directions to obtain the 20° sector.
3. A search step of a pixel width is defined in the Q range from 2 to 20 \AA^{-1} , at each pixel step, Fit2D is used to calculate the average intensity by integrating into 1D spectra. Any pixel with 10% higher intensity than this average value is considered as the diffraction information from the crystalline phases, and therefore masked out using the threshold masking function in Fit2D.
4. After the first masking out, the average diffraction intensity along the same arc is re-calculated, and any pixel with 10% higher intensity than the newly average value is again masked out.
5. Procedure 4 is carried out iteratively until no pixel within the search arc with 10% higher intensity than the average value calculated at the current search. In this way, the Bragg's spots that have sufficient distance can be completely masked out.

Using above procedure, the mask to remove the crystalline phase was created and showed in Figure 4.27b. The diffraction information of the matrix is completely separate from the composite diffraction rings. Figure

4.27 shows the 1D spectrum of the amorphous matrix extracted through the separation process compare with the original composite 1D spectrum.

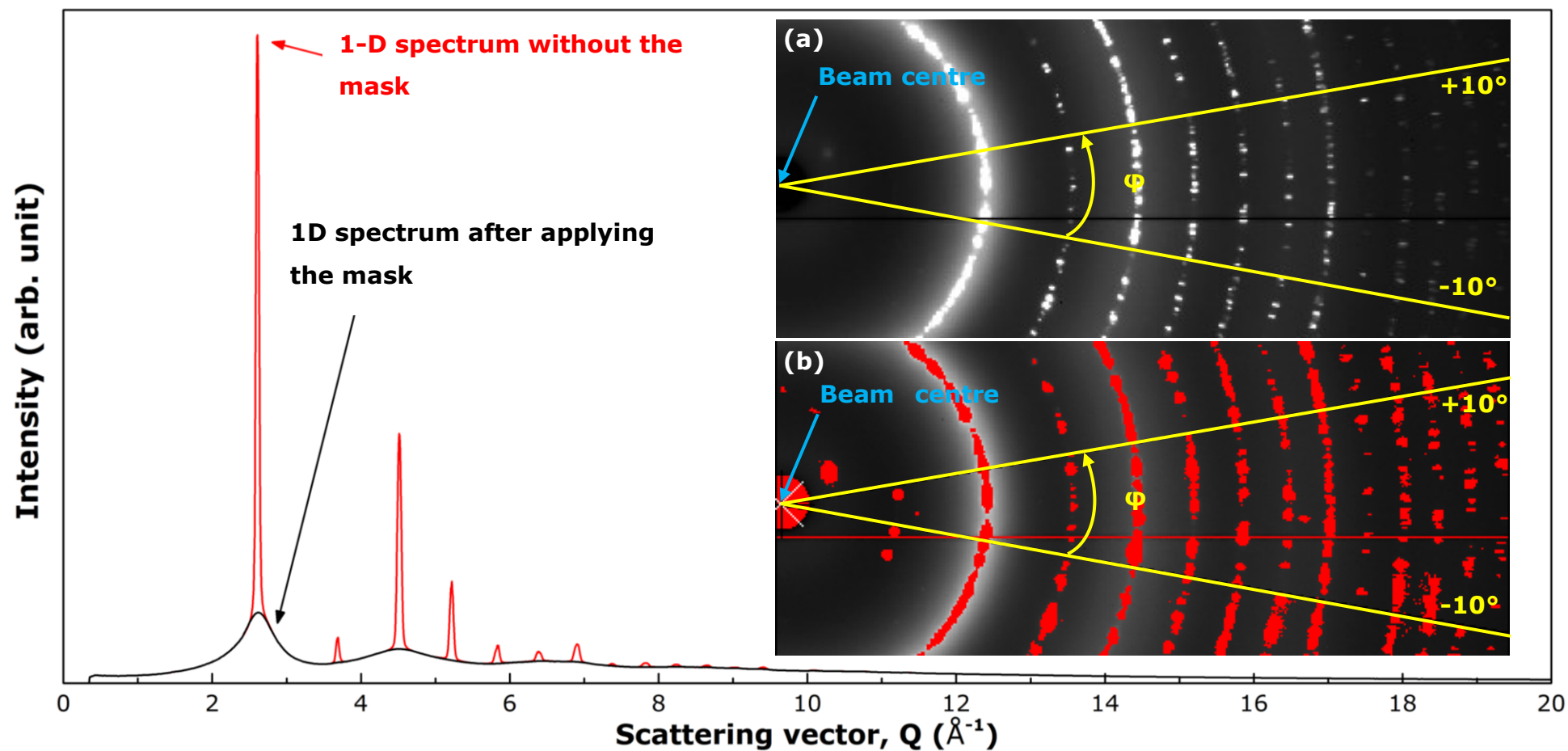


Figure 4.27 An integrated 1D spectrum after applying the mask which separates the scattering information from the crystalline dendrites and amorphous matrix (a) an enlarged image from Figure 4.26b, showing the Bragg's spots (b) Fit2D mask that applied on the Bragg's spots.

However, with the increase in tensile stress, the spacing between the Bragg's spots become closer. Hence the Bragg's spots are nearly touching each other like those show at the FSDP in Figure 4.28a and Figure 4.28b corresponding to 0 MPa and 1626 MPa tensile stresses. The 1st algorithm and procedure we used are not able to completely remove this features and another procedure was applied.

After using the first procedure, we obtained the 1D spectrum as shows in Figure 4.28c which did not mask out the "joined" Bragg's spots, which is similar to the powder diffraction ring as shows in the insert image. It is clearly shows in the 1D spectrum a suddenly increase in intensity due to the scattering information from the crystalline phases. The data points between 2.47 \AA^{-1} and 2.69 \AA^{-1} as shows in Figure 4.28d were taken out from the 1-D spectrum and leaving a void in the Q space. In order to recover the missing data, Gaussian fitting function (blue line) was used with the surrounding data points (black points) to create the new missing data points. Using this method we are able to resolve the FSDP at tensile stress 1626MPa, 1680MPa and 1763MPa.

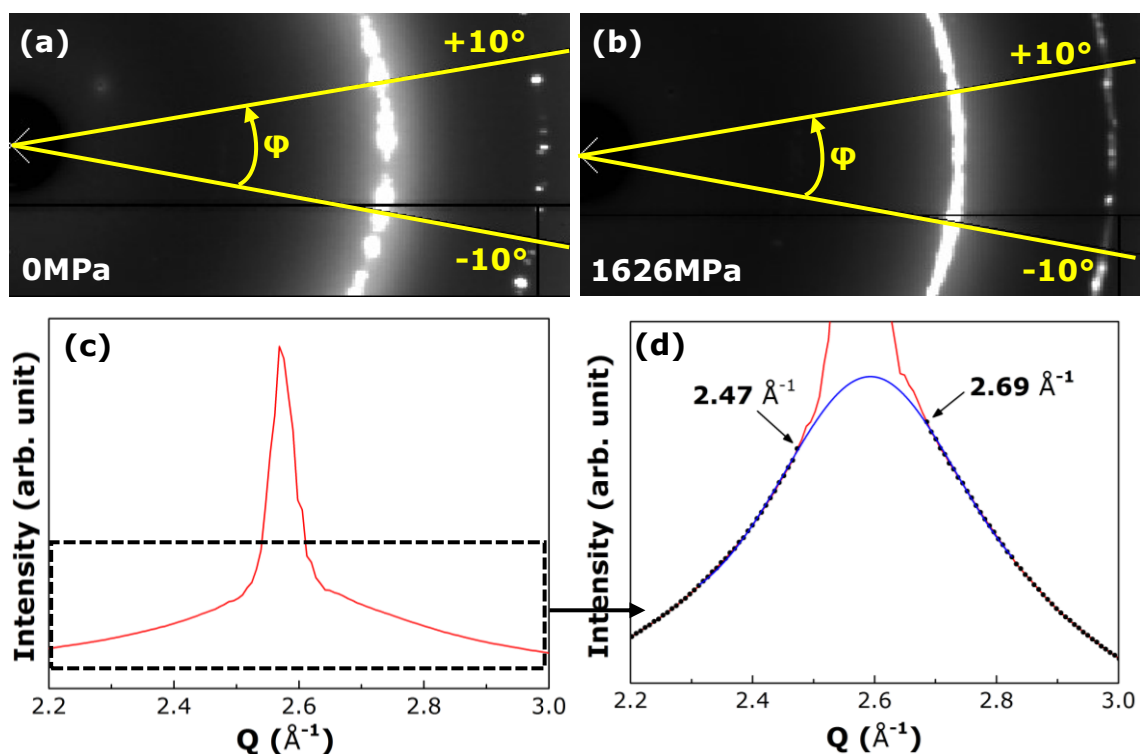


Figure 4.28 The FSDP of the ZrTi SXR D patterns (a) the enlarged 2D pattern at 0 MPa (b) the enlarge 2D pattern at 1626 MPa (c) the enlarge 1D spectrum at 1626 MPa (d) The recovered missing data points (black dots) using the Gaussian fitting function (blue line).

Because this method is separating the crystalline and amorphous scattering information through image processing technique, therefore it cannot be used for the total scattering studies. It is because during the image processing, some diffuse scattering might be removed. Therefore, the quantification of the strain at different stresses for the amorphous are carried out only using the shift of the FSDP instead of the shift of the atomic shells.

Figure 4.29 shows the tensile stress and load versus stress rig extension for the ZrTi composite sample from the microtester. Due to the time required to acquire the SXR patterns, at each step, there was a relaxation in force. The arrows in the curve show where the SXR patterns were acquired at. Similar to the in situ SXR experiment for Vit-1 sample, the strain measurement is unavailable.

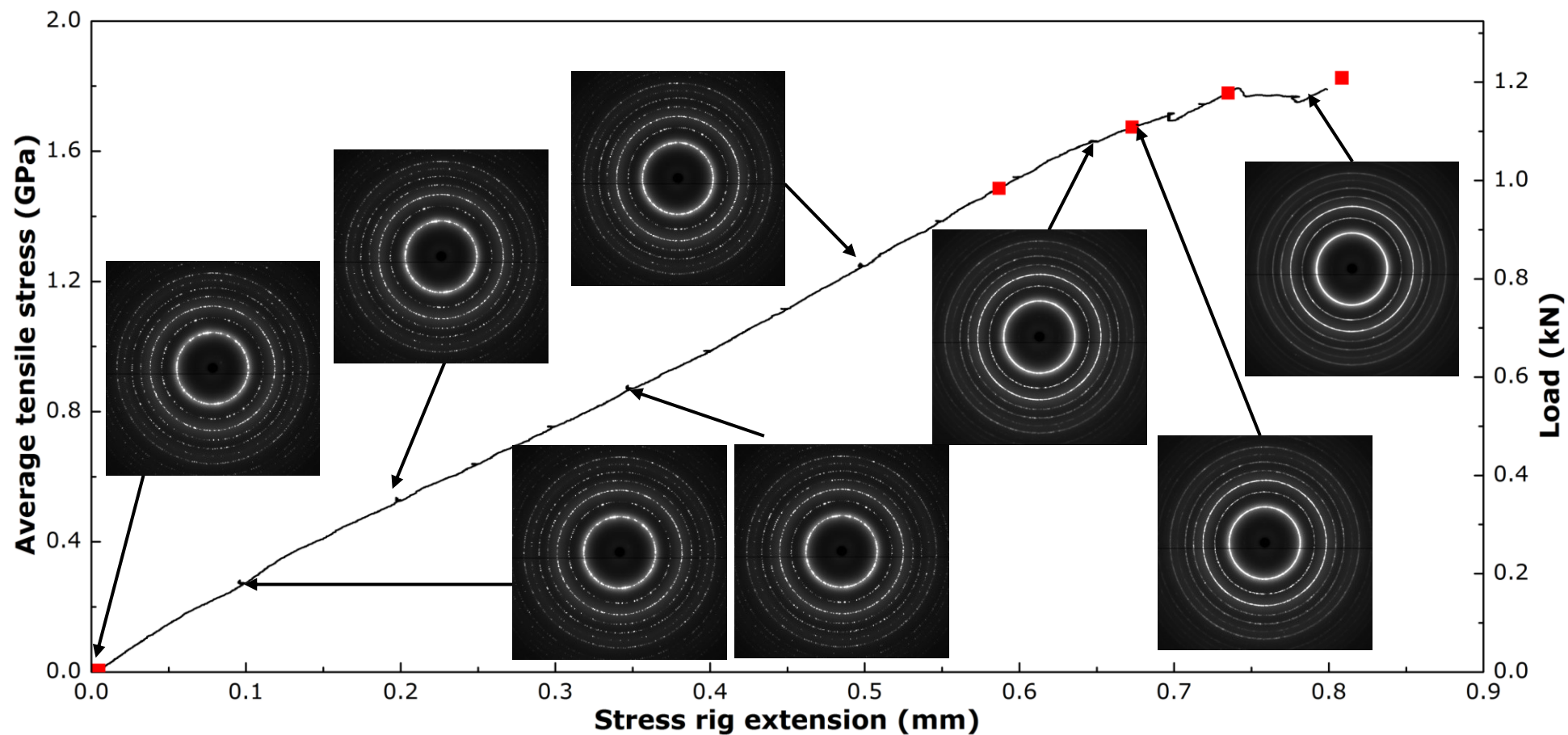


Figure 4.29 Average tensile stress and load versus stress rig extension recorded from the microtester for the ZrTi composite sample in situ tensile tested at I12 of DLS. The arrows show where the SXR D patterns were collected. The red squares show the stress where the SEM images showed in Figure 4.23c were taken.

Figure 4.30 shows one of the examples of the 1D spectra of location P2 at different stresses in the axial direction. The 1D spectra of amorphous matrix are shown in the solid thick lines, whereas the crystalline dendrites are shown in the thin line.

To quantify the strain in the amorphous matrix, the shift of the position of the first sharp diffraction peak (FSDP) in 1D spectra (the peak point by the black arrow in Figure 4.30 insert figure) versus the increase of tensile stress are found by fitting the FSDP using the Gaussian fitting function. Using the FSDP position, the strains for the amorphous matrix at different stresses were calculated using Eq. (6). Figure 4.31 shows the tensile stress versus axial and transverse strain for the amorphous matrix at the 9 locations.

To quantify the strains in the crystalline dendrites, the shift of the first 6 Bragg's peak position in the 1D spectra (the 6 peaks pointed by the red arrows in Figure 4.30 insert figure) versus the increase in tensile stress are found by fitting the peaks at different tensile stress using the Gaussian fitting function. Using the first 6 Bragg's peaks position, d-spacing of each peak is calculated (Eq. (8)) and converted into the lattice parameter with their corresponding hkl planes (as labelled in the Figure 4.30 insert figure) using Eq. (9). Subsequently, the tensile strains of the crystalline dendrites are obtained by using the changes in these lattice parameters with the increase in tensile stress in Eq. (10). Figure 4.31 shows the tensile stress versus axial and transverse strain for the crystalline dendrites calculated.

$$n\lambda = 2d \sin \theta \quad (8)$$

$$\alpha_{\sigma} = d_{hkl} \times \sqrt{(h^2 + k^2 + l^2)} \quad (9)$$

$$\varepsilon_{\alpha} = \frac{\alpha_{\sigma} - \alpha_0}{\alpha_0} \quad (10)$$

Where d is the d-spacing, hkl is the corresponding planes in the crystalline system, α_{σ} and α_0 are the lattice parameter at σ stress and zero stress, respectively and ε_{α} is the strain.

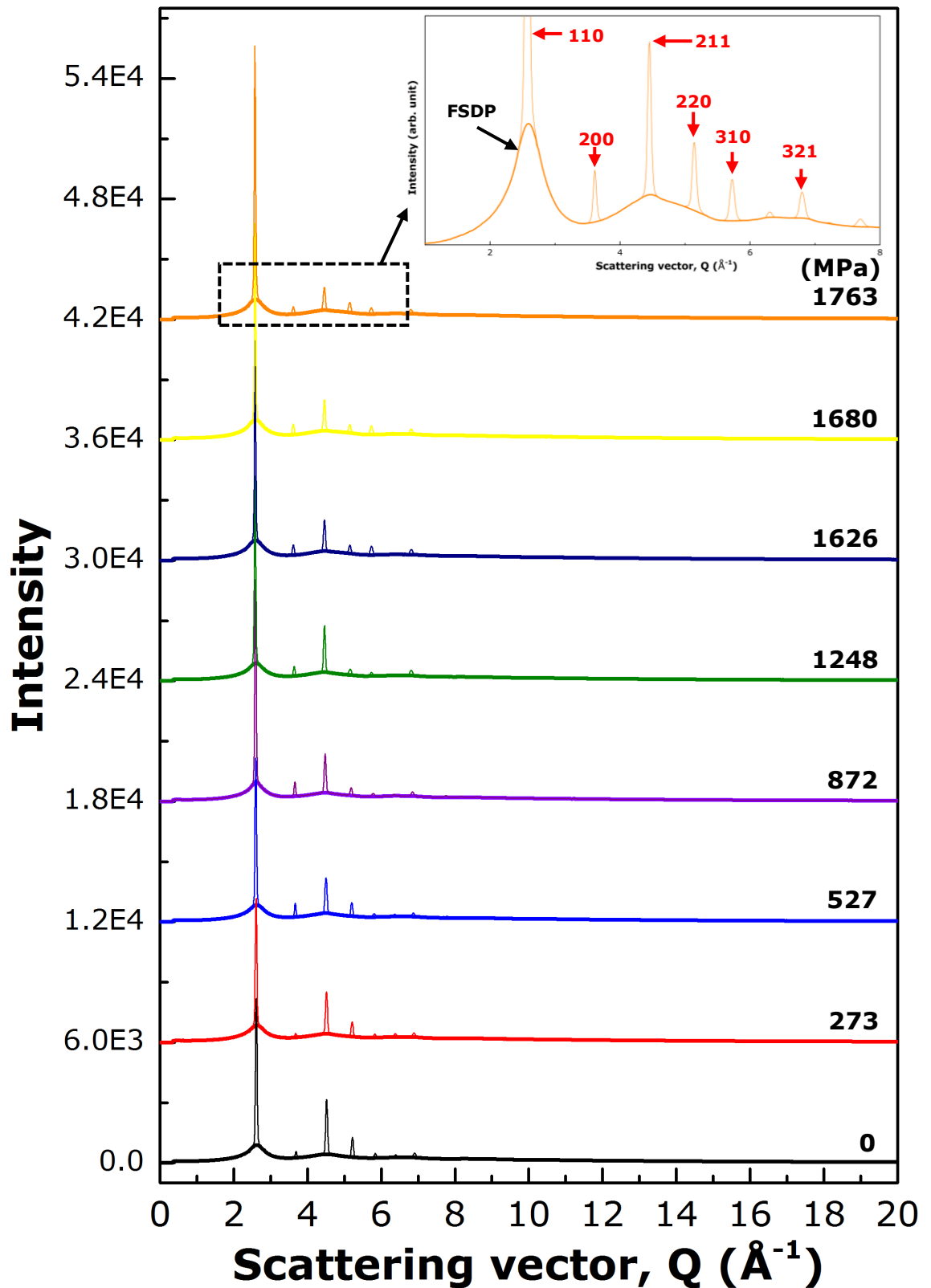


Figure 4.30 A example of 1D XRD spectra from location P2 in axial direction, showing the scattering information from the amorphous matrix (solid line) and the crystalline dendrite (dotted line) in the ZrTi composite sample at different stress.

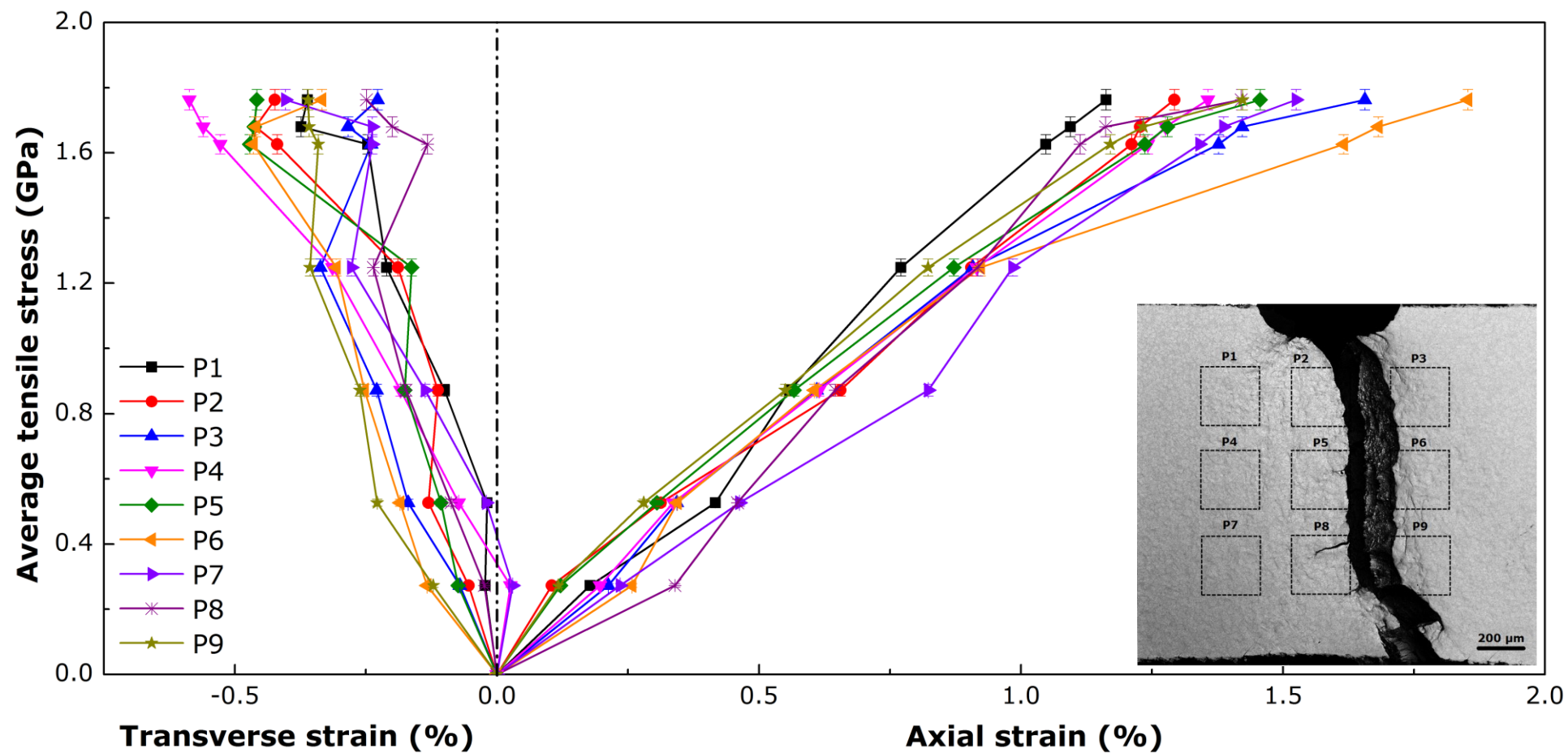


Figure 4.31 The calculated axial and transverse strain for the amorphous matrix versus the increase in tensile stress for the 9 locations.

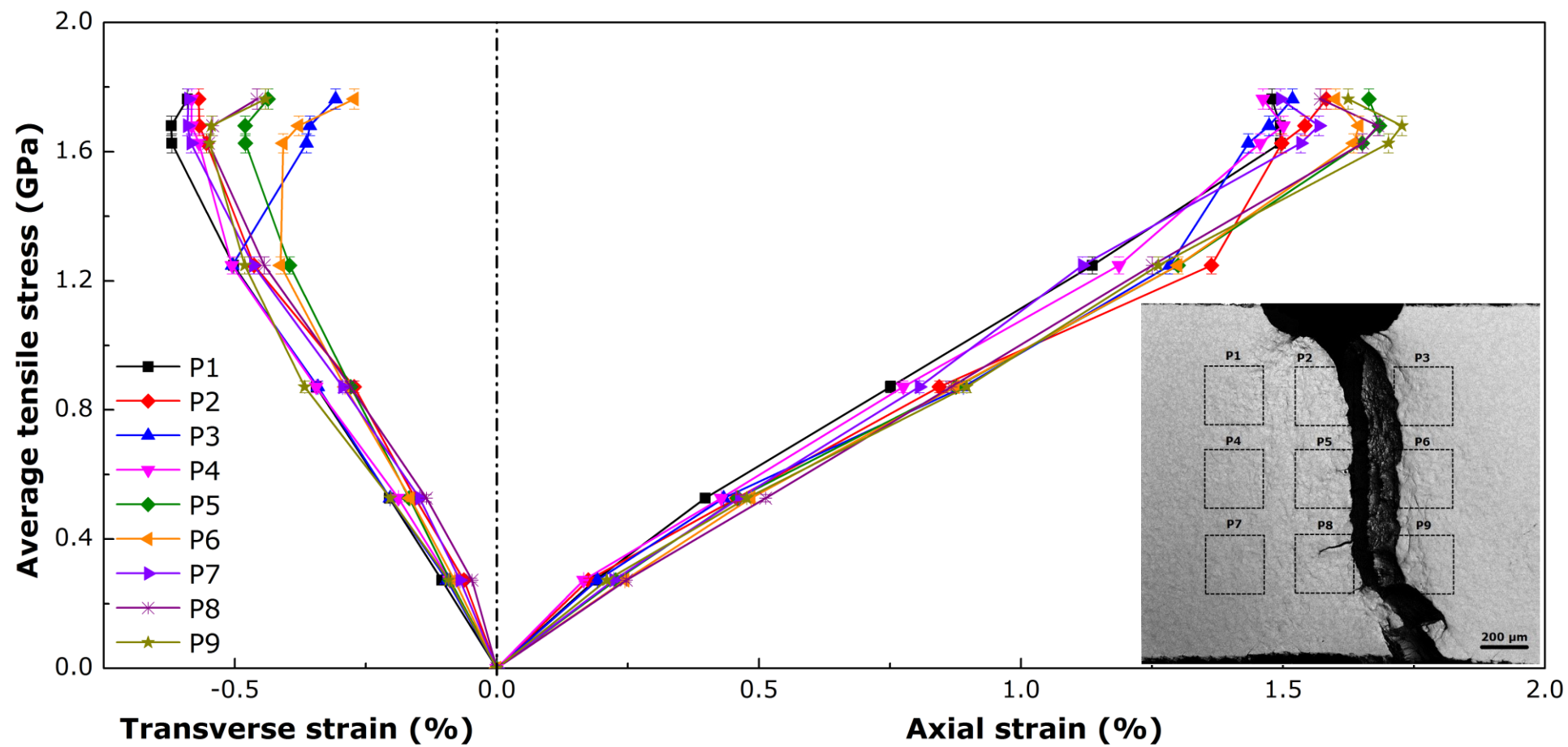


Figure 4.32 The calculated axial and transverse strain for the crystalline dendrites against the increase in tensile stress at the 9 positions.

4.7 Finite element modelling of tensile deformation of ZrTi composite

To further investigate the local stress field around the stress concentrator ($\emptyset 0.25$ mm semi-circular notch), especially when the shear band nucleation and propagation occur in the location near P2, 2D finite element models were created using COMSOL Multiphysics software (V 4.3). The simulation was carried out using the linear elastic model therefore the simulation is valid until the yield strength. The tensile load is applied onto the 4 edges of the dog-bone shoulder. The model is meshed using the built-in "free triangular" mesh function. Figure 4.33a shows the enlarged view around the initial notch cracks.

Unlike the monolithic Vit-1 sample, the ZrTi composite sample composed of the amorphous matrix and crystalline dendrites which has different material properties. To model the composites, the combined and averaged material properties for the two features were used as discussed in chapter 4.1. In addition, a local area which consists of the separated dendrites and matrix are included in the model as shows in the top insert figure in Figure 4.33. The area was selected because it is the highest stress concentration area due to the crack formed during the EDM.

The dendrites and matrix within the area are applied with different Young's modulus extracted from the Nano-indentation test. Table 4.2 summarises the important samples geometries and material properties used in the model. The Young's modulus and yield strength used in the model are obtained from the nano-indentation test and in situ SEM tensile test. Whereas, the Poisson's ratio and density of the ZrTi composite is obtained from Hofmann's paper [7].

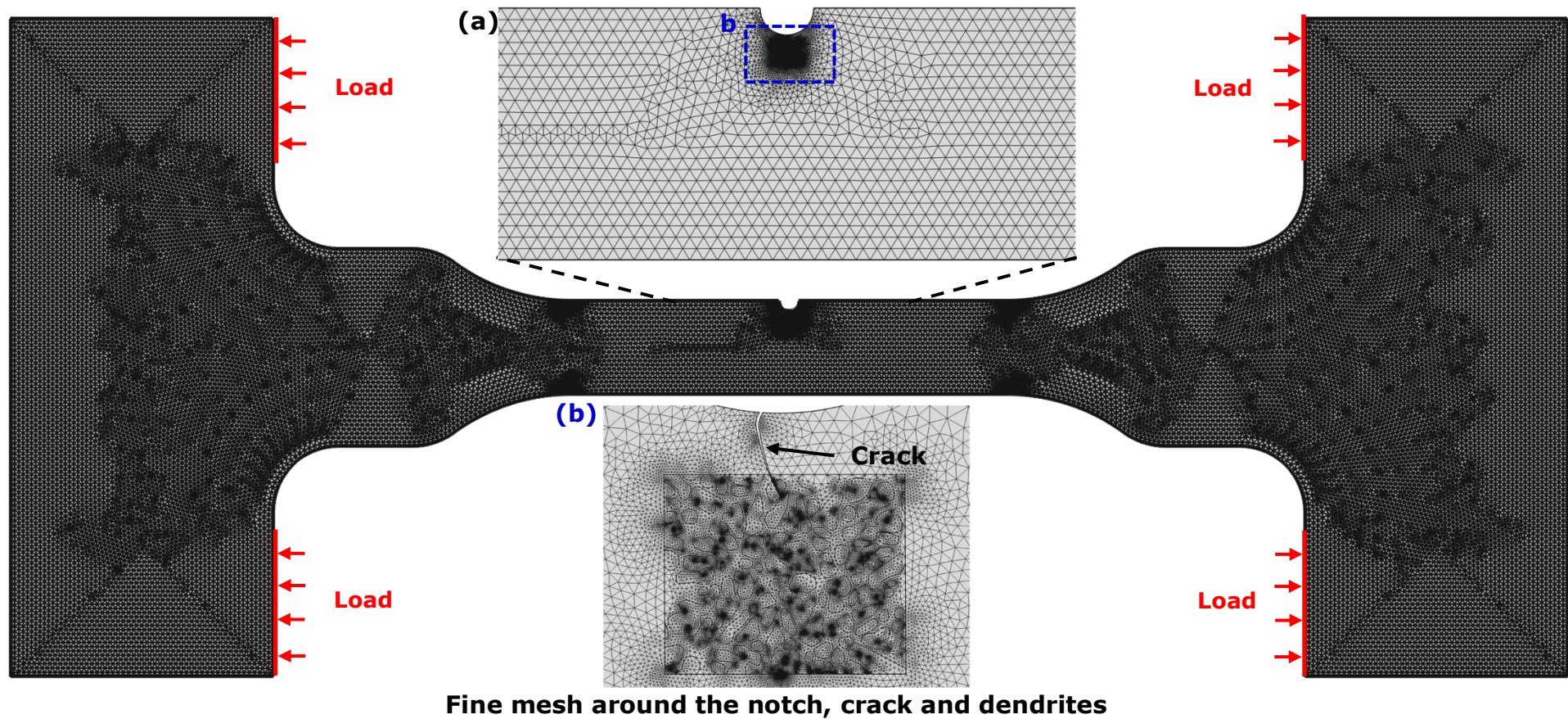


Figure 4.33 The dog-bone sample is meshed using the “free triangular” mesh at 618 MPa. (a) An enlarged image at the centre of the gauge section, showing the mesh around the notch. (b) An enlarged image from the framed area in a, showing the mesh around the crack and the local area with dendritic structure.

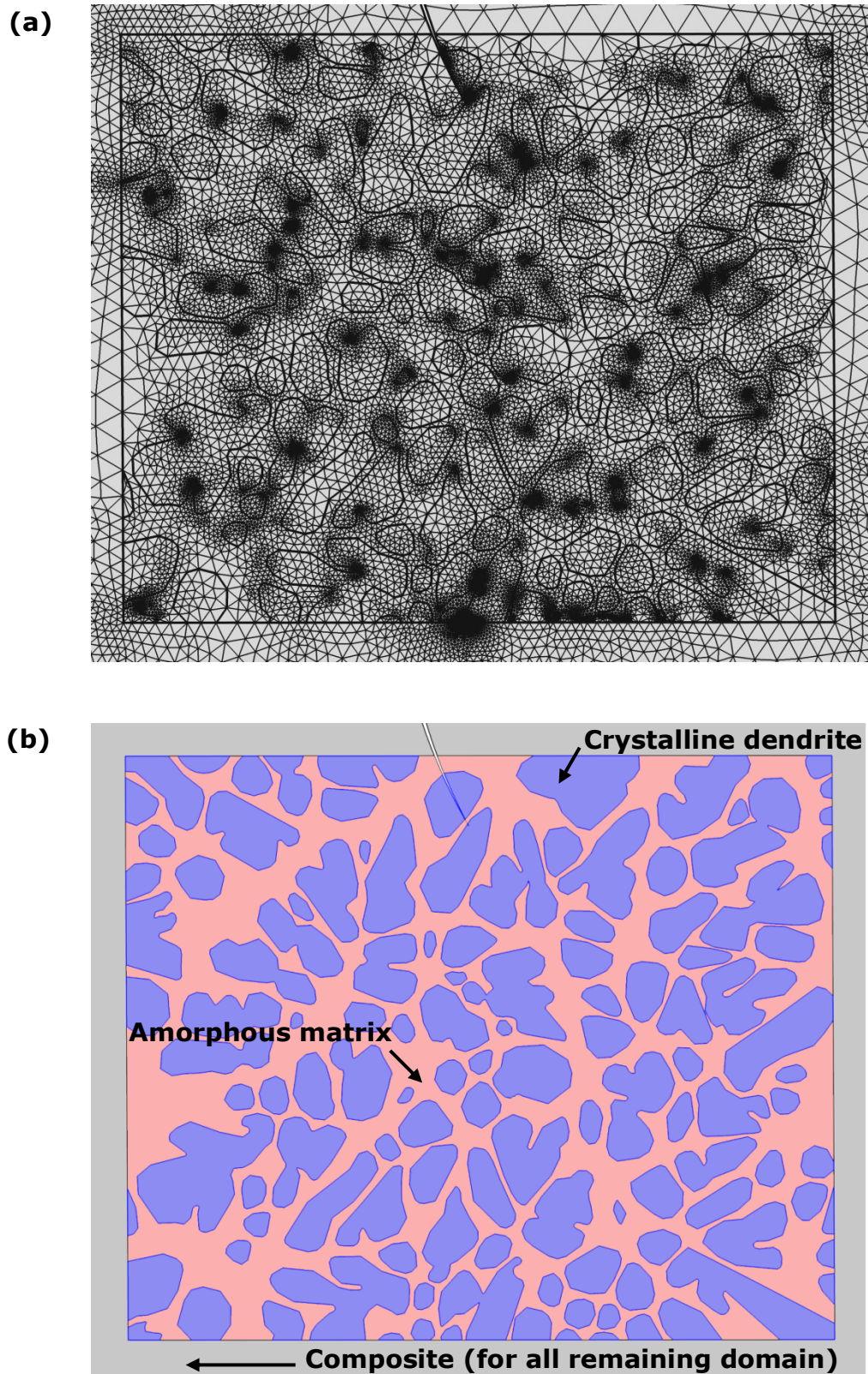


Figure 4.34 (a) an enlarged image from Figure 4.33b, showing the mesh around the dendrites and crack tip, (b) the material domain from a, showing the material properties applied for the crystalline dendrite, amorphous matrix and composite (for all the remaining domain as shows in Figure 4.33)

Figure 4.35a and Figure 4.35b show the simulated contour plots of the ZrTi sample in axial and transverse stress direction. The enlarged images at local area of the dendrites and matrix are show in Figure 4.36 b2 and Figure 4.36 b3. The figure shows the axial and transverse contour plots of the local stress within the dendrites and matrix around the notch at 616 MPa and 834 MPa respectively. Both tensile stresses were selected because of shear bands were observed in a small area of dendrites as shows in the SEM image in Figure 4.36 b1 (as pointed by the black arrows). Using this model, we extracted consecutively the axial stress during the shear bands formation in location P2, and the axial stress field plots are superimposed with the SEM images as shows in Figure 4.24

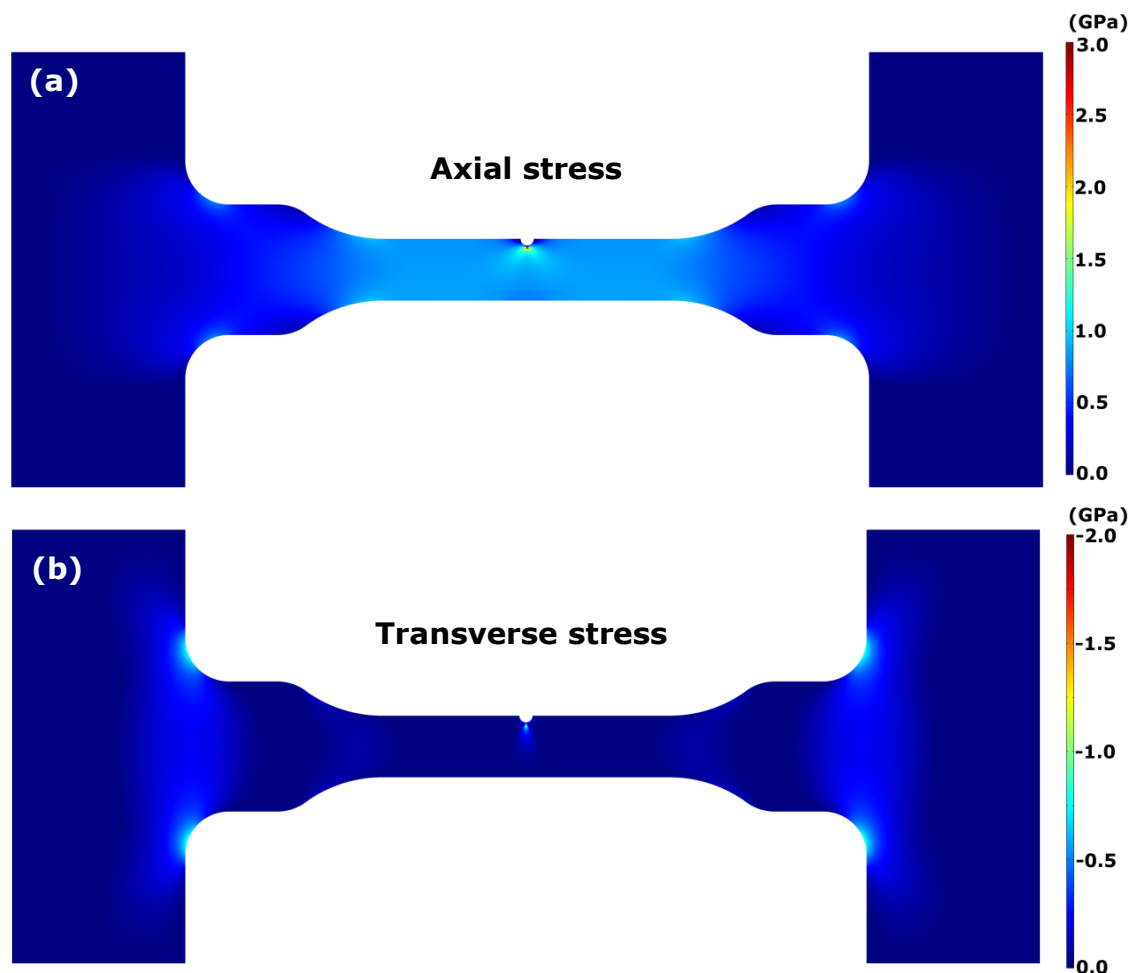


Figure 4.35 The simulated contour plots of the stresses of ZrTi composite sample in (a) axial and (b) transverse direction at the sample yield stress of 834 MPa.

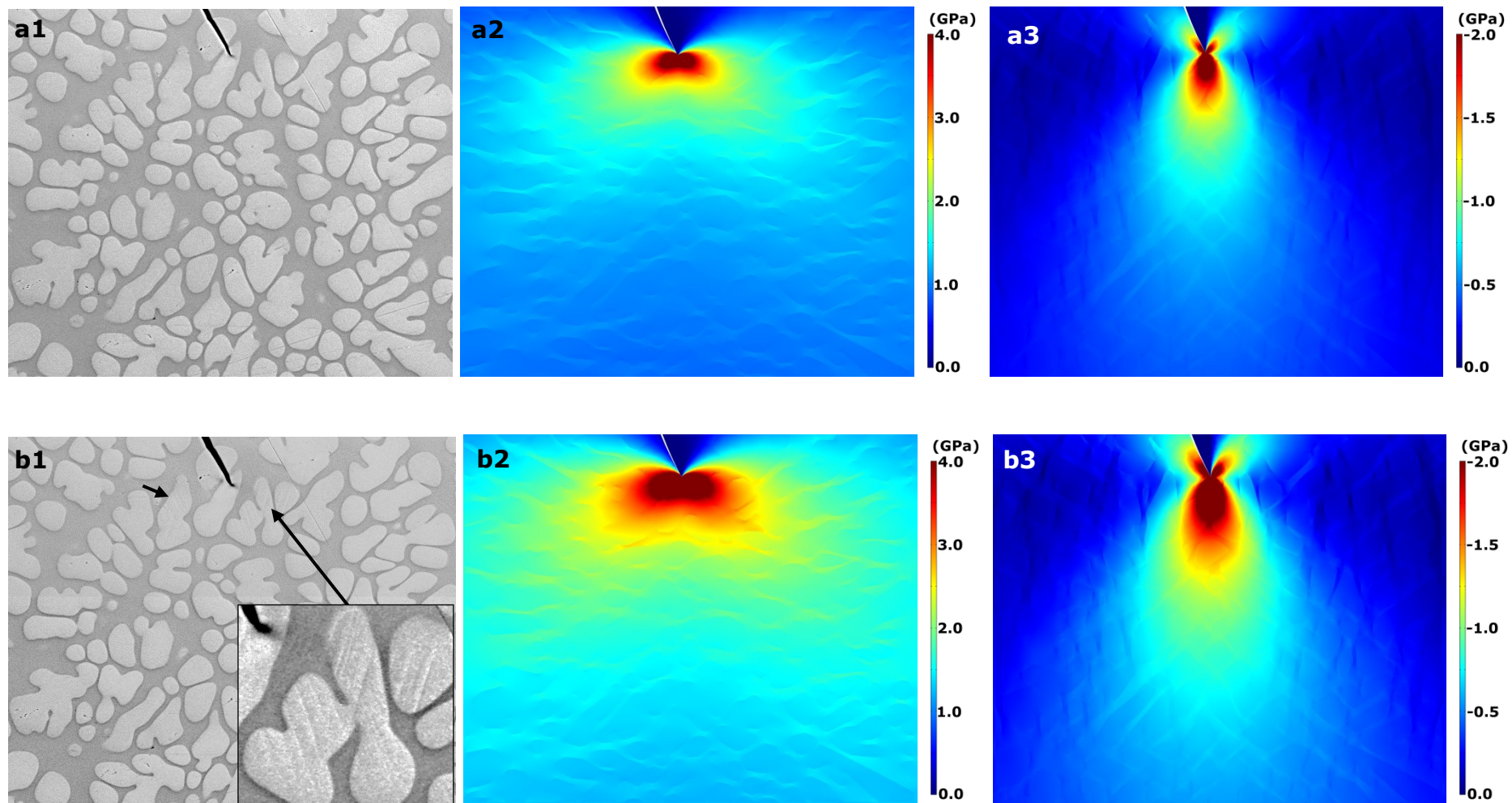


Figure 4.36 (a1) A SEM image of ZrTi composite near the crack area at 616MPa. The simulated stress field at the (a2) axial and (a3) transverse direction corresponding to a1 and (b1 – b3) are for those at 834 MPa.

4.8 Discussion

The tensile deformation of monolithic bulk metallic glass and bulk metallic glass matrix composite were studied under well controlled load and displacement steps to allow similar tensile stress condition to be conducted in situ inside SEM and at synchrotron X-ray beamline. The combined techniques provide real time quantitative information to study the deformation mechanisms of the two materials. In addition, finite elements simulations were used to provide complementary information about stress/strain field near the notch area.

The findings in the 1st and 2nd years of my PhD published in the Scripta Materialia for $\text{Ti}_{40}\text{Zr}_{25}\text{Ni}_{12}\text{Cu}_3\text{Be}_{20}$ (Ti40) [11], International Journal Plasticity for $\text{Zr}_{41.2}\text{Ti}_{13.8}\text{Cu}_{12.5}\text{Ni}_{10}\text{Be}_{22.5}$ (Vit-1) [12] and Applied Physic Letters for $\text{Zr}_{39.6}\text{Ti}_{33.9}\text{Nb}_{7.6}\text{Cu}_{6.4}\text{Be}_{12.5}$ (ZrTi) [13] BMGMC were discuss in this section together with the tensile test samples results show in Chapter 4.

4.8.1 Shear bands initiation and propagation control

The introduction of local stress concentrator; an artificial notch [11] or a hole [12] into the gauge length allows better control of the shear band initiation and propagation. The notch and hole enable high stress concentrated at area directly below the feature (for hole sample is at both the top and bottom areas) and create the strain gradient to slow down shear bands propagation in order to capture the deformation mechanism.

Figure 4.9a shows the simulated axial stress field of the Vit-1 sample at the fracture strength of 2032 MPa. The axial stress field shows that nearly half of the sample width below the notch are above the fracture strength of Vit-1 (1.9 GPa [7, 156]) while the other end still around ~ 1.3 GPa. The introduction of this local stress field results in the shear bands initiation and propagation to be captured during the tensile test, for example the successfully in capturing formation of the "step".

Figure 4.37b and Figure 4.37c show the relationship between the local strains at P1, P2 and P3 as shows in Figure 4.37a (which is P2, P5 and P8 in the thesis), and the global tensile stresses applied on the $\varnothing 0.25$ mm semi-circular notch and non-notch samples, respectively. For both samples,

the strain increases linearly with increasing stress in both the tensile and transverse directions, as expected from a linear elastic material. For the non-notch sample, identical strains were obtained at P1, P2, and P3 (Figure 4.37c), and the ratio of the strains between the tensile and the transverse directions gives Poisson's ratio of 0.330. For the notch sample, different tensile and compressive strains were obtained, with $\epsilon_{P1} > \epsilon_{P2} > \epsilon_{P3}$ (Figure 4.37b), showing a clear strain gradient near the notch.

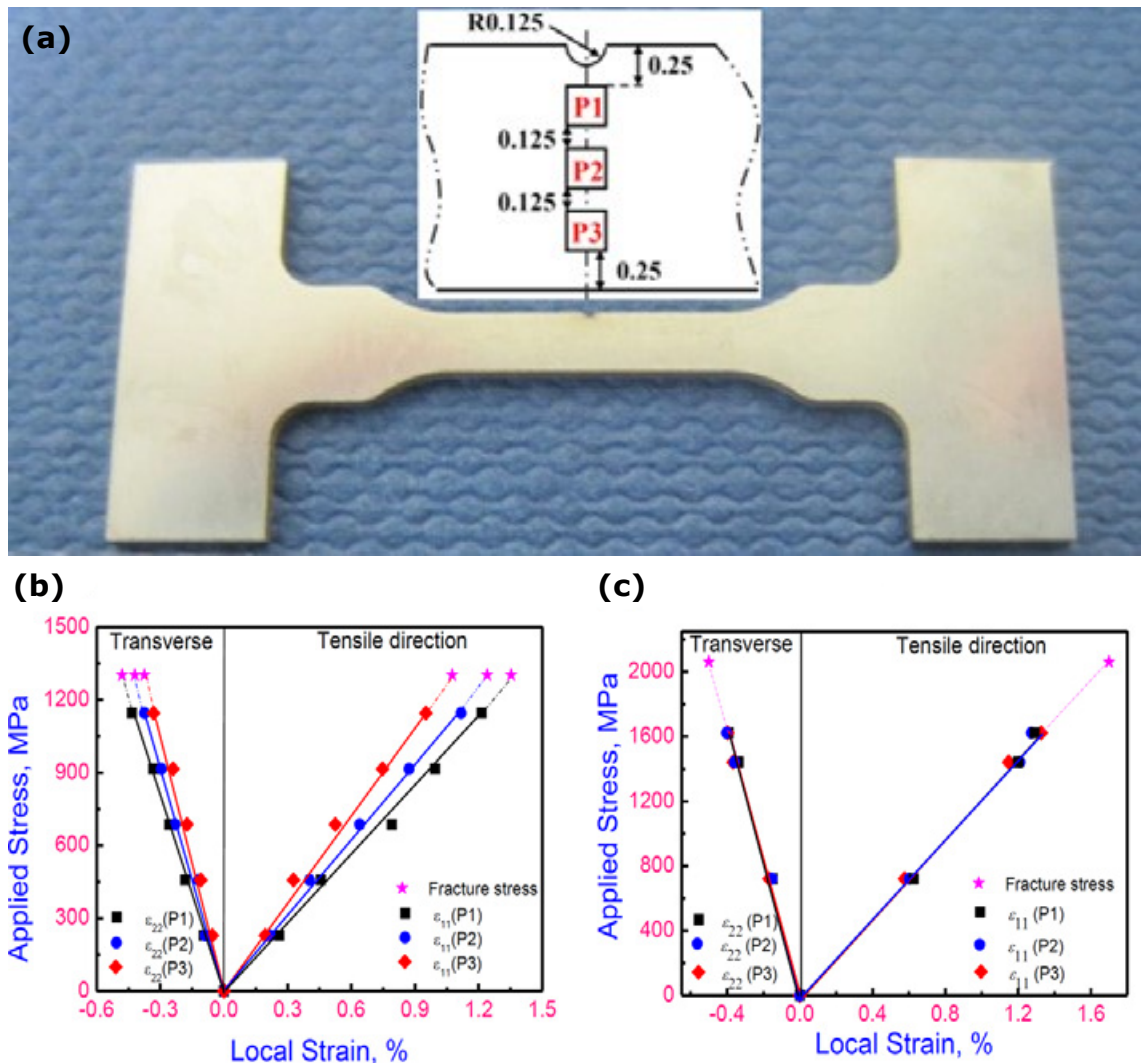


Figure 4.37 In situ tensile test of $\text{Ti}_{40}\text{Zr}_{25}\text{Ni}_{12}\text{Cu}_3\text{Be}_{20}$ (Ti40) BMG. (a) a dog bone sample with a \varnothing 0.25 mm semi-circular notch and the schematic diagram showing the position of P1, P2 and P3. Tensile and compressive strain calculated from the shift of the FSDP at P1, P2 and P3, of the samples (b) with and (c) without a notch as a function of applied stress [11].

On the other hand, a \varnothing 0.4mm circular hole was drilled at the middle of the gauge length to create a stress concentration, to control shear band nucleation and propagation as show in Figure 4.38a [12]. The P1, P2 and P3 locations (Figure 4.38b) were selected to acquire the diffraction pattern. Figure 4.38c and Figure 4.39 show the presence of a hole in the middle of the gauge length produced variations in the local strains for the locations P1, P2, and P3 with the absolute strain values of $P1 > P2 > P3$.

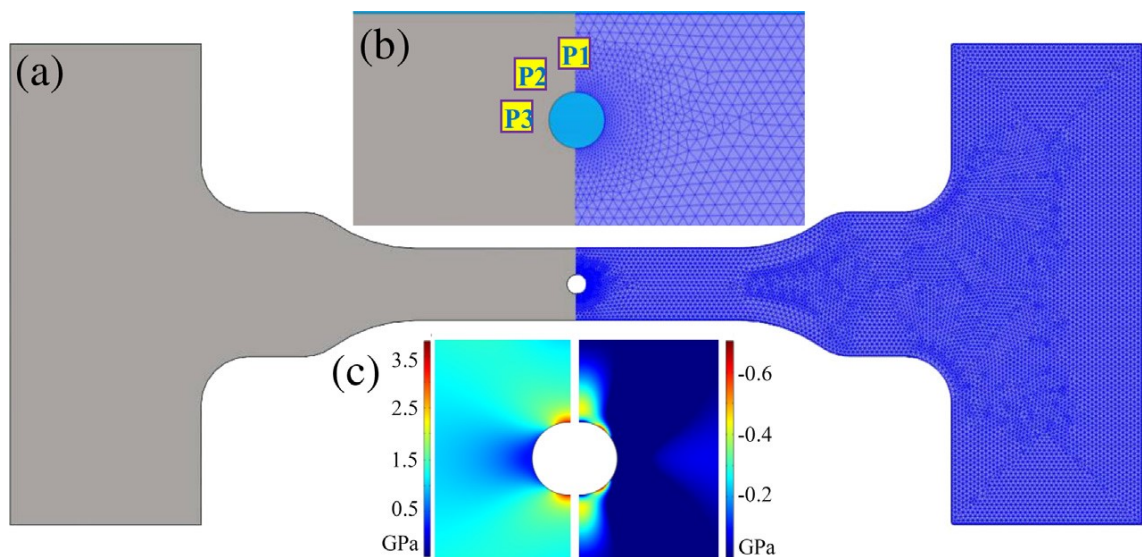


Figure 4.38 (a) A $Zr_{41.2}Ti_{13.8}Cu_{12.5}Ni_{10}Be_{22.5}$ (Vit-1) sample with the right half showing the 2D triangular meshes used in the finite element strain/stress analysis, (b) an enlarged view of the region with hole and the three locations, P1, P2, and P3, where diffraction patterns were acquired; and (c) the simulated tensile stress tensor (left half) and compressive stress tensor (right half) around the hole under an applied average stress of 647 MPa, (d) the relationships of the applied stresses as functions of the local strains in the tensile and compressive for the Vit-1 sample. The calculated local strains using finite element method are also superimposed for comparison [12].

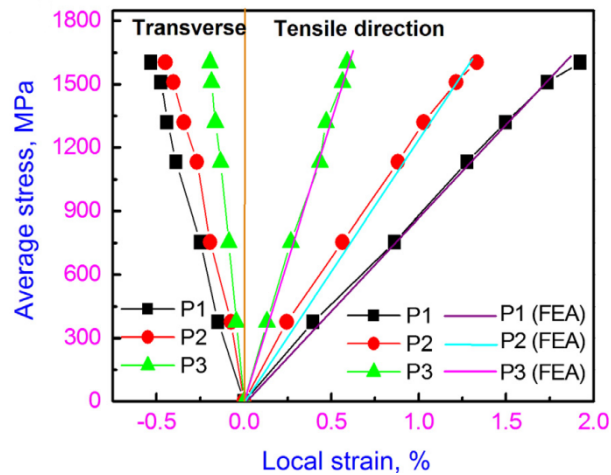


Figure 4.39 The relationships of the applied stresses as functions of the local strains in the tensile and compressive for the Vit-1 sample. The calculated local strains using finite element method are also superimposed for comparison [12].

In addition, the results show that the propagation of shear bands is strongly dependent on the nature of the stress field ahead, and all evidences obtained in this study indicates to that a compressive stress field of > -0.5 GPa can hold or slow down the propagation of shear bands. Figure 4.40 shows the Vit-1 hole sample SEM images and the simulate stress fields (the tensile stress tensor, σ_{xx} and compressive stress tensor, σ_{yy}) at different stress levels. The corresponding shear bands images obtained at those areas and the contour lines of the compressive stress tensor were superimposed onto the colour stress maps for comparison. Figure 4.40q shows that the tips of the shear bands first entered a region with a compressive stress of ~ -0.5 GPa and in the next few load steps (Figure 4.40q to Figure 4.40t), the area of the region that has a compressive stress of ~ -0.5 GPa increase as the average stress increased. However, it seemed that the existing shear bands were confined within the ~ -0.5 GPa compressive stress region and cannot grow outside the region, propagated very fast and overtook all the previous shear bands and developed into visible cracks as clearly show in Figure 4.40m - Figure 4.40o and Figure 4.40r - Figure 4.40t.

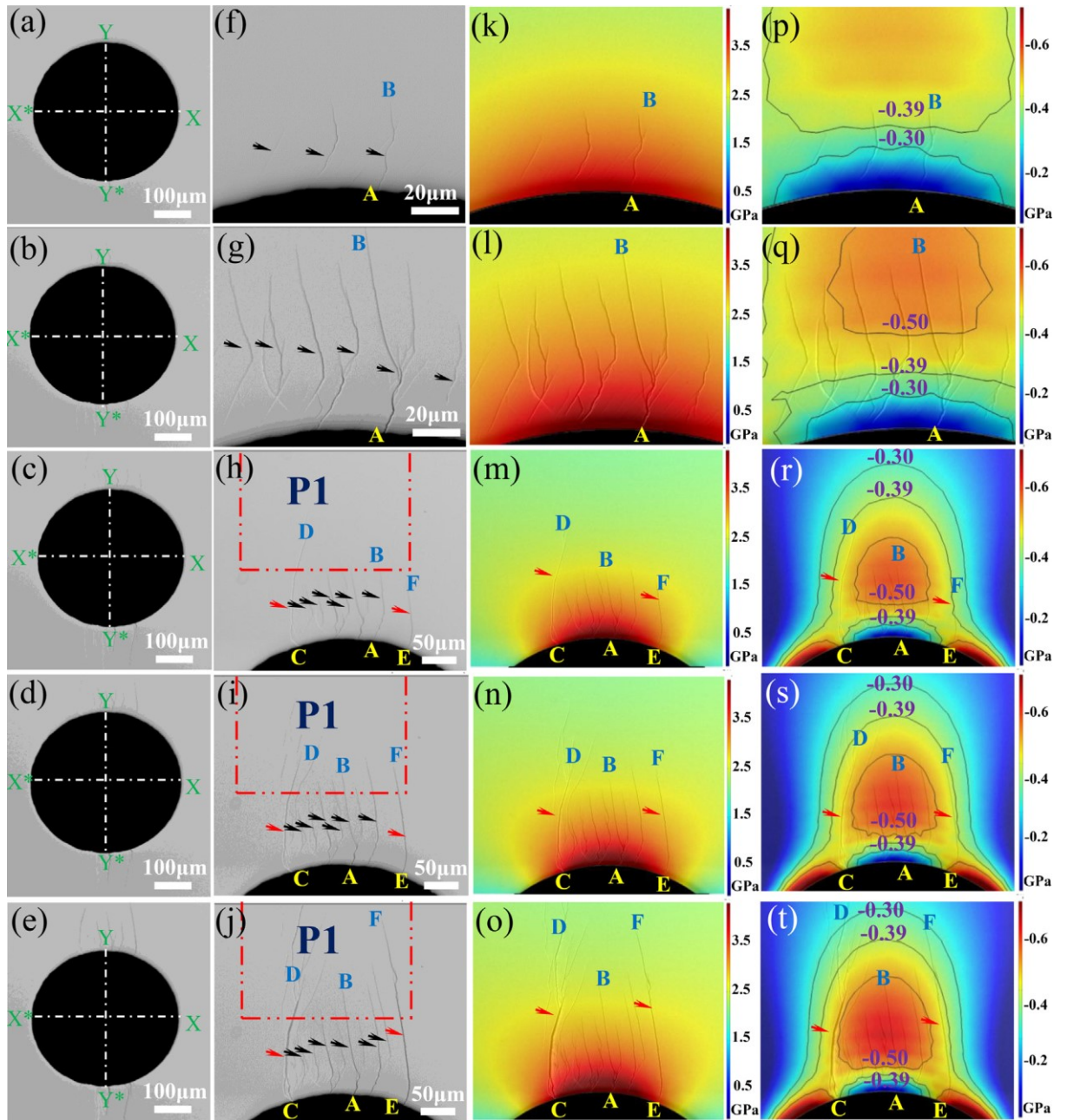


Figure 4.40 A series of SEM images of Vit-1 sample taken at the applied average stresses of (a) 755 MPa, (b) 1132 MPa, (c) 1321 MPa, (d) 1509 MPa and (e) 1604 MPa. (f) - (j) are the higher magnification of images (a) - (e) at the upper edge of the hole respectively, highlighting the shear bands at the areas above point Y. (k) - (o) and (p) - (t) are the simulated tensile stress tensor, σ_{xx} and compressive stress tensor, σ_{yy} for the areas show in (f) - (j) respectively. The red dash lines in (h) - (j) indicate the lower boundary of location P1. In order to clearly link the shear band formation of the stress distribution, the shear bands are also superimposed in figure (k) - (t) [12].

4.8.2 Shear band propagation in BMGs

Figure 4.6 shows the SEM images at different critical stresses for the Vit-1 \emptyset 0.25 mm semi-circular notch. The sequence SEM images show the shear bands initiation and propagation and the axial stress field shows the local stress.

At 1263 MPa, Figure 4.6 b2 shows the shear bands were found under the crack. The formation of the shear band is due to localised plasticity deformation [141]. The superimposed axial stress field in Figure 4.6 b3 shows that high stress concentration the crack tip with the primary shear bands fall within the 3.1 GPa stress field, and the secondary shear bands were found within the 2.5 GPa axial stress field, with the right side growing longer. This suggests that the shear bands initiation might be due to the local stress at the crack tip was beyond the elastic limit of Vit-1. However, away from the crack, the tensile stress was lower. The differences in stress level results in the shear band only initiated and propagated from the direction of the stress gradient.

In Figure 4.6 b2, it shows that the primary shear bands (black arrows) were growing outwards at around the crack without any particular angle, whereas secondary shear bands (red arrows) were found growing only vertically. The formation of a single secondary shear band was also captured during the in situ test as shows in Figure 4.6 c2 at 1343 MPa. The formation of the secondary shear band is the result of further increase in plasticity in the area due to the continuous increasing in stress after the primary shear bands formed [223] which again is because of the stress concentrator. Figure 4.6 c3 shows the formation of a single secondary shear band (black arrow) which is within the 2.3 GPa axial stress field, suggesting that the formation of secondary shear bands does not require as high stress as the primary shear bands.

Figure 4.6 d3 shows that the increase in tensile stress causes the shear bands to propagate into P2 at 1676MPa. It clearly shows that the shear bands are within the 2.1 GPa stress field, much lower than the earlier images. At 1829 MPa, Figure 4.6 e3 shows the shear bands have propagated up to half of the P2 area. The axial stress contour plot shows

that most of the shear bands are within 2.1 GPa stress field, except one shear band propagate to 1.85 GPa. Finally, at 1952 MPa and 1991 MPa, Figure 4.6 f3 and Figure 4.6 h3 show that the shear bands enter P5 area. This is the last two stress levels captured before the sample fractured during the in situ test. As show in the axial stress contour plots, almost half of the total shear bands form outside the 2.1 GPa stress field until ~ 1.7 GPa. The in situ test shows that, once the shear bands achieved 1/3 of the sample width, it will propagate in a lower axial stress field. By combining the FEM modelling and the in situ observation using the SEM, it enables us to relate the influence of the axial and transverse stress field to shear bands formation.

The formation of "step"

Figure 4.6 f2 and Figure 4.6 g2 show the formation of "step" on top of the shear band was observed during the in situ tensile test inside SEM. Similar phenomena were reported by Zhao , who proposed that these steps will eventually form cracks [224]. However, to understand this phenomenon, it requires real time observation. In the past, several attempts have been made to try and capture the in situ shear bands propagation using TEM [193], SEM [9, 225] and high-speed camera [226]. However, real time capture this phenomenon is not widely reported.

Figure 4.7 shows a series of SEM images captured at the "step" formation location from the average tensile stress of 1703 MPa to 1992 MPa, each captured with a small tensile stress step increase (20 – 90 MPa). The image clearly shows that it begins with a single shear band (1703 MPa), followed by a second shear band that formed $\sim 5 \mu\text{m}$ away from first shear band (1810 MPa) and crossly joined at 1829 MPa. It clearly shows that the shear band behave differently compared to the reported continuous growing single shear bands [227]. Next, a "step" was formed at 1871 MPa. It is believed that this "step" area was highly stress concentrated, with the evident from several shear bands observed around it (as pointed by the red arrows). This step eventually formed another bigger step as shows in the SEM image taken at 1992 MPa.

Shear induced dilatation

Figure 4.41 shows the sample surface SEM images of Ti40 \varnothing 0.25 mm semi-circular notch samples during in situ tensile tests and the related statistical information of shear bands. When increasing the applied stress, the existing shear bands propagate and widen, and new shear bands form continuously, as show in Figure 4.41b Figure 4.41c. To clearly show the shear band nucleation and propagation, the shear band marked AB in Figure 4.41b and Figure 4.41c is selected as an example. Figure 4.41d presents the increase in the length of shear band AB upon loading. After the shear band nucleates at 687MPa, its length increases dramatically upon further loading. When the applied stress reaches 916MPa, shear band AB, together with other shear bands, propagates into location P1, as highlighted by a square in Figure 4.41c. The shear band density (defined as the total line length of shear bands visible divided by the area of location P1) as a function of the applied stress is also presented in Figure 4.41d. Clearly, at applied stress larger than 916MPa, the shear band density in P1 suddenly increases until fracture. Combining Figure 4.41c and Figure 4.41d with Figure 4.41c, it can be seen that once the shear band has propagated into location P1, the local atomic-pair strains increase suddenly, indicating that there exists a strong correlation between sudden increase in the local atomic-pair strain and the shear band formation. Thus the generation of multiple shear bands in location P1 (Figure 4.41c), which can be measureable increase in the strain values, can be directly linked with the higher micro-level strains in P1, calculated from I(Q) peak shifts and atomic-level strains calculated from the PDF technique.

Shear band formation is recognized to be a result of deformation-induced strain softening [228], which is directly related to the atomic-scale flow processes generating structural disorder associated with shear transformation zone (STZ) evolution during shear deformation. Such structural change is prominently attributed to shear induced dilatation of randomly close-packed atoms in BMGs [229]. The dilatation or increase in excess free volume, associated with the formation of STZs, dramatically increases the distribution of bond lengths. In this case, the atomic pair rapidly extends along the loading direction when the shear bands form. Therefore, shear-induced dilatation of the randomly close-packed atomic configuration resulting from the shear band formation contributes to the

sudden increase in the atomic-pair strains for P1 in the notch sample, as shows in Figure 4.42a whereas no observation on the non-notch sample (Figure 4.42b). The results in this study obtained from in situ SEM and SXRD provide direct experimental evidence linking the local atomic rearrangement and the shear band formation.

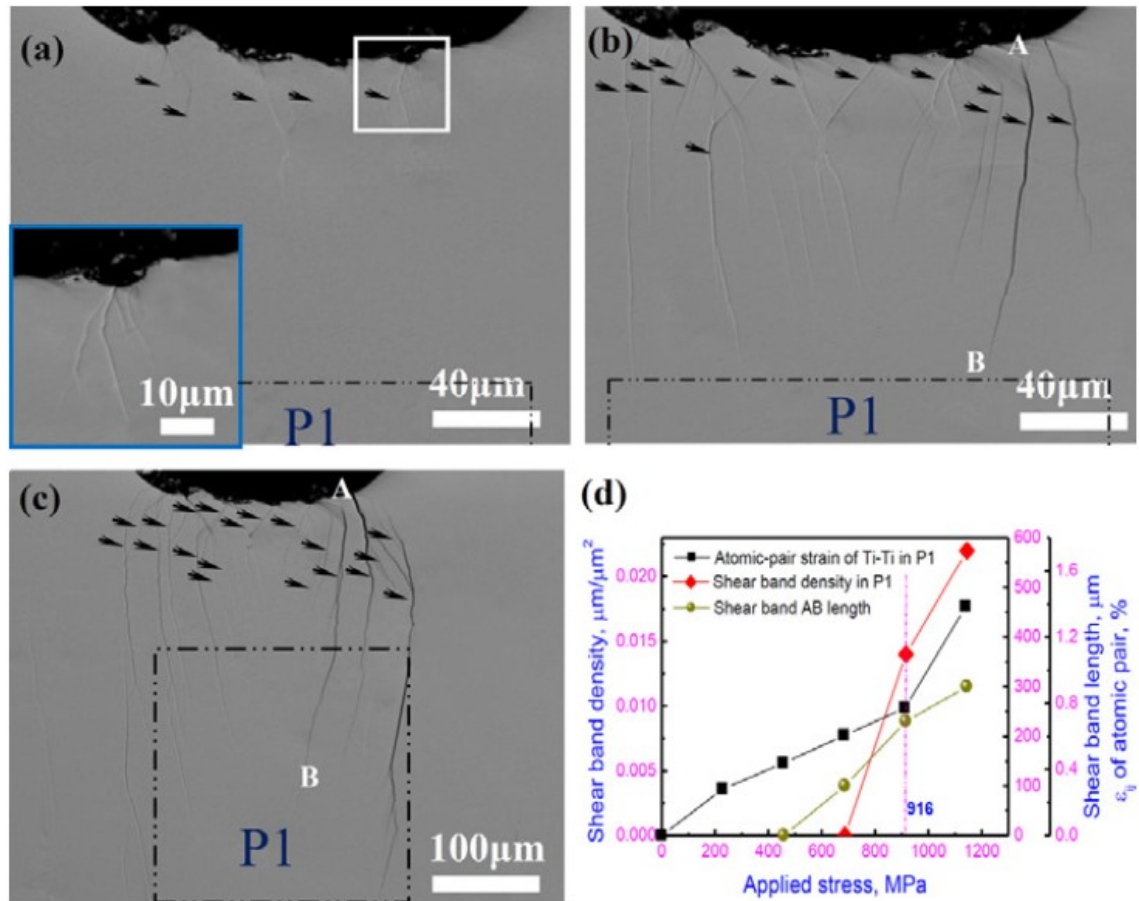


Figure 4.41 The sample surface SEM images of notched sample under (a) 458 MPa, with an inset highlighting the shear band nucleating in the rectangular area, (b) 687 MPa and (c) 916 MPa applied stress (the dash lines show the upper boundary of location P1); and (d) the shear band density in location P1 and the shear band AB length as a function of applied stress. For comparison, the atomic pair strain of Ti-Ti in P1 calculated from the SXRD pattern is also presented in (d) [12].

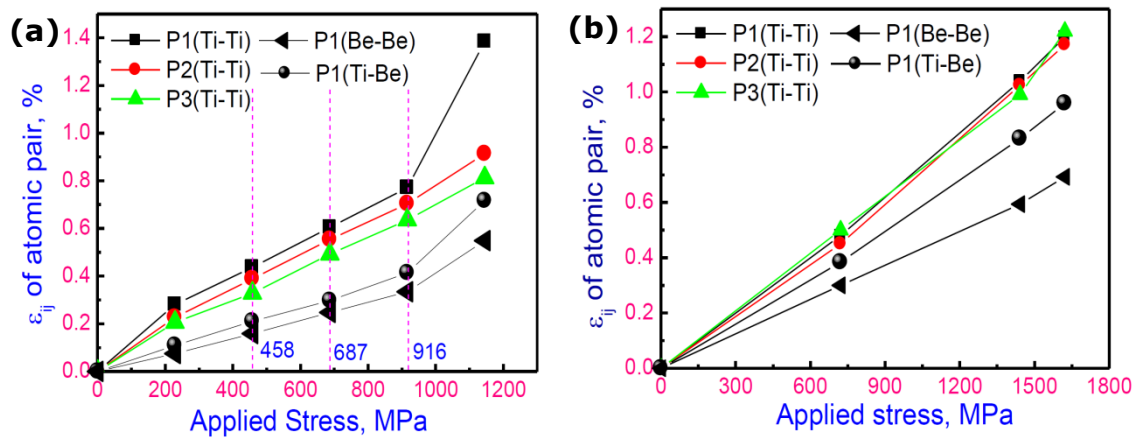


Figure 4.42 The strains of Ti-Ti, Ti-Be and Be-Be atomic pairs for P1, P2 and P3 in the samples (a) with and (b) without notch as a function of the applied stress [12].

4.8.3 Shear band propagation in ZrTi BMGMC

The tensile deformation of a ZrTi BMGMC were studied in-situ using SXRD and SEM. A generic procedure [13] is developed to separate the diffraction information of the crystalline dendrites away from that of the matrix. Using this method, the stresses at which the dendrites and the glassy matrix start to deform plastically are quantitatively determined and are confirmed by the in situ SEM observations of the shear band formation at those stress levels.

Figure 4.23c shows the average tensile stress versus the tensile strain of the sample. The tensile strain increases linearly with the increasing tensile stress until the yielding point at 2.07% tensile strain and 1714 MPa tensile stress. Above the yielding point, in the plastic deformation region, the tensile stress appeared to be without much increment with tensile strain. Eventually the sample fractured at the tensile strain of 5.06% with the tensile stress at 1817 MPa, exhibiting 2.99% plastic deformation.

Figure 4.24 shows the SEM images captured during the in situ tensile tests. The images show that the shear bands initiated and propagated in the crystalline dendrites and amorphous matrix. Before load was applied onto the sample, Figure 4.24 a1 shows that there is a crack right at the end of the notch (as pointed by the black arrow) which was formed during EDM. Initially, the crack was closed and begins to expand when tensile stress was applied. It was showed in Figure 4.24 b2, at 1492 MPa where the crack expanded, and at the crack tip, there is high number of shear bands formed

in a wave like patterns (greyish area) in the area 30° clockwise to the axial direction. It is unlike the shear band formed on the Vit-1, to spread along the crack tip. The image also shows that the shear bands are present in both matrix and dendrites. It is difficult to determine whether the shear bands first formed in the matrix or dendrites. However, away from the crack tip, shear bands were showed firstly found in the dendrites (black arrows) as shows in Figure 4.24 b4. It is because the dendrites are relatively soft as compared to the amorphous matrix plastic deformation occurs firstly on dendrite. Figure 4.32 shows the axial and transverse strains of the crystalline dendrites. At 1626 MPa, it shows on the curves that stresses for location P2 and P3 moved away from its linear relationship. Suggesting that less stress was taken by the two locations because of yielding occur in the crystalline dendrites. Similarly to the phenomena reported by Balch, *et al* [152] regarding the load transfer into the amorphous matrix, once yielding occur in the crystalline particle in the composite. Further evidence was showed in Figure 4.31. It clearly shows that there is a slightly increase in the strain rate in P3 and P6 (beneath P3) once the strain reduce in P2 and P3.

At 1663 MPa, Figure 4.24 c4 shows that shear bands were found in the matrix (white arrows) which suggested the tensile stress in the matrix is above its yielding strength. From the FEM modelling axial stress field show in Figure 4.24 c4, the shear bands in matrix are within the >1.9GPa. This indicates that, the shear bands initiation in the matrix required the local stress of >1.9 GPa.

With further increase in the tensile stress at 1786 MPa, the density of the shear bands in the matrix was increased as shows in Figure 4.24d4. It is unlike the Vit-1 case where the shear bands can propagate through the matrix. It is because of the additional dendrites and the interface [8]. This strong interface is able to effectively deflect or arrest the fast propagation of the shear bands, causing more shear bands to nucleate (white arrow) and changing the propagation orientation across the interface (yellow arrow). The shear band is the local plastic deformation of the material, therefore the increase in the shear band density resulting in increasing in overall plasticity. This phenomenon was reflected on the overall tensile stress-strain curve in Figure 4.23b. However, as shows in graph above 1714MPa. Figure 4.24 d4 shows more shear bands in the matrix at the local

stress of $>2\text{GPa}$. This is because the dendrites prevent the shear bands to propagate and cause high stress required to form more shear bands.

Finally, at 1847 MPa, 5.3%, Figure 4.25a shows the fractured sample. The SEM image shows the sample fracture along the propagated crack as shows in Figure 4.24 e1. Unlike the Vit-1 sample, the ZrTi is more controllable near the fracture point and allow us to observe the crack propagation. In the plastic deformation region, the dendrites undergo heavy distortion which agree with Qiao argument in that, the dendrites is acting as a barrier to the shear band propagation between the matrix, forcing more shear bands nucleates in the matrix, hence enhanced overall plasticity [230].

Similar observation also reported for another ZrTi BMGMC notch sample in the Applied Physical Letter. In this composite, the crystalline dendrites are relatively soft and ductile as confirmed by the nano-indentation. This soft nature allows the dendrites to deform plastically and causes dislocation first at 1500 MPa (Figure 4.43 b), and most nucleated shear bands were confined within the domains having a spatial scale of the order of the dendrite axe length. The strong interface dendrite and matrix is again shows able to effectively deflect or arrest the fast propagation of shear bands, as show in Figure 4.43 c inset where the shear bands change the propagation orientation across the interface. Hence, more energy (stress) is needed for the shear bands to propagate in a highly zig-zag manner as shows in Figure 4.43 d, resulting in the enhanced plasticity and strength of the composite. However, at the later stage of plastic deformation, when many nearly parallel shear bands form and pass through the dendrite network collectively, the interfaces cannot deflect the collective movement of the shear band clusters, work softening occurs and the sample fails as the shear bands quickly propagate through the sample.

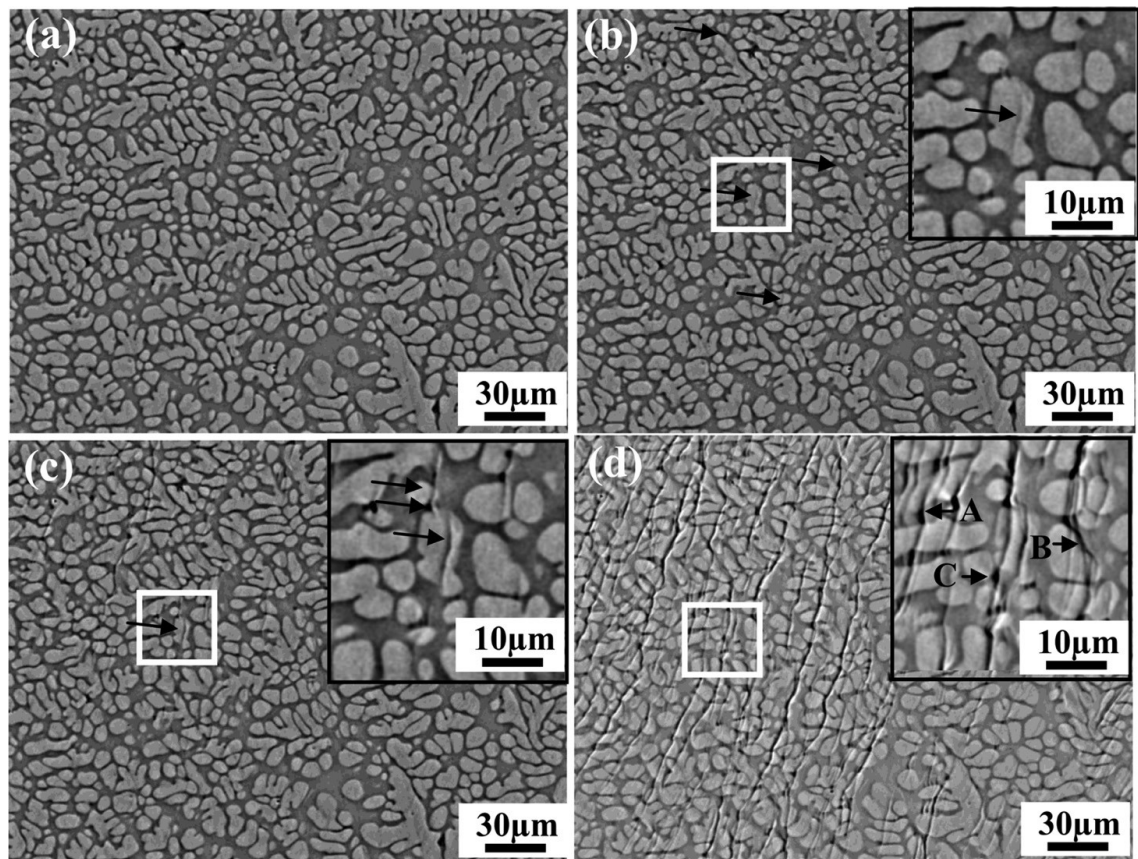


Figure 4.43 The backscattered scanning electron images, showing the microstructure, the shear band nucleation and propagation at the location where the diffraction patterns are acquired at different stress levels of: (a) 588 MPa, (b) 1500 MPa, (c) 1680MPa and (d) 1782MPa. For (b), (c), and (d), the insets show the enlarged images of the rectangular areas [13].

4.9 Summary

This chapter describes the in situ tensile test results for the Vit-1 monolithic BMG and ZrTi composite in Chapter 4, and the key findings in the 3 journals publication. The load step and displacement step control of the in situ experiments allowed us to duplicate the similar stress condition for the in situ SEM and in situ SXR experiment to investigate the shear bands initiation and propagation within the two alloys. The in situ results provide new insight on the formation of the “step” that lead to crack and the load transferred into the amorphous matrix when yielding occur in the crystalline dendrites.

Chapter 5 High pressure compression of metallic glass and anomalous X-ray scattering

This chapter describes in details the high pressure compression experiments of a binary alloy ($\text{Cu}_{50}\text{Zr}_{50}$) and a ternary alloy ($\text{Fe}_{60}\text{Nb}_{15}\text{B}_{20}$) metallic glass ribbons using Diamond Anvil Cell (DAC). Synchrotron X-ray was used to acquire diffraction patterns in situ at different pressure steps and pair distribution function was used to study the evolution of atomic structures at different pressures. The relevant proposals and awarded beam times at beamline I15 of Diamond Light Source (DLS) are detailed in Table 1.1. In addition, anomalous X-ray scattering experiments were also carried out at beamline I11 of DLS to decouple the convoluted diffraction information for the $\text{Cu}_{50}\text{Zr}_{50}$ and $\text{Fe}_{60}\text{Nb}_{15}\text{B}_{20}$ alloys at ambient pressure to facilitate the analyses of partial pair distribution functions for the two alloys.

5.1 High pressure compression experiments

5.1.1 Diamond Anvil cell and sample loading

DAC is a type of the so called opposed anvil pressure devices [231] and the most commonly used device to create very high pressures. Figure 5.1 shows a schematic illustration of using DAC to do high pressure in situ synchrotron X-ray diffraction experiments. The diamond anvil has a table face where an external force is applied and a very tiny culet face where the force is transmitted onto the sample. High pressure is created at the culet face because of the huge difference in area between the table face and the culet face. Any sample positioned and trapped between the two tiny culet faces of two oppositely arranged diamond anvils is therefore subject to the high pressure [231]. To create a quasi-hydrostatic pressure between two culet faces, more complicated arrangement is needed and the one used in the experiments of this research is showed schematically in Fig. 5.2a, and it is a membrane driven DAC (Betsa type) [232]. The key components consist of a Rhenium (Re) gasket, two diamond anvils and two Tungsten carbide backing plates. The gasket is made of a 250 μm thin sheet of Re with a small hole in the middle (see the photo in Figure 5.1) as the sample chamber to hold a sample and any liquid confining medium surround the sample. The gasket also contains the very steep pressure gradient generated by the

diamond anvils, allowing more homogeneous pressure be acted onto the sample. This gasket arrangement plus a liquid confining medium surround the sample allows a quasi-hydrostatic pressure within the sample chamber to be realised [233, 234]. The two diamond anvils are held by the two Tungsten backing plates which in turn held by a cell body [232].

Loading a sample of a few tens of micrometres into the DAC sample chamber is a relative complicated procedure, and a very steady operation performed under a binocular stereomicroscope is often needed. Trained and guided by the beamline scientist, Dr Dominik Daisenberger, the following procedure was used to prepare and load the samples into the DAC.

1. The culet faces of both diamond anvils (showed in Figure 5.2b and seated on two tungsten carbide backing plates) was carefully cleaned using a cotton swap with acetone under a Leica Z6 Apo stereomicroscope with Mitutoyo objective to remove any remaining samples and/or dust from previous experiments.
2. A Re metal sheet of 250 μm thick was placed on top of the culet face of a diamond anvil and then pressed to create an indentation mark. Figure 5.2c shows such an arrangement before making the indentation mark.
3. The Re sheet was drilled a 150 μm diameter hole in the centre of the indentation mark using electrical discharge machining (a Betsa spark eroder). It was then placed back to the original position on the culet face to form the sample chamber.
4. Metallic glass ribbon sample was cut into ~ 50 μm piece using a tungsten carbide tweezers and placed into the sample chamber using a fine needle via the electrostatic force.

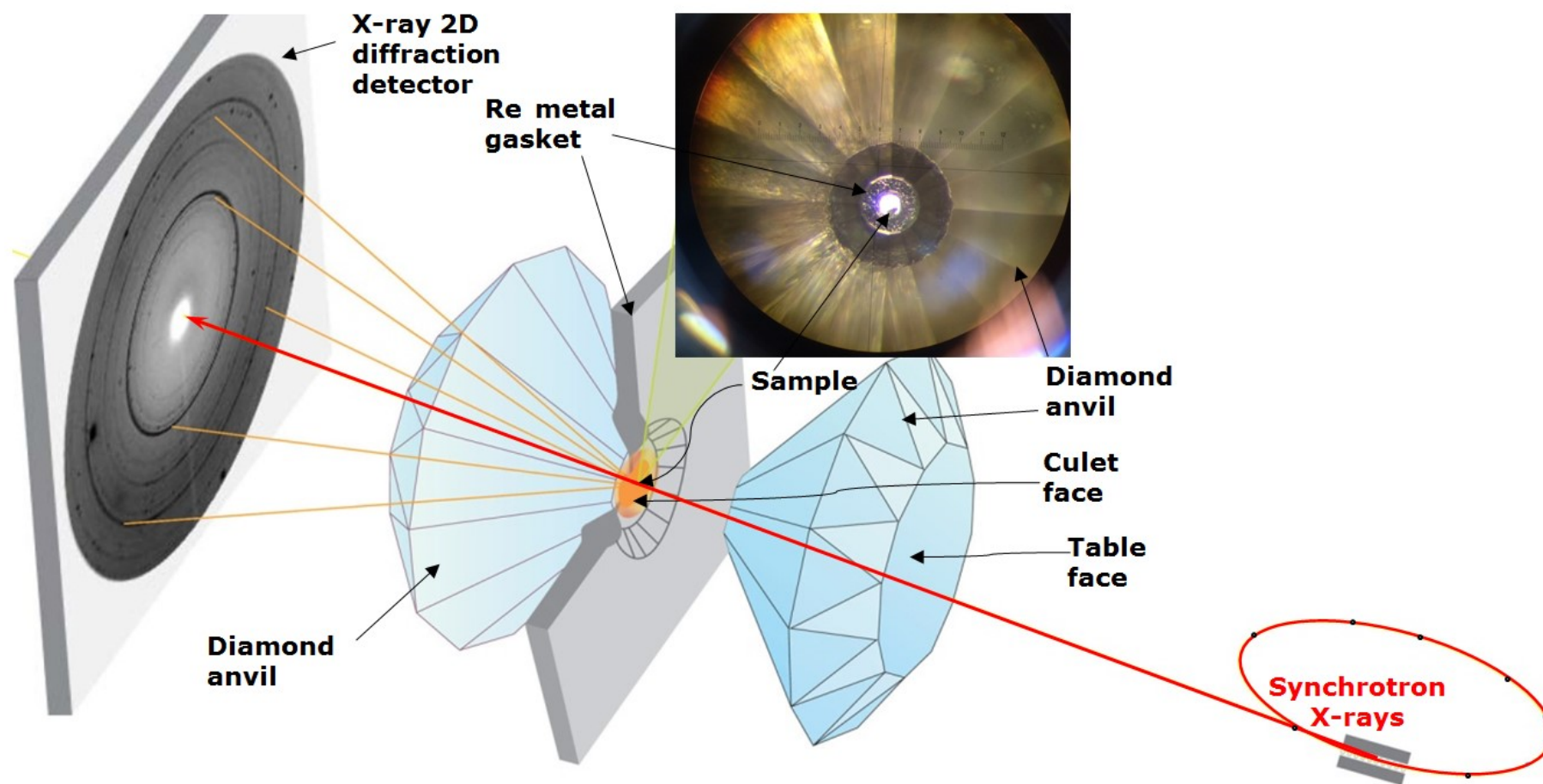


Figure 5.1 A schematic illustration, showing two diamond anvils, a metal gasket and a sample illuminated under Synchrotron X-ray beam. The inserted photo shows the diamond anvil and its culet face with the Re gasket and metallic glass ribbon sample (inside the hole of the gasket) used in this research. The photo was taken using a binocular stereomicroscope during sample loading at beamline I15 of Diamond Light Source.

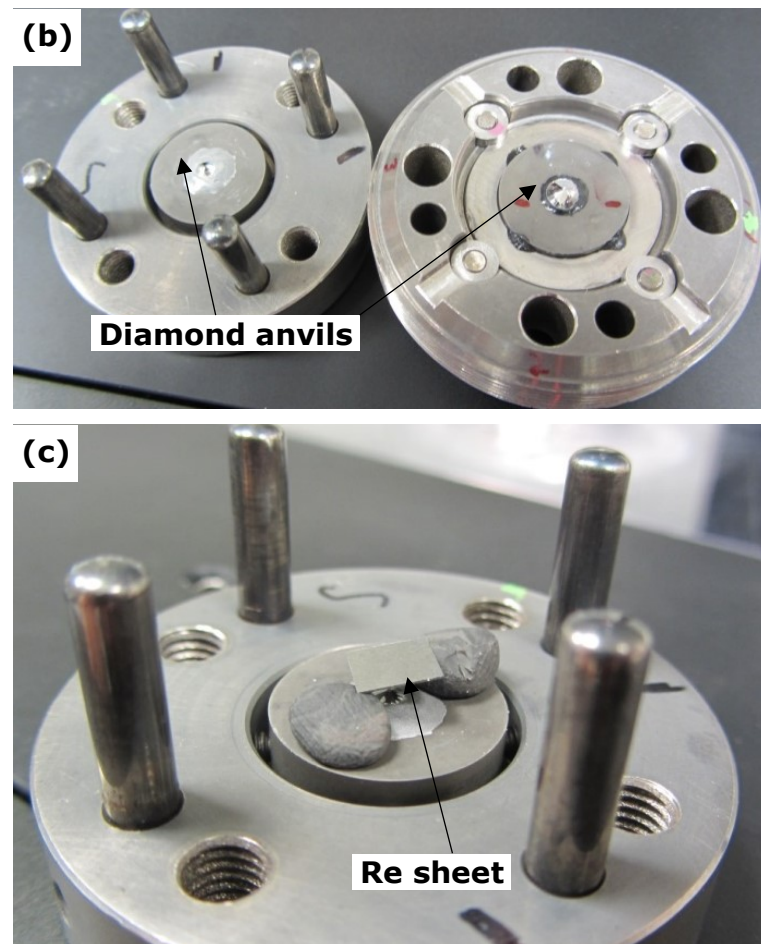
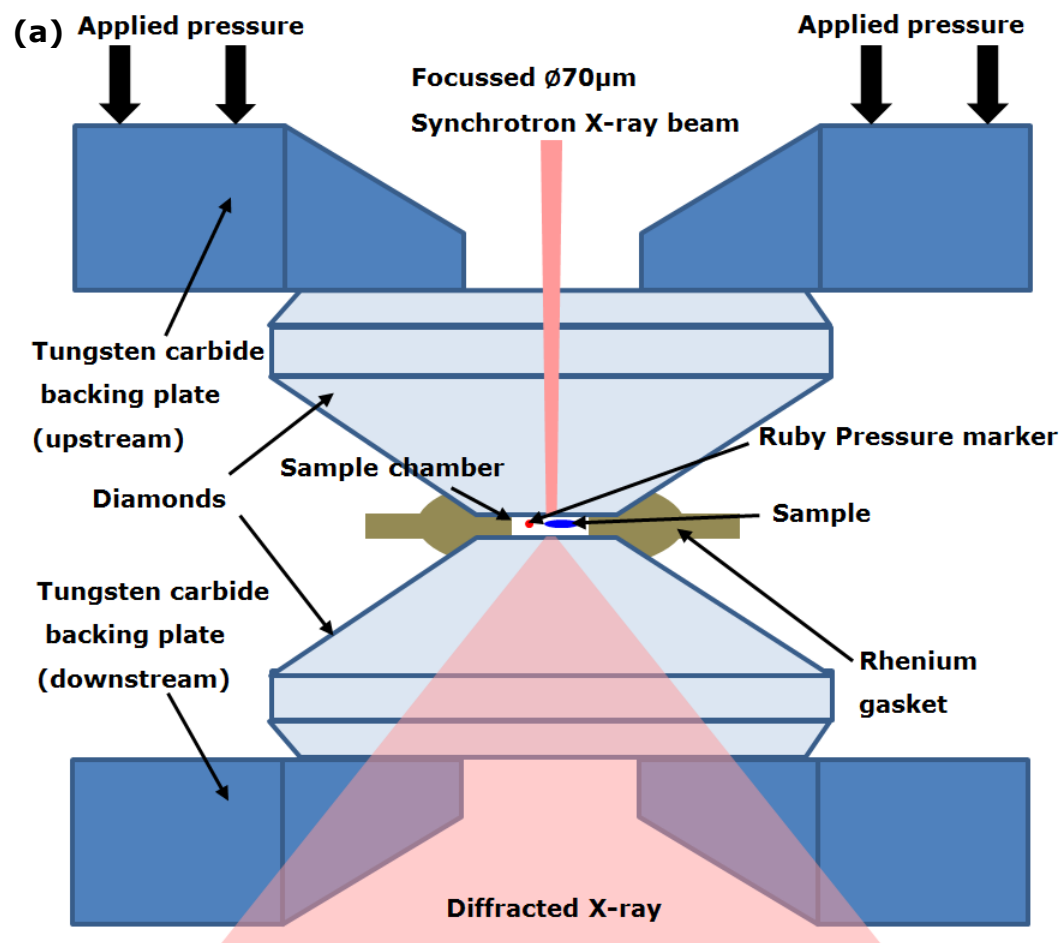


Figure 5.2 DAC (a) schematic diagram of the DAC (b) photo of the DAC showing the position of the DAC in the in situ SXR D experiment.

5. The sample was positioned intentionally offset from the centre of the sample chamber (Figure 5.5) to create a sufficient empty area for collecting the background diffraction pattern during the experiments.

6. A ruby sphere (as pressure calibrant) of $\sim 10\ \mu\text{m}$ in diameter was placed closely to the sample (Figure 5.5) for measuring the pressure in the sample chamber during the experiments.

7. Finally, the sample chamber was filled with methanol-ethanol (4:1) solution before carefully closing the cell body. The liquid solution is used as the confining medium to homogenise the pressure within the sample chamber, realising a quasi-hydrostatic compression environment inside the sample chamber.

A membrane is placed at the end of the upstream backing plate as shows in Figure 5.3.

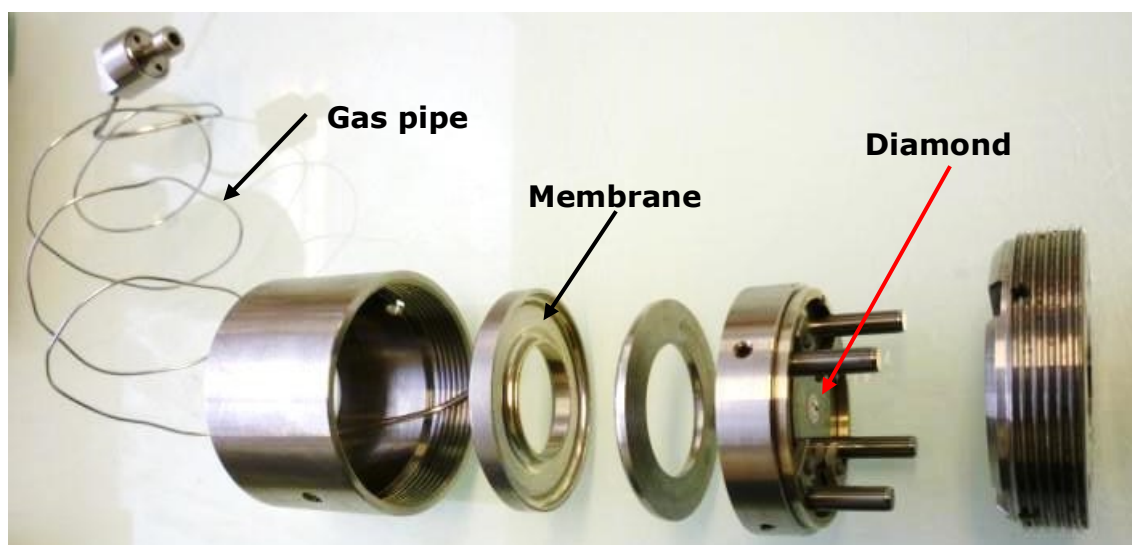


Figure 5.3 Membrane Diamond Anvil Cell [235].

The DAC was mounted onto a standard V-block and then together onto the sample stage of beamline 15 of DLS as typically showed by the three photos in Figure 5.4. The superhead equipped with a 20x objective lens was used to view the sample chamber and take optical images during experiments. Figure 5.5 are two optical images of the sample chambers taken using the spearhead, showing the $\text{Cu}_{50}\text{Zr}_{50}$ and $\text{Fe}_{60}\text{Nb}_{15}\text{B}_{25}$ samples together with the ruby spheres inside the sample chamber formed by the Re gasket.

5.1.2 Alignment of X-ray beam with DAC and samples

The alignment of X-ray beam with samples is very critical for the acquisitions of diffraction patterns either from the samples or from the background (see Figure 5.5). A retractable X-ray photodiode (Figure 5.4a) that can detect the X-ray intensity was used to find the centre of the sample chamber and the sample itself inside the chamber. The procedure is as below.

1. Firstly, the DAC was rotated to face the objective lens as showed in Figure 5.4a, and an optical image of the DAC sample chamber was projected onto the monitor screen. Then the centre of the sample chamber was moved to coincide with the predefined reference centre of the screen by moving the sample stage. An image (such as those showed in Figure 5.5) was taken to record the location of the sample chamber centre, and the location of the sample relative to the sample chamber centre.
2. Secondly, the sample stage was rotated to allow the DAC to face the X-ray beam (Figure 5.4b). Then, the X-ray photodiode was moved out and onto the X-ray path to measure the intensity of the X-ray passing through the DAC in order to align the X-ray beam with the sample chamber centre.
3. To find the sample chamber centre in the horizontal direction, the DAC was first moved in the horizontal axis with a step of 0.02 mm, while the transmitted X-ray through the DAC was recorded by the photodiode as typically showed in first scan in Figure 5.6a. Because of the sample chamber is off centre (insert figure in Figure 5.6a), the first scan only show a broad peak profile. Using the Gaussian fitting to find the peak position, the new sample chamber centre was set accordingly to the peak position.
4. Step 3 was repeated to find the vertical sample chamber centre by moving the DAC vertically. Figure 5.6b shows readout from the photodiode. The first scan of the vertical sample chamber shows the scan profile which containing 2 flat plateaus which are different from the

broad peak profile in the first scan for the horizontal sample chamber. It is because after the horizontal sample chamber centre was found in step 3. The highest intensity plateau is the sample chamber followed by a steep reduction in intensity which is the edge of the sample chamber and Re gasket. The 2nd plateau is the Re gasket which is sandwiched between the two diamond culets and the second steep reduction in intensity is the Re gasket outside the diamond culet. Again, using the Gaussian fitting, the peak position was found and was used as the vertical sample chamber position.

5. A second scan was carried out similar to step 3 and 4 first for the horizontal sample chamber followed by vertical sample chamber with a step size of 0.01mm. This operation is to refine the sample chamber position with a smaller step scan. Once both centre positions were found, the sample stage position was recorded.
6. Once the centre position was decided, the sample stage position was recorded. Using the image taken earlier by the telescope (Figure 5.5) the sample and background position were also found and recorded offsetting the centre positions.
7. Finally the photo diode was retracted to its original position.

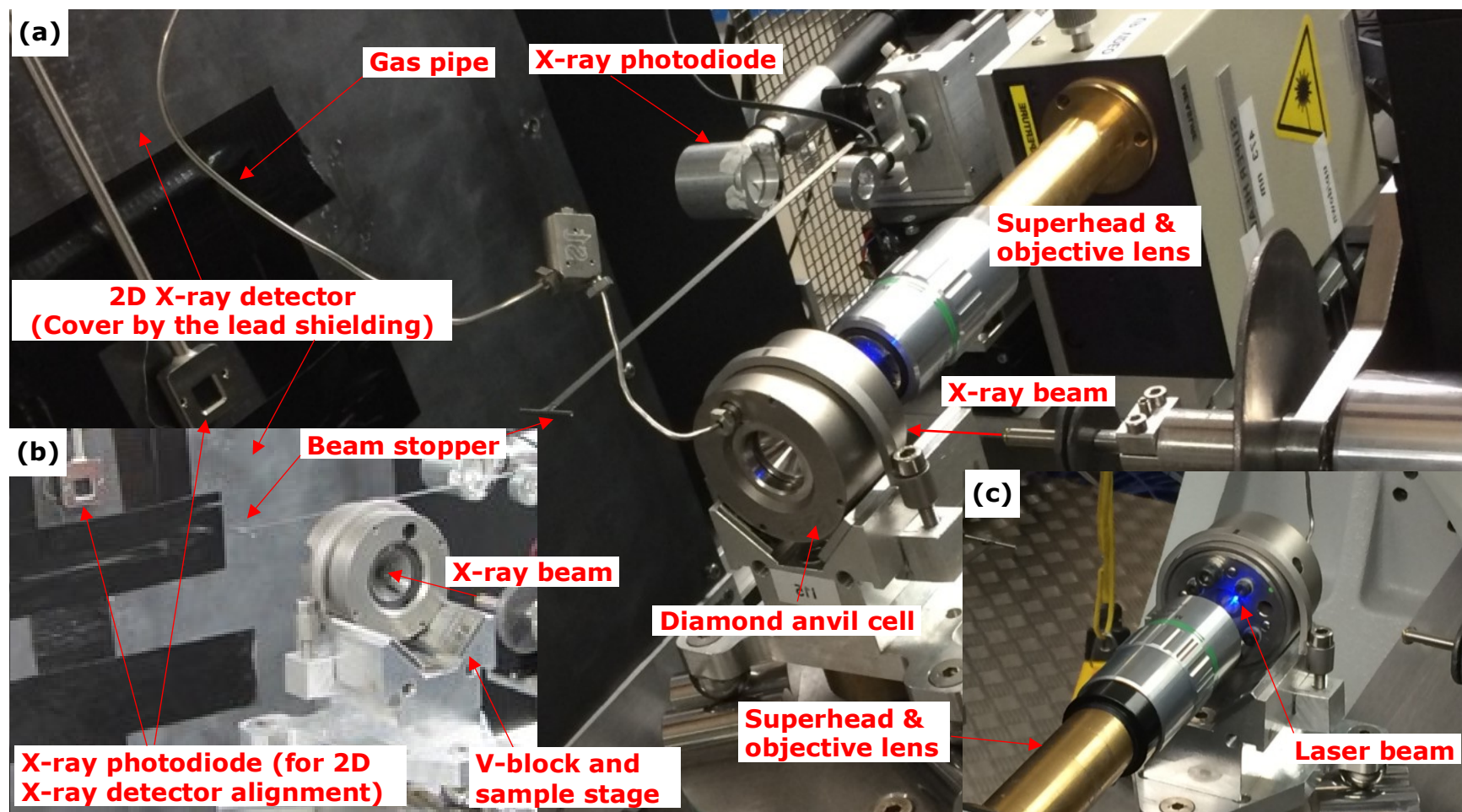


Figure 5.4 The setup of high pressure experiments at I15 of DLS. (a) A top view of the DAC on the sample stage with the superhead and objective lens facing the DAC and using blue laser to measure the pressure. (b) An insert photo, showing the DAC facing the X-ray beam for diffraction measurement. (c) A close-up of the DAC facing the objective lens and the laser beam.

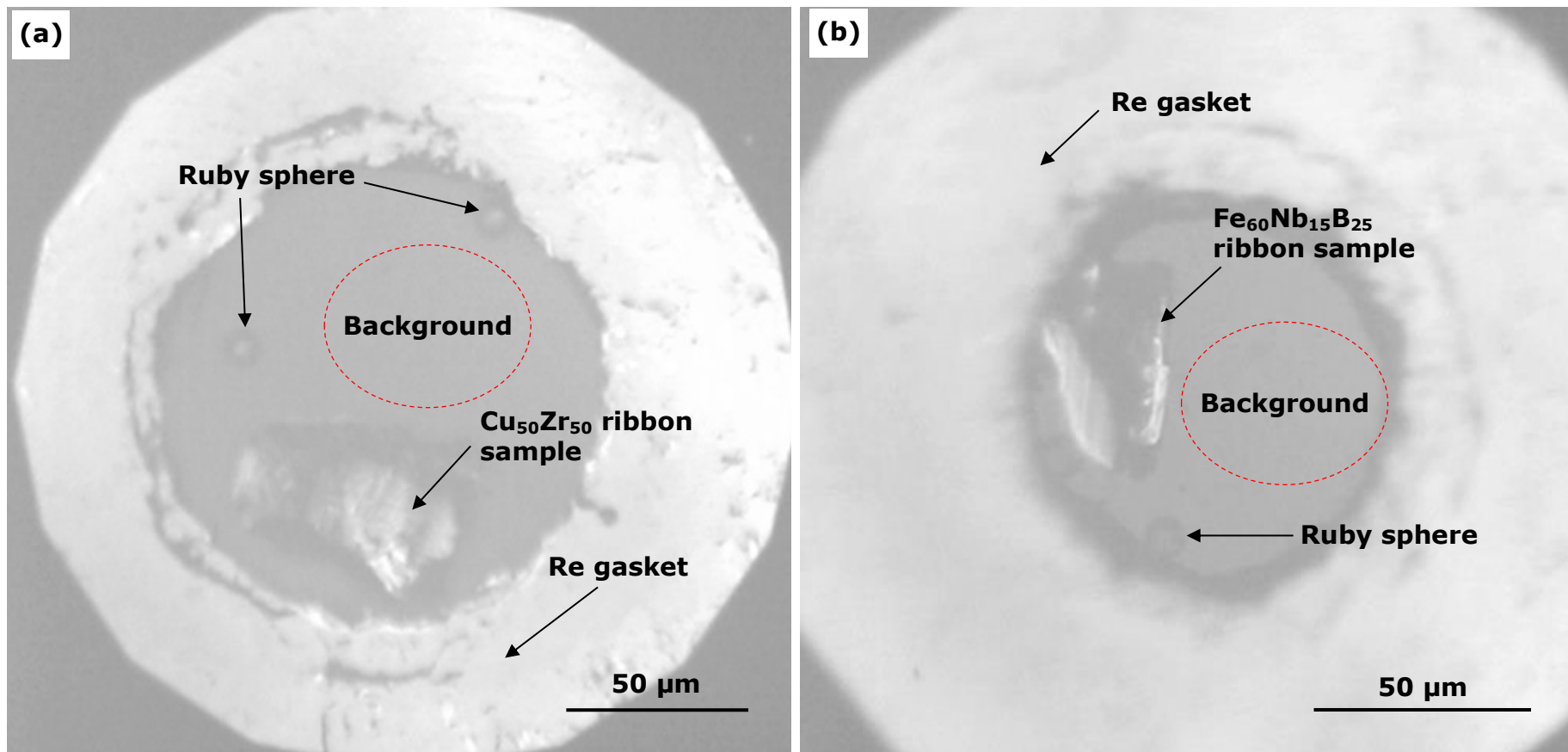


Figure 5.5 Two optical microscopy images, showing (a) the Cu₅₀Zr₅₀ and (b) Fe₆₀Nb₁₅B₂₅ samples, each together with the ruby spheres (as pressure calibrants) inside the sample chamber formed by the Rhenium gasket and the diamond anvils.

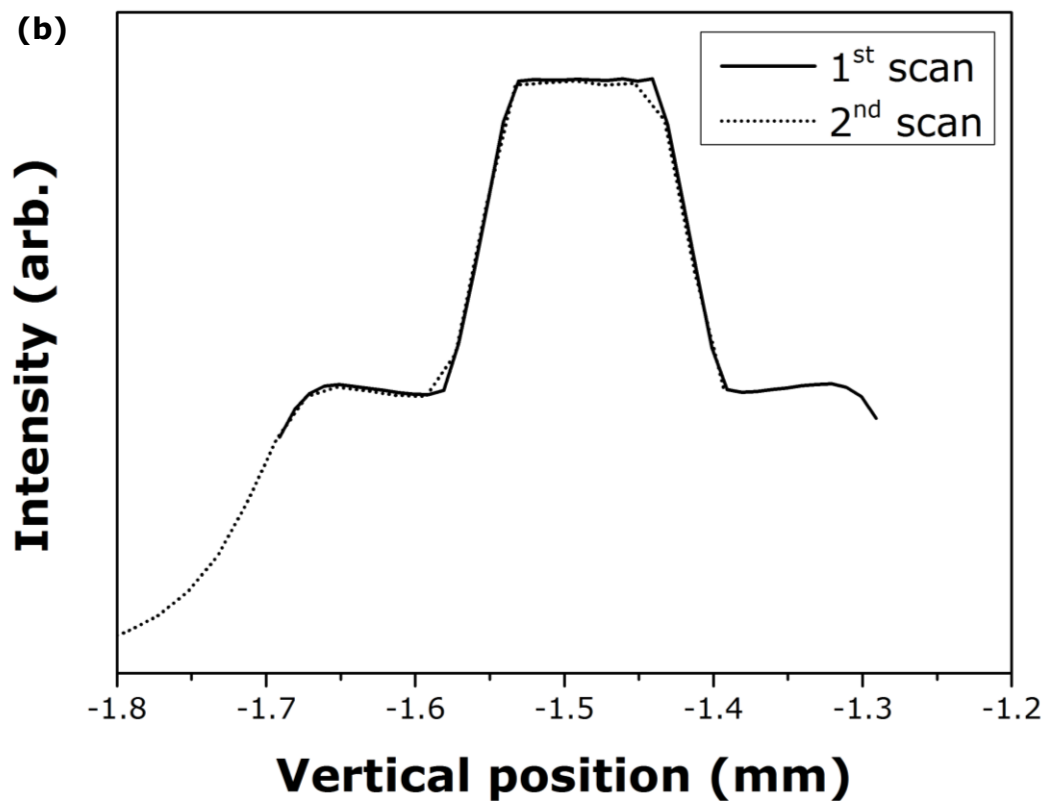
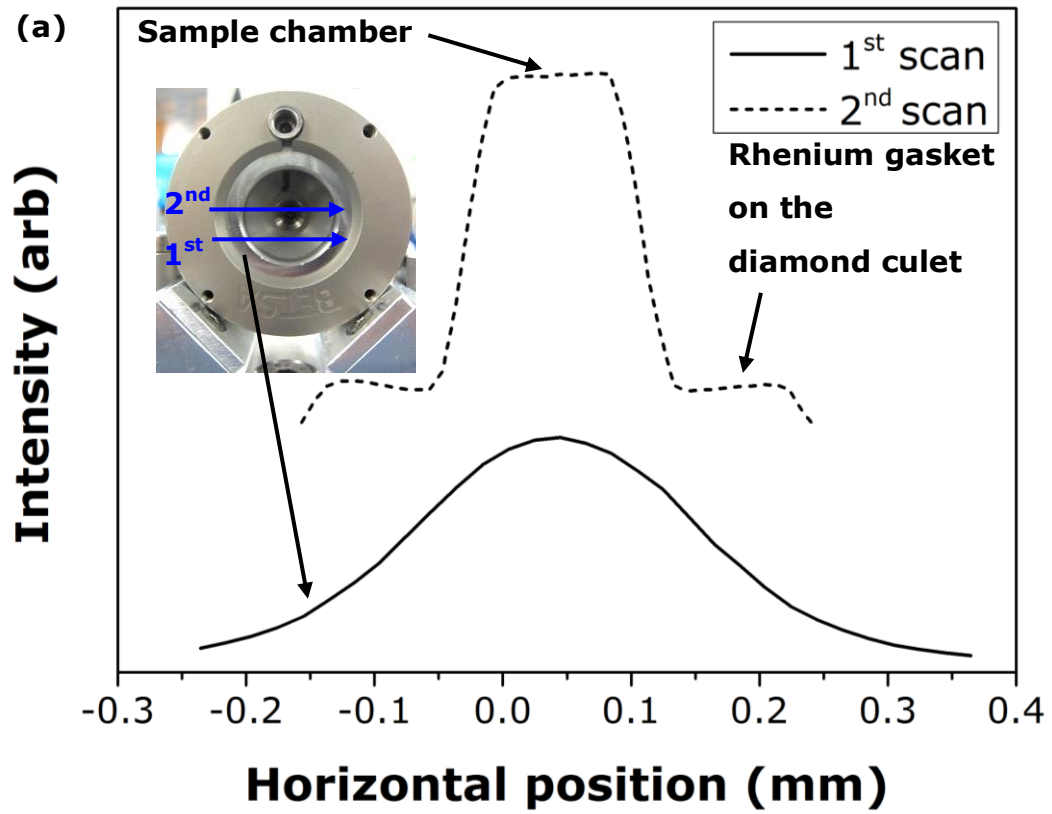


Figure 5.6 Sample chamber step scan with X-ray photodiode readout (a) horizontal scan (b) vertical scan.

5.1.3 DAC pressure control and measurement

Ruby fluorescence is one of the very common methods used for pressure measurement [236]. The Ruby sphere placed inside the sample chamber is chemically inert, and has strong fluorescence when illuminated by a green laser light [237]. The superhead (from Horiba Jobin-Yvon) has built-in optical fibres and fibre coupled 473 nm laser (from Laser Quantum) which is sensitive for ruby fluorescence to at least 100 GPa [238]. The iHR320 spectrometer was used to detect fluorescence from the Ruby. The fluorescence peak position was used to determine the pressure [239-241].

At each pressure step, the targeted pressure inside the DAC sample chamber was realised by increasing the membrane pressure using the gas pressure controller mounted outside the experiment hutch. Pressure measurement was made by using the following procedure:

1. Firstly, the DAC was rotated towards and aligned with the objective lens of the superhead, and the objective lens was moved close enough to the DAC and in focus with the sample chamber as showed in Figure 5.4a and Figure 5.4c.
2. Secondly, the laser beam was turned on and the Ruby sphere inside the sample was moved under the direct illumination of the laser beam. The resulting Ruby fluorescent spectrum was then projected onto the monitor screen.
3. Thirdly, the fluorescent spectrum was fitted using Gaussian distribution function and the position of the Ruby fluorescence peak was determined by maxima of the fitted curve.
4. Finally, the pressure was calculated by the putting the peak position into the well-calibrated state function [239-241]. The pressure was measured before and after collecting the diffraction patterns to monitor and record any pressure relaxation while taking measurement at each pressure step.

Table 5.1 lists the pre-set membrane pressure and the measured DAC chamber pressure for the $\text{Cu}_{50}\text{Zr}_{50}$ and $\text{Fe}_{60}\text{Nb}_{15}\text{B}_{25}$ experiments. The

pressure of the membrane and images of the sample chamber were also recorded at each pressure step to monitor the DAC behaviour for any sign of premature failure.

Table 5.1 The present membrane pressure and measured DAC chamber pressures for $\text{Cu}_{50}\text{Zr}_{50}$ and $\text{Fe}_{60}\text{Nb}_{15}\text{B}_{25}$ experiments.

The membrane pressure and measured DAC chamber pressure for $\text{Cu}_{50}\text{Zr}_{50}$			The membrane pressure and measured DAC chamber pressure for $\text{Fe}_{60}\text{Nb}_{15}\text{B}_{25}$		
Membrane (bar)	Chamber before measurement (GPa)	Chamber after measurement (GPa)	membrane (bar)	Chamber before measurement (GPa)	Chamber after measurement (GPa)
0	9.95	10.05	24.5	10.36	11.34
21	16.75	16.93	37.5	20.41	21.15
32	21.04	21.25	44.3	25.19	25.67
37.8	23.73	24.07	51.7	30.18	30.58
44	27.37	27.87	59	35.16	35.495
49	30.95	31.35	66.5	40.09	40.545
53.7	34.35	34.74	74	45.34	45.735
55.8	37.10	37.62	81.2	50.21	50.73
67	42.52	43.78	89.2	55.60	56.2
			96.6	60.28	60.96
			105	65.26	65.9
			114.5	70.34	70.94

Figure 5.7 plots the averaged chamber pressure (before and after diffraction measurements) versus the pre-set membrane pressure, and the error bars represent the pressure before (the lower pressure) and after (higher pressure) collecting the diffraction patterns. It clearly demonstrates the almost linear relationships for the two cases.

For the $\text{Cu}_{50}\text{Zr}_{50}$ experiment Figure 5.8a taken at 43.15 GPa pressure showed that it was very likely that the gasket would fail if pressure were further increased. Hence the experiment stopped at this pressure to prevent the possible crush of the two diamond culet faces. While for the $\text{Fe}_{60}\text{Nb}_{15}\text{B}_{25}$ experiment, the linear relationship maintains until the target pressure of 70 GPa (the maximum required pressure stated in the user proposal) was reached and the gasket remained in a good functional shape.

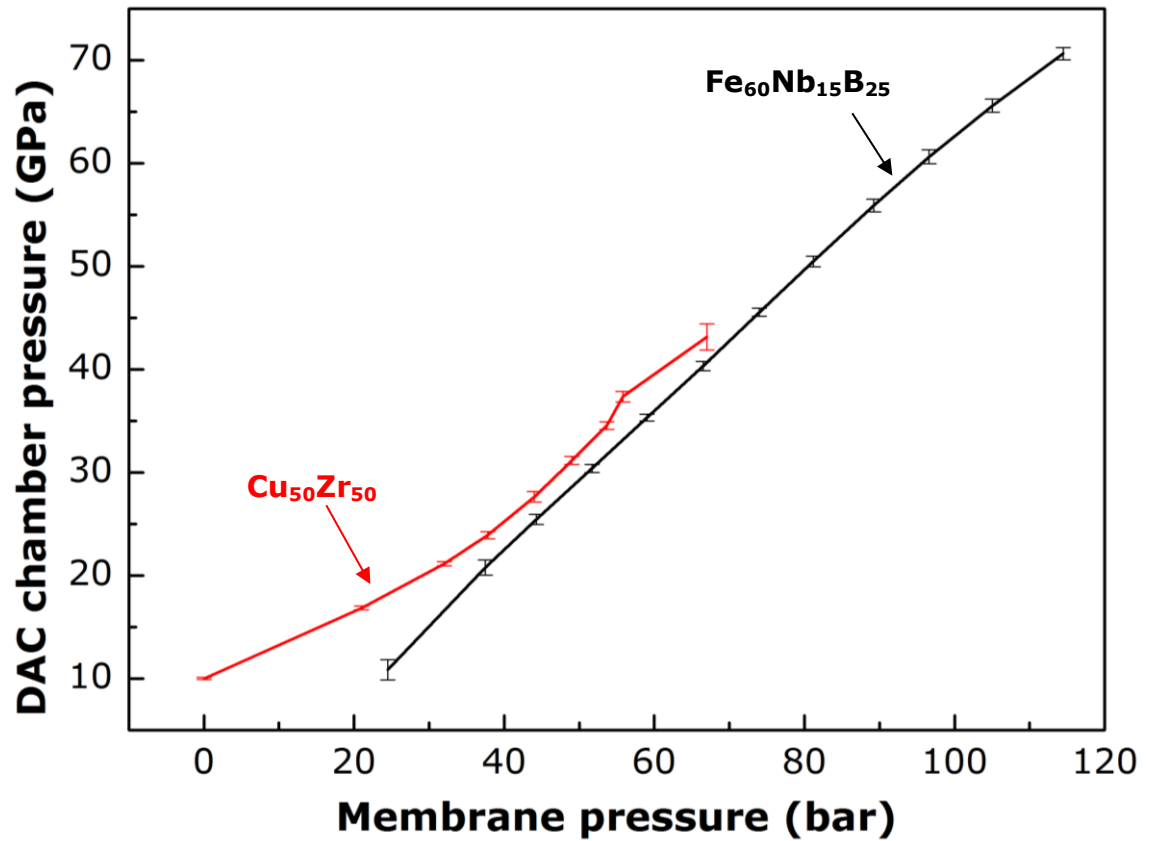


Figure 5.7 The measured DAC sample chamber pressure versus the set membrane pressure. The lower and higher pressure error bars are corresponding to the DAC chamber pressure before and after taking the XRD patterns.

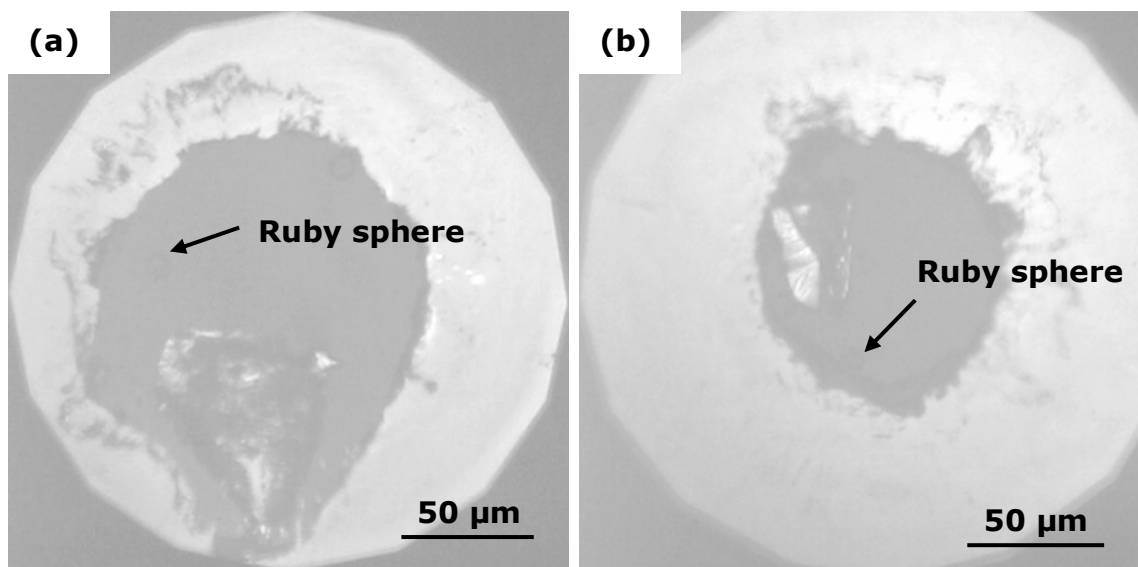


Figure 5.8 Images of the DAC sample chamber at the final pressure step (a) $\text{Cu}_{50}\text{Zr}_{50}$ at 43.15 GPa, (b) $\text{Fe}_{60}\text{Nb}_{15}\text{B}_{25}$ at 70.64 GPa.

5.1.4 In situ acquisition of X-ray diffraction patterns

A monochromatic $\sim 70\mu\text{m}$ spot size X-ray beam of 72 keV was focussed using a $\varnothing 70\ \mu\text{m}$ pin hole onto the sample contained inside the DAC chamber as schematically showed in Figure 5.2a. At each pressure step, the X-ray exited from the sample is diffracted, travelling in a solid angle (2θ) before being detected by a 2-D detector (Perkin Elmer flat panel 1621 EN) placed 327.65mm away from the sample to record the intensity of the diffracted X-ray signals within the solid angle. The exposure time of 120 sec per SXRD pattern was used to acquire the 2D diffraction patterns as show in Figure 5.9a and Figure 5.9c for $\text{Cu}_{50}\text{Zr}_{50}$ at 10 GPa and $\text{Fe}_{60}\text{Nb}_{15}\text{B}_{25}$ at 10.85GPa, respectively. To acquire diffraction patterns through DAC, longer exposure time is needed as compared to the measurements made at ambient pressure without DAC. It is because of (1) the small sample size (only $\sim 30\ \mu\text{m}$ thick), (2) small X-ray beam size ($\sim \varnothing 70\ \mu\text{m}$), and (3) the X-ray absorption by the DAC, which limited the amount of scattering information from the sample. In addition, the diffuse scattering information from the amorphous sample is much weaker as compared to that from crystalline materials. Hence, five diffraction patterns were acquired for the sample and background at each pressure step to ensure sufficient signal-to-noise ratio for the data collection. The background diffraction patterns were acquired by moving the sample away and allowing the incident X-ray beam to focus onto the empty area within the sample chamber as illustrated in Figure 5.5.

At each pressure step, a quick background subtraction was carried out using the Fit2D software to ensure the diffraction patterns from the sample were indeed obtained before proceeding to the next pressure step.

5.2 Data processing and analyses

5.2.1 Masking of the unwanted diffraction information

Apparently, the acquired diffraction patterns contain the coupled diffracted information from the diamond anvils and the sample, and partially from the downstream backing plate (see Figure 5.2a) as well. Figure 5.9a and Figure 5.9c show the convoluted diffraction information acquired from the $\text{Cu}_{50}\text{Zr}_{50}$ sample and the $\text{Fe}_{60}\text{Nb}_{15}\text{B}_{25}$ sample inside the 53H and ST2 DAC,

respectively. Clearly, the bright Bragg's spots on the diffraction patterns are produced by the diamond anvils. These unwanted features need to be masked out together with the dead pixels from the detector. Figure 5.9b and Figure 5.9d show the masking templates created using the Fit2D software for the two samples.

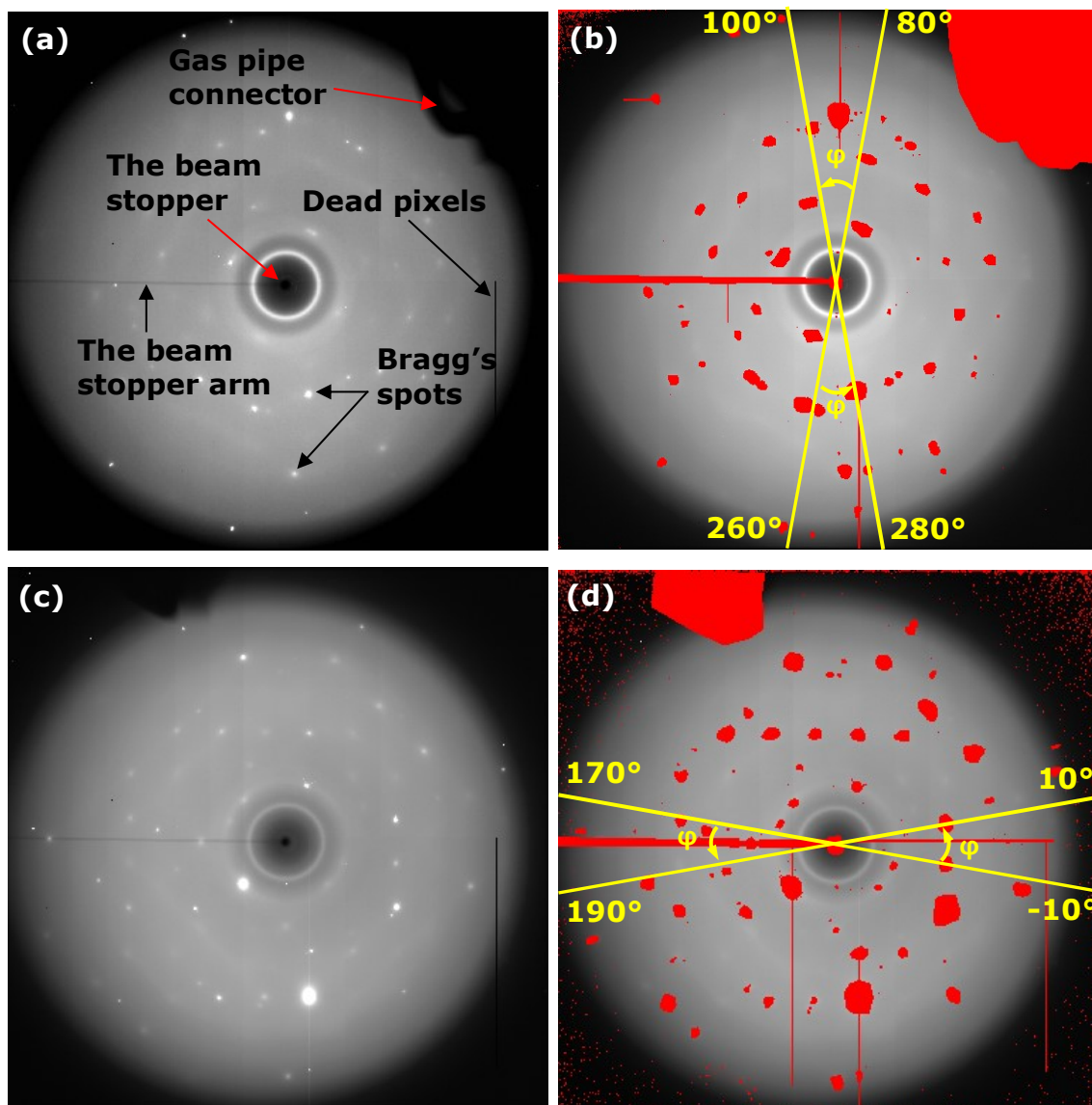


Figure 5.9 The 2D diffraction patterns acquired for (a) the $\text{Cu}_{50}\text{Zr}_{50}$ sample at 10 GPa and (c) the $\text{Fe}_{60}\text{Nb}_{15}\text{B}_{25}$ sample at 10.85 GPa inside the DAC respectively, showing the convoluted diffraction information including those from the beam-stopper, beam-stopper arm, the dead pixels from the detector, and the Bragg's spots from the diamond anvils. Using Fit2D, mask was created to remove these unwanted features before integrating those 2D patterns into 1D spectrum. The corresponding masks for (a) and (c) are showed in (b) and (d) respectively.

5.2.2 Compensation of X-ray intensity attenuated by diamond anvil and backing plate

In addition to those unwanted features showed in Figure 5.9b and Figure 5.9d, the diffracted X-rays (after exiting the sample) are also attenuated by the downstream diamond anvil and the tungsten carbide (WC) backing plate (only the diffracted X-rays that hit on the backing plate at higher 2θ angle as illustrated by Figure 5.2a). Such attenuated X-ray intensity needs to be taken into account and compensated for the total scattering analyses. A DAC transmission coefficient, $T(2\theta)$, is introduced for such compensation and it can be calculated by [242]:

$$T(2\theta) = \frac{I_1}{I_0} = \exp[-\mu_1 t_1(2\theta)] + \exp[-\mu_2 t_2(2\theta)] \quad (11)$$

Where I_0 and I_1 are the diffracted X-ray intensity before and after passing through the diamond anvil and downstream WC backing plate, $\mu_1 = 0.057508 \text{ mm}^{-1}$ and $\mu_2 = 14.349 \text{ mm}^{-1}$ are the attenuation coefficient [243] of the diamond anvils and WC backing plate, $t_1(2\theta)$ and $t_2(2\theta)$ are the diffracted X-ray travel paths corresponding to the 2θ in the diamond and the backing plate calculated from the geometry of the DAC as show in Figure 5.10a and Figure 5.10b corresponding to the 53H DAC used for $\text{Cu}_{50}\text{Zr}_{50}$ and ST2 DAC used for $\text{Fe}_{60}\text{Nb}_{15}\text{B}_{25}$. The detail of the dimension of both DACs is in Appendix 7 and Appendix 8.

The calculated $T(2\theta)$ for the two DACs used in the project is shows in Figure 5.10. The calculation was made by assuming the X-ray beam is at the centre of the sample chamber.

After obtaining $T(2\theta)$, the corrected sample diffraction patterns with the compensation accounted for the attenuation from the downstream diamond anvil and backing plate can be obtained using the following operation [244].

$$I_{cor}(2\theta) = \frac{I^S(2\theta) - n I^B(2\theta)}{T(2\theta)} \quad (12)$$

Where $I_{cor}(2\theta)$ is the corrected sample diffraction pattern, $I^S(2\theta)$ is the acquired sample diffraction pattern, $I^B(2\theta)$ is the acquired background diffraction pattern, n is the normalisation factor for scaling the background intensity (within 1.2 to 0.8) and $T(2\theta)$ is the calculated DAC transmission coefficient.

Using Eq. (12) to calculate $I_{cor}(2\theta)$ is based on the assumption that the background diffraction pattern (with the sample removed from the DAC) is acquired with the X-ray beam at the exact spatial position when acquiring the diffraction patterns from the sample (before sample is removed from the DAC). Such condition ensures that the same $T(2\theta)$ can be used for both $I^S(2\theta)$ and $I^B(2\theta)$, so, Eq. (12) is valid.

However, in our experiments, the background diffraction patterns were acquired from the background areas within the sample chamber (see the dotted red line circles in Figure 5.5) at the same pressure level, and the X-ray beam was shifted away from the original sample position, resulting in different $T(2\theta)$ for the $I^S(2\theta)$ and $I^B(2\theta)$. Hence, in this project, different approach was used to calculate $T(2\theta)$.

The positions for both samples and background as shows in Figure 5.5 were recorded and taken into account during the calculation using a matlab code (Appendix 9). To simplify the $T(2\theta)$ calculation, we only calculated the $T(2\theta)$ at $\varphi = 90^\circ$ and 270° for $\text{Cu}_{50}\text{Zr}_{50}$ and horizontal $\varphi = 0^\circ$ and 180° for $\text{Fe}_{60}\text{Nb}_{15}\text{B}_{25}$. Figure 5.11a and Figure 5.11b show the calculated $T(2\theta)$ for $\text{Cu}_{50}\text{Zr}_{50}$ and $\text{Fe}_{60}\text{Nb}_{15}\text{B}_{25}$, correspondingly. The reason for 4 selected φ angles were to match the 1D spectra integration as shows in Figure 5.9.

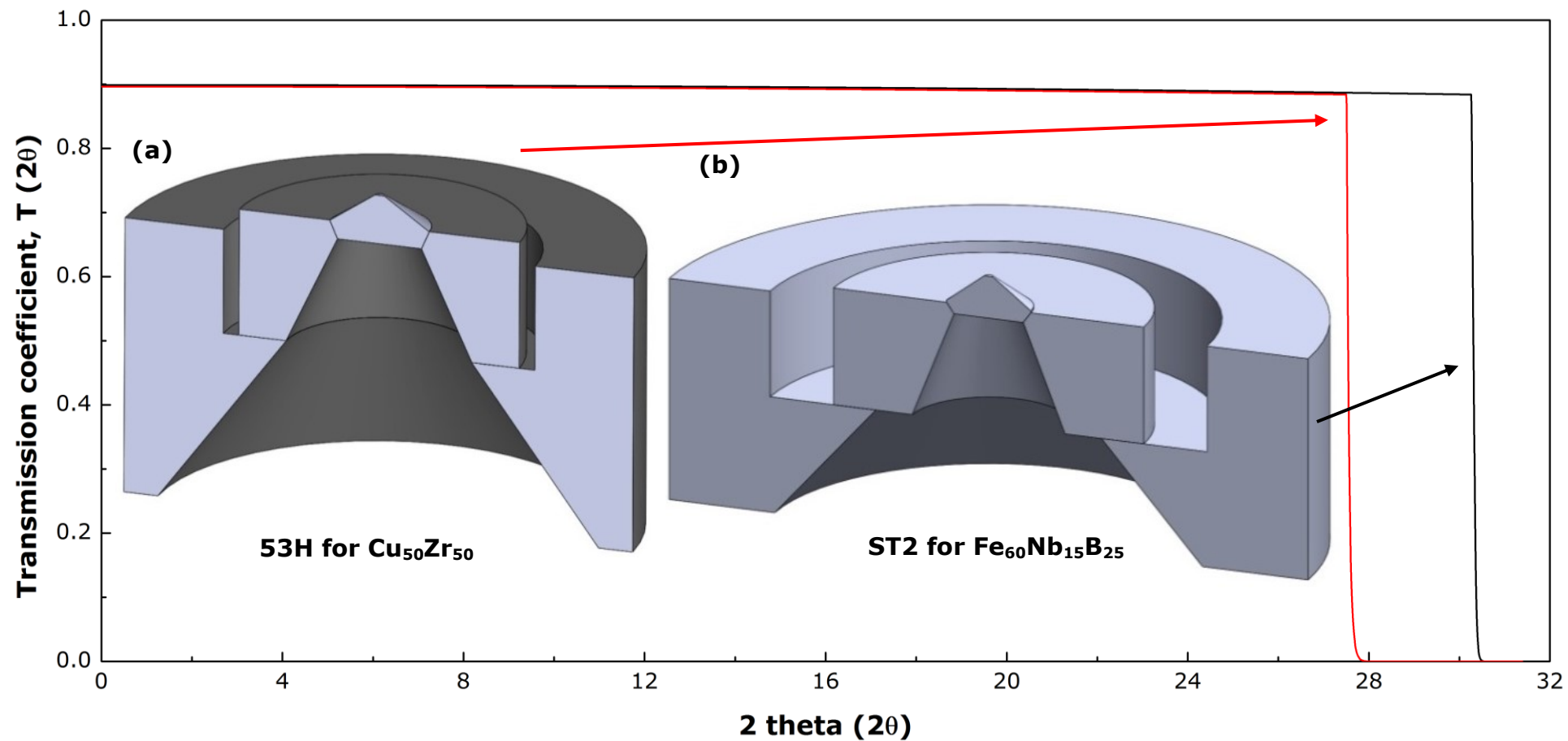


Figure 5.10 The calculated transmission coefficients for the DAC backing plates (a) 53H for $\text{Cu}_{50}\text{Zr}_{50}$ (b) ST2 for $\text{Fe}_{60}\text{Nb}_{15}\text{B}_{25}$.

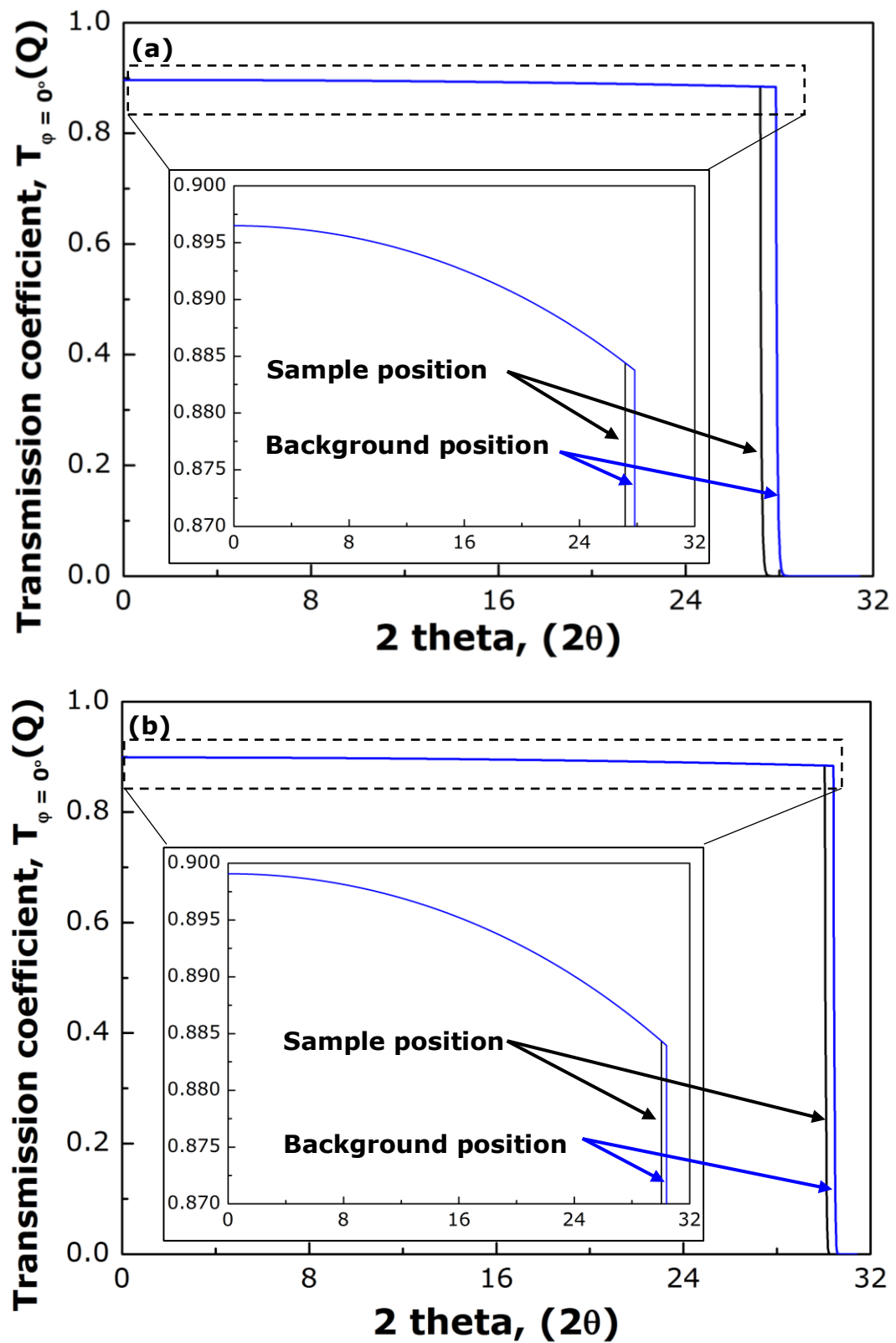


Figure 5.11 The example of calculated DAC transmission coefficients, $T(Q)$ at $\varphi = 0^\circ$ for (a) $\text{Cu}_{50}\text{Zr}_{50}$ and (b) $\text{Fe}_{60}\text{Nb}_{15}\text{B}_{25}$ corresponding to their sample and background position.

5.2.3 Integration of 2D diffraction pattern into 1D spectra

Based on the diffraction patterns and the masking patterns showed in Figure 5.9, several integration trials were made using different ranges of sector areas from the 2D diffraction patterns, and the resulting integrated 1D spectra for 20° sector as showed in Figure 5.12. Apparently, the four sectors (each of 20°) marked in Figure 5.9b and Figure 5.9d give the best quality of integrated 1D spectra in terms of containing sufficient diffraction information from the sample and minimum error in $T(2\theta)$ (because only specific 4 angles of $T(2\theta)$ were calculated instead of a sector). The actual correction of the background and attenuation from the diamond anvil and backing plate is as follow

For $\text{Cu}_{50}\text{Zr}_{50}$:

$$I_{cor}(2\theta) = \left[\frac{I_{\varphi=90^\circ}^S(2\theta)}{T_{\varphi=90^\circ}^S(2\theta)} - n \left(\frac{I_{\varphi=90^\circ}^B(2\theta)}{T_{\varphi=90^\circ}^B(2\theta)} \right) \right] + \left[\frac{I_{\varphi=180^\circ}^S(2\theta)}{T_{\varphi=180^\circ}^S(2\theta)} - n \left(\frac{I_{\varphi=180^\circ}^B(2\theta)}{T_{\varphi=180^\circ}^B(2\theta)} \right) \right] \quad (13)$$

For $\text{Fe}_{60}\text{Nb}_{15}\text{B}_{25}$:

$$I_{cor}(2\theta) = \left[\frac{I_{\varphi=0^\circ}^S(2\theta)}{T_{\varphi=0^\circ}^S(2\theta)} - n \left(\frac{I_{\varphi=0^\circ}^B(2\theta)}{T_{\varphi=0^\circ}^B(2\theta)} \right) \right] + \left[\frac{I_{\varphi=270^\circ}^S(2\theta)}{T_{\varphi=270^\circ}^S(2\theta)} - n \left(\frac{I_{\varphi=270^\circ}^B(2\theta)}{T_{\varphi=270^\circ}^B(2\theta)} \right) \right] \quad (14)$$

The corrected $I_{cor}(2\theta)$ for $\text{Cu}_{50}\text{Zr}_{50}$ and $\text{Fe}_{60}\text{Nb}_{15}\text{B}_{25}$ are show in Figure 5.19a and Figure 5.19b, respectively. Similar procedure was used for all diffraction patterns acquired at all other pressure steps, and a series of $I_{cor}(2\theta)$ were obtained and plotted as a function of the scattering vector, $Q = 4\pi \sin\theta/\lambda$ as described in the next section. Based on the obtained $I_{cor}(2\theta)$, pair distribution functions can be also calculated using software PDFGetX by adopting the procedure described in the literature review.

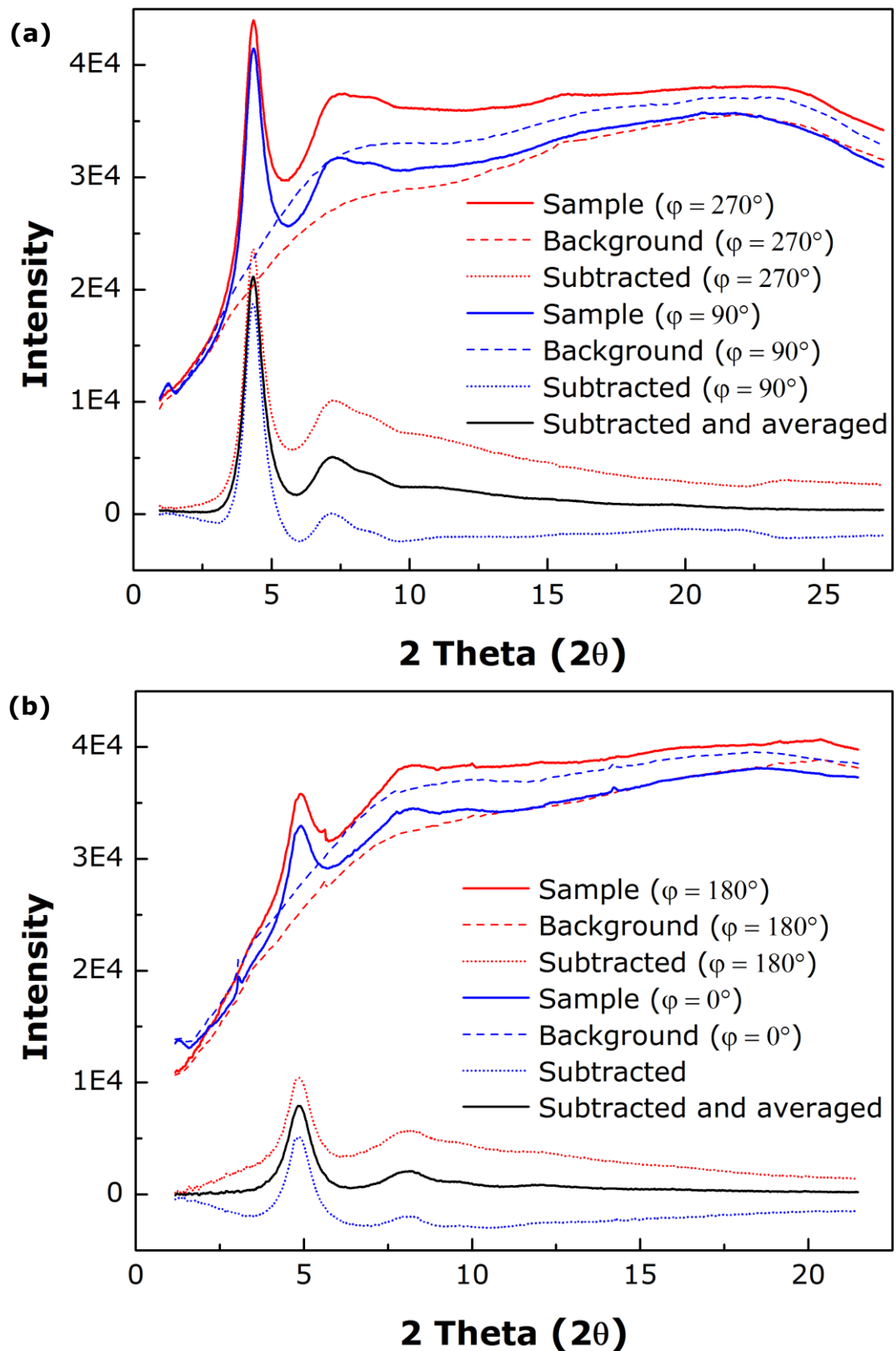


Figure 5.12 The 1D diffraction spectra for (a) $\text{Cu}_{50}\text{Zr}_{50}$ and (b) $\text{Fe}_{60}\text{Nb}_{15}\text{B}_{25}$ samples and their backgrounds integrated from the 2D patterns within the defined angles with $T(2\theta)$ correction showed on the figures, and those after background subtraction, and finally averaging to obtain the corrected $I_{cor}(2\theta)$.

5.3 The experimental results for $\text{Cu}_{50}\text{Zr}_{50}$

Figure 5.13 shows the $I_{cor}(2\theta)$ as a function of Q for the $\text{Cu}_{50}\text{Zr}_{50}$ sample at different pressure steps. The $I_{cor}(2\theta)$ at ambient pressure was obtained at the ambient pressure with the sample placed outside the DAC. The first sharp diffraction peak (FSDP) of each $I_{cor}(Q)$ is fitted using Gaussian distribution function to find the exact location of the maxima of the peak.

Figure 5.14 shows the FSDP shift as a function of pressure. Clearly, the FSDP shifts toward higher Q as pressure increases, reflecting that the distances among atoms within the alloy become closer as pressure increases. This phenomenon is similar to the FSDP shift in the transverse direction for the sample subject a uniaxial tensile load described in section 4.3.

From ambient pressure to 34.55 GPa, the FSDP shifts with a relative constant rate versus the increase of pressure, while just one point (that measured at 10.00 GPa) is deviated from the linear relationship. Between 34.55 GPa and 43.15 GPa, the FSDP was found to shift backwards to lower Q . This might be due to during the experiment measurement at the last two pressure points; the $\text{Cu}_{50}\text{Zr}_{50}$ sample was pushed toward the edge of the sample chamber and away from the pressure marker as shows in Figure 5.8a. This results in different pressure acting on the sample compared to the measurement from the ruby pressure marker, as the Diamond Anvil Cell tend to have uniform stress within the sample chamber [245].

Figure 5.15 shows the structure factors at different pressures obtained from the $I_{cor}(Q)$ showed in Figure 5.13. Each curve is plotted with an equal spacing of 2 for easy comparison. The $S(Q)$ curves show that there are no apparent changes in the shapes of the curves throughout the whole pressure process, suggesting that there are no significant structure changes in the $\text{Cu}_{50}\text{Zr}_{50}$ alloy from ambient pressures up to 43.15 GPa.

Figure 5.16 shows the reduced pair distribution function, $G(r)$ curves at different pressures. The $G(r)$ curves are Fourier transformed from the $S(Q)$ curves. The information showed below $r < 2$ contains errors generated during the Fourier transformation which are directly related to the

normalisation and background subtraction [246, 247]. The $G(r)$ curves show that there are several peaks with their intensity reduced toward longer atomic distance, r . These peaks represent the probability of occurrence of the atoms at those particular distances (atomic shells) in the metallic glass alloy.

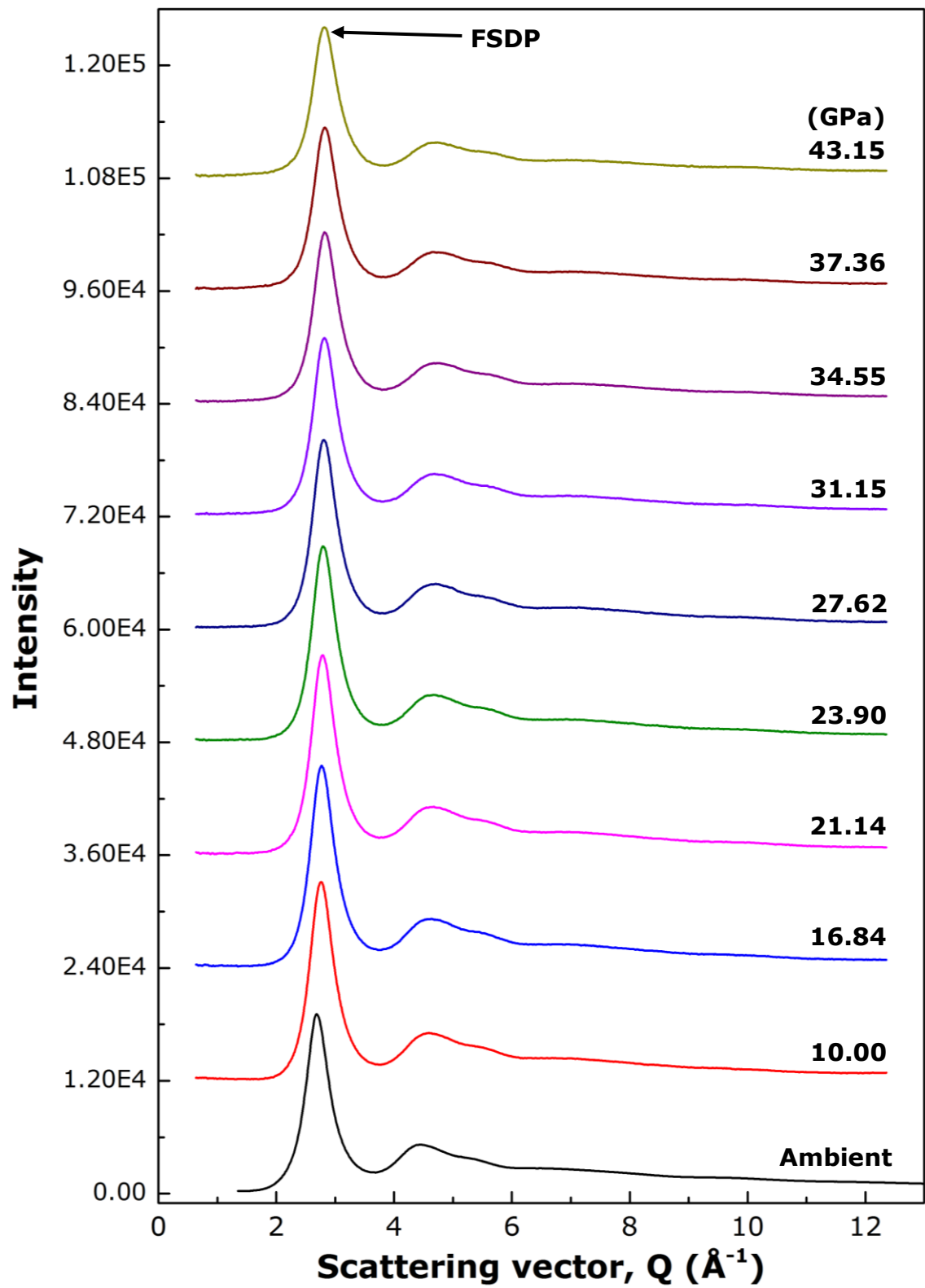


Figure 5.13 The X-ray intensity, $I_{\text{cor}}(Q)$ as a function of scattering factor, Q for the $\text{Cu}_{50}\text{Zr}_{50}$ sample at different pressures.

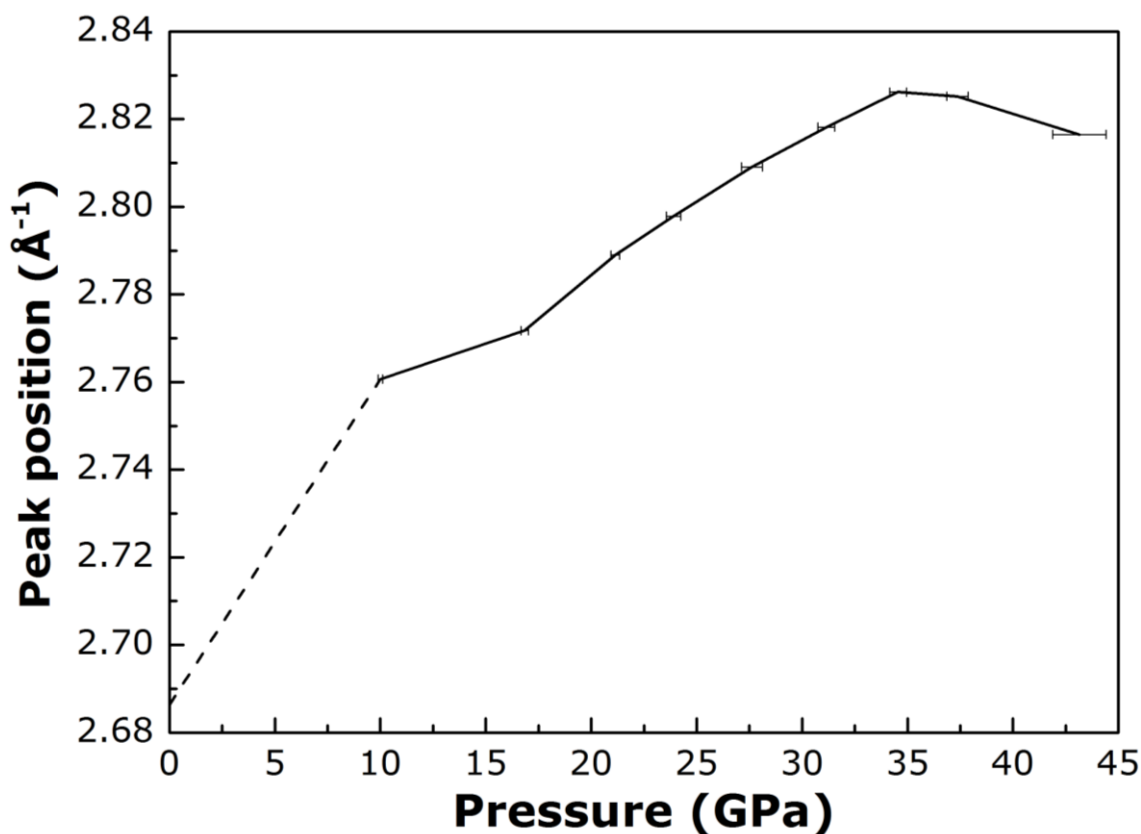


Figure 5.14 The shift of $\text{Cu}_{50}\text{Zr}_{50}$ first sharp diffraction peak position at different pressure step.

The $G(r)$ curves show that the 1st, 2nd and 3rd atomic shells are composed of several sub peaks. The 1st atomic shell and half of the 2nd atomic shell are in the short range order region, whereas the 3rd atomic shell is within the medium range order region. As the pressure increases, the 3 atomic shells shift toward the lower atomic radii, especially for the 2nd atomic shell where its peak moved into the short range order region.

Figure 5.17 shows the shifts of the 1st, 2nd and 3rd atomic shells versus the increase of pressure. For the 1st atomic shell, the peak shifts from 2.775 Å to 2.691 Å, when the pressure increase from ambient pressure to 34.55 GPa, and maintains a near linear relationship with the increase of pressure. However, from 34.55 GPa to 43.15 GPa, the 1st peaks stay at approximately the same location of 2.691 to 2.693 Å.

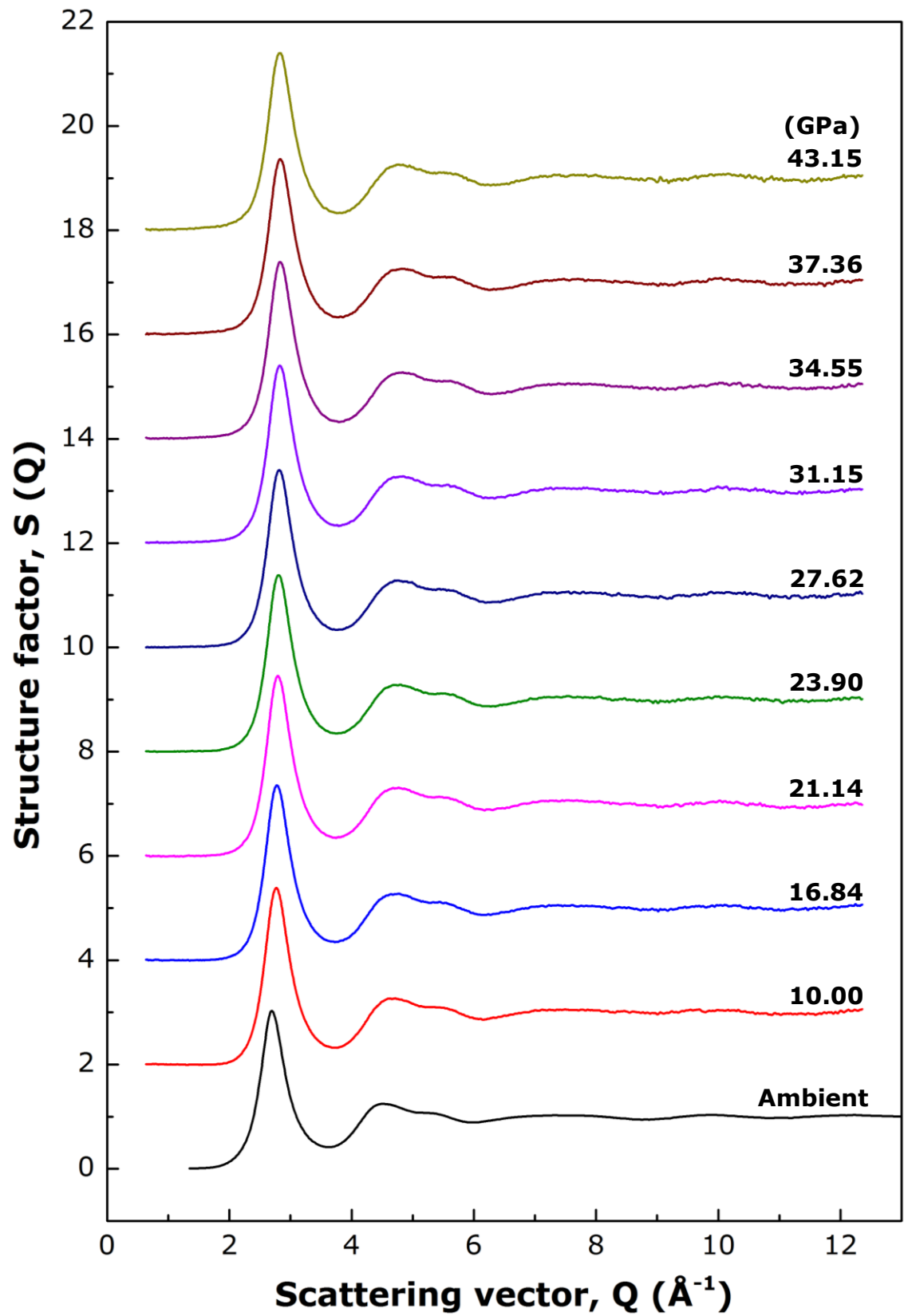


Figure 5.15 The structure factor as a function of scattering factor for the $\text{Cu}_{50}\text{Zr}_{50}$ sample at different pressures.

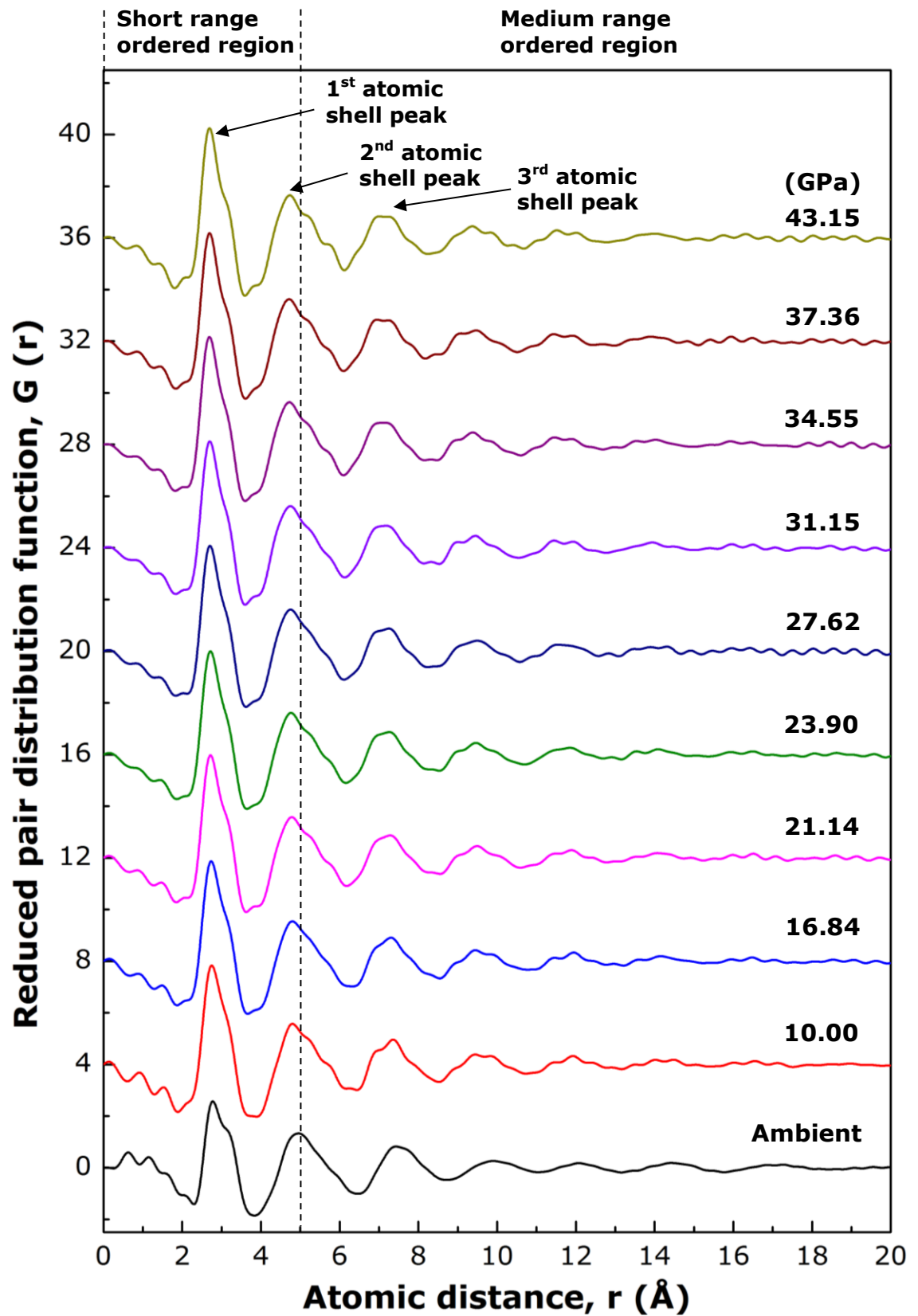


Figure 5.16 The reduced pair distribution function, $G(r)$ for the $\text{Cu}_{50}\text{Zr}_{50}$ sample at different pressures.

For the 2nd atomic shell, the peak shifts from 4.955 Å to 4.715 Å, when the pressure increase from ambient pressure to 37.36 GPa, and between 10 GPa and 37.36 GPa, the peak shift follows a roughly linear relationship with the increase of pressure. However, from ambient pressure to 10 GPa, the peak shift deviates from the linear trend found for the higher pressures and also from 37.36 GPa to 43.15 GPa the trend the shift stop.

For the 3rd atomic shell, the peak shifts from 7.429 Å to 7.163 Å, when the pressure increases from ambient pressure to 34.55 GPa. Again the peak seems to shift linearly towards lower atomic distance with the increase of pressure until 34.55 GPa. Above 34.55 GPa, the 3rd peak split into two peaks as highlighted by Figure 5.18 (two minor peaks at 6.949 Å and 7.237 Å respectively at 37.36 GPa). The two minor peaks (at 7.006 Å and 7.234 Å respectively) become more obvious at the final pressure step, i.e. 43.15 GPa.

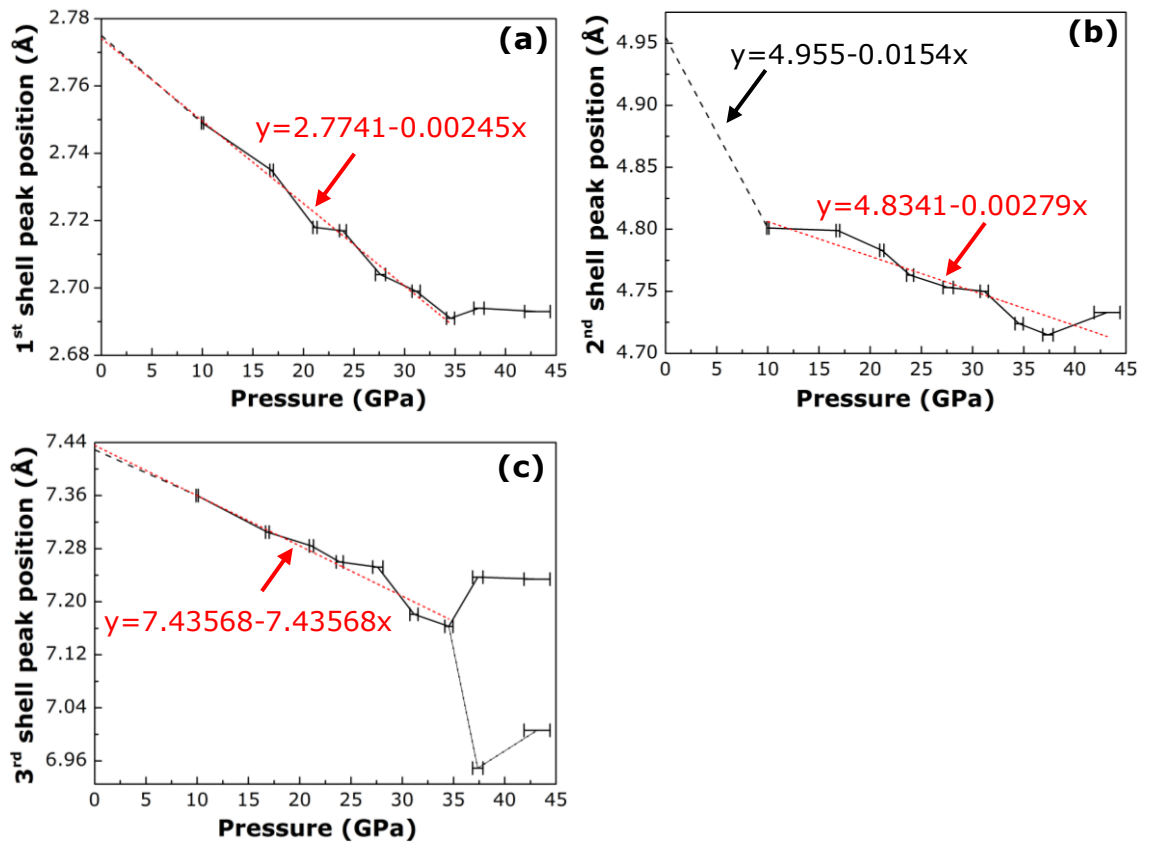


Figure 5.17 The shifts of the positions of the PDF peaks (atomic shells) for the $\text{Cu}_{50}\text{Zr}_{50}$ alloy as the pressure increases: (a) the 1st atomic shell, (b) the 2nd atomic shell, and (c) the 3rd atomic shell.

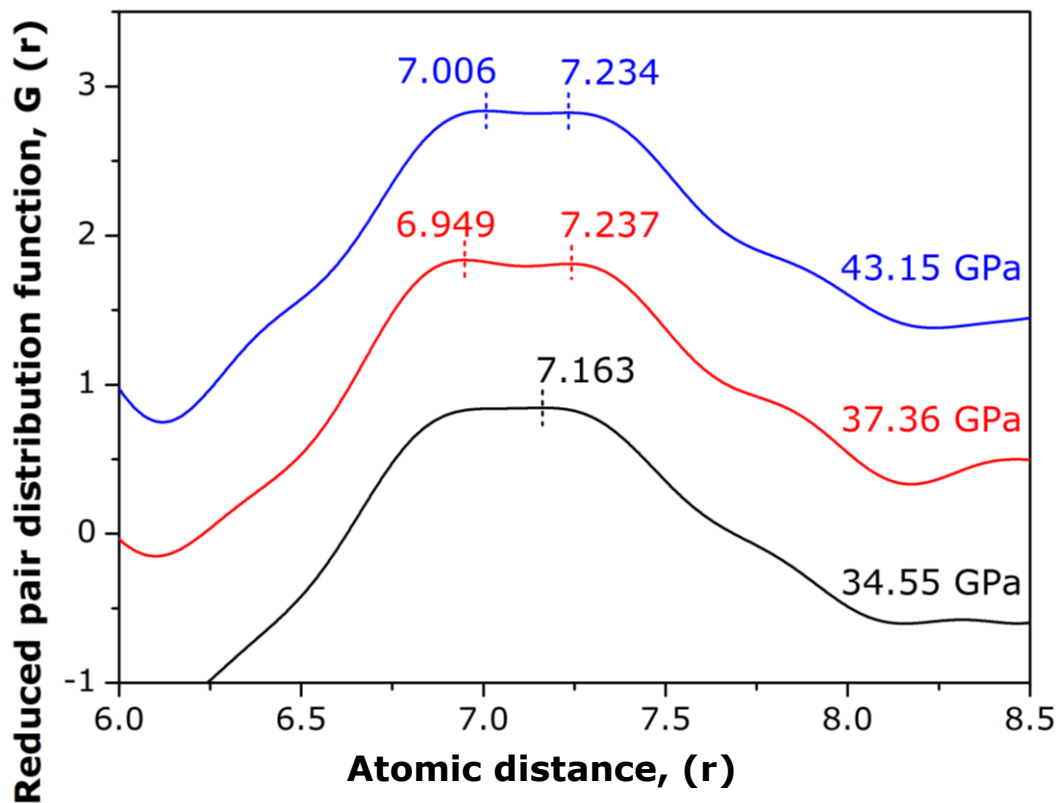


Figure 5.18 The 3rd PDF peak (the 3rd atomic shell) of the $\text{Cu}_{50}\text{Zr}_{50}$ at 34.55, 37.36 and 43.15 GPa, highlighting the split of the 3rd peak in the last 2 pressure steps.

5.4 The experimental results for $\text{Fe}_{60}\text{Nb}_{15}\text{B}_{25}$

Figure 5.19 shows a series of $I_{cor}(Q)$ stacked together for the $\text{Fe}_{60}\text{Nb}_{15}\text{B}_{25}$ alloy obtained at different pressures. Again, the ambient pressure $I_{cor}(Q)$ was measured outside the DAC. Compared to those of $\text{Cu}_{50}\text{Zr}_{50}$, the $I_{cor}(Q)$ curves for the $\text{Fe}_{60}\text{Nb}_{15}\text{B}_{25}$ contain high frequency noises because the diffraction-to-background ratio for the $\text{Fe}_{60}\text{Nb}_{15}\text{B}_{25}$ sample is lower than those for the $\text{Cu}_{50}\text{Zr}_{50}$ sample as illustrated by the integrated 1D spectra showed in Figure 5.12a and Figure 5.12b, respectively.

Again, the positions of the FSDP at different pressures were fitted using Gaussian distribution function and the shift of the FSDP against the increase of pressure was plotted and showed in Figure 5.20. It clearly shows that, above 10 GPa, the FSDP shifts towards higher Q in a nearly linear manner.

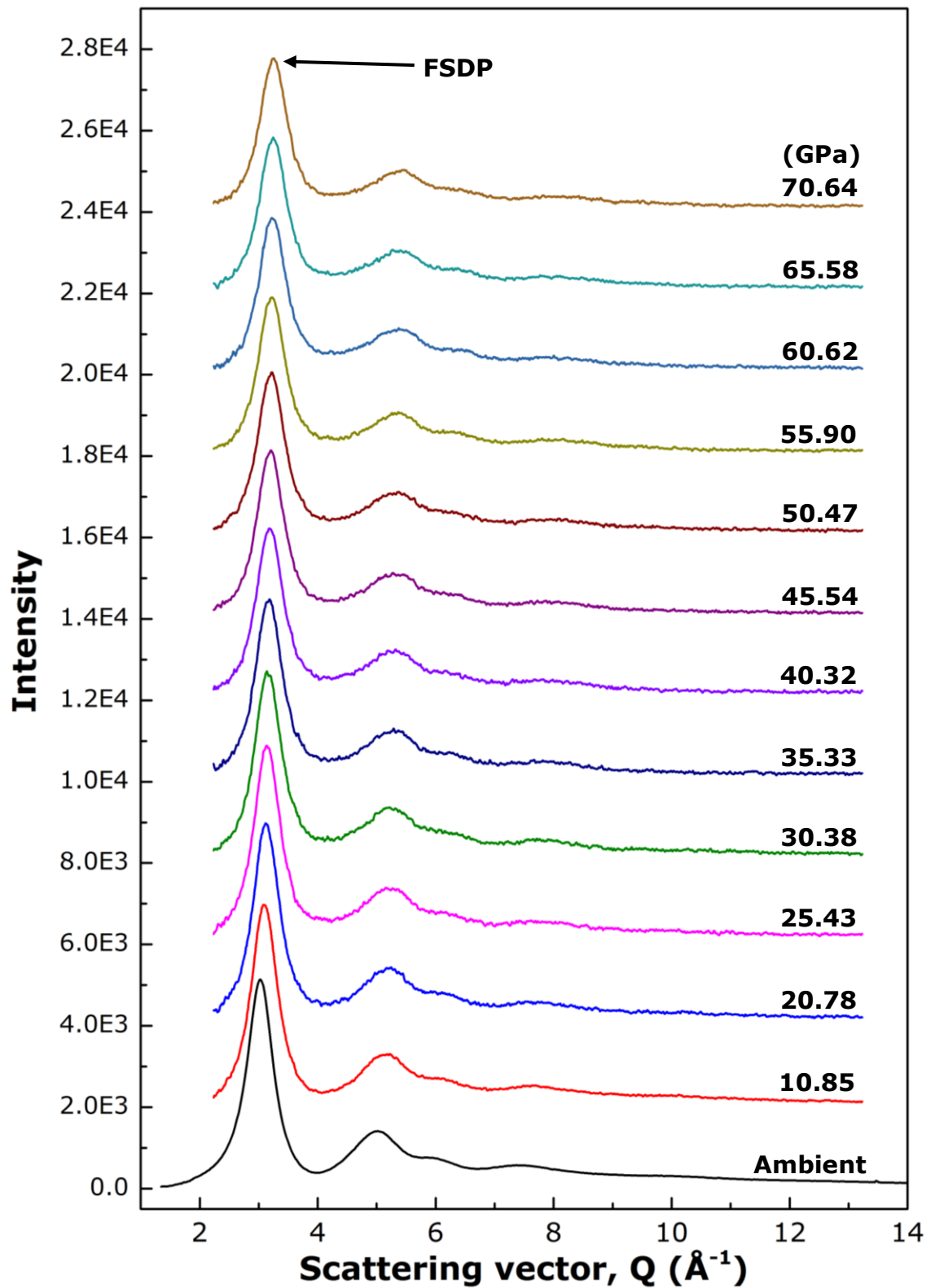


Figure 5.19 The X-ray intensity, $I_{\text{cor}}(Q)$ as a function of scattering factor, Q for the $\text{Fe}_{60}\text{Nb}_{15}\text{B}_{25}$ sample at different pressures.

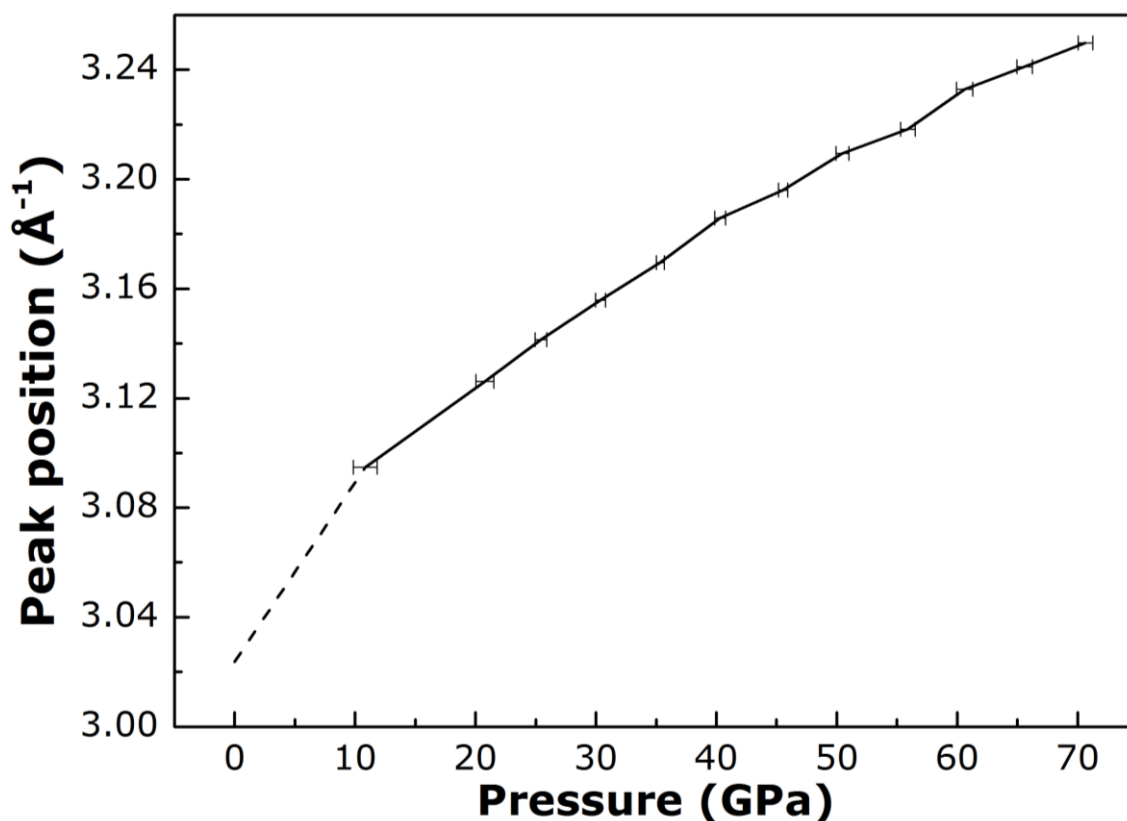
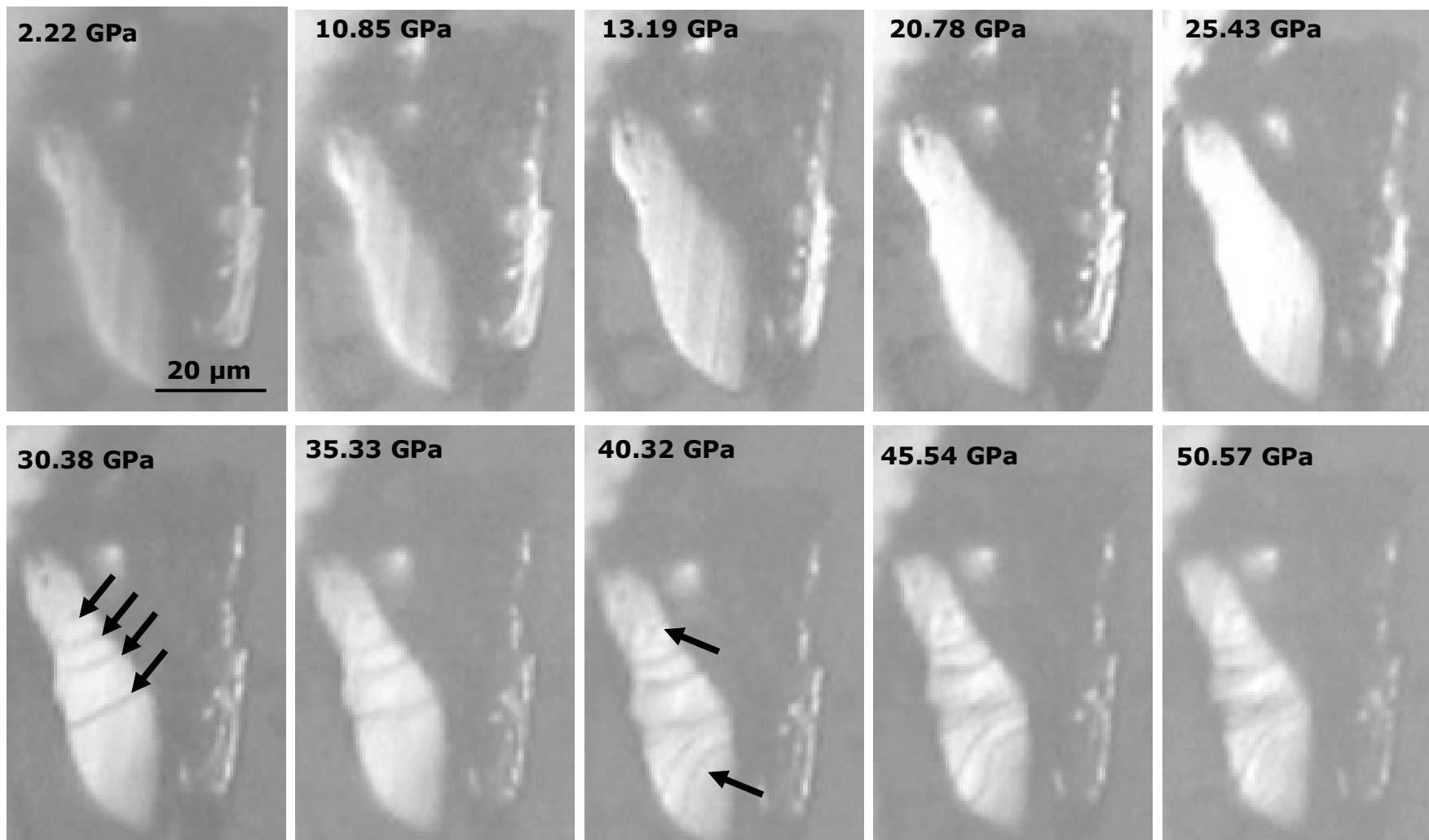


Figure 5.20 The shift of first sharp diffraction peak (FSDP) position for the $\text{Fe}_{60}\text{Nb}_{15}\text{B}_{25}$ sample at different pressures.

The changes of the $\text{Fe}_{60}\text{Nb}_{15}\text{B}_{25}$ sample surface to the increase of pressure were investigated with the optical microscope “superhead”. Figure 5.21 shows a series of images taken at different pressure steps. The images show two different contrast, because the sample do not have a completely flat surface like a polished sample, this result in more than half of the sample surface reflect the fibre optic light to other direction. Therefore, only the bottom left sample surface was concerned in the study. Between 2.22 GPa to 25 GPa, there is no obvious change occur on sample surface. At the 30 GPa, there are 4 features observed at the sample surface. With the increase of pressure, more of these kinds of features were found. However, the sample did not appear to be fractured in pieces even after the experiment return to ambient pressure. These features still remained on the surface as observed from the superhead.



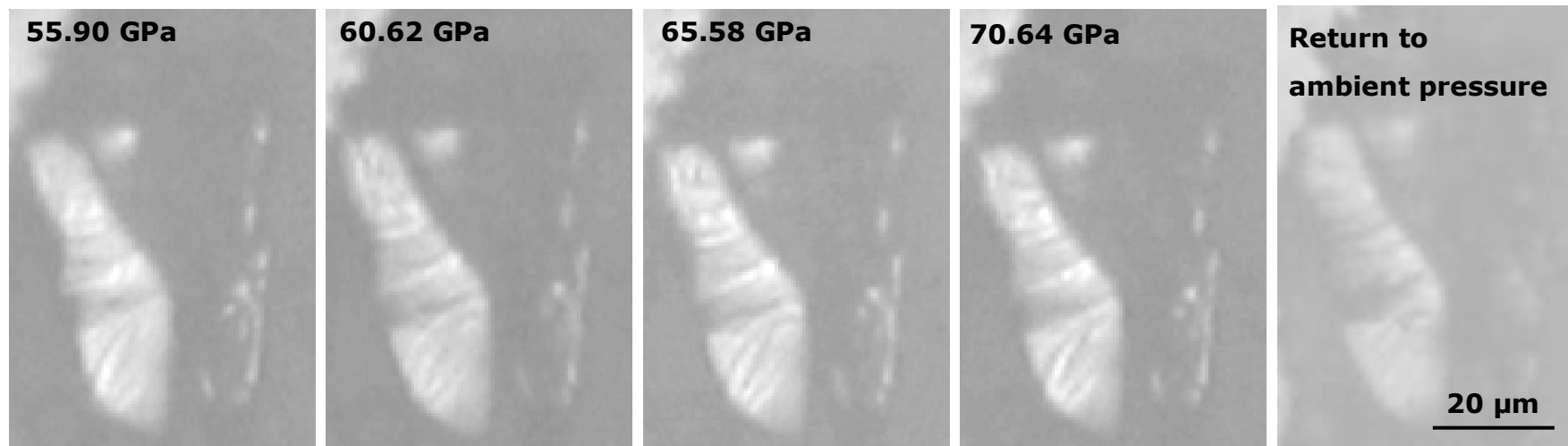


Figure 5.21 The optical images of Fe₆₀Nb₁₅B₂₅ sample taken at different pressure step.

The $S(Q)$ curves for the $\text{Fe}_{60}\text{Nb}_{15}\text{B}_{25}$ sample at different pressures are plotted together (stacked with an equal spacing of 2) and showed in Figure 5.22. The noise is due to the low diffraction-to-background ratio. Similar to the $\text{Cu}_{50}\text{Zr}_{50}$ case, there are no obvious changes found in the $S(Q)$ curves which suggest there are no significant structural changes throughout the high pressure experiment.

The $S(Q)$ curves were then Fourier transformed into the reduced pair distribution functions, $G(r)$ and is shows in Figure 5.23 (stacked with an equal spacing of 5). Similar to those curves in Figure 5.16, the information at $r < 2$ is the transformation noise and has no information concerning any atomic structures of the sample.

Similar to Figure 5.17, the peak positions of the 1st, 2nd and 3rd atomic shells are plotted against the increase in pressure and is shows in Figure 5.24a, Figure 5.24b and Figure 5.24c, respectively.

For the 1st atomic shell, the peak shifts from 2.639 Å to 2.453 Å, when the pressure increase from ambient pressure to 70.64 GPa, and maintains a near linear relationship with the increase of pressure, except that there is one data point at 55.90 GPa deviated from the linear trend.

For the 2nd atomic shell, there is noticeable point, i.e. at 35.33 GPa where the slope of the curve changes. Below that the peak shift follows an approximately linear line with the slope of -0.00764 \AA/GPa . However above 35.33 GPa, the peak shift "slows down" as the pressure continue to increase, and follows an approximately linear line with the slope of -0.00167 \AA/GPa .

As for the 3rd atomic shell, again the peak seems to shift approximately linearly towards lower atomic distance with the increase of pressure until 65.58 GPa. However, there are two obvious pressure points (at 30.38 and 40.32 GPa, respectively) where the linear trend is violated, and finally the last point at 70.64 GPa is not on the linear line either. The deviated from the linear trend at 30.38 GPa and 40.32 GPa were found together with the features occurred on the sample surface as shows in Figure 5.21.

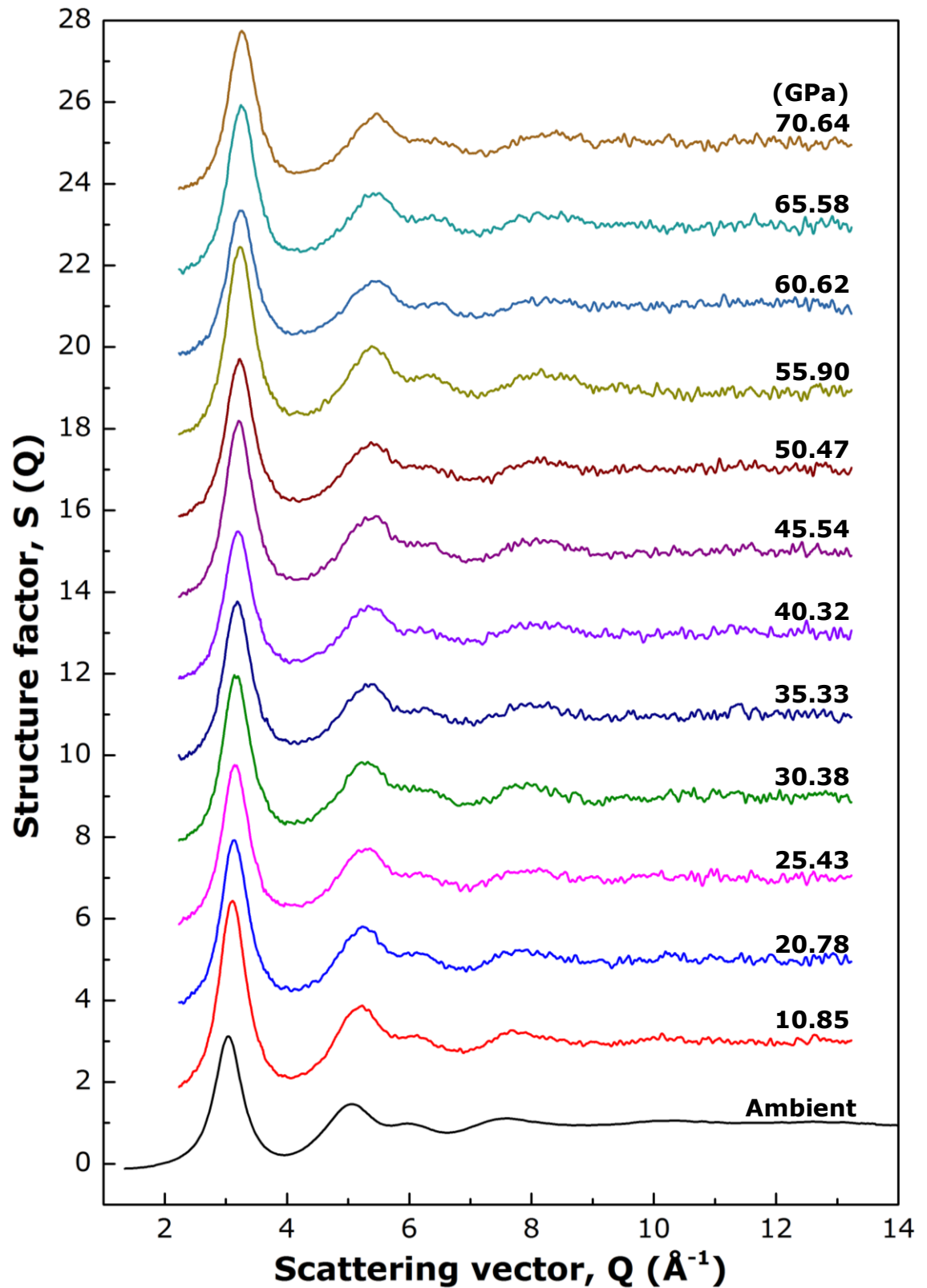


Figure 5.22 The structure factor as a function of scattering factor for the $\text{Fe}_{60}\text{Nb}_{15}\text{B}_{25}$ sample at different pressures.

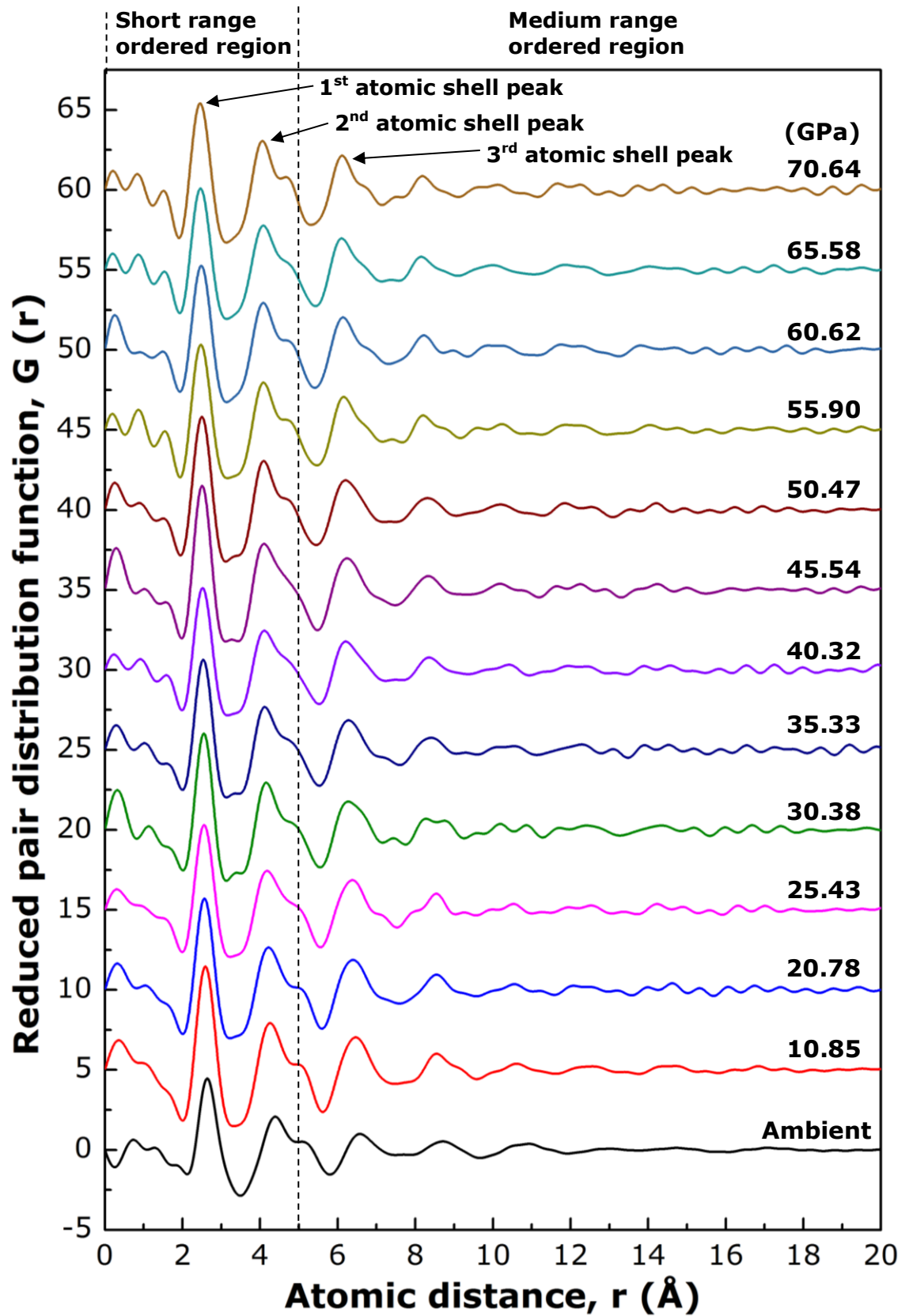


Figure 5.23 The reduced pair distribution function, $G(r)$ for the $\text{Fe}_{60}\text{Nb}_{15}\text{B}_{25}$ sample at different pressures.

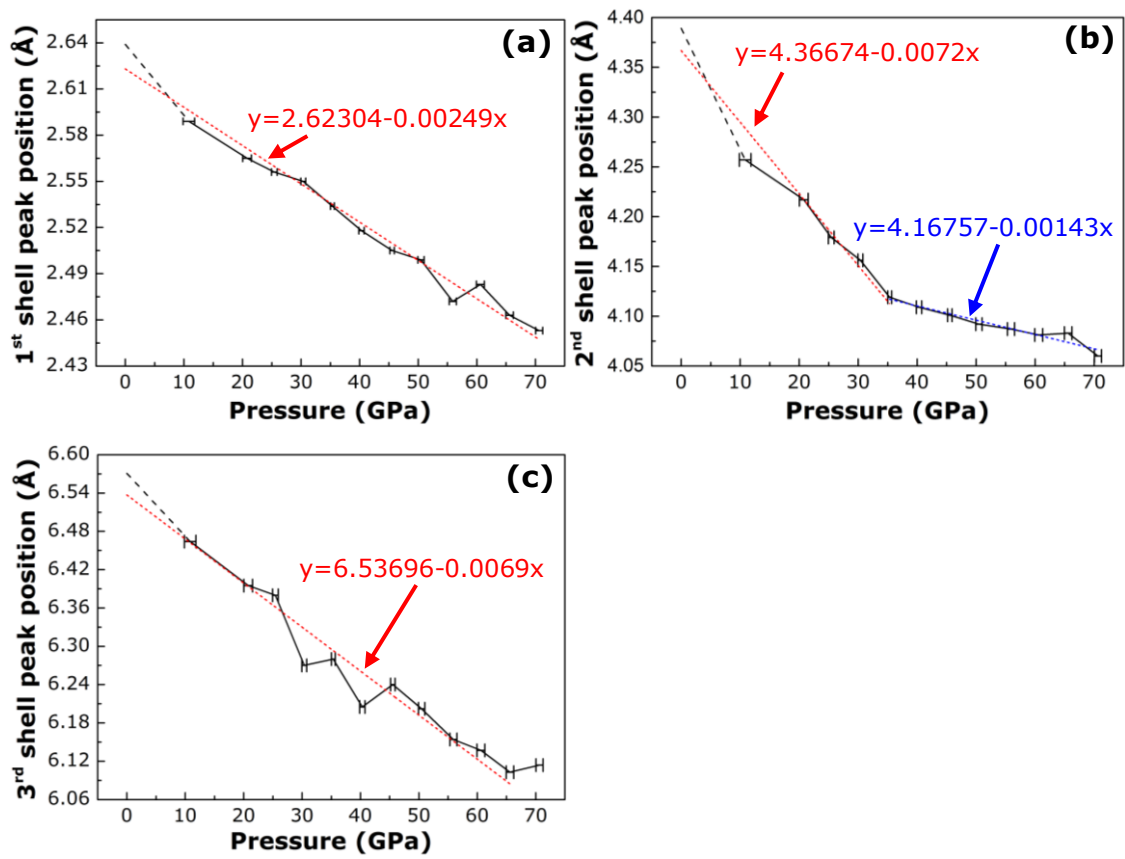


Figure 5.24 The shifts of the positions of the PDF peaks (atomic shells) for the Fe₆₀Nb₁₅B₂₅ alloy as the pressure increases: (a) the 1st atomic shell, (b) the 2nd atomic shell, and (c) the 3rd atomic shell.

5.5 Anomalous X-ray scattering

5.5.1 Experiment setup for anomalous X-ray scattering

The anomalous X-ray scattering experiments were carried out at the High Resolution Powder Diffraction beamline (I11). The experiment setup at beamline I11 is shown in Figure 5.25. Unlike beamline I12 and I15 which use the 2D detector, I11 uses the position-sensitive detector (PSD) Mythen-II which can scan a wider range of 2θ to complement the reduction in scattering vector due to low X-ray energy.

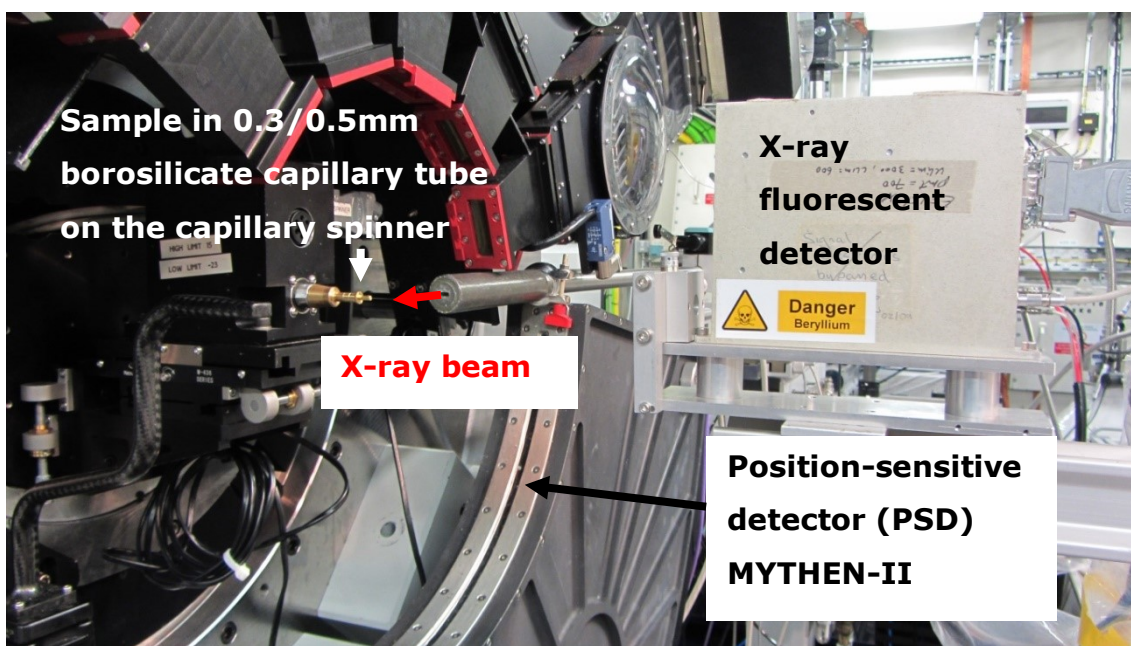


Figure 5.25 Experiment setup of anomalous X-ray scattering experiment at I11 of DLS.

5.5.2 Sample preparation

The anomalous X-ray scattering experiment was used to extract the specific partial pair distribution function of individual element, especially for the elements contained in the alloys subject to high pressure experiments; $\text{Fe}_{60}\text{Nb}_{15}\text{B}_{25}$, $\text{Cu}_{50}\text{Zr}_{50}$ and $\text{Ti}_{55}\text{Cu}_{45}$. The ribbon samples were cut into thin strips of $\sim 100\text{-}150\mu\text{m}$ using a tungsten carbide cutter and loaded into a borosilicate capillary tubes held by brass sample holders as shown in Figure 5.26a.

The capillary tube samples were then labelled and placed on the carousel as shows in Figure 5.26b. The samples were automatically placed on the capillary spinner using a robotic arm.



Figure 5.26 Samples prepared for the anomalous X-ray scattering experiments, (a) thin strips samples in the borosilicate capillary tubes and brass sample holders (b) samples placed on the carousel.

5.5.3 X-ray energy tuning and flatfield correction

Initially, the X-ray scattering edge (f') was determined from the calculated f' edge [248]. The exact X-ray energy was determined using the fluorescent detector by scanning the sample under the calculated energy range. The X-ray fluorescent detector was placed perpendicular to the sample as shows in Figure 5.25. Ideally the edge was selected around middle of the slope as shows in Figure 5.27. Once the energy was determined, it was shifted 15 eV to the lower energy region to reduce the X-ray absorption. It is because if the X-ray absorption was too high, it will be difficult for the PSD detector to pick up the scattering signal and causes high noise-to-signal ratio. Table 3.9 summarises the X-ray energies used in the experiment.

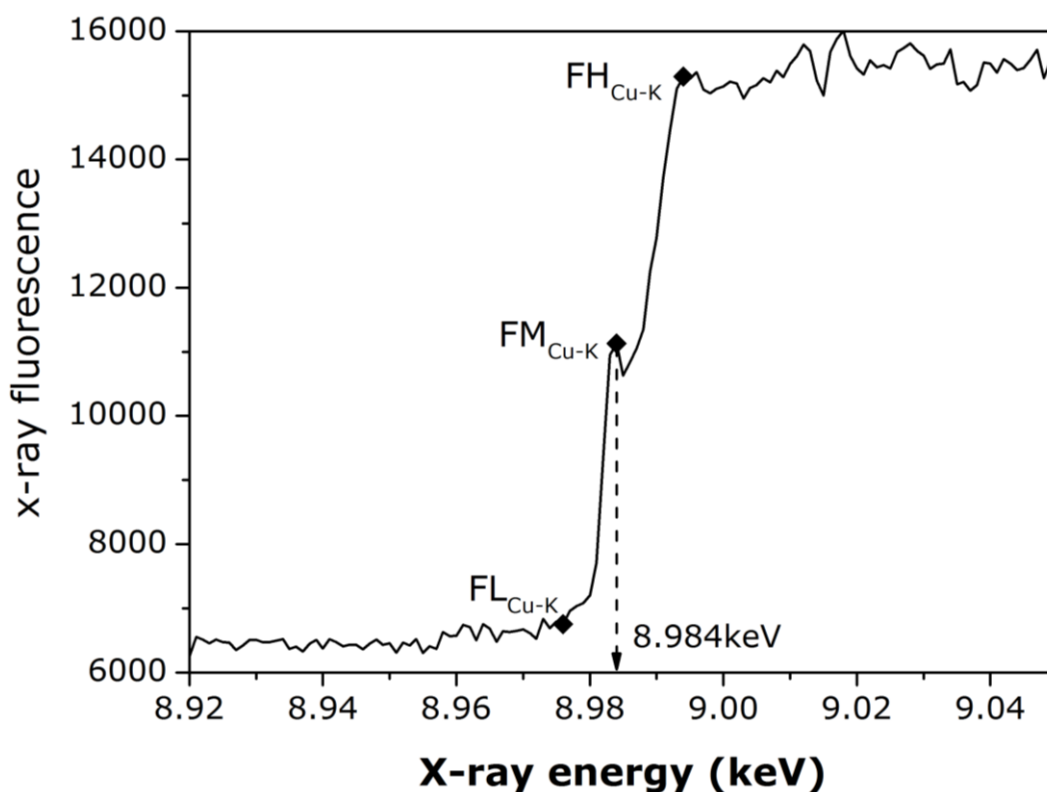


Figure 5.27 X-ray fluorescence count from the $Cu_{50}Zr_{50}$ sample near the Cu k-edge.

Because the PSD detector is composed of 1028 Si strips, each of them has different characteristic in photon read-out. To correct the difference in the signal detection sensitivity, flatfield patterns were collected for the selected X-ray energies. After applying the flatfield correction for the selected X-ray energies, the samples, background and air scattering patterns were collected by scanning the PSD detector along the arc at the exposure time of 1 to 3 secs depending on the X-ray fluxes and fixed step size of 0.25° .

5.5.4 Experimental results for $Cu_{50}Zr_{50}$ and $Fe_{60}Nb_{15}B_{25}$

Theoretically, the 1st, 2nd and 3rd peaks of the $G(r)$ curves show in Figure 5.16 and Figure 5.23 are the probability of occurrence of the atom coordination number at those atomic shells [55]. The intensity of a peak actually contains the contributions from different atom pairs within that particular atomic shell [249]. For example, for the $Cu_{50}Zr_{50}$, the $G(r)$ contains the information from Cu-Cu, Cu-Zr and Zr-Zr atom pairs. To obtain and decouple those convoluted atomic structural information, anomalous X-ray scattering technique was used in this research. Figure 5.28 shows the

scattering factors for the Fe, Cu, Zr and Nb elements as a function of X-ray energy from 0 to 25 keV, referenced from the database [56] and then converted into the plot. At the edge, the scattering intensity of the element is reduced significantly and therefore for the alloy that containing the element, the X-ray scattering contribution from this particular element is at its minimum and can be considered as being “removed” from the contribution from the remaining alloy elements.

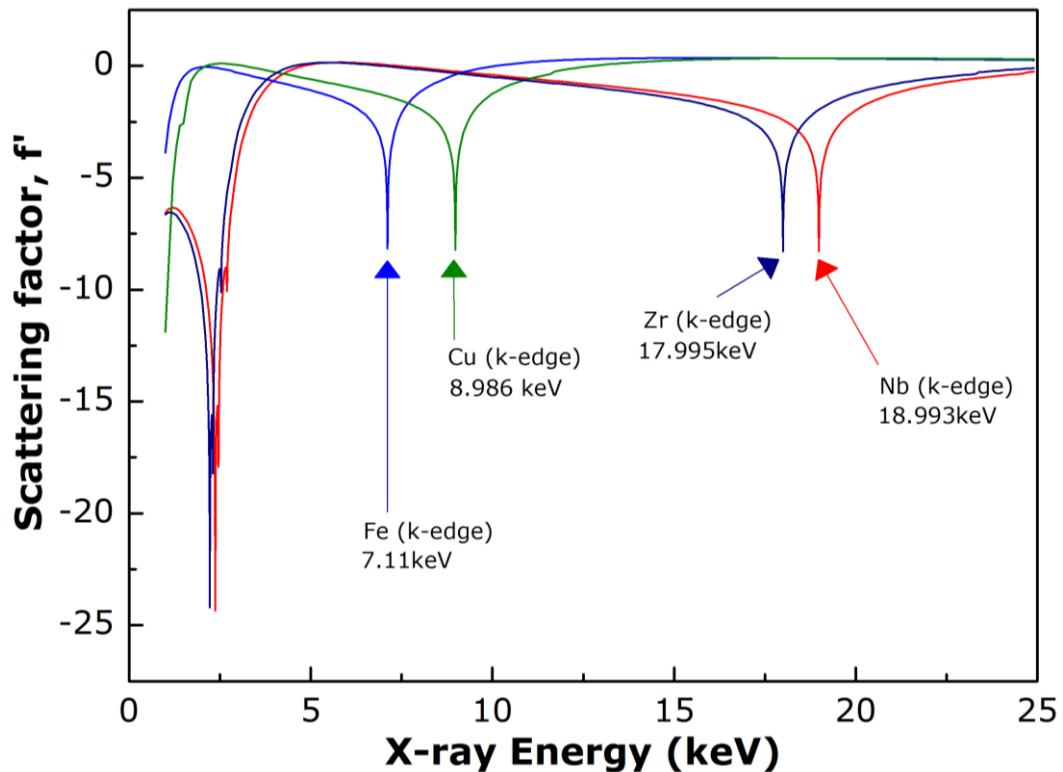


Figure 5.28 The X-ray scattering factor as a function of X-ray energy for the elements studied, showing clearly the X-ray edge for the Fe, Cu, Zr and Nb in the energy range from 0 to 25 keV [56].

The weighting factor, $\omega_{ab}(Q, E)$ is dependent on X-ray energy and can be calculated using Eq. (15) [250].

$$\omega_{ab}(Q, E) = \frac{c_a c_b f_a(Q, E) f_b(Q, E)}{[f_{total}(Q, E)]^2} \quad (15)$$

Where c_a and c_b are the atomic concentration of the element in the system, $f_a(Q, E)$ and $f_b(Q, E)$ are the X-ray energy dependent scattering factor of the element, and $f_{total}(Q, E)$ is the total scattering factor of the system at a specific X-ray energy. $f_a(Q, E)$ can be calculated using Eq. (16) [251]:

$$f_a(Q, E) = f_0(Q) + f'(E) + if''(E) \quad (16)$$

Where $f_0(Q)$ is the usual atomic scattering factor which can be calculated using Eq. (17), $s = Q/4\pi$, a , b and c is the parameter from scattering factor functions for free atoms [252], $f'(E)$ and $f''(E)$ are the anomalous scattering depending on the X-ray energy [56]. $f'(E)$ is the real part which is related to the scattering of the atom, and $f''(E)$ is the imaginary part which is related to the absorption of the atom.

$$f(s) = \sum_{i=1}^5 a_i e^{-b_i s^2} + c \quad (17)$$

Table 5.2 shows the weighting factor for the $\text{Cu}_{50}\text{Zr}_{50}$ and $\text{Fe}_{60}\text{Nb}_{15}\text{B}_{25}$ samples at 76keV (the energy used during the experiments at I15 in ambient pressure condition). It clearly shows that for the $\text{Cu}_{50}\text{Zr}_{50}$ alloy, the Cu-Zr and Zr-Zr pairs are the dominant atom pairs to contribute the scattering information, while the Cu-Cu pair just accounts for 18.4%. For the $\text{Fe}_{60}\text{Nb}_{15}\text{B}_{25}$ alloy, the Fe-Fe and Fe-Nb pairs are the dominant pairs and together, they contribute nearly $\sim 85\%$ of the total scattering information. The other two pairs that contain B element (Fe-B and N-B pairs) just contribute $\sim 8\%$ of the total scattering information, and therefore can be neglected at certain conditions.

Table 5.2 The calculated weighting factors for the atom pairs in $\text{Cu}_{50}\text{Zr}_{50}$ and $\text{Fe}_{60}\text{Nb}_{15}\text{B}_{25}$ alloys.

Alloy and their weighting factors for each element pairs (E = 76 keV, Q = 2)	
$\text{Cu}_{50}\text{Zr}_{50}$	$\text{Fe}_{60}\text{Nb}_{15}\text{B}_{25}$
$\omega_{\text{Cu-Zr}} = 0.4899$	$\omega_{\text{Fe-Fe}} = 0.4675$
$\omega_{\text{Zr-Zr}} = 0.3262$	$\omega_{\text{Fe-Nb}} = 0.3748$
$\omega_{\text{Cu-Cu}} = 0.1840$	$\omega_{\text{Nb-Nb}} = 0.0751$
	$\omega_{\text{Fe-B}} = 0.0577$
	$\omega_{\text{Nb-B}} = 0.0232$
	$\omega_{\text{B-B}} = 0.0018$

To obtain the partial pair scattering information, we performed the anomalous X-ray scattering at the Cu and Zr edge for the $\text{Cu}_{50}\text{Zr}_{50}$ sample and Fe and Nb edge for the $\text{Fe}_{60}\text{Nb}_{15}\text{B}_{25}$ at the beamline I11 of DLS. Unfortunately, due to the Fe k-edge X-ray energy is at 7.11keV, and the window material of I11 absorbs much of the X-ray around this energy level before it hits on the sample. Hence, the scattering information at the Fe k-edge cannot be obtained in the experiment.

Figure 5.29 shows the calculated weighting factors for the atom pairs in the $\text{Cu}_{50}\text{Zr}_{50}$ for the X-ray energy from 5 to 25keV. It clearly shows that the weighting factors are energy dependent and at Cu k-edge and Zr k-edge, near zero weighting factors are found for the Cu-Cu and Zr-Zr, respectively.

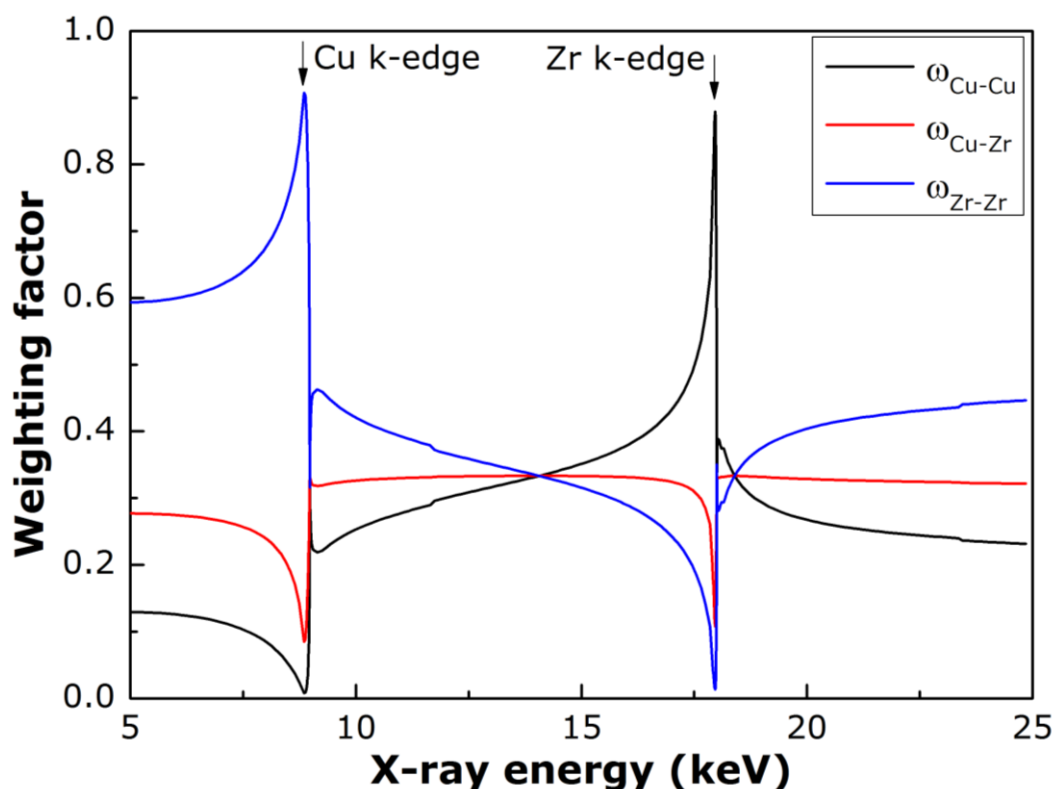


Figure 5.29 The calculated weighting factors for each atomic pair in the $\text{Cu}_{50}\text{Zr}_{50}$ alloy as a function of X-ray energy, showing near-zero weighting factor across the k-edge for the Cu and Zr element.

Figure 5.30a and Figure 5.30b show the XRD spectra of $\text{Cu}_{50}\text{Zr}_{50}$ and $\text{Fe}_{60}\text{Nb}_{15}\text{B}_{25}$, respectively obtained at different X-ray energies. Those at 76 keV were obtained at beamline I15 in ambient pressure. Those at the X-ray energies of 8.984 keV, 17.983 keV and 18.963 keV were measured at

beamline I11 using anomalous X-ray scattering technique. The samples used in both measurements are from the same batch of samples. The obtained XRD patterns were corrected for the background patterns and incoherent scattering to obtain the structure factors as shows in Figure 5.31a and Figure 5.31b. However, except those measurements made by 76 keV at I15, the structure factors are in different Q range because of the different X-ray energies used at I11 with limited 2 theta angle. Therefore, to standardise Q-range data for Fourier transformation, only Q range up to 8.4 \AA^{-1} and 13 \AA^{-1} were used for the following analysis to obtain the PDF patterns for $\text{Cu}_{50}\text{Zr}_{50}$ and $\text{Fe}_{60}\text{Nb}_{15}\text{B}_{25}$, respectively.

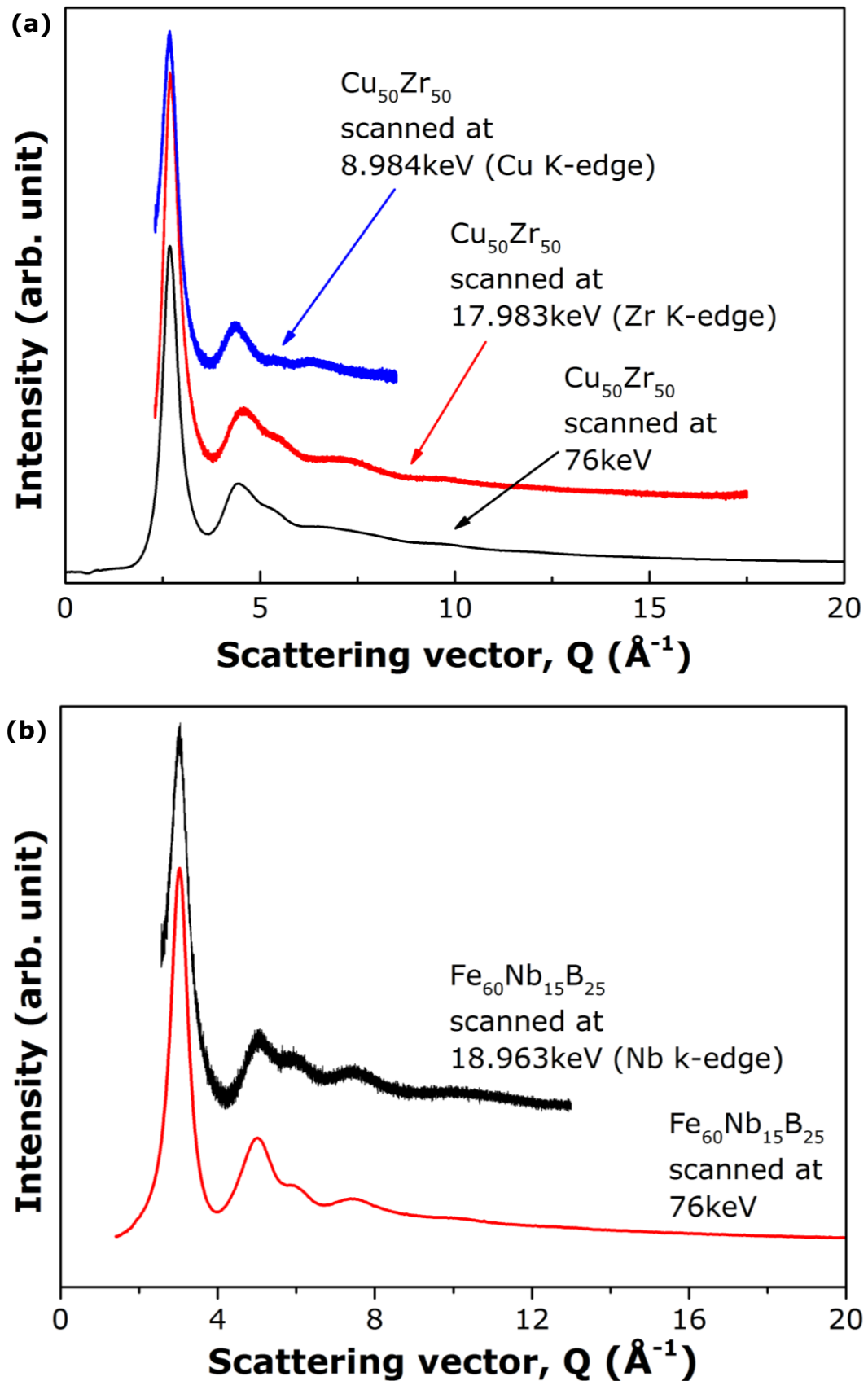


Figure 5.30 The XRD patterns measured using different X-ray energies for (a) $\text{Cu}_{50}\text{Zr}_{50}$ (b) $\text{Fe}_{60}\text{Nb}_{15}\text{B}_{25}$.

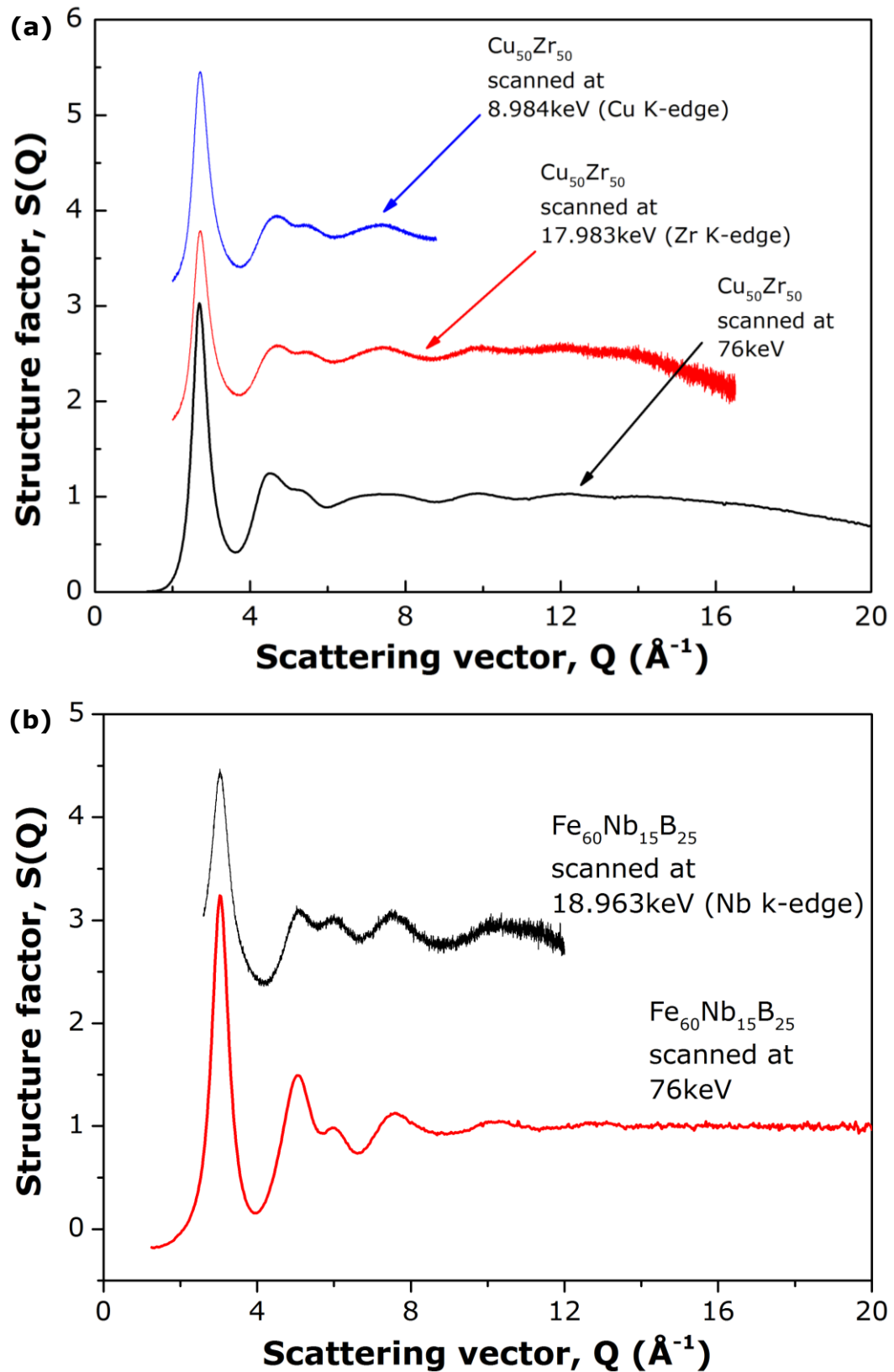


Figure 5.31 Structure factors obtained from the XRD patterns collected at different X-ray energies for (a) $\text{Cu}_{50}\text{Zr}_{50}$ (b) $\text{Fe}_{60}\text{Nb}_{15}\text{B}_{25}$.

Using the $\text{Cu}_{50}\text{Zr}_{50}$ as an example, the procedure to obtain the partial PDF is as below.

1. The total PDF can be expressed as the sum of each partial PDF, i.e. $G_{\text{Cu-Cu}}(r)$, $G_{\text{Zr-Zr}}(r)$ and $G_{\text{Cu-Zr}}(r)$ times its weighting factor as shows in Eq. (18).
2. To obtain each partial PDF, the weighting factor for each individual atomic pair was calculated using Eq. (12) for the X-ray energy at 76 keV. Table 5.2 shows the calculated weighting factors for the 2 alloys.
3. Using the calculated weighting factors showed in Table 5.2, the total PDF at 76keV for $\text{Cu}_{50}\text{Zr}_{50}$ can be calculated and showed in Eq. (19). Now, we have three unknown partial PDFs, i.e. $G_{\text{Cu-Cu}}(r)$, $G_{\text{Zr-Zr}}(r)$ and $G_{\text{Cu-Zr}}(r)$ to be solved.
4. Figure 5.29 shows the calculated weighting factors for each atomic pair in the $\text{Cu}_{50}\text{Zr}_{50}$ alloy as a function of X-ray energy. The weighting factor almost approaches zero for the Cu and Zr element at their respective X-ray k-edge. For example, using the anomalous X-ray scattering at the Cu k-edge, the $w_{\text{Cu-Cu}}$ and $w_{\text{Cu-Zr}}$ are close to zero. Hence the PDF only contains the scattering information from the Zr element as showed in Eq. (20) which only contains $G_{\text{Zr-Zr}}(r)$ information.
5. Similarly, at the Zr k-edge, the resulting PDF only contain $G_{\text{Cu-Cu}}(r)$ information as showed in Eq. (21).
6. Consequently, using Eq. (19), (20) and (21) together, the partial $G_{\text{Cu-Zr}}(r)$ can be obtained.

$$G_T(r) = w_{\text{Cu-Cu}} \times G_{\text{Cu-Cu}}(r) + w_{\text{Zr-Zr}} \times G_{\text{Zr-Zr}}(r) + w_{\text{Cu-Zr}} \times G_{\text{Cu-Zr}}(r) \quad (18)$$

$$G_{T@76\text{keV}}(r) = 0.1840 \times G_{\text{Cu-Cu}}(r) + 0.3262 \times G_{\text{Zr-Zr}}(r) + 0.4899 \times G_{\text{Cu-Zr}}(r) \quad (19)$$

$$G_{\text{Total}@Cu\ k\text{-edge}}(r) = 0 \times G_{\text{Cu-Cu}}(r) + 1 \times G_{\text{Zr-Zr}}(r) + 0 \times G_{\text{Cu-Zr}}(r) = G_{\text{Zr-Zr}}(r) \quad (20)$$

$$G_{Total@Zr\ k-edge}(r) = 1 \times G_{Cu-Cu}(r) + 0 \times G_{Zr-Zr}(r) + 0 \times \quad (21)$$

$$G_{Cu-Zr}(r) = G_{Zr-Zr}(r)$$

Figure 5.32a shows the total and partial PDF for the $Cu_{50}Zr_{50}$ alloy, each partial PDF is multiplied by its own weighting factor calculated at 76 keV. Figure 5.32b shows the enlarged section from Figure 5.32a, showing the first 3 atomic shells.

For the $Fe_{60}Nb_{15}B_{25}$, the X-ray scattering for the atomic pairs that contain B element is ignored due to its low scattering from the B element at 76 keV. Therefore, Figure 5.33a only shows the total and partial PDF for the Fe and Nb element pairs multiply with their weighting factors. Because the anomalous X-ray scattering at Fe k-edge cannot be done, only $G_{Fe-Fe}(r)$ is obtained at the Nb k-edge. The combined partial PDF of $G_{Nb-Nb}(r) + G_{Fe-Nb}(r)$ can be obtained by subtracting $G_{Fe-Fe}(r)$ away from the total PDF.

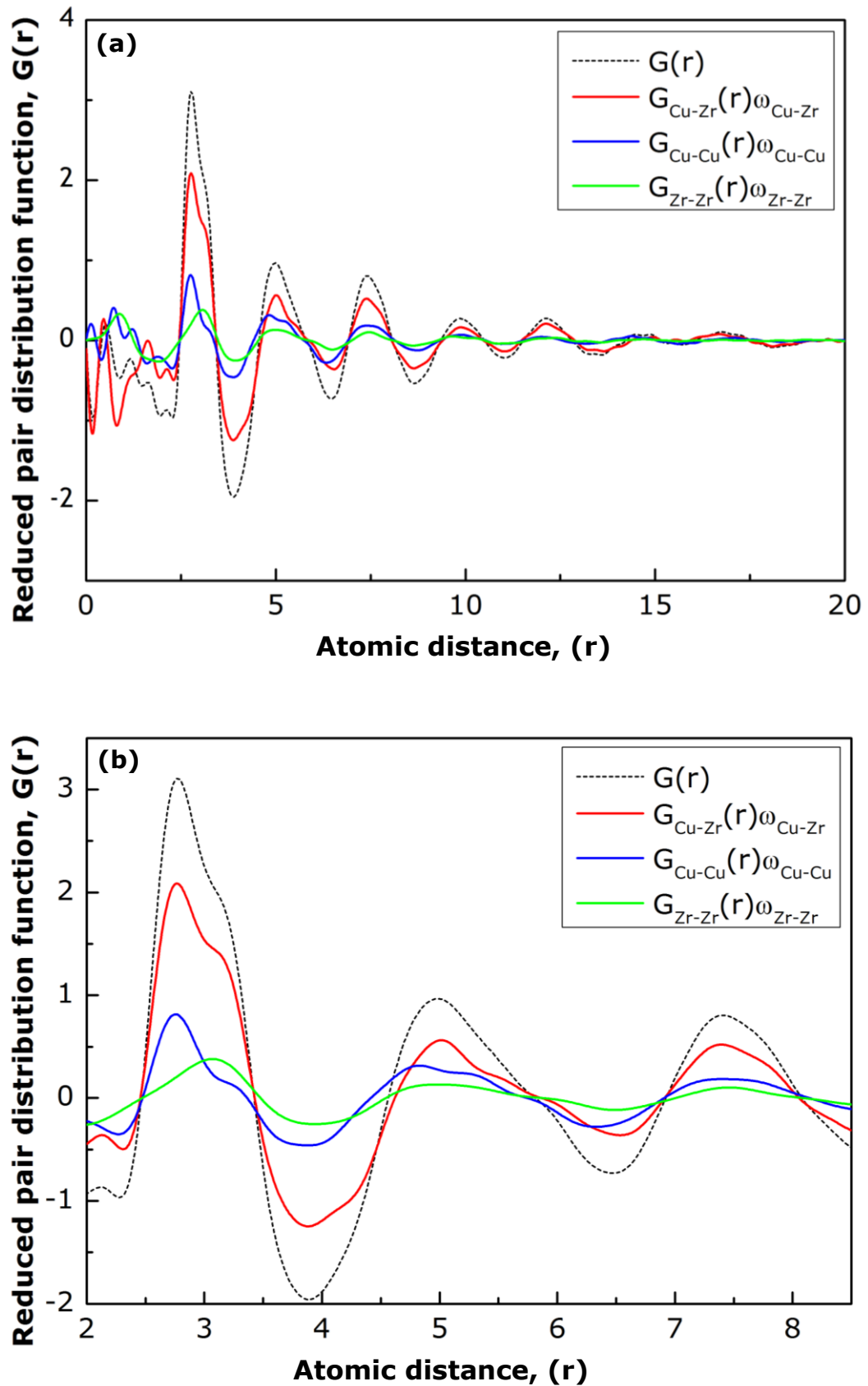


Figure 5.32 The PDF and partial PDFs for $\text{Cu}_{50}\text{Zr}_{50}$, showing the (a) SRO and MRO region, (b) an enlarged view for the first atomic shell.

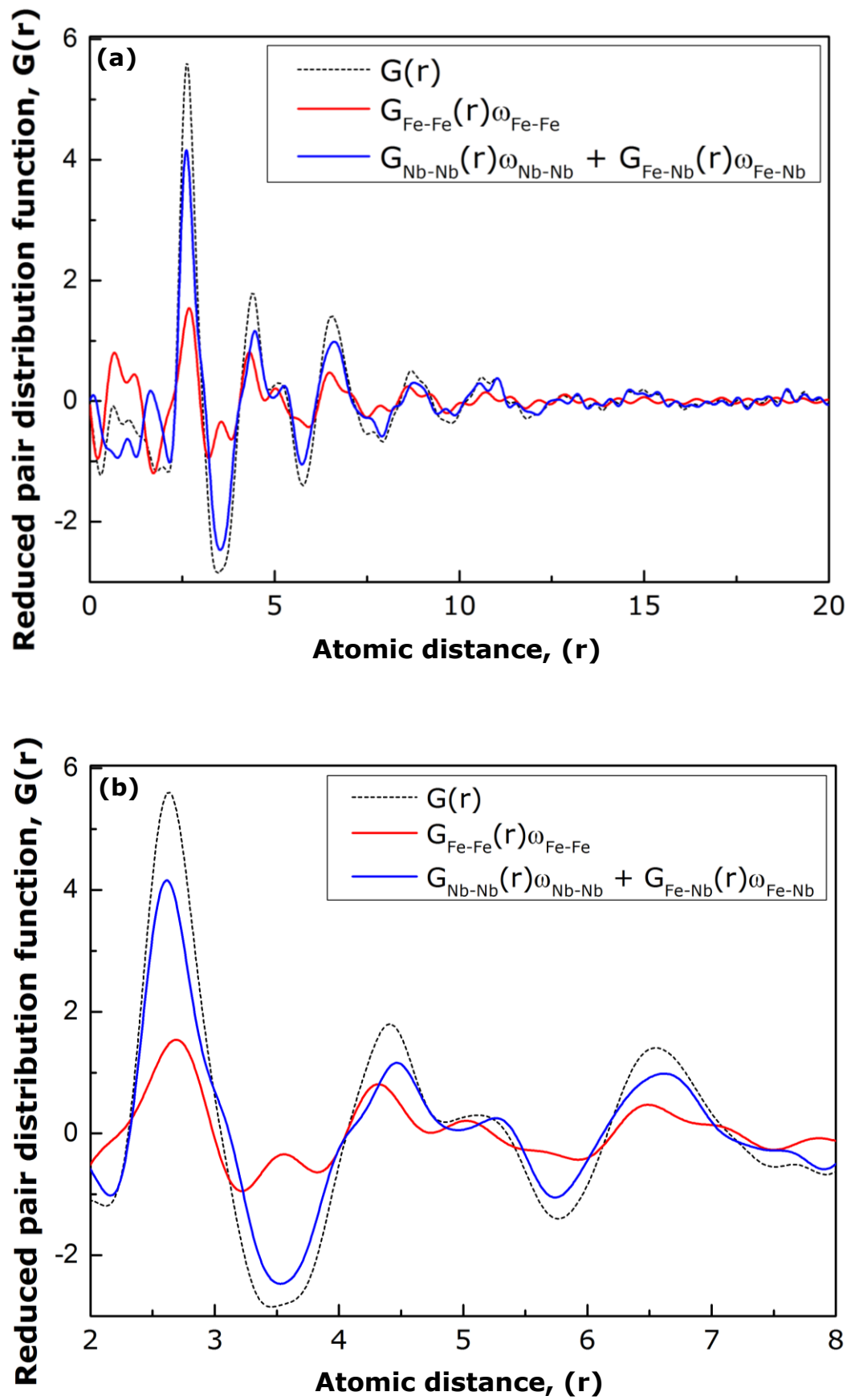


Figure 5.33 The PDF and partial PDFs for $\text{Fe}_{60}\text{Nb}_{15}\text{B}_{25}$, showing the (a) SRO and MRO region, (b) an enlarged view for the first atomic shell.

5.6 Discussion

5.6.1 Atomic structure evolution under high pressure

For the $\text{Cu}_{50}\text{Zr}_{50}$ and $\text{Fe}_{60}\text{Nb}_{15}\text{B}_{25}$, Figure 5.14 and Figure 5.20 show that, between the ambient pressures to 10 GPa and 10.85 GPa, the $\text{Cu}_{50}\text{Zr}_{50}$ FSDP shift from 2.6863 \AA^{-1} to 2.7607 \AA^{-1} at the rate of $0.00744 \text{ \AA}^{-1}\text{GPa}^{-1}$ which is higher than the $\text{Fe}_{60}\text{Nb}_{15}\text{B}_{25}$ at the rate of $0.006545 \text{ \AA}^{-1}\text{GPa}^{-1}$ (shift from 3.02374 \AA^{-1} to 3.09475 \AA^{-1}). This suggests that the $\text{Cu}_{50}\text{Zr}_{50}$ might have lower resistance to high pressure compression, hence lower bulk modulus, as compared to the $\text{Fe}_{60}\text{Nb}_{15}\text{B}_{25}$ at the initial compression stage.

Above 10 GPa and 10.85 GPa, there is a significant change in the gradient of the curve, showing the FSDP shift at a lower rate with the increase pressure. This might be due to the material enter higher density region similar phenomenon reported by Sheng regarding the polyamorphism in the $\text{Ce}_{55}\text{Al}_{45}$ MG [253]. However, without the extra measuring points between the two pressures, it is hardly to support the argument.

However, it was found that the change in the resistance of the $\text{Cu}_{50}\text{Zr}_{50}$ FSDP at 10 GPa is reflected on the 2nd atomic shell movement as shows in Figure 5.17b.

At 34.55 GPa, there is a peak split in the 3rd atomic shell as show in Figure 5.17c and Figure 5.18. This suggesting that the binary alloy might reaches its limit for compression, result in the 3rd atomic shell is begin to split and forming a second coordination.

For $\text{Fe}_{60}\text{Nb}_{15}\text{B}_{25}$, the gradual change of the shape of the 2nd atomic shell as pressure increase as shows in Figure 5.24c, implies that the changes in the resistivity of the atomic shell for further compression. Figure 5.23 shows that at ambient pressure, second half of the 2nd atomic shell are moved into the medium range order region, and with pressure increases, it was compressed into the short ranger order region (for example at 70.64 GPa). The changes in the slope in Figure 5.24c might be due to the 2nd atomic shell shifted into the short range order region, and formed densely pack metallic glass and causes increase in resistivity for compression. This was also captured in the PDF curve at 35.33 GPa, where the shoulder peak entered the short range order region.

5.6.2 The effect of atomic ratio

The two alloys selected for the high pressure experiments based on $\text{Cu}_{50}\text{Zr}_{50}$ have two different atomic radii (Cu 145pm, Zr 206pm [254]) with around 30% different from the bigger atom and same atomic concentration between the two elements. Whereas, $\text{Fe}_{60}\text{Nb}_{15}\text{B}_{25}$ ($r_{\text{Fe}} = 156\text{pm}$, $r_{\text{Nb}} = 198$, $r_{\text{B}} = 87$ [254]) have 3 huge different atomic radii with 21% and 56% different from the bigger atom and additional small B metalloid element which was found in most of the Fe-based BMG to improve their glass forming ability [255]. The shift in FSDP at different pressure level for both alloy in Figure 5.14 and Figure 5.20 show that, the $\text{Cu}_{50}\text{Zr}_{50}$ do not have a constant shift rate with the increase pressure as compared to the $\text{Fe}_{60}\text{Nb}_{15}\text{B}_{25}$ which have 3 different atomic radii with the additional small B element in its system. It might be due to the B can easily fit into the gap between the Fe and Nb which have bigger atomic radii as compared to the $\text{Cu}_{50}\text{Zr}_{50}$. Similar trend was found in the 3rd atomic shell shift, where the ternary alloy in general have consistent shift toward the lower atomic distance with significant shift rates changes at several point which suggested increase in resistance for further compression, for example in the 2nd atomic shell shows in Figure 5.24b. Whereas, for the $\text{Cu}_{50}\text{Zr}_{50}$ the atomic shell movement is more fluctuating, for example in the 3rd atomic shell shows in Figure 5.17c. The fluctuation might be due to the rearrangement between the Cu and Zr atoms for further compression.

5.6.3 The advantage of anomalous scattering

After obtaining the partial PDF for each atomic pair, especially the case for the $\text{Cu}_{50}\text{Zr}_{50}$ alloy where a full solution of the partial PDF is achieved. This allows information is revealed for the atomic distance of the different atomic pairs.

For the $\text{Cu}_{50}\text{Zr}_{50}$, it is shows in Figure 5.32b that the highest peak (2.7Å) in the 1st atomic shell is dominant by Cu-Zr pair (red curve) peak at 2.7 Å follow by the Cu-Cu pair (blue curve) at 2.76 Å. The Cu-Zr pair show significantly higher intensity as compare to the other pairs is because of the combination of two factors; (1) the weighting factor of the Cu-Zr is 0.4899 at 76keV X-ray energy, which contribute to nearly half of the scattering

signal, and (2) the highest probability of the Cu-Zr pair existing in the 1st atomic shell which show the Cu-Zr pair has more ordered structure. Whereas the Zr-Zr pair (green curve) has higher probability at 3.07 Å which is offset from the 1st atomic shell, causing a shoulder profile to form on the right of the 1st peak of the total PDF, indicating that the Zr-Zr pair has more probability in occupying the location beyond the 1st atomic shell.

For the 2nd atomic shell, the peak at 4.98 Å is found dominated by the Cu-Zr pair (red curve) which has the highest probability at 4.99 Å. The Zr-Zr pair was found to have a quite flat profile beyond ~4.5 Å, implying that beyond the 1st atomic shell, the Zr-Zr pair is quite randomly distributed, contributing much to the amorphous structure of this particular alloy.

For the 3rd atomic shell, the peak at 7.41 Å is again found dominated by the Cu-Zr pair (red curve) which peak was found at 7.38 Å. The Cu-Cu pair was found similar to the Zr-Zr pair with quite flat profile in the 3rd atomic shell.

For the Fe₆₀Nb₁₅B₂₅, Figure 5.33b shows that in the first atomic shell at 2.63 Å, the Fe-Fe pair (red curve) peak at 2.69 Å are slightly offset from the 1st atomic shell. Whereas the combined Nb-Nb and Fe-Nb pairs (blue curve) were found to have the highest probability in the 1st atomic shell with peak at 2.61 Å.

For the 2nd atomic shell, the peak at 4.41 Å was found to be composed of the Fe-Fe pair (red curve) at 4.32 Å and the combined Nb-Nb and Fe-Nb pairs (blue curve) at 4.47 Å. Both Fe-Fe and the combined Nb-Nb and Fe-Nb pairs peaks are not similar to the 2nd atomic shell. It suggested that the 2nd atomic shell is composed of the different distribution of the partial pairs.

For the 3rd atomic shell, the peak at 6.55 Å is dominated by the distribution of the Nb-Nb and Fe-Nb pairs, which peak at 6.62 Å. Whereas, the Fe-Fe pair peak was found at 6.49 Å. Again, this is similar to the 2nd atomic shell, where the 3rd atomic shells are composed of the different distribution of the partial pairs. However, without the partial PDF, $G_{Nb-Nb}(r)$ information, we cannot resolve it completely.

Using the anomalous X-ray scattering, (1) the Cu-Zr pair was found to be the dominant in the 2nd atomic shell, which is the atomic shell that correlated to the changes in the FSDP shift at 10 GPa. (2) Similarly, the Cu-Zr pair has the highest probability that correlated to the peak split phenomenon occur in the 3rd atomic shell at 34.55 GPa. Which the splitting

is caused by the unevenness of polyhedral connecting styles in the amorphous, which results from its higher density and different style of cluster dense packing [256]. (3) Compared to the partial pair between the $\text{Cu}_{50}\text{Zr}_{50}$ and $\text{Fe}_{60}\text{Nb}_{15}\text{B}_{25}$, the partial pair of the Fe-Fe pair and the combined Nb-Nb and Fe-Nb pair were always found offset in the 2nd and 3rd atomic shells. This suggest that the difference in atomic ratio causes the distribution of difference in the atomic pair distance in the 2nd and 3rd atomic shell, making the atomic shells compression less fluctuation as compare to the $\text{Cu}_{50}\text{Zr}_{50}$, in which the 2nd and 3rd atomic shells are dominated by single Cu-Zr atomic pair.

5.7 Summary

This chapter contains the results and discussion for the binary alloy $\text{Cu}_{50}\text{Zr}_{50}$ and ternary alloy $\text{Fe}_{60}\text{Nb}_{15}\text{B}_{25}$ under high pressure compression. The chapter discusses in details the data analysis procedure to extract the crucial atomic structure information in order to investigate their changes under high pressure compression. The shift in the atomic shells for the binary and ternary alloys are discussed with their possible partial atomic pair information obtained using anomalous X-ray scattering.

Chapter 6 Novel metallic glass alloys for neutron absorption studies

This chapter describes systematically the design, making and characterisation of a series of new Fe-based metallic glassy alloys. One of the main target applications is neutron shielding, for example as coating materials for containers to store nuclear waste generated from nuclear power plants over very long period of time. Section 6.1 describes the design and making of the alloys. Section 6.2 and 6.3 present the structures and properties of those alloys characterised using synchrotron X-ray diffraction (SXRD), scanning electron microscopy (SEM) and nano-indentation. Section 6.4 summarises the neutron transmission results measured on those alloys followed by a discussion in Section 6.5.

6.1 Design, making and characterisation of new glassy alloys

The aim of the research is to develop novel metallic glass based alloys with high corrosion resistance and high neutron shielding capability. The alloys need to be competitive in cost and therefore the major alloy elements considered should be abundant in nature and cheaper in market and can be manufactured using conventional and lower-cost metal mass production techniques, such as casting.

Based on those above requirements, Fe is chosen as the matrix element because of its abundance in nature and low cost. After the first successful synthesis of Fe-based BMG $\text{Fe}_{72}\text{Al}_5\text{Ga}_2\text{P}_{11}\text{C}_6\text{B}_4$ in 1995 by Inoue [257], many Fe-based bulk metallic glassy alloys have been successfully developed in the past 20 years or so [255], for example $\text{Fe}_{66}\text{Nb}_4\text{B}_{30}$ [258], $\text{Fe}_{48}\text{Cr}_{15}\text{Mo}_{14}\text{C}_{15}\text{B}_6\text{Er}_2$ [216], $\text{Fe}_{48}\text{Cr}_{15}\text{Mo}_{14}\text{C}_{15}\text{B}_6\text{Y}_2$ [259]. The alloy design principles and alloy composition ranges of those alloys can be adopted in this research. Cr and Mo are selected because they are the major elements for providing corrosion and wear resistance properties for metal alloys and metal based glassy alloys as reported in [260, 261]. C is the key element in Fe based alloys to contribute hardness, and more importantly, C and B atoms have smaller radii and form the metalloids required for high glass-forming ability [262]. To enhance neutron shielding or reduce neutron

transmission, Gd and B are chosen because of their high neutron total cross section (called NTCS hereafter) [263]. Especially, Gd is an element with the highest NTCS among all naturally occurred metal elements [263].

Figure 6.1 shows that the NTCS of Gd is approximately two orders of magnitude higher than that of B in neutron energy below ~ 50 meV. Above ~ 50 meV, the NTCS of Gd begins to fall off but is still higher than B until ~ 500 meV. However, in the energy range ~ 500 meV to ~ 190 eV, the NTCS of Gd is lower than B except at the resonance peak energies. Therefore the presence of B is beneficial in compensating the low NTCS of Gd in this energy range. In the fast neutron energy region (10 KeV – 20 MeV), although the NTCS of both elements reduces significantly, Gd is still about 1 order of magnitude higher than that of B. Hence Gd can still provide a certain shielding capability to capture the fast neutron (0 – 8 MeV as shows in Figure 6.2 [264]) emitted from the waste generated by the spontaneous fission and alpha decay (α, n) reaction with the oxygen. Of course, in reality, other neutron moderating materials (groundwater) are always needed to “slow down” the fast neutrons before they reach the shielding materials [265]. For example, the neutron moderator (110 K methane) used in the pulsed neutron source [266]. In the designed alloys, Gd and B are the most important elements that provide the function of shielding neutrons of a wide energy range. The ultimate goal of this study is to tailor the concentrations of Gd, B and other major elements in the alloys to achieve the maximum neutron shield capacity with maximum glass forming ability. It is worth to point out that natural Gd and B were used in the alloy development rather than the high neutron cross section isotopes. Therefore it is possible to further improve the neutron shielding capability by replacing Gd and B with their isotopes, i.e. Gd-157 and B-10 [267].

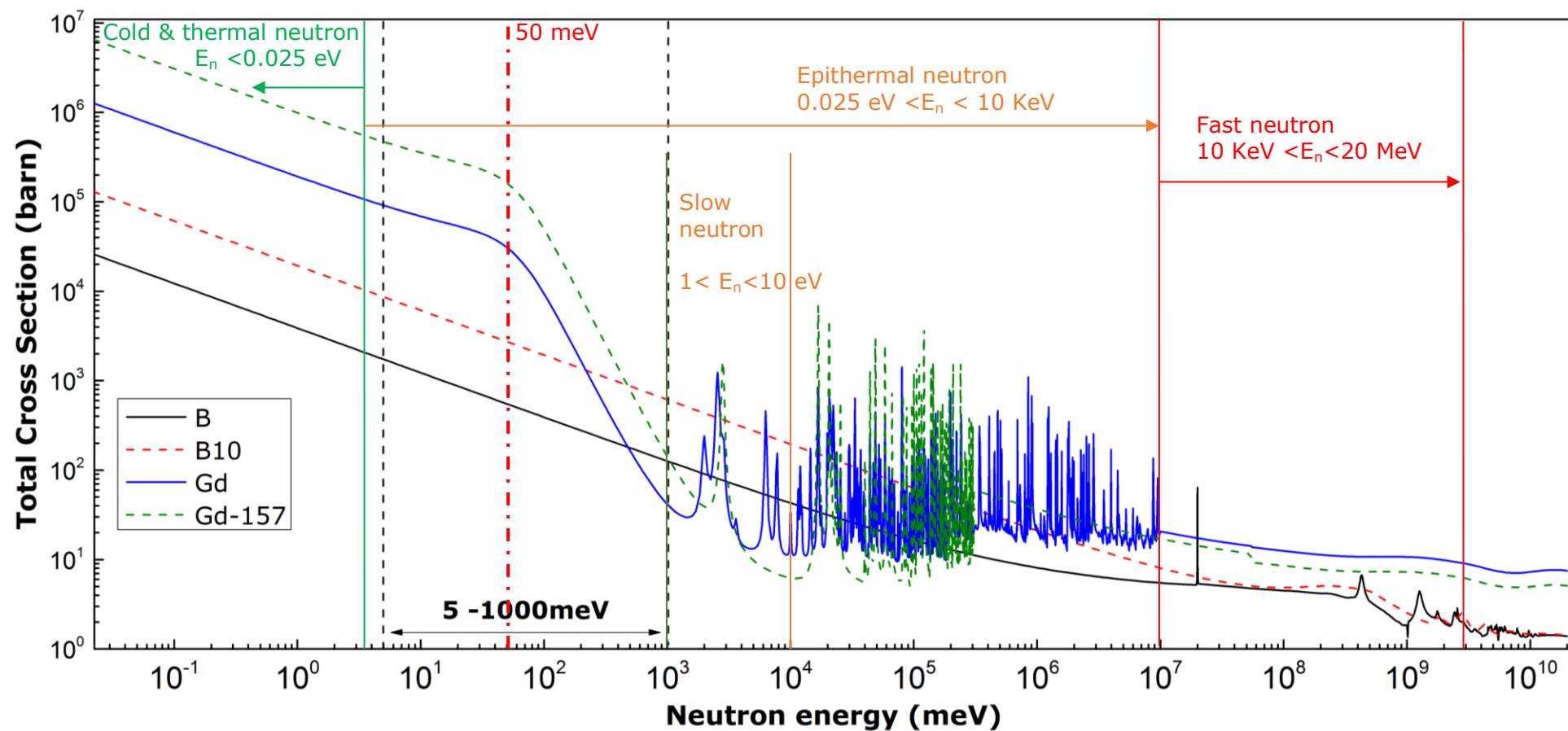


Figure 6.1 Total cross section as a function of neutron energy for Gd-157 and B-10 isotopes [267], compared to calculated cross sections according to the natural abundance of Gd and B [268]. and the classification of neutrons based on their kinetic energy, i.e. thermal, epithermal, slow and fast neutron [269].

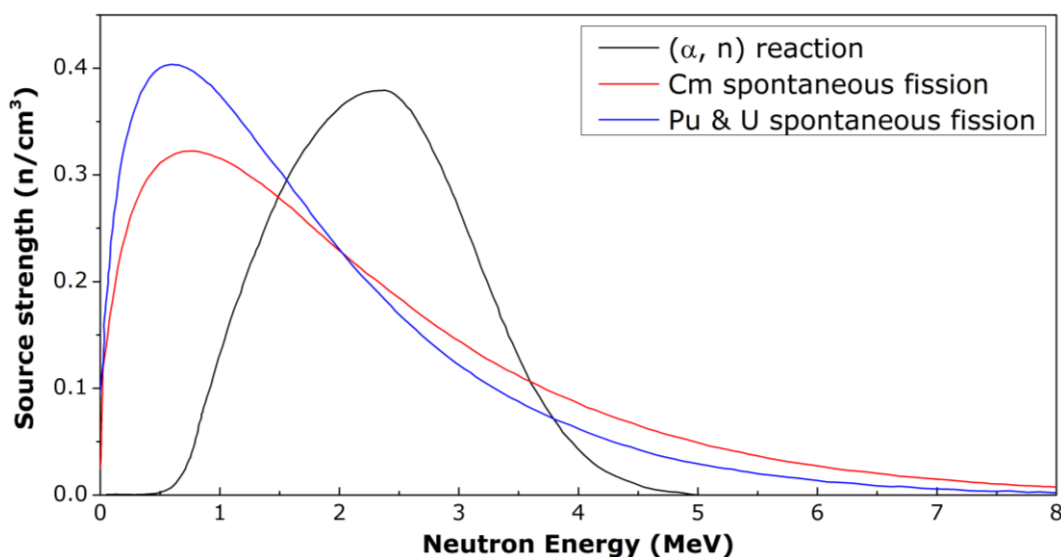


Figure 6.2 The calculated weighting factor of neutron generated from the pressurised water reactor spent fuel through (α, n) reactions with the oxygen and spontaneous fission from the plutonium, uranium nuclide and curium nuclide as a function of neutron energy [264].

Iterative approach was used to design, make and characterise new alloys in three rounds over 3 years from 2012 to 2014. Table 6.1, Table 6.2 and Table 6.3 summarise the designed alloy compositions in each round. The corresponding ingots and samples for each alloy were melt in an arc melting furnace and then cast into a water cooled copper mould to form rod bars of stepped diameters as described in Section 3.2 of Chapter 3. The different diameter sections have different cooling rates, facilitating the studies of cooling rates on the glass forming ability of the designed alloys.

The relationships between crystalline structures or glassy states of the designed alloys were characterised using synchrotron X-ray diffraction (SXR) method and scanning electron microscopy (SEM). Pair distribution function was also used to study the changes of atomic structures of Fe-B₆Gd₂ and Fe-B₆Y₂ alloys produced at different cooling rates. In addition, nano-indentation was also carried out to obtain hardness and Young's modulus for the Fe-B₆Gd₂ and Fe-B₆Y₂ alloys at different cooling rates.

The SXR measurements on the newly designed alloys and samples were mainly carried out at the high pressure experiments in beamline I15 (Table 1.1 during the free time between preparing and loading a sample into Diamond Anvil Cell. The SXR data of $\varnothing 5.8$ mm Fe-B₆Y₂ were measured

separately at beamline I12 during the EE10440-1 experiment of 4-6 Feb 2015. Figure 6.3 shows the SXR patterns for Fe-B₆Y₂ sample acquired at I15 and I12. Due to different detector setup, a full 2D ring pattern was acquired at I15 (Figure 6.3a), While a slightly bigger than half ring patterns was obtained at I12 because of the offset detector setup in that particular experiment for acquiring SXR patterns in higher Q range.

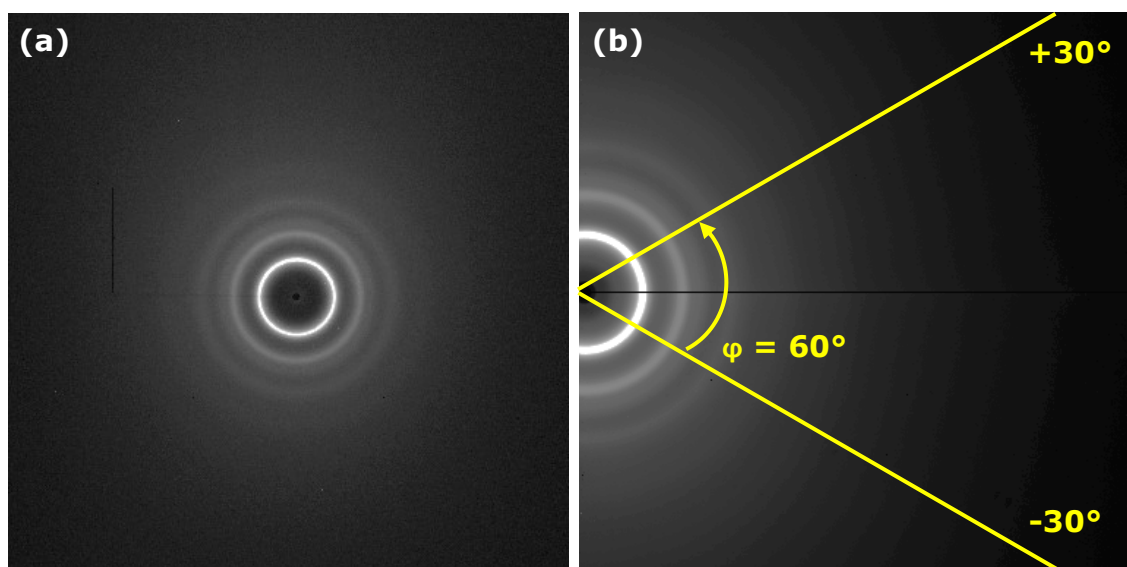


Figure 6.3 Typical 2D SXR patterns of Fe-B₆Y₂ step rod bar sample acquired at (a) I15 for the ø4 mm section, and (b) at I12 for the ø5.8 mm section.

To integrate the 2D patterns into 1D spectrum, the shadows caused by the beam stopper and detector dead pixels were firstly masked out using the threshold method in software Fit2D. The integration was made with φ angle from 0 to 360° for the SXR patterns obtained from I15. While for those from I12, the integration was made for φ angle from -30° to 30° as shows in Figure 6.3b.

6.1.1 The 1st round alloy design: selection of basic alloy systems

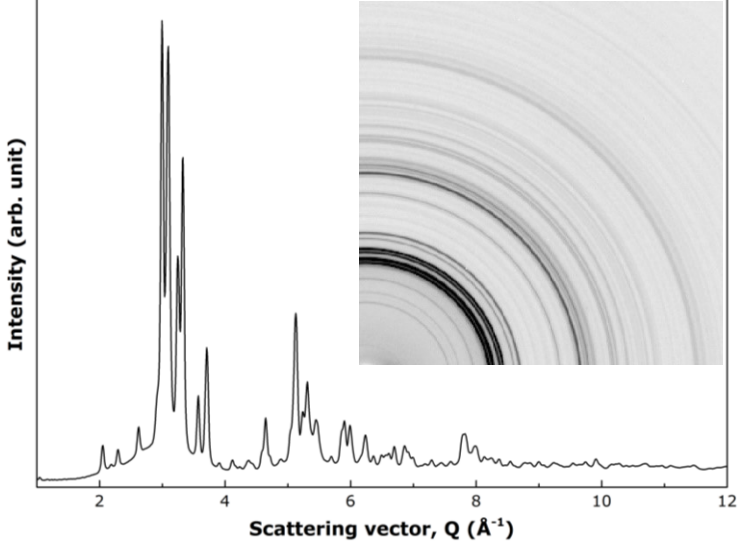
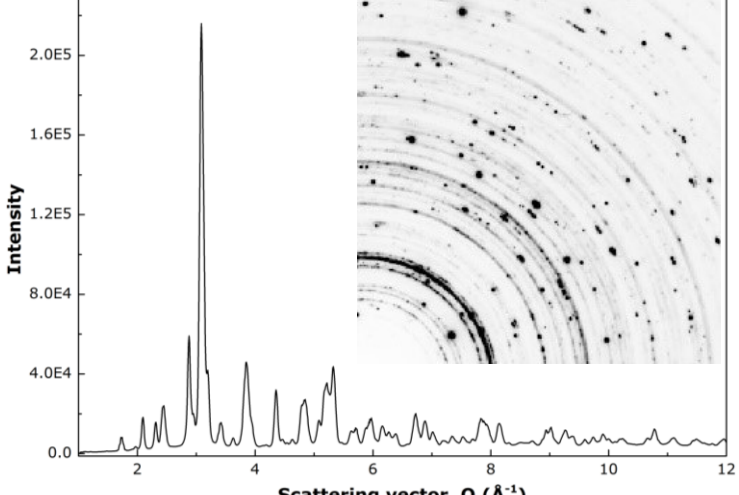
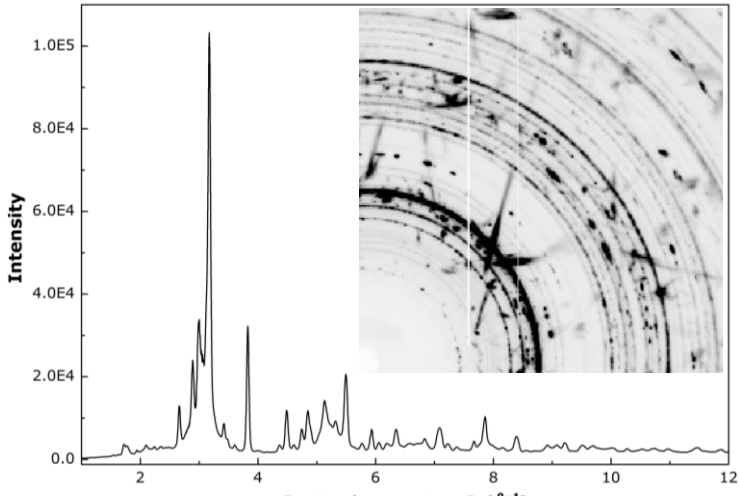
The 1st round alloys designed are summarised in Table 6.1. Firstly, a Fe₇₅B₂₅ binary alloy was used as the baseline system, because B is one of the typical element (other include C, Si and P) to form metalloid structures which is essential for Fe-based metallic glasses [270]. Then, Nb was added into the system to create a ternary system (Fe₆₆Nb₄B₃₀) that has 3 different atomic radii ($r_{\text{Fe}} = 156\text{pm}$, $r_{\text{Nb}} = 198$, $r_{\text{B}} = 87$ [254]) which is another important empirical rule for designing metallic glasses and has been reported

successfully to manufacture into \varnothing 1mm rod BMG [258]. However both alloys contain crystalline phases with intense crystalline peaks present in their 1D SXRD spectra. Thirdly, Cr was added into the ternary system to improve the corrosion resistance, and Si added as the secondary metalloid element to form a five-element alloy (FeNb-Si₅), which shows a slight decrease in the intensity of the crystalline peak of its 1D spectrum. In addition, needle shape feature was found on the 2D pattern. Finally, the Nb was replaced by the Mo to improve the corrosion resistance, and concentration of Si and B were slightly changed to form the Fe-Si₃B₃ and Fe-Si₆ alloys. Unfortunately both alloys still have crystalline structures.

6.1.2 The 2nd round alloy design: improving glass forming ability

The 2nd batch alloys designed are summarised in Table 6.2. Firstly, using the Fe-Si₃B₃ developed in the 1st round, the Si was replaced by C to form the Fe-B₅ five-element system. C can also improve the hardness of the alloy. In general, the 1D spectrum from Fe-B₅ shows slightly reduced crystalline peaks intensity as compared to that from Fe-Si₃B₃. However, needle features were again found on the 2D pattern from Fe-B₅. To further improve the glass forming ability, Elements with large atomic radii, such as Sn ($r_{\text{Sn}} = 145\text{pm}$) and Zr ($r_{\text{Zr}} = 206\text{pm}$) were added into the system to form Fe-B₆Sn₂ and Fe-B₆Zr₂ which show a significant improvement in glass forming ability. Especially, for the case of Fe-B₆Zr₂, its 1D spectrum shows almost a fully amorphous state with only a few very small crystalline peaks present. To further improve the glass forming ability, the 2% of Zr was replaced by 1% of Sn and 1% Zr to form Fe-B₆Zr₁Sn₁. Again, the 1D spectrum shows an improvement in the glass forming ability with further reduction in the crystalline peak intensity. Lastly, by replacing 1% Sn and 1% Zr with 2% Y (a rare earth element), an alloy similar to the published composition [259] was made, and its 1D spectrum and 2D pattern show a complete amorphous state.

Table 6.1 The 1st round alloys designed and their SXRD patterns and spectra.

Alloy code (at. %)	Synchrotron X-ray diffraction result
$\emptyset 2\text{mm Fe}_{75}\text{B}_{25}$ ($\text{Fe}_{75}\text{B}_{25}$)	
$\emptyset 3\text{mm Fe}_{66}\text{Nb}_4\text{B}_{30}$ ($\text{Fe}_{66}\text{Nb}_4\text{B}_{30}$)	
$\emptyset 2\text{mm FeNb-Si}_5$ ($\text{Fe}_{50}\text{Cr}_{25}\text{Nb}_4\text{Si}_5\text{B}_{16}$)	

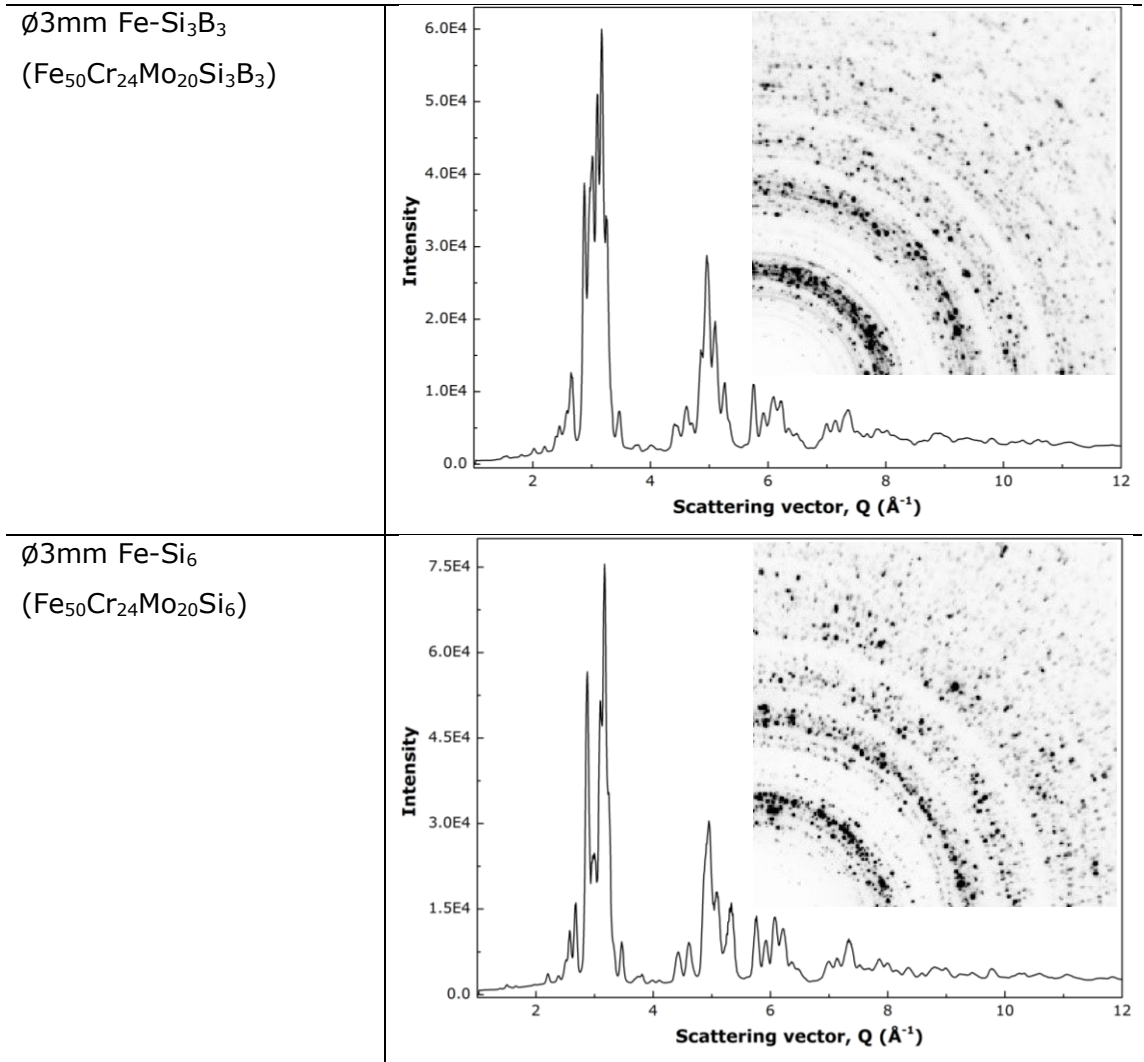
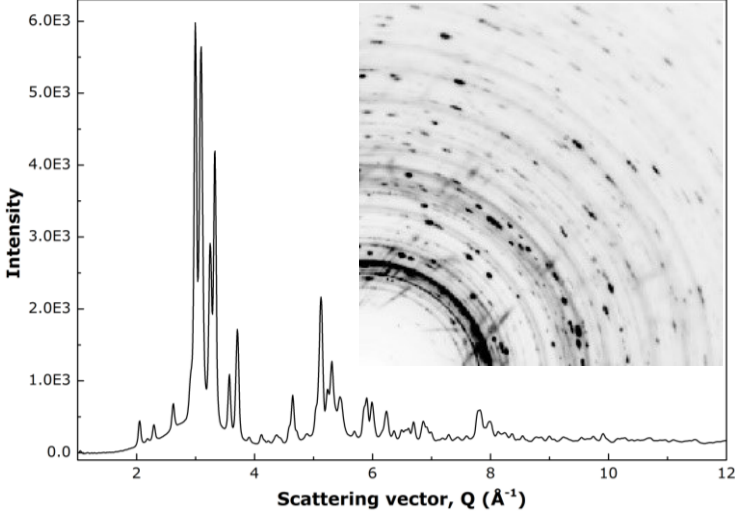
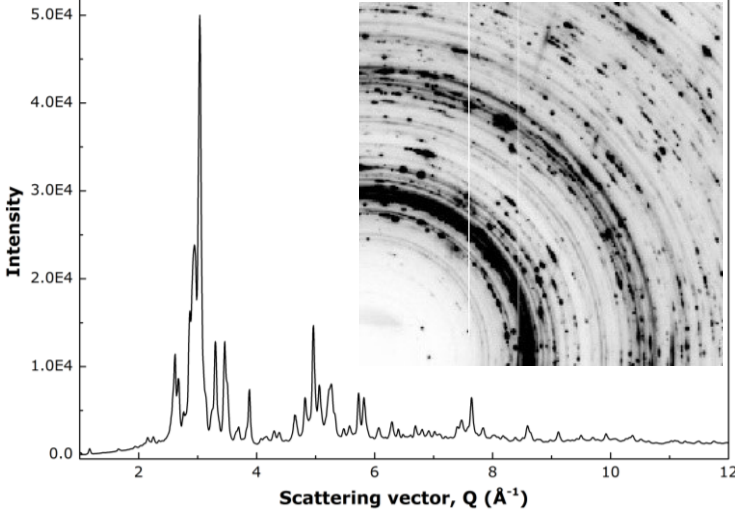
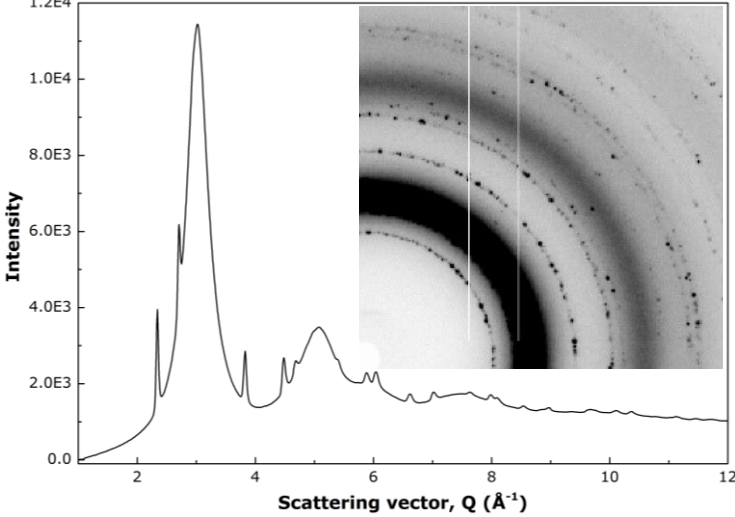
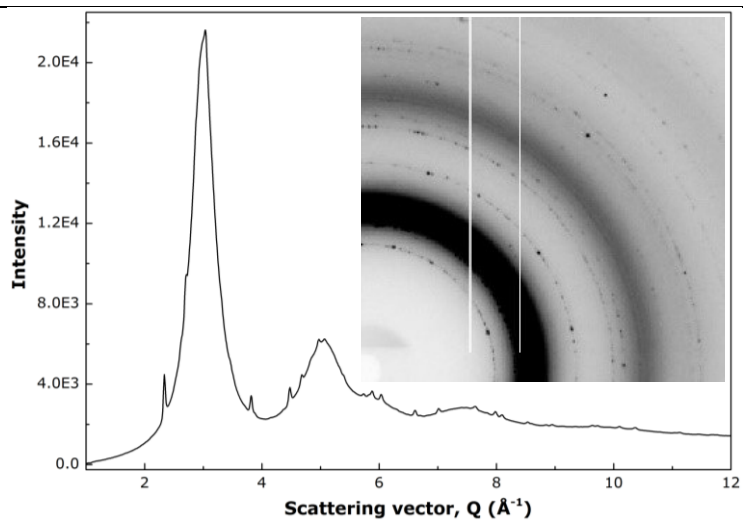


Table 6.2 The 2nd round alloys designed and their SXRD patterns and spectra.

Alloy (at %)	X-ray diffraction 2D pattern and 1D spectrum
Ø2mm Fe-B ₅ (Fe ₄₅ Cr ₁₆ Mo ₁₆ C ₁₈ B ₅)	
Ø2mm Fe-B ₆ Sn ₂ (Fe ₄₈ Cr ₁₅ Mo ₁₄ C ₁₅ B ₆ Sn ₂)	
Ø2mm Fe-B ₆ Zr ₂ (Fe ₄₈ Cr ₁₅ Mo ₁₄ C ₁₅ B ₆ Zr ₂)	

$\varnothing 2\text{mm Fe-B}_6\text{Zr}_1\text{Sn}_1$
($\text{Fe}_{48}\text{Cr}_{15}\text{Mo}_{14}\text{C}_{15}\text{B}_6\text{Zr}_1\text{Sn}_1$)



$\varnothing 3\text{mm Fe-B}_6\text{Y}_2$
($\text{Fe}_{48}\text{Cr}_{15}\text{Mo}_{14}\text{C}_{15}\text{B}_6\text{Y}_2$)

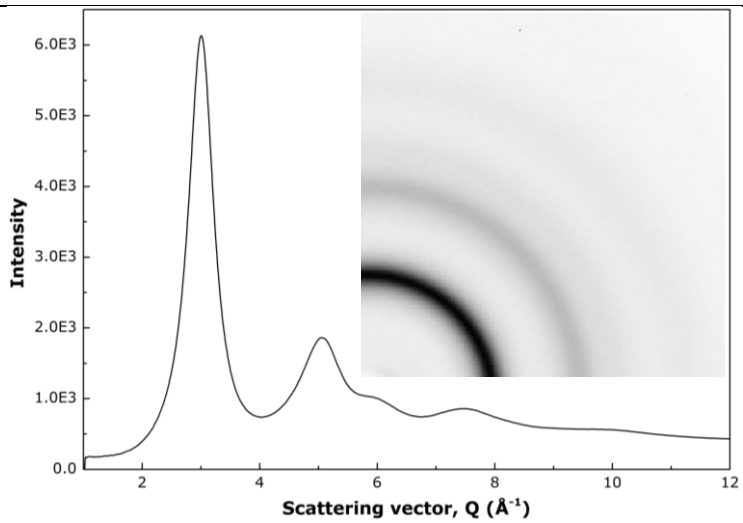
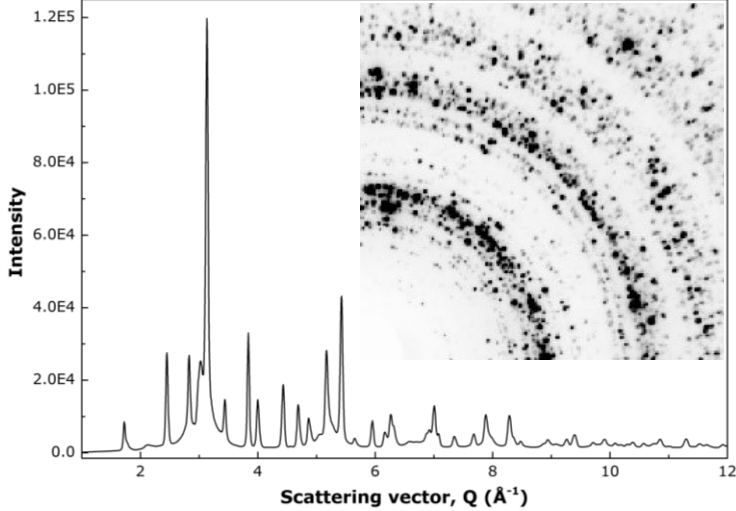
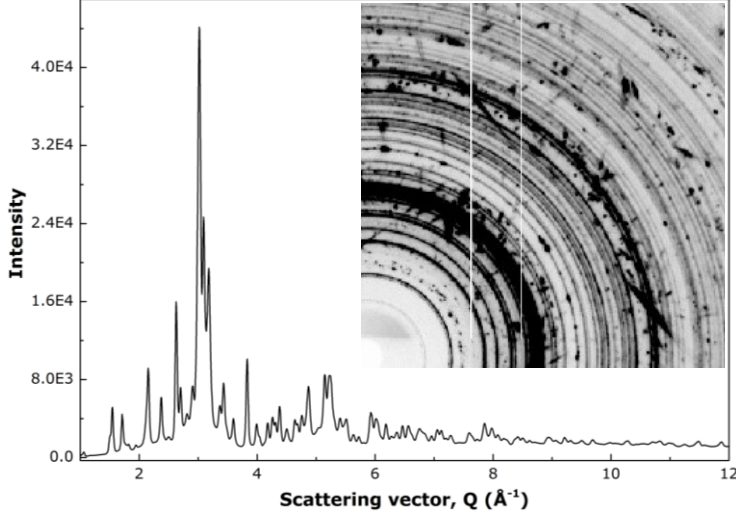
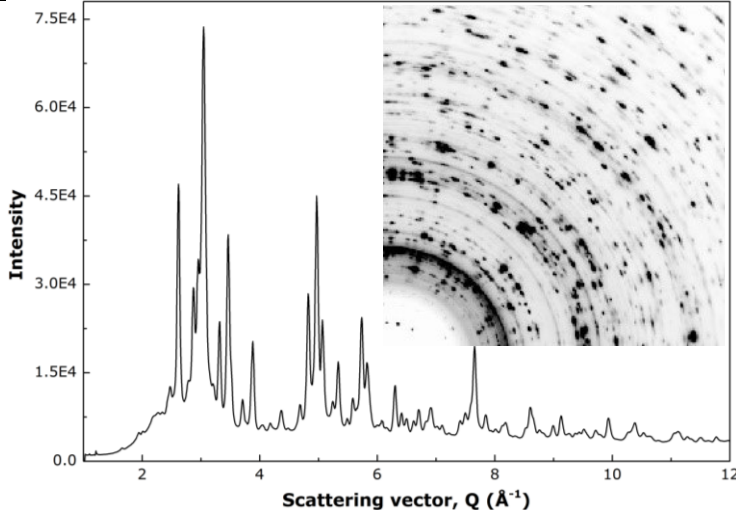
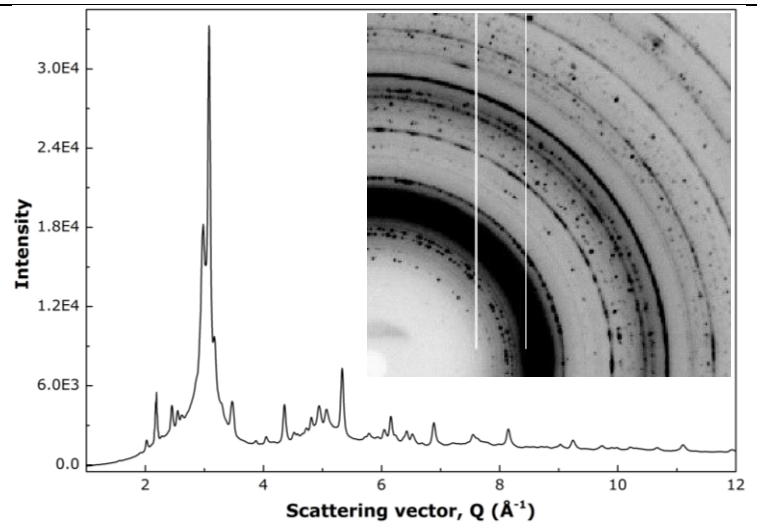


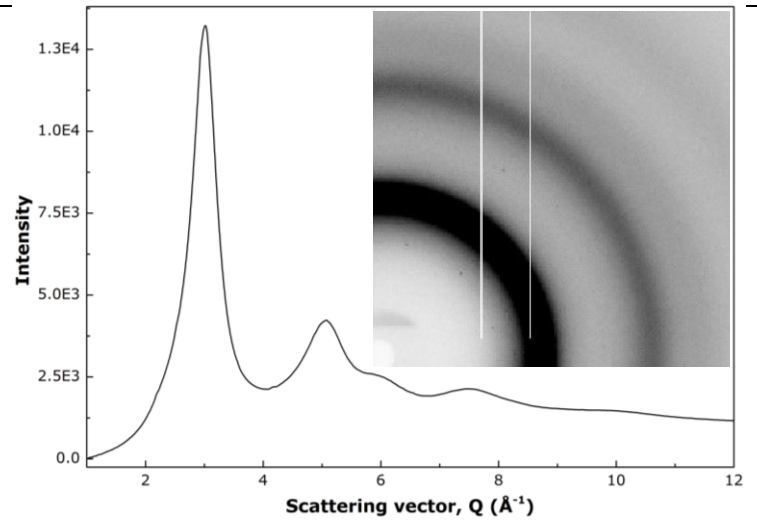
Table 6.3 The 3rd round alloys designed and their SXRD patterns and spectra.

Alloy (at %)	X-ray diffraction 2D pattern and 1D spectrum
Ø2mm Fe-B ₁₆ (Fe ₅₂ Cr ₁₉ Mn ₂ Nb _{4.5} B ₁₆ C ₄ Si _{2.5})	
Ø2mm FeNb-Si ₅ Gd ₃ (Fe ₅₀ Cr ₂₂ Nb ₄ B ₁₆ Si ₅ Gd ₃)	
Ø2mm FeMn-B ₆ Gd ₂ (Fe ₄₈ Cr ₁₅ Mn ₁₄ C ₁₅ B ₆ Gd ₂)	

∅2mm Fe-B₁₅Gd₂
(Fe₄₈Cr₁₅Mo₁₄C₆B₁₅Gd₂)



∅2mm Fe-B₆Gd₂
(Fe₄₈Cr₁₅Mo₁₄C₁₅B₆Gd₂)



6.1.3 The 3rd round alloy design: improving neutron shield capacity

The 3rd round alloys designed are summarised in Table 6.3. Built upon the success of the 2nd alloy design, the 3rd round was mainly focused on improving the neutron shielding capability. Firstly, alloy Fe-B₁₆ was designed based on the composition of SAM2X5 (Fe_{49.7}Cr_{17.7}Mo_{7.4}W_{1.6}Mn_{1.9}Si_{2.4}B_{15.2}C_{3.8}) [162] by replacing the very high melting point element Mo (2896 K) and W (3695 K) with Nb (2742 K). However, the result was not encouraging, and crystalline phases were present as shows in the 1D spectrum. Then, Mn and C were replaced by Gd to improve neutron shielding capability, and form the FeNb-Si₅Gd₃. Its 1D spectrum shows very complicated crystalline structures with needle features again found in the 2D pattern. Thirdly, in the FeMn-B₆Gd₂, Nb was replaced by Mn and the corresponding 1D spectrum shows a less complicated crystalline structures. For Fe-B₁₅Gd₂, Mo was again added into the system to replace Mn, and 1D spectrum shows a significant improvement in glass forming ability. Lastly, the concentration of the two metalloid elements, C and B were reversed to form Fe-B₆Gd₂, and the 2D pattern and 1D spectrum show that a fully amorphous state is achieved again for this alloy. The neutron shield capacity for these alloys are described in section 6.4 later.

6.2 Effect of cooling rates on glass forming of the designed alloys

The two amorphous alloys, Fe-B₆Gd₂ and Fe-B₆Y₂, were chosen to investigate their atomic structures formed at different cooling rates, using the different diameter samples taken from the as-cast step rod bars.

Total synchrotron X-ray scattering and pair distribution function method were used for such studies. Figure 6.4 and Figure 6.5 show the SXR patterns obtained for the different diameter samples from the as cast step bars of Fe-B₆Gd₂ and Fe-B₆Y₂ alloys, respectively. A quarter of the 2D SXR pattern acquired for each different diameter sample is cropped from its whole pattern, magnified and showed together with the corresponding 1D spectrum to highlight the transition from crystalline structure to amorphous structure for the different diameter samples. Each 1D spectrum was then subtracted from its background diffraction pattern and imported into pdfgetX2 software to obtain the reduced pair distribution function (PDF).

Figure 6.6a and Figure 6.6b show the calculated PDF patterns for the different diameter samples from the Fe-B₆Gd₂ and Fe-B₆Y₂ alloys.

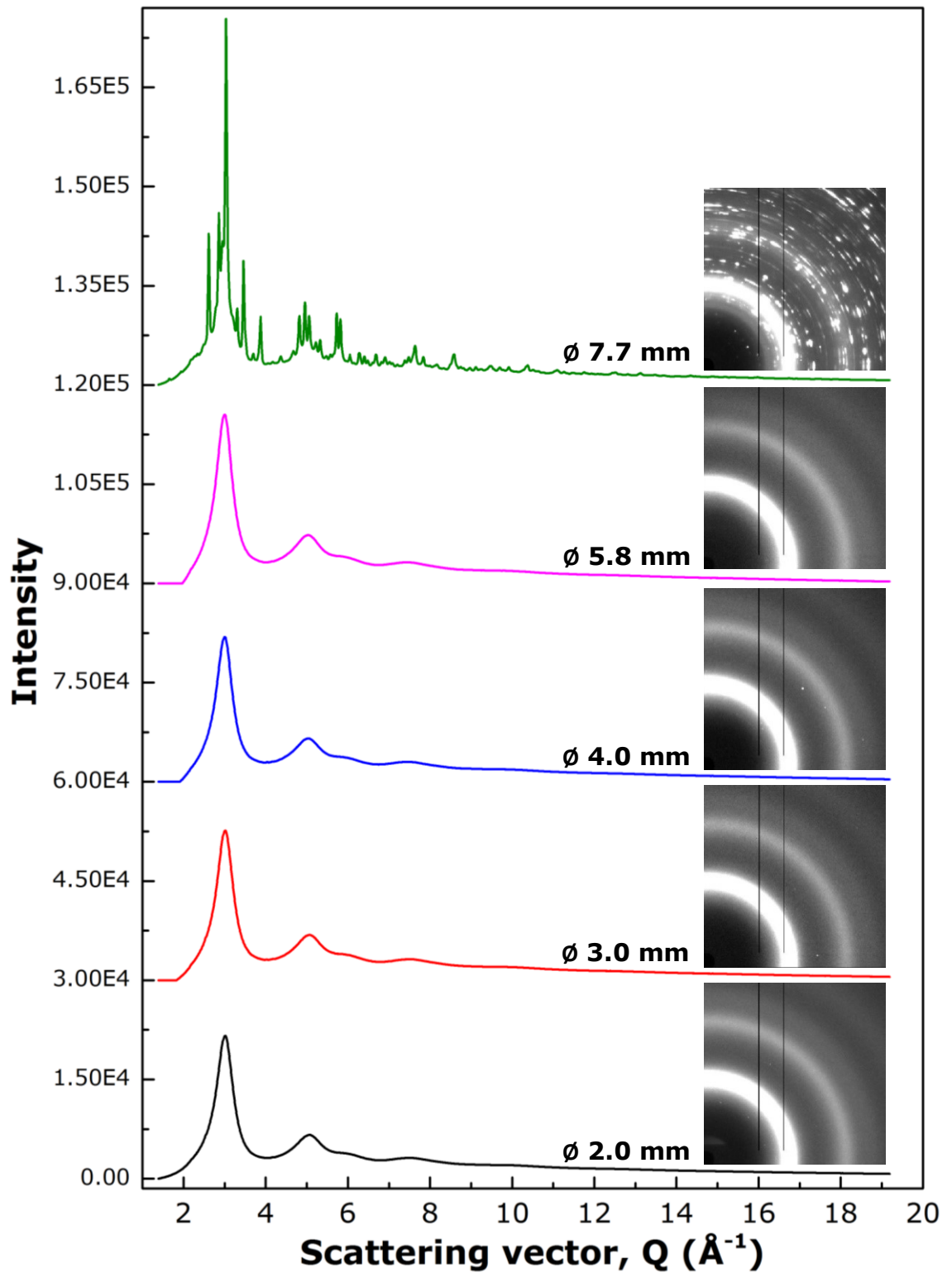


Figure 6.4 The 1D spectra and corresponding 2D SXR patterns for the different diameter samples from the Fe-B₆Gd₂ alloy.

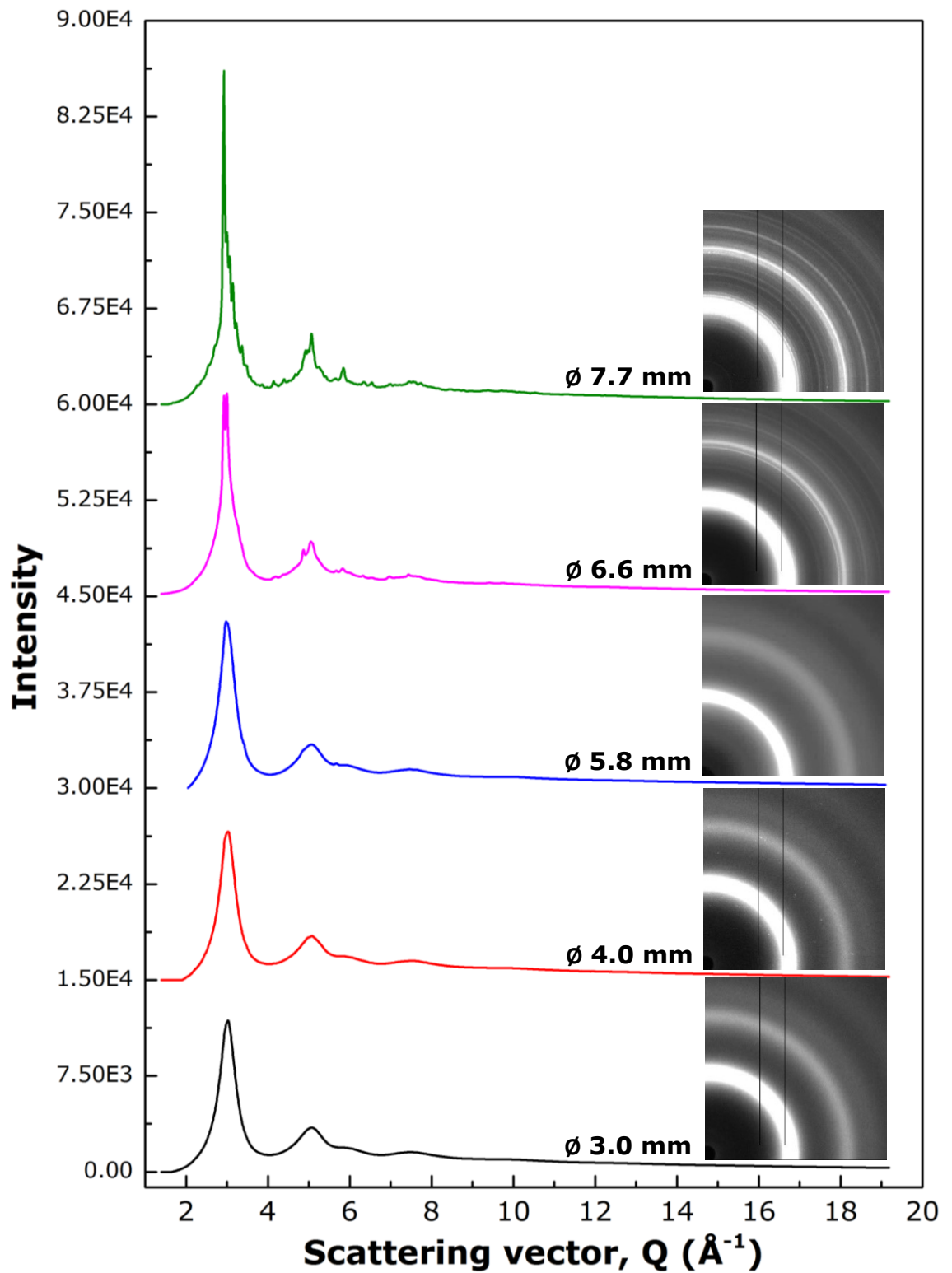


Figure 6.5 The 1D spectra and corresponding 2D SXR patterns for the different diameter samples from the Fe-B₆Y₂ alloy.

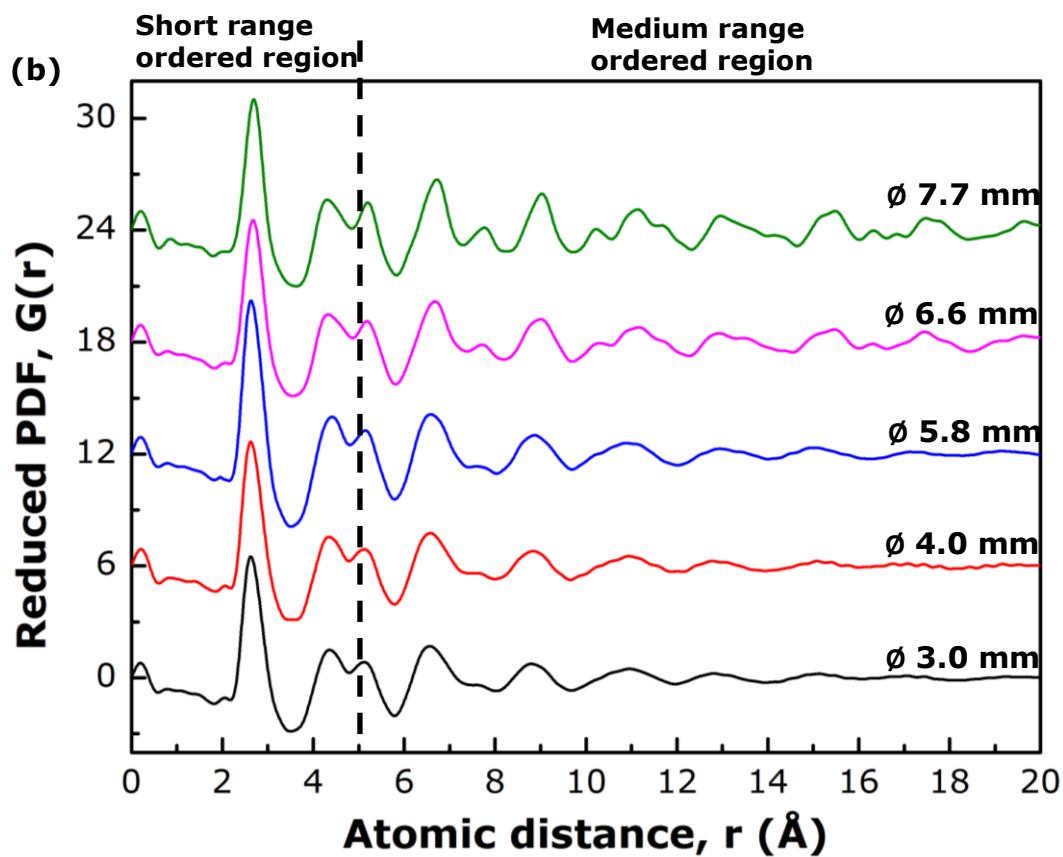
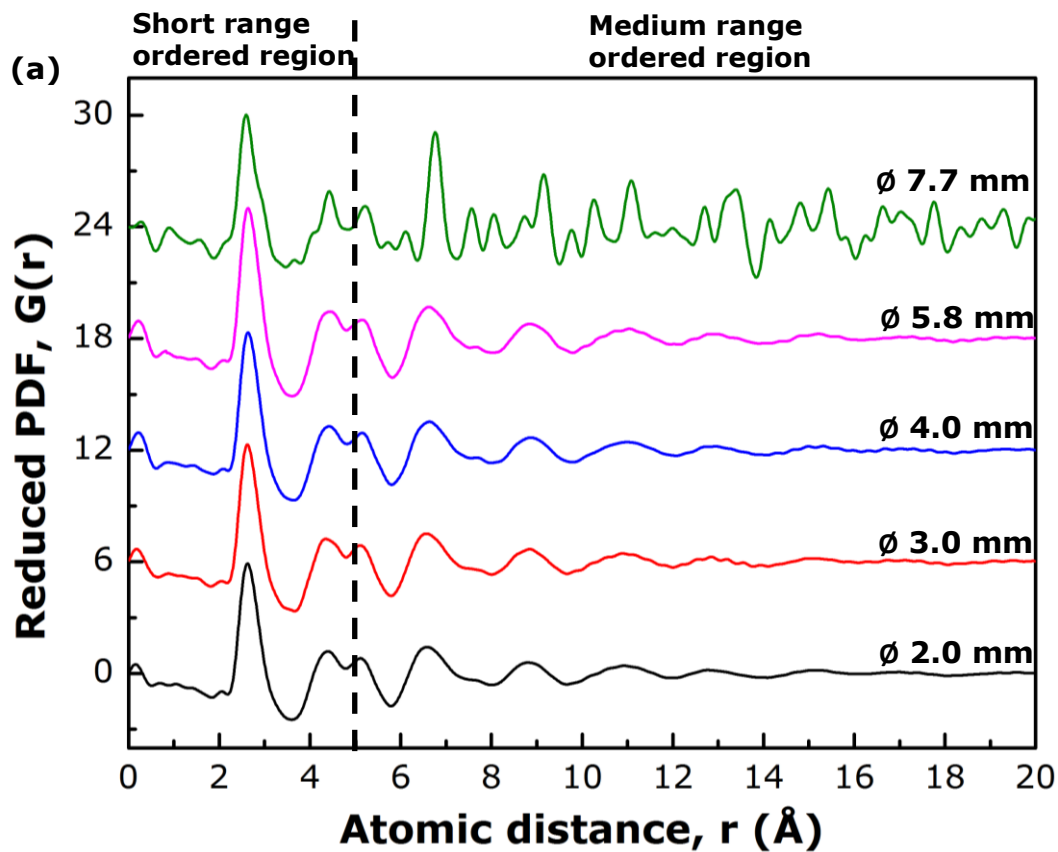


Figure 6.6 Reduced pair distribution functions for the different diameter samples from the (a) Fe-B₆Gd₂, and (b) Fe-B₆Y₂ stepped rod bars. The PDF curve is stacked with an equal spacing of 6.

6.3 Hardness and Young's modulus of the designed alloys

Nano-indentation was used to study the changes in material properties for the different diameter samples from the step rod bars, especially for the transition from a crystalline state to a fully amorphous state for each alloy. Figure 6.7a and Figure 6.7b show the typical load-depth curves for the different diameter bars from the Fe-B₆Gd₂ and Fe-B₆Y₂ alloy samples respectively. The hardness (H_{it}), and Young's modulus (E_{it}) and Vickers hardness are calculated using the equations discussed in section 3.4 of Chapter 3.

The arrays of indents captured using SEM are showed in Table 6.4, together with the harness and Young's modulus calculated based on the averaged data from an array of 30 indents for each case.

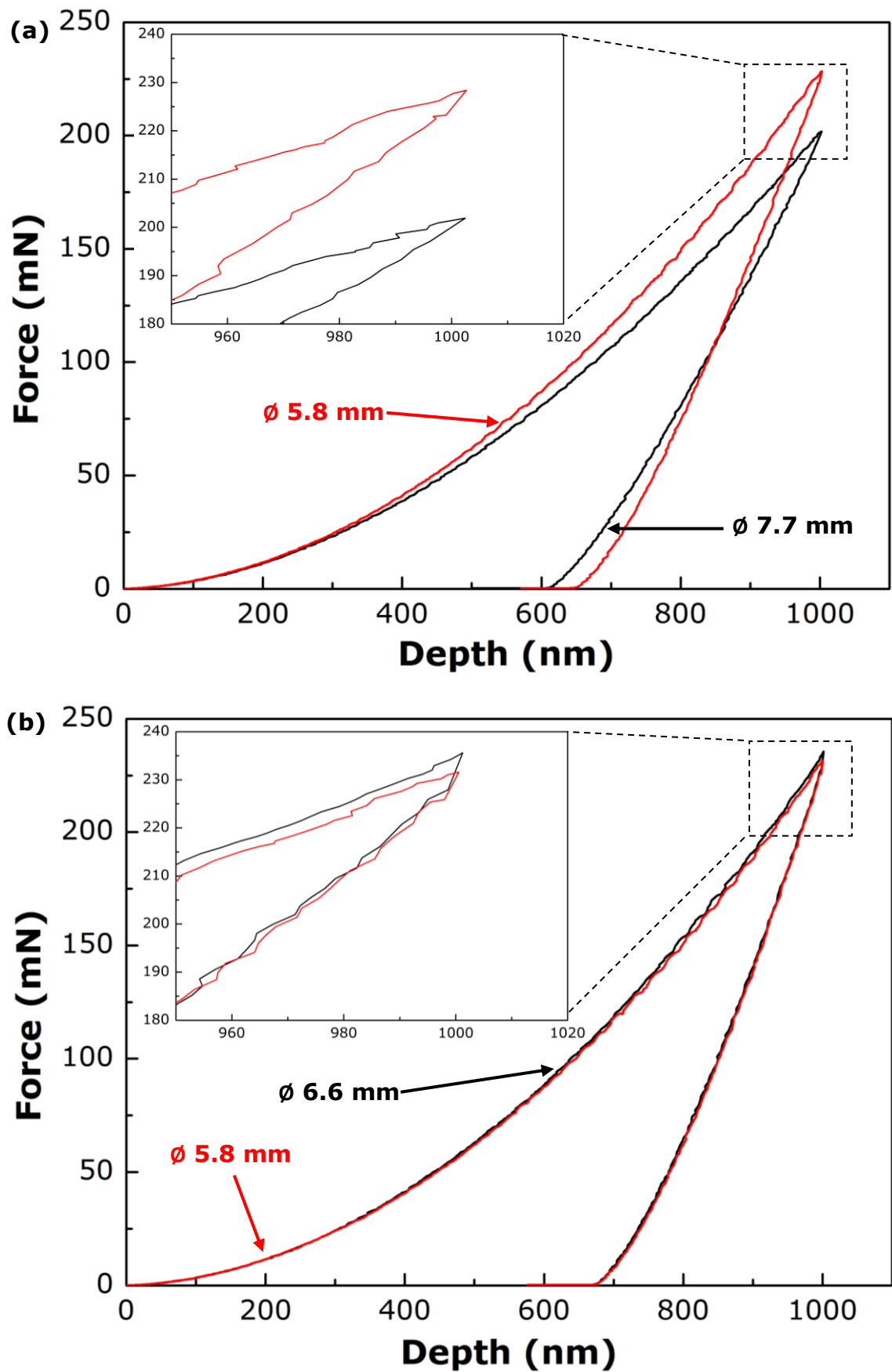
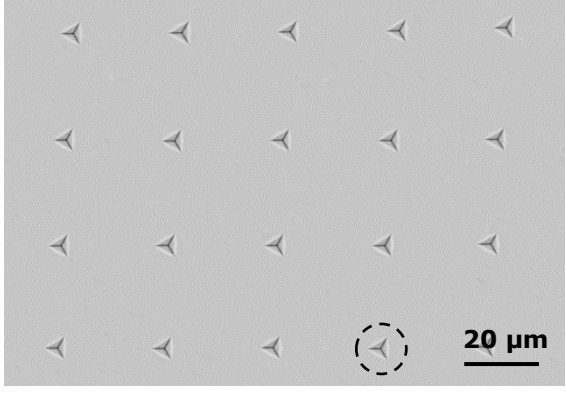
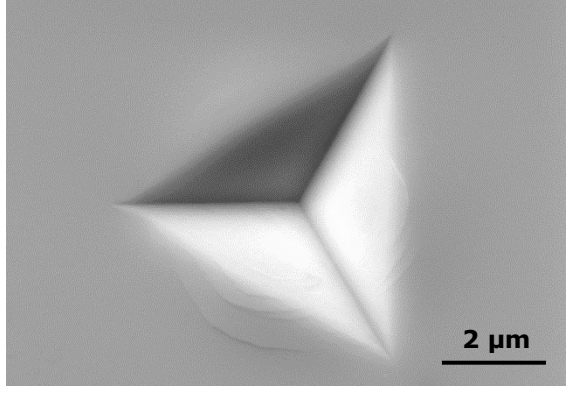
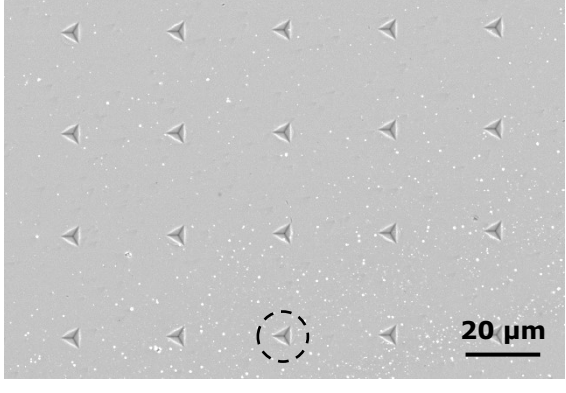
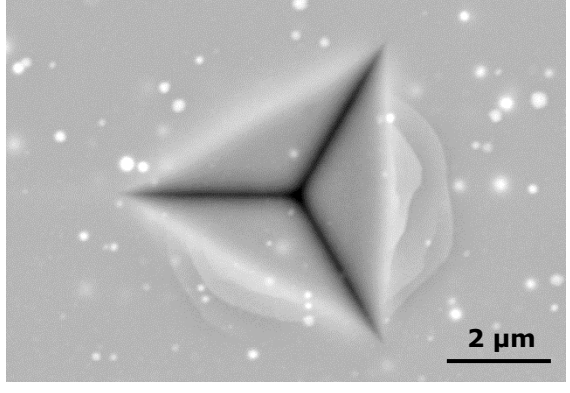
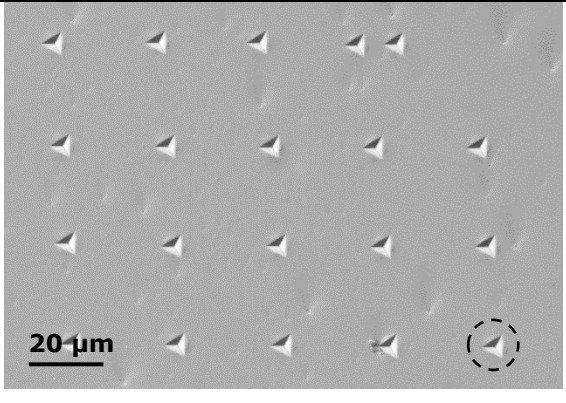
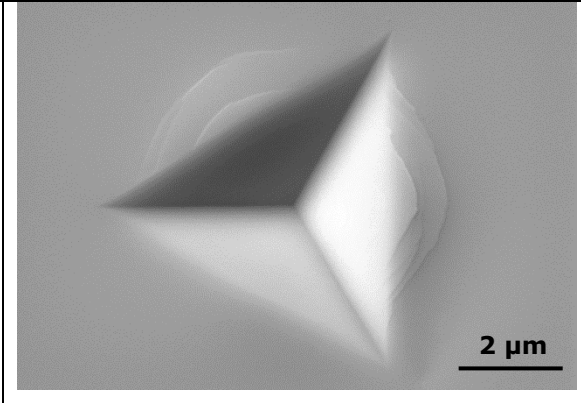
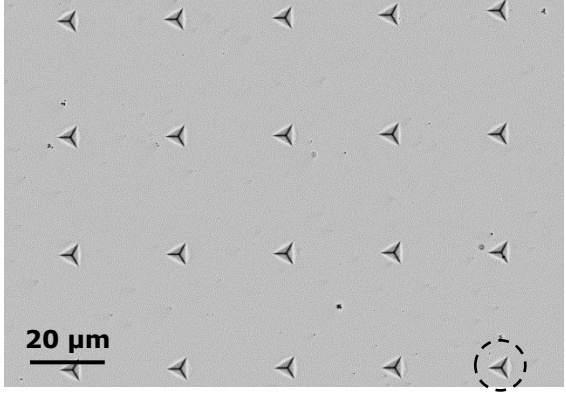
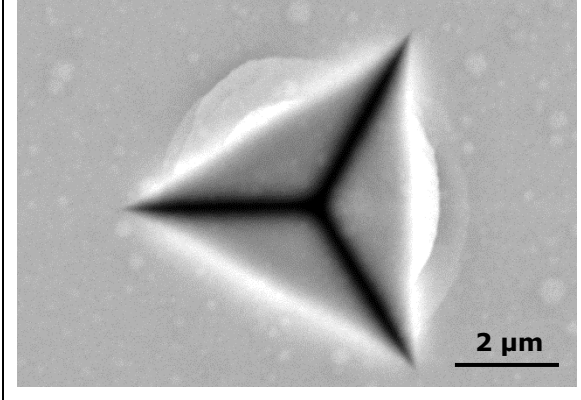


Figure 6.7 Load versus indentation depth curves from the nano-indentation tests for (a) the ϕ 5.8mm and ϕ 7.7mm samples from Fe-B₆Gd₂, and (b) the ϕ 5.8mm and ϕ 6.6mm samples from Fe-B₆Y₂.

Table 6.4 Nano-indentation tests made on the Fe-B₆Gd₂ and Fe-B₆Y₂ alloy samples, and the hardness and Young's modulus calculated.

Alloy	SEM images on the Nano-indentation		Material properties
Fe-B ₆ Gd ₂ ø5.8mm (Amorphous)			Hit: 13.60 GPa Eit: 228.83GPa Vickers hardness: 1259.85
Fe-B ₆ Gd ₂ ø7.6mm			Hit: 12.60 GPa Eit: 189.04GPa Vickers hardness: 1167.23

<p>Fe-B₆Y₂ ø5.8mm (Amorphous)</p>			<p>Hit: 13.08 GPa Eit: 282.58GPa Vickers hardness: 1211.68</p>
<p>Fe-B₆Y₂ ø6.6mm</p>			<p>Hit: 13.28 GPa Eit: 275.91GPa Vickers hardness: 1229.95</p>

6.4 Neutron absorption measurement

To study the neutron absorption capabilities of the designed glassy alloys, neutron transmission measurements were carried out at the test beamline ROTAX of spallation neutron source ISIS, UK. The measurement was done by the IMAT beamline scientist, Dr Genoveva Burca with the strong support from the principal scientist, Dr Winfried Kockelmann of IMAT and Dr Anton Tremsin of Space Science Laboratory, University of California.

6.4.1 Sample preparation for neutron absorption measurement

Neutron absorption measurements were made on four alloys using their as-cast step rod bars. Thin disk samples of 0.5 mm and 0.8 mm thick were firstly sectioned from each diameter sections of the step bars using electric discharging machining. For each diameter section, three 0.5 mm thick samples and three 0.8 mm thick sample were cut in order to have enough samples to obtain sufficient statistic data during absorption measurement. To remove the surface imperfection and maintain a perfect parallel thickness, the 0.5 mm and 0.8 mm thick samples were double-side ground and polished into thin disks of a nominal thickness of 0.3 mm and 0.5 mm respectively using the procedure described in section 3.3.2 of Chapter 3. To control the sample thickness during grinding, a small 0.3 mm or 0.5 mm thick piece cut from a standard Feeler Gauge was placed nearby the samples to be ground and mounted together into the special sample grinding holder as illustrated in Figure 3.4. Once the initial grinding (P400) touched the Feeler Gauge piece surface, it was believed that the right thickness was reached and the fine grinding and polishing was proceed with great care to maintain the thickness in an acceptable tolerance. The final sample thicknesses were measured using a micrometre (with $\pm 1 \mu\text{m}$ resolution), and the effect of sample thickness difference on neutron transmission were taken into account during the transmission calculations as described later.

Figure 6.8 shows the double side polished thin disk samples for the Fe-B₁₆, Fe-B₁₅Gd₂, Fe-B₆Gd₂ and Fe-B₆Y₂ alloys, and they were carefully placed on a 30 x 30 mm aluminium thin foil of 0.1 mm thick. Each sample was held firmly and positioned using aluminium adhesive at the edge of each sample,

leaving most of the area of the sample without any other obstacle when facing the incident neutron beam for measurement.

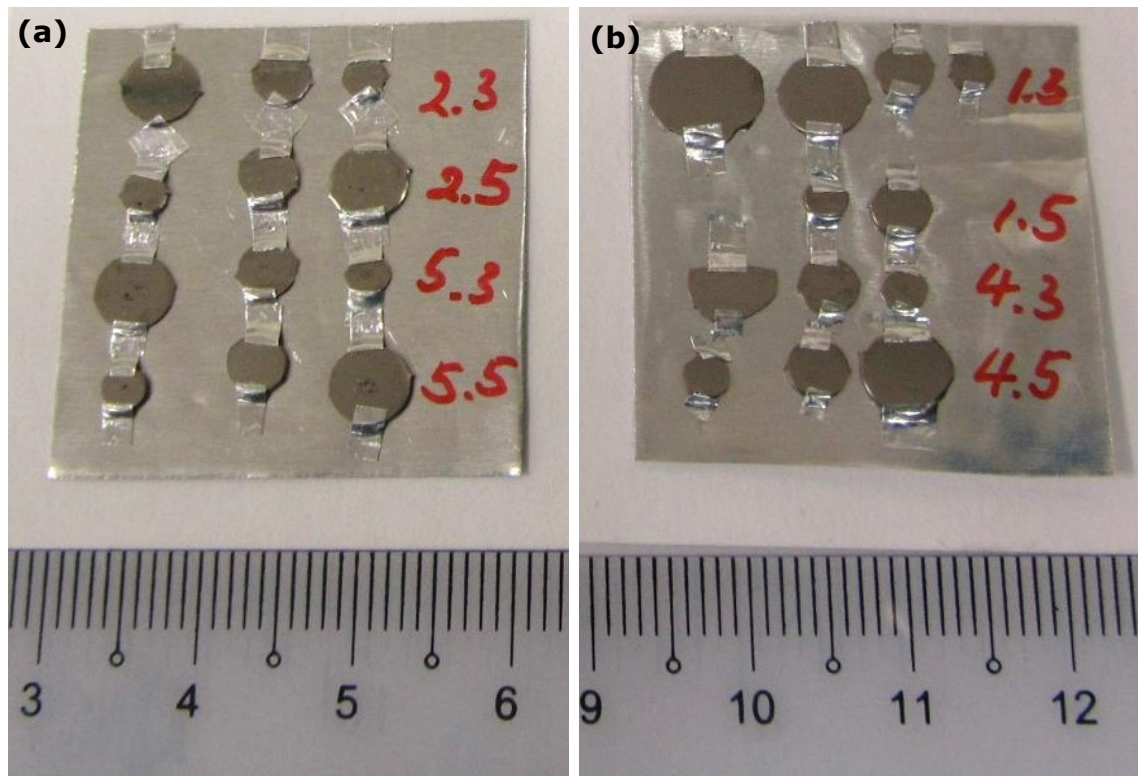


Figure 6.8 Double side polished thin disk samples with the nominal thickness of 0.3 mm and 0.5 mm for the Fe-B₁₆, Fe-B₁₅Gd₂, Fe-B₆Gd₂ and Fe-B₆Y₂ alloys. (a) Plate A (Plate B).

Table 6.5 summarises the alloys and samples (including the measured thickness for each sample) used in the measurements.

Table 6.5 The alloys and double-side polished thin disk samples (with the measured thickness) prepared for the neutron transmission measurement.

Alloys	Diameter (mm)	Thickness (mm)	Plate
Fe-B ₁₆ : Fe ₅₂ Cr ₁₉ Mn ₂ Nb _{4.5} B ₁₆ C ₄ Si _{2.5}	5.8	0.544	A: 5.5
	4.0	0.550	A: 5.5
	3.0	0.549	A: 5.5
	5.8	0.244	A: 5.3
	4.0	0.305	A: 5.3
	3.0	0.285	A: 5.3
Fe-B ₁₅ Gd ₂ : Fe ₄₈ Cr ₁₅ Mo ₁₄ C ₆ B ₁₅ Gd ₂	5.8	0.528	A: 2.5
	4.0	0.581	A: 2.5
	3.0	0.567	A: 2.5
	5.8	0.291	A: 2.3

	4.0	0.304	A: 2.3
	3.0	0.303	A: 2.3
Fe-B ₆ Gd ₂ : Fe ₄₈ Cr ₁₅ Mo ₁₄ C ₁₅ B ₆ Gd ₂	4.0	0.526	B: 1.5
	3.0	0.537	B: 1.5
	7.6	0.358	B: 1.5
	5.8	0.319	B: 1.5
	4.0	0.361	B: 1.3
	3.0	0.353	B: 1.3
Fe-B ₆ Y ₂ : Fe ₄₈ Cr ₁₅ Mo ₁₄ C ₁₅ B ₆ Y ₂	5.8	0.563	B: 4.5
	4.0	0.546	B: 4.5
	3.0	0.582	B: 4.5
	5.8	0.296	B: 4.3
	4.0	0.294	B: 4.3
	3.0	0.289	B: 4.3

6.4.2 Neutron source, detector, experiment setup

The ISIS spallation neutron source was used for the experiments, it consists of a tungsten target and a cold 110 K methane neutron moderator at a pulse repetition rate of 50 Hz [266]. A chopper system consists of a 't-zero' chopper and a disk chopper were used to filter out gamma radiation generated at the time of neutron production in the spallation target and to remove very slow neutrons below 5 meV from the incident beam, respectively. The flight path from the moderator to the detector was measured to be 15.865 m and was used to calculate the time-of-flight (TOF – the travelling time of different energies neutrons from the moderator to the MCP detector) and neutron energies [266].

A microchannel Plate (MCP) detector with Timepix readout 32 was used in this measurement. The detector has a detecting area of 28 x 28 mm² and 512 x 512 total pixels with 55 x 55 μm² pixel size accordingly. The aluminium foil with the set of samples was then placed 5 mm in front of a 1 mm thick aluminium window of the MCP detector which is operated in vacuum. With a distance of the window to the neutron sensitive MCP of 1 mm, the sample to sensor distance was about 7 mm. In order to prevent any neutron damage to the readout electronics and reduce background

neutron scattering, boron carbide shielding was also placed around the detector area as shows in Figure 6.9.

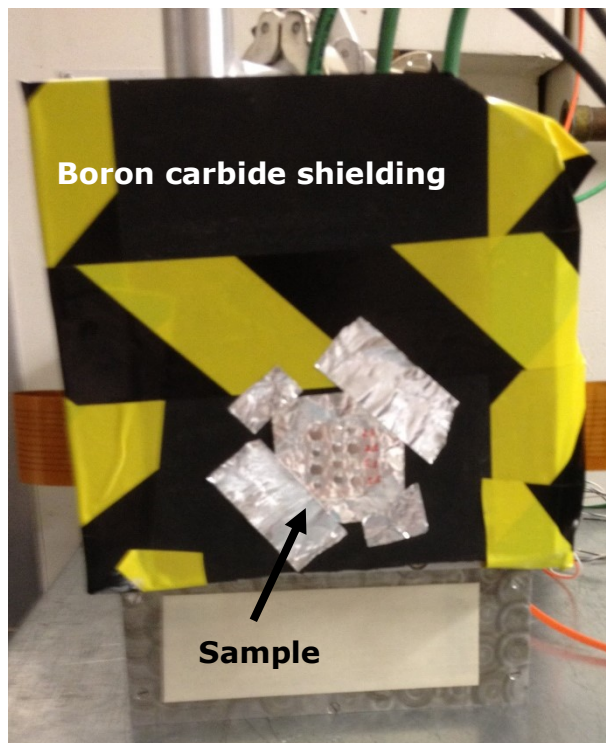


Figure 6.9 Samples positioned in front of the MCP detector (the detector window was behind the sample) and with boron carbide shielding surrounding the detector to reduce the background neutron scattering.

The actual experiment setup is showed in the schematic diagram in

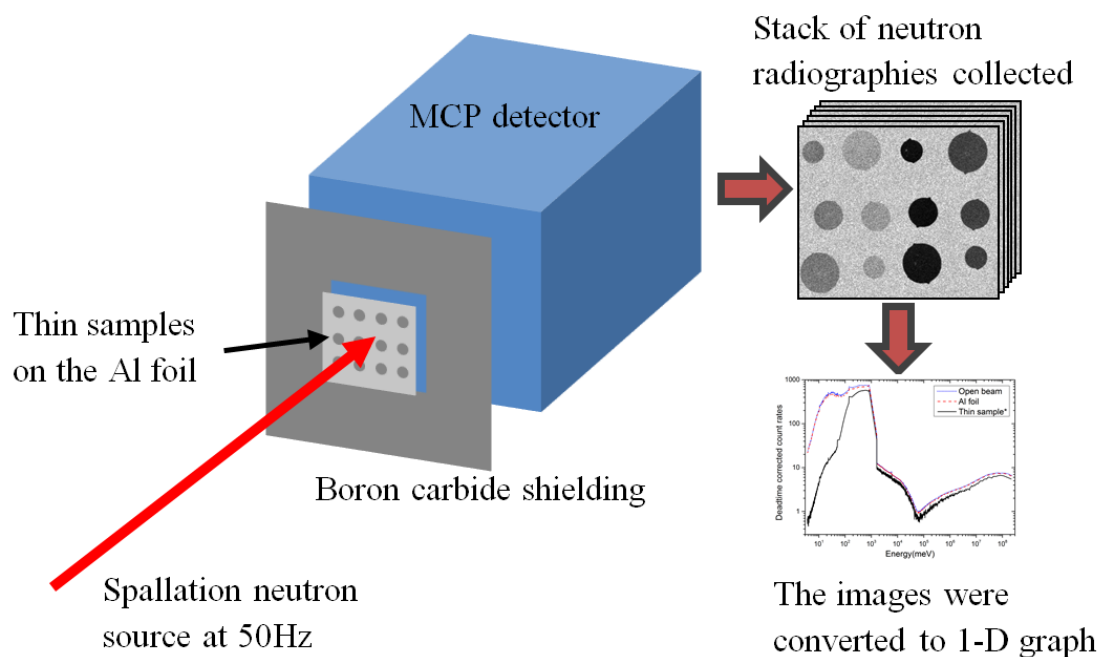


Figure 6.10 A schematic experiment setup for neutron transmission measurement at beamline ROTAX of ISIS.

6.4.3 Data acquisition and analyses

For each pixel the time of arrival of each detected neutron was registered and transferred into a histogram of 2676 time channels, i.e. a single measurement results in a stack of as many time-of-flight radiographies. Therefore, to minimize deadtime effects, the entire TOF range was separated into six regions separated by five 320 μs readout gaps and the acquired image sequence was further corrected for the detector deadtime using an overlap correction algorithm [271]. For all the thin disk samples, transmission images with the energy range between 5 meV to 2×10^8 meV were collected. However, >1000 meV, the neutron count rates was too low hence only the energy range between 5-1000 meV was analysed, for the purpose to investigate the neutron shielding for the neutron energy range where a rapidly decrease in Gd total cross section occurs. In addition, neutron transmission images were also collected without the presence of samples and the aluminium foil (the so called "open beam" condition) and were used to normalize the difference in neutron counts at different energies. I performed primarily the data analyses for all samples with the essential inputs from Dr Genoveva Burca, Dr Winfried Kockelmann of IMAT and Dr Anton Tremsin of Space Science Laboratory, University of California.

Figure 6.11a and Figure 6.11b show examples of the raw radiography images from the stack images taken by the Microchannel Plate (MCP) detector for the samples mounted on plate A and plate B with their corresponding alloys summarise in Table 6.5. The raw images were deadtime corrected using an overlap correction algorithm from A. S. Tremsin [271]. In addition to those sample images, "open beam" images were also taken for the purpose of correcting the difference in neutron flux along the TOF. Figure 6.12 shows the neutron count rates along the TOF for (1) the sample marked by the dotted square in Figure 6.11a, (2) the Al foil (with the sample removed from the neutron beam path) where the sample was mounted on, and (3) the "open beam" (without sample and Al foil).

The unusual shapes of neutron count rates along the TOF in Figure 6.12 is caused by (1) a combination of the energy dependent beam flux profile on the beamline, (2) different TOF bin widths used for different sections of the covered time regime, and (3) at higher energies (shorter TOF values), an

effect of the 50 Hz 't-zero' chopper blade moving out of the beam. The drop of count rates at $\sim 10^3$ meV is due to change of the bin-width from 20.48 μ s to 0.48 μ s.

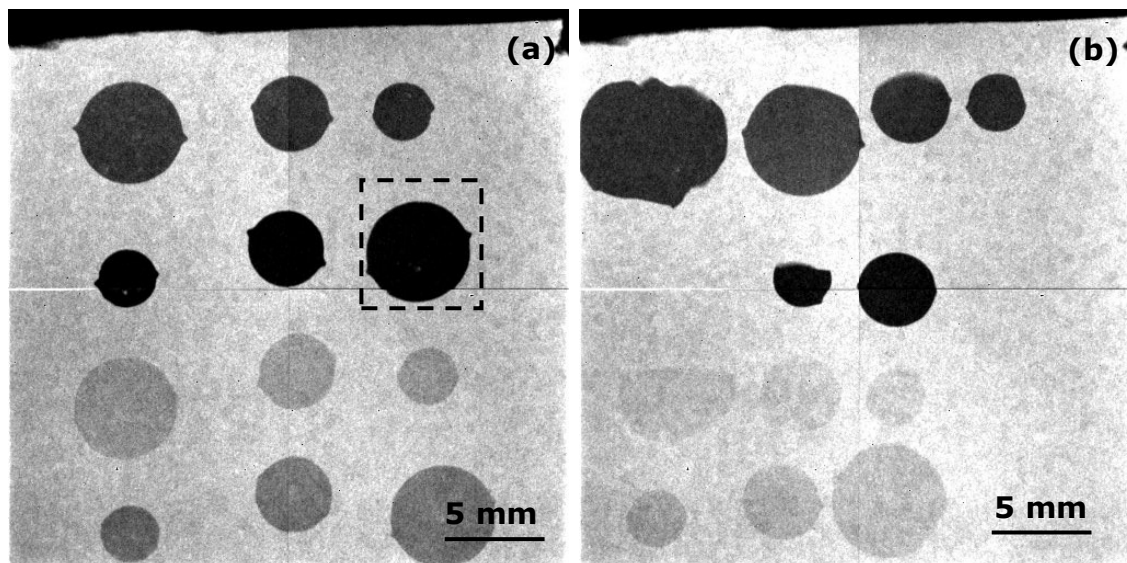


Figure 6.11 Examples of raw radiography images from the stack of images acquired at 80 meV neutron energy by the MCP detector for the samples on (a) plate A, and (b) plate B.

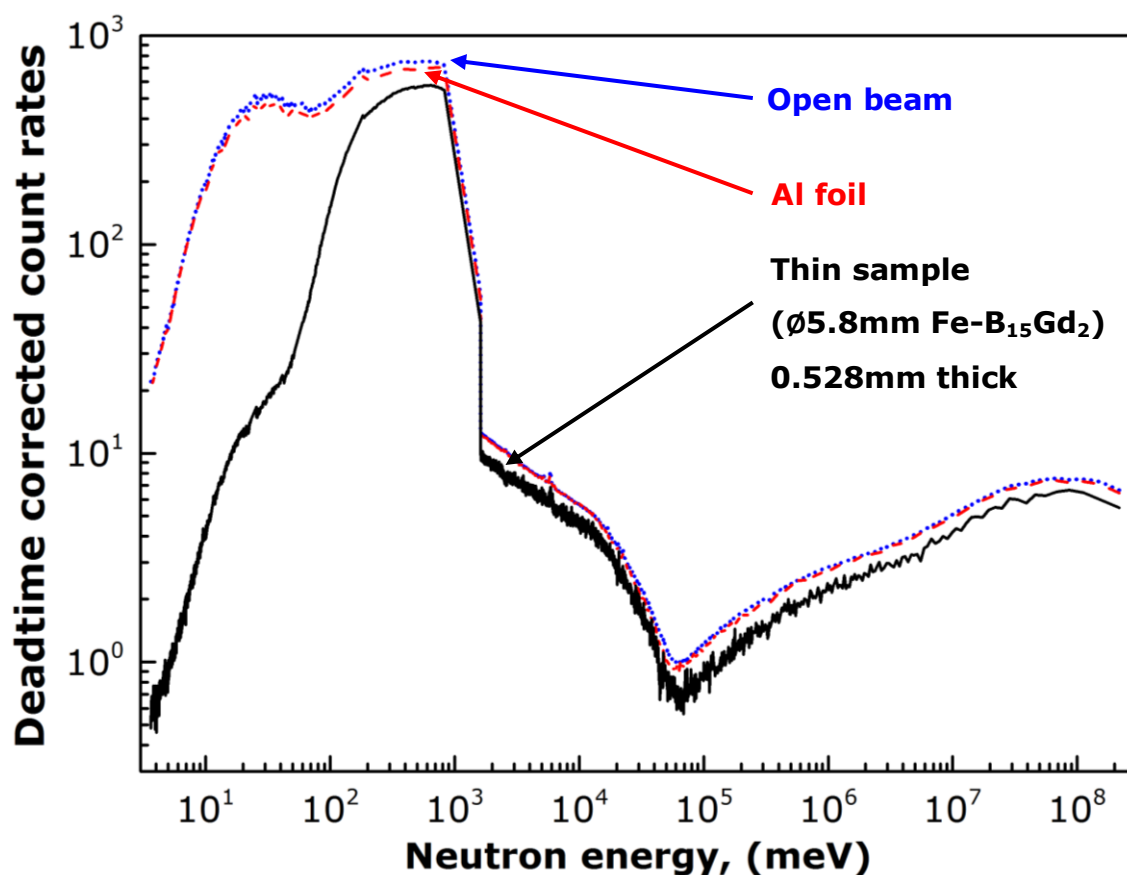


Figure 6.12 Neutron count rates at different neutron energies captured for the "open beam", the Al foil, and the thin sample marked by the dotted square in Figure 6.11b.

These raw data were then corrected for the difference in neutron count rates along the TOF, and the neutron transmission T_s of each alloy was calculated with following procedure.

Firstly, the TOF neutron intensity was normalised by dividing the raw samples images with the 'open beam' images. Normally, neutron transmission T_s was obtained by dividing the sample images to the open beam images. However, in our case, the effect of the aluminium foil needs to be removed and to improve the counting statistics as described below.

Secondly, the neutron TOF neutron transmission profile of a sample (with Al foil behind it) from a particular area of $\sim\text{Ø}10$ pixels in diameter was extracted from each sample. When selecting the area, its neutron transmission image was visually inspected to avoid any obvious area that exhibits pores. To minimize the error generated by any visually unnoticed pores, 3 areas were selected from each sample and their neutron transmission profiles were averaged, and taken as the transmission profiles for sample plus Al foil.

Next, the neutron attenuation generated from the Al foil needs to be corrected. The transmission profile of an empty area (with the Al foil but without sample) as shows in Figure 6.11 were extracted from an area of the same size $\sim\text{Ø}10$ pixels in diameter, and data from at least 3 different such locations were extracted and averaged, and taken as the Al only neutron transmission profile. Finally, the sample transmission was obtained by dividing the sample plus Al foil neutron transmission profile by the Al only neutron transmission profile. This operation is, of course, assumes that the incident neutron beam is spatially and spectrally homogeneous across the effective detector area of $28 \times 28 \text{ mm}^2$.

Figure 6.13 shows the neutron transmissions measured for the alloy samples with different thickness. Only neutron energy from 5 meV to 1000 meV range were included here because at above 1000 meV, the neutron count rate falls off (Figure 6.12) and the noise increases significantly which might affect the transmission measurement.

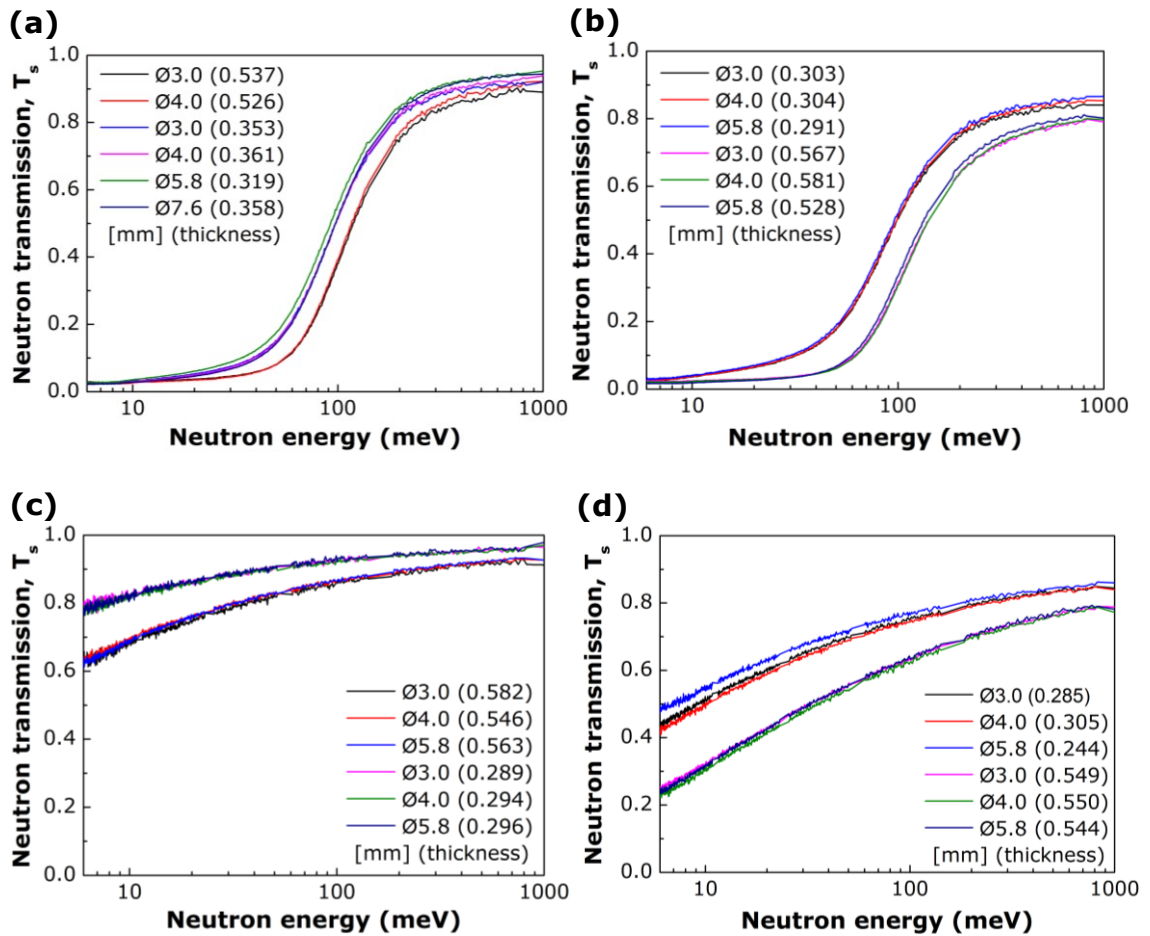


Figure 6.13 Neutron transmission profiles between 5 meV to 1000 meV for the samples of (a) Fe-B₆Gd₂, (b) Fe-B₁₅Gd₂, (c) Fe-B₆Y₂ and (d) Fe-B₁₆ alloy.

Neutron transmission is apparently affected by the thickness of the samples and also varies with incident neutron energy. However, in general among the four alloys, Fe-B₁₅Gd₂ (Figure 6.13b) demonstrated the highest neutron shielding capability with the lowest neutron transmission, followed by Fe-B₆Gd₂ (Figure 6.13a), Fe-B₁₆ (Figure 6.13d) and Fe-B₆Y₂ (Figure 6.13c). For <30 meV, the neutron transmission for Fe-B₆Gd₂ and Fe-B₁₅Gd₂ are as low as 0.1, while those of the Fe-B₆Y₂ and Fe-B₁₆ are much higher. However, >200 meV, the neutron shielding capability for Fe-B₆Gd₂ and Fe-B₁₅Gd₂ falls off significantly. At 1000 meV, Fe-B₁₅Gd₂ and Fe-B₆Y₂ are over 0.8.

To investigate the effects of alloy compositions on neutron shielding, the sample thickness factor was taken into account by the macroscopic attenuation coefficient (MAC), Σ_t calculated using the Lambert-Beer's law:

$$T_s = e^{-N\sigma_t x} \quad (22)$$

$$\Sigma_t = N\sigma_t$$

Where x is the thickness of the sample, σ_t is the total cross section of the sample with its composition taken into account, and N is the number density. The MAC for different thick samples of Fe-B₆Gd₂ and Fe-B₆Y₂ alloys are compared in Figure 6.14a. The average MAC from different thickness samples are shows in Figure 6.14b. Finally using the obtained MAC, the neutron transmission at the thickness of with the thicknesses of 0.1, 0.5, 1.0 and 1.5 mm for the Fe-B₆Gd₂ and Fe-B₆Y₂ alloys were calculated and shows in Figure 6.15.

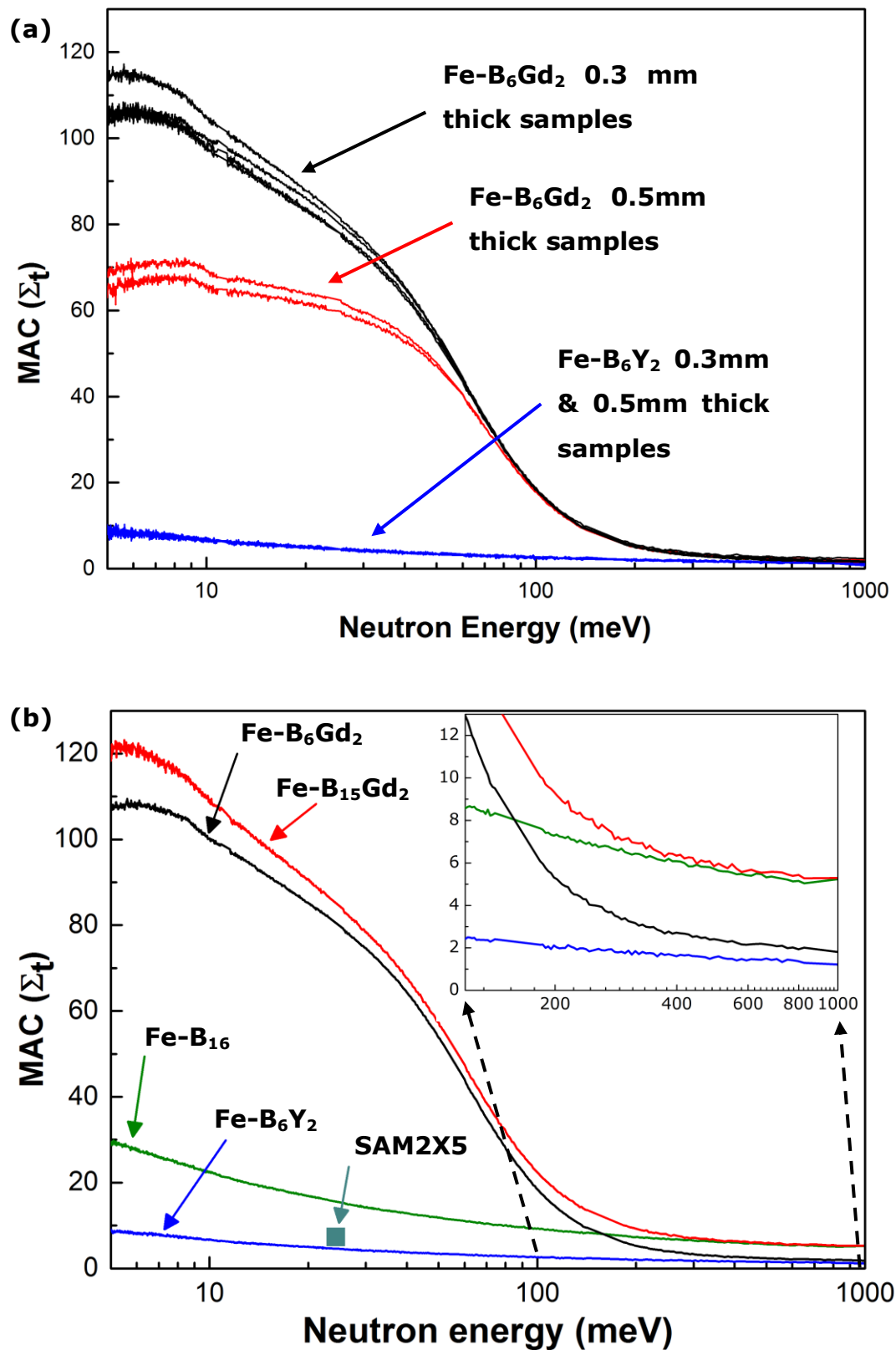


Figure 6.14 Calculated MAC from the neutron absorption measurement between 5-1000 meV for the samples: (a) Fe-B₆Gd₂ vs. Fe-B₆Y₂ at different sample thicknesses (b) averaged MAC for all 4 alloys at different sample thicknesses and SAM2X5 at 25.3meV.

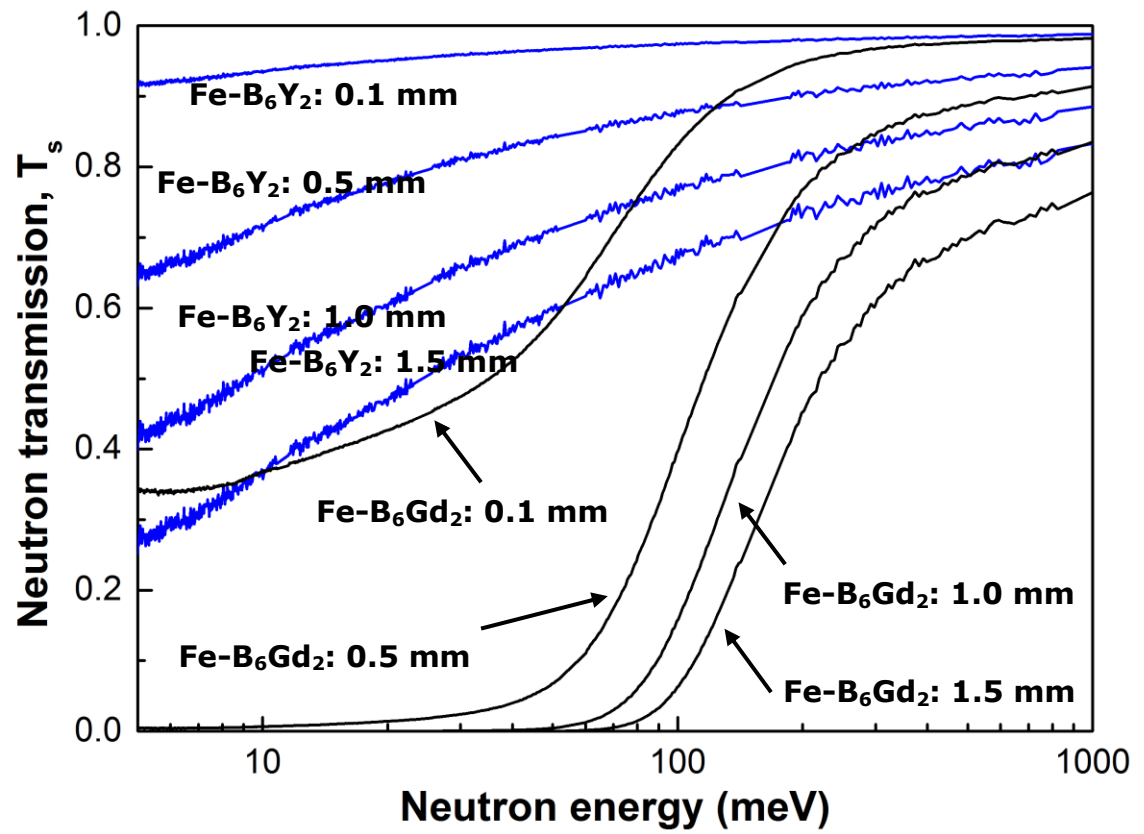


Figure 6.15 The calculated neutron transmission for the Fe-B₆Y₂ and Fe-B₆Gd₂ alloys at different thicknesses.

6.5 Discussion

6.5.1 Composition design for Fe-based metallic glassy alloys

The Fe-based alloys designed in this project are based on the empirical rule that multiple elements, significant atomic size mismatch $>12\%$ and negative heats of mixing among the three main elements [82]. Elements with different atomic radii are categorised into the group of large ($\geq 1.5 \text{ \AA}$) such as Nb, Mo, Mn, Gd, Y, W and Zr, medium ($1.2 \text{ \AA} \sim 1.5 \text{ \AA}$) such as Fe and Cr, and small ($< 1.2 \text{ \AA}$) B, C and Si [254]. Metalloid elements such as B, C, and Si were also included in the alloys to improve glass forming ability [270]. Table 6.1 shows the Fe-based alloys designed in the project and their corresponding XRD patterns. Unfortunately, as shows in their SXRD patterns, most of the alloys do not form glassy state. However, those attempts pointed us the right direction for choosing the potential baseline alloy systems.

The alloy Fe-B₁₆ was designed based on the composition of SAM2X5 (Fe_{49.7}Cr_{17.7}Mo_{7.4}W_{1.6} Mn_{1.9}Si_{2.4}B_{15.2}C_{3.8}) [162] by replacing the very high melting point element Mo (2896 K) and W (3695 K) with Nb (2742 K). The aim is to low the melting temperature of the alloy and remove the expensive alloy element Mo and W, and at the same time to retain the glass forming ability as claimed by Farmer [162]. Unfortunately, this design is not successful.

The FeNb-Si₅Gd₃ was designed based on Fe-B₁₆ by replacing C₄ with Gd₃, and removing Mn completely. The aim is to study the neutron absorption capability by using the highest atomic percentage of (B+Gd), i.e. 19 at% in this alloy, and also study the possibility of using B without C to retain the glass forming capability. The 1D spectrum shows that, compared with that of the Fe-B₁₆, the crystalline peaks are less intense, suggesting that the majority of alloy is in amorphous state, and this is confirmed by the relative smooth halo with faint crystalline rings in the corresponding 2-D pattern. The result shows that the adding of 3 at% Gd shows an apparent benefit in improving the glass forming capability. However, more crystalline peaks were found, which suggested the system contain more complicated crystalline system. The needle-shaped features present in the 2D diffraction

pattern, indicate that, for this particular composition, crystal structures form with possible change of the orientation during the solidification process because similar needle-shaped features were observed in situ for TiAl during the transformation from α to γ phases using synchrotron X-ray diffraction [272].

In the FeMn-B₆Gd₂, Nb was replaced by the Mn, and Si was replaced by C to improve the hardness of the alloy system. The 1D spectrum shows a less complicated crystalline alloy with less crystalline peaks and bigger amorphous profile was observed. This indicates an improvement in the glass forming ability.

Encouraged by the results from the FeMn-B₆Gd₂, we replaced the Mn with Mo to form the Fe-B₁₅Gd₂. The 1D spectrum and the 2D diffraction pattern obtained from this alloy (Table 6.3) show that this alloy exhibits almost a complete amorphous feature with very faint overall crystalline features. The results from the Fe-B₁₅Gd₂ suggest that with a minor tuning of its composition, it is very possible to design an alloy to have a more stable amorphous state. By further analysing the Fe₄₈Cr₁₅Mo₁₄C₁₅B₆Y₂ alloy reported by Ponnambalam, *et al* [259], we believe that the key for the fine tuning of the alloy composition is by tailoring the ratio of the C and B. and based on this judgment, we designed the alloy Fe-B₆Gd₂ by replacing the Y₂ with Gd₂, and retaining the ratio of C:B = 15:6. Table 6.6 summarises all metallic glassy alloys successfully designed in this project.

6.5.2 Effect of cooling rates on glass forming ability

Figure 6.4 shows the 1D spectra for the \varnothing 2, 3, 4, 5.8 and 7.7 mm sections and the corresponding 2D diffraction patterns for the alloy Fe-B₆Gd₂. Clearly for the sections of diameter less than or equal to \varnothing 5.8 mm, A full amorphous state is achieved. Unfortunately the sample of \varnothing 6.6 mm was lost, so no data is given for this diameter section. Crystalline peaks only appear in the \varnothing 7.7 mm diameter section, indicating that this alloy has at least a glass forming ability of $\sim\varnothing$ 5.8 mm. We also analysed the benchmark alloy, Fe-B₆Y₂, and similar results are showed in Figure 6.5 where full amorphous state can retain up to \varnothing 5.8 mm diameter section. In the \varnothing 6.6

mm section, minor crystalline peaks do appear in the 1D spectrum, and more is showed in the $\varnothing 7.7$ mm section materials.

Based on these systematic SXRD studies, it is confident to conclude that the newly designed alloy Fe-B₆Gd₂ has a similar glass forming ability as the widely studied Fe-based metallic glass alloy, Fe₄₈Cr₁₅Mo₁₄C₁₅B₆Y₂ [216, 273]

The PDFs for Fe-B₆Gd₂ and Fe-B₆Y₂ alloys are show in Figure 6.6a and Figure 6.6b for the different diameter sections. The PDF patterns include two ranges of atomic distances: short atomic range (SR) (<5 Å) and medium atomic range (MR) (5 Å ~ 20 Å). Whereas, any ordered atomic structures formed in those atomic distances are normally called short-range order (SRO) and medium-range order (MRO) structures. While long atomic range often refers an atomic distance of >20 Å. A typical glassy PDF pattern contain broad peaks in the SR and MR region [274]. A crystalline system shows sharp peaks in all atomic distances, especially in the long range, indicating the repeated unit cells in the crystal structure [275].

For Fe-B₆Gd₂ and Fe-B₆Y₂, the onset of the crystal growth can be easily seen where the peaks appear in the bigger atomic distance in the MRO region as the step-bar diameter increases and the cooling rate is reduced. For Fe-B₆Gd₂ (Figure 6.6a), the SRO and MRO do not exhibit any significant changes in the G(r) profiles until $\varnothing 5.8$ mm. At $\varnothing 7.7$ mm, three broad peaks at 4.2, 4.4 and 7 Å turn in to sharper peaks, and additional peaks appear in the MRO region. Apparently, the volume fraction of crystalline phases increases significantly at $\varnothing 7.7$ mm. However the broad peaks imbedded in the SRO region of the G(r) suggest that there is SRO structure present. It should be noted that the SRO features are also observed in the 1D diffraction spectra. Unfortunately, the PDF for $\varnothing 6.6$ mm is missing, therefore whether onset of the crystallite formation starts at $\varnothing 6.6$ is not clear. A small peak is spotted at 7.9 Å between $\varnothing 3$ mm and $\varnothing 5.8$ mm indicating that the glass structure has started to form crystals; however at a cooling rate which is still fast enough to prevent the crystal formation occur. This shows that the Fe-B₆Gd₂ chemical composition is stable at $\varnothing 5.8$ mm without any obvious peaks found in the bigger atomic distance in MRO, suggest a fully amorphous system.

As for Fe-B₆Y₂ (Figure 6.6b), the SRO and MRO regions show practically the same G(r) up to Ø5.8 mm, indicating that there is no crystal formation. At Ø6.6 mm, LRO structural information is observed in the corresponding region. However there are no new peaks or more intense peaks within the SRO range. This observation suggests that the volume fraction of the crystals within the Fe-B₆Y₂ in comparison to Fe-B₆Gd₂ is low and covered by the broad peaks of the SRO peaks. In addition, the peaks in the bigger atomic distance MRO region are broader compared to Fe-B₆Gd₂ at Ø7.7 mm which suggests a lower degree of crystallization. The degree of crystallisation is reflected in PDF curves by peak sharpening in the bigger atomic distance MRO region. This can be observed ex situ between Ø5.8 mm and Ø7.7 mm sections where the PDF peaks at 13 Å, 15 Å and 17 Å become sharper where the reduced cooling rates allow the atoms have more time for rearrangement in order to form bigger crystals. These features are difficult to pick up by lab-based XRD analysis, and especially for the Ø6.6mm case, lab based X-rays might wrongly indicate complete amorphous structures whereas first indications of crystallisation is visible in the SXRD patterns. Hence, the PDF analyses based on SXRD data is more accurate and effective in determining the glass forming ability. All experimental results show that both Fe-B₆Gd₂ and Fe-B₆Y₂ exhibit no crystallization up to Ø 5.8 mm. Fe-B₆Y₂ has been successfully used as a fully amorphous coating materials [165], Fe-B₆Gd₂ is a promising candidate for a BGM coating with high neutron shielding capability.

6.5.3 Improvement in mechanical properties

The changes in material properties because of the transition from crystalline phase to amorphous state were studied using nano-indentation (Table 6.4) for the Fe-B₆Gd₂ and Fe-B₆Y₂ alloy samples. Using the Fe-B₆Y₂ as the benchmark, Ø5.8 mm diameter sample was used as fully amorphous sample and Ø6.6mm diameter sample was used crystalline sample. Similarly, for Fe-B₆Gd₂, Ø5.8 mm diameter sample was used as fully amorphous sample; and the Ø7.7 mm sample was used for crystalline sample.

For the Fe-B₆Gd₂ sample, Figure 6.7a shows that Ø5.8 mm diameter sample, compared to the Ø7.7 mm diameter sample, needs a higher load

(~25mN or 12.5%) to achieve 1000 nm indentation depth. This shows that the crystalline phases in the Fe-B₆Gd₂ sample reduce the hardness of the material. Whereas for the Fe-B₆Y₂, there are no obvious changes in the load versus indentation depths curve (Figure 6.7b). It might be because the crystalline phases are so small at ϕ 6.6 mm diameter sample and therefore do not affect much on its hardness at larger scale. The crystalline phase in both alloys can be visualised by the backscattered SEM images in Table 6.4.

The SEM images show that the crystalline phases in the Fe-B₆Gd₂ ϕ 7.7 mm diameter sample (white spots) are much clearer and bigger than those in the Fe-B₆Y₂ ϕ 6.6 mm diameter sample (grey spots). The material properties of both alloys were extracted and shows in Table 6.4. In general, at the fully amorphous state, the Fe-B₆Gd₂ is slightly harder than the Fe-B₆Y₂ with addition (0.5 GPa higher in hardness); whereas Fe-B₆Y₂ has higher elasticity (54 GPa higher in Young's modulus).

In Fe-B₆Gd₂, the material properties are compared between amorphous and crystalline states. The result shows that indentation hardness (13.60 to 12.60GPa) and Vickers hardness (1259.85 to 1167.23) are reduced with the appearance of crystalline phases. An obvious change occurs in the Young's modulus, reducing from 228.83 GPa to 189.04 GPa. For the Fe-B₆Y₂, just a slightly change in material properties occurs with the introduction of crystalline phases. It is interesting to note that the indentation hardness (13.08 to 13.28 GPa) and Vickers hardness (1211.68 to 1229.95) was slightly increased, whereas the Young's Modulus reduced from 282.58 GPa to 275.91 GPa. The changes in the hardness is so small which might be caused by the sensitivity from the machine. The reduction in Young's modulus was because of lower BMG fraction in the material as BGM sample tended to feature with high elasticity in general.

The high glass forming ability of up to ϕ 5.8mm for the newly designed Fe-B₆Gd₂ alloy make it possible to be used as amorphous coatings without difficulty, and the increase in hardness compared to that of the Fe-B₆Y₂ is another beneficial property.

6.5.4 Improvement in neutron shielding capability

Figure 6.14a shows the calculated MAC for the Fe-B₆Gd₂ and Fe-B₆Y₂ at 0.5mm and 0.3mm thick samples. For the Fe-B₆Gd₂ alloy, at ≤ 80 meV, the Σ_t for 0.5 mm and 0.3 mm thick samples show a distinct difference which is not compatible with Lambert-Beer's law. This is due to a combination of three effects: for low energy neutrons the sample are completely opaque ("black") for the thinner samples already, so any further increase in thickness does not result in any reduce in transmission. With only 2% of Gd element within the alloy, it is capable to completely prevent transmission of neutron radiation due to the high neutron cross section of Gd. Therefore for the 0.5 mm thick disk, Lambert Beer's law gives an underestimation of the MAC. For the Fe-B₆Y₂ alloy with no Gd, the attenuation agrees for the 0.5 mm and 0.3 mm thickness samples. The result shows that the effectiveness of Gd doping of the BMG system and using it as a coating layer can significantly block off the neutron radiation of ≤ 80 meV even just use a thin layer of 0.3 mm of such material. Therefore, for the MAC measurements, the thin Gd-doped samples (0.3 mm) give better estimates in the sense of lower limits for the actual attenuations coefficients.

Figure 6.14b shows the averaged MAC for the four alloys and the MAC of SAM2X5 at 25.3 meV is also showed in the figure (the green square). Clearly, Fe-B₆Y₂ has the lowest MAC in this neutron energy range followed by Fe-B₁₆. Actually, in both Fe-B₆Y₂ and Fe-B₁₆, the neutron absorption contributions are mainly due to B, which has a total neutron cross section[268] of 767 barn at 25.3 meV, and significantly higher than that of Cr (3.05 barn), Nb (1.15 barn), Mn (13.3 barn), Si (0.171 barn), C (0.0035 barn), Mo (2.48 barn), and Y (1.28 barn). On the other hand, in addition to B, both Fe-B₆Gd₂ and Fe-B₁₅Gd₂ alloys contain Gd (49700 barn at 25.3 meV). In theory, Gd should provide approximately 2 orders of magnitude higher in neutron absorption than that of B in the energy range of below ~ 50 meV. In this study, the neutron transmission measurement (Fig. 8 in the Method part), and the calculated MAC in Figure 6.14b give more systematic data for us to evaluate the designed alloys' performance in terms of neutron absorption versus neutron energy. In the neutron energy of >200 meV, the four alloys actually show approximately the similar MAC trends in Fig. 4a. It is interesting to see that Fe-B₁₅Gd₂ has almost the same

profile as that of Fe-B₁₆ in the neutron energy of >400 meV, because the two alloys just have 1 at% difference in B, while the 2% Gd added into Fe-B₁₅Gd₂ does not enhance the neutron absorption capability anymore above 400 meV. This is simply because the drop of the neutron total cross section of Gd in that energy range as showed in Figure 6.1. The insert figure in Figure 6.14b also shows that the MAC of Fe-B₁₆ is higher than that of Fe-B₆Gd₂ when neutron energy is >180 meV, indicating that B is taking over Gd in that energy range to provide the neutron absorption capability. Hence, both Gd and B are the essential alloy elements for designing alloys with high neutron absorption capability in a wider neutron energy range.

Fe-B₁₅Gd₂ is slightly better than Fe-B₆Gd₂ with the addition of the B component. However, the SXRD data show that Fe-B₁₅Gd₂ is a crystalline alloy, which will most likely to significantly reduce the corrosion resistance[276]. While Fe-B₆Gd₂ has a glass forming ability of Ø 5.8mm, and the glass nature of the alloy allows a much more homogeneous distribution of Gd and B elements in the glassy matrix. Therefore at micro level, the effect of neutron absorption will be much more homogeneous.

Figure 6.15 shows the effectiveness of Fe-B₆Gd₂ alloy for absorbing neutrons if used as a coating material with the thicknesses of 0.1, 0.5, 1.0 and 1.5 mm, and the comparisons with the benchmark Fe-B₆Y₂ alloy. At approximately below 100 meV, Fe-B₆Gd₂ alloy materials are generally performed much better than those of Fe-B₆Y₂ alloy materials. From engineering point of view, only 1/4 or 1/5 of the thickness of Fe-B₆Gd₂ alloy materials would achieve the similar neutron absorption capability as those of Fe-B₆Y₂ alloy materials. In the energy range of 10-50 meV, the 0.1 mm thick Fe-B₆Gd₂ alloy has a better neutron absorption capability than the 1.5 mm thick Fe-B₆Y₂ alloy material. So far, Fe-B₆Gd₂ is an amorphous alloy (with Ø 5.8mm glass forming ability) with the highest neutron shielding capabilities. However, the radiation induced crystallization and corrosion resistance of the alloys were not measured in the thesis and further measurement is required for the alloy if was intended to use as a neutron shielding material.

Table 6.6 The compositions of the designed alloys, their glass forming ability and the measured MAC at 25.3 meV (thermal neutron).

Alloy	Nominal composition	Glass forming ability (diameter, mm)	MAC, Σ_t (cm ⁻¹ @25.3meV)
Fe-B ₁₆	Fe ₅₂ Cr ₁₉ Nb _{4.5} Mn ₂ Si _{2.5} B ₁₆ C ₄	< Ø 2	15.48
Fe-B ₁₆ Gd ₃	Fe ₅₀ Cr ₂₂ Nb ₄ Si ₅ B ₁₆ Gd ₃	< Ø 2	Not available
Fe-B ₁₅ Gd ₂	Fe ₄₈ Cr ₁₅ Mo ₁₄ C ₆ B ₁₅ Gd ₂	< Ø 2	73.32
Fe-B ₆ Gd ₂	Fe ₄₈ Cr ₁₅ Mo ₁₄ C ₁₅ B ₆ Gd ₂	Ø 5.8	73.64
Fe-B ₆ Y ₂	Fe ₄₈ Cr ₁₅ Mo ₁₄ C ₁₅ B ₆ Y ₂	Ø 5.8	4.56

6.6 Summary

This chapter contained the results and discussions for the novel metallic glass alloys designed and the neutron absorption experiments. The results included the X-ray diffraction, total scattering studies, nano-indentation and neutron absorption for the designed alloys. The alloy composition for designing the Fe-based metallic glass alloys throughout the research period was discussed in details. The effect of different cooling rates on the Fe-B₆Gd₂ and Fe-B₆Y₂ alloys particularly in the atomic structure were discussed together with their mechanical performance measured using the nano-indentation tests. Lastly, the neutron shielding capabilities of the newly designed Fe-based alloys were discussed at the final section.

Chapter 7 Conclusions and future work

7.1 Conclusions

Three systematic experimental studies on metallic glass alloys were conducted in my PhD project. They are:

1. A systematic in situ tensile deformation studies of a bulk metals glass alloy, $Zr_{41.2}Ti_{13.8}Cu_{12.5}Ni_{10}Be_{22.5}$, and a bulk metallic glass matrix composite, $Zr_{39.6}Ti_{33.9}Nb_{7.6}Cu_{6.4}Be_{12.5}$ using scanning electron microscopy and synchrotron X-ray diffraction. The key scientific findings for this part of research are:

- Introduction of a notch-type stress concentrator at the gauge length can control the initiation and propagation of shear bands, and therefore they can be imaged in situ at the particular load where the phenomena occur.
- Using this technique, the local stresses/strains in front of the shear band can be measured using in situ synchrotron X-ray diffraction technique. Then this allows the shear band initiation and propagation is directly linked to the local stress field.
- For the Vit-1, the SEM images taken between 1703 MPa and 1992 MPa captured the formation of “step” when two propagating shear bands are cross over each other. This phenomenon can only be observed in-situ, while previous reports always to argue that the propagation of shear bands only goes along a single direction. Actually, the in-situ imaging shows that, at the cross-over point, a “step” was first formed, then a bigger “step” is formed, driven by the concentrated local stress at this point.
- For the ZrTi composite, the SEM image of the in situ tensile test at 1492 MPa captured the plastic deformation first occurred on the dendrites in P2 location. At 1626 MPa tensile stress, in situ SXRD result shows that the dendrites at P2 location reduced in axial strain

rate whereas, the amorphous matrix at same location shows increase in strain rates. The combined techniques explained that, when the yielding occurs in the dendrites, the load was transferred to the matrix.

2. A systematic in situ high pressure compression studies of a binary metallic glass alloy, $\text{Cu}_{50}\text{Zr}_{50}$, and a ternary metallic glass alloy, $\text{Fe}_{60}\text{Nb}_{15}\text{B}_{25}$ composite were studied using Diamond Anvil Cell and synchrotron X-ray diffraction. The key scientific findings for this part of research are:

- For $\text{Cu}_{50}\text{Zr}_{50}$, when pressed until 43.15 GPa, there is no obvious polyamorphism structural changes. However the pair distribution function analysis shows that the 3rd atomic shell start to split into two minor peaks, indicating that, at that pressure, the atom coordination number in the 3rd shell start to change.
- For the $\text{Fe}_{60}\text{Nb}_{15}\text{B}_{25}$, when pressed until 70.64 GPa, there is no obvious polyamorphism structural changes either. However the pair distribution function analysis shows that the rate of deformation for the 2nd atomic shell is different to those of the 1st and the 3rd shells, especially above 35.33 GPa, the rate of deformation slows down nearly 5 times.
- Comparing the binary with the ternary alloy, the $\text{Cu}_{50}\text{Zr}_{50}$ has ~30% difference between the size of the Cu atom and Zr atom; while for $\text{Fe}_{60}\text{Nb}_{15}\text{B}_{25}$, the atomic radii between Nb and Fe is 22% and that between Nb and B is 56%. So the bigger atomic size ratio showed in the $\text{Fe}_{60}\text{Nb}_{15}\text{B}_{25}$ alloy resulted in a more smooth change in the atomic shell distance during compression. While the 3rd atomic shell of $\text{Cu}_{50}\text{Zr}_{50}$ fluctuates more because of the relatively smaller atomic size ratio.

3. A systematic studies were also carried out to design, make and characterise a series of new Fe-based bulk metallic glass alloys with the objective of achieving a sufficient glass forming ability and neutron absorption capability. Through 3 round of iterative studies, alloy with the

composition of $\text{Fe}_{48}\text{Cr}_{15}\text{Mo}_{14}\text{C}_{15}\text{B}_6\text{Gd}_2$ were successfully designed and developed with the glass formation ability up to $\varnothing 5.8$ mm which is very suitable for making powders for coating applications. While this alloy also has so far the highest neutron absorption cross section with 73.64 cm^{-1} at thermal neutron 25.3 meV, as compared with other existing Fe-based metallic glass alloys.

7.2 Future work

For the in situ SEM and in situ SXR D experiments, the introduction of the artificial notch allowed a better control on the shear bands formation and propagation. However, due to the larger X-ray beam size used in our experiments, the local atomic structure strain measurements from the SXR D were averaged within the $0.25 \times 0.25 \text{ mm}^2$ area, resulting in nearly linear relationship for the strains. Therefore, for the future work, it is a good direction to re-evaluate the shear bands formation and propagation by using a smaller X-ray beam size to measure the local strains during the shear band initiation and propagation.

For the in situ SXR D under high pressure compression, the result shows that there is a small deviation from the linear relationship between the ambient pressure to 10 GPa. It is a good direction to acquire the SXR D patterns at pressure between the ambient to 15 GPa with a smaller pressure step size, i.e. ~ 1 GPa.

Lastly, for the neutron shielding alloy design, further tuning of the B and C concentrations for $\text{Fe-B}_{15}\text{Gd}_2$ is required to form a fully amorphous system with high glass forming ability such as exhibited by $\text{Fe}_{48}\text{Cr}_{15}\text{Mo}_{14}\text{C}_{15}\text{B}_6\text{Gd}_2$. The radiation induced crystallization and corrosion resistance of the alloys were not measured in the thesis and further measurement is required for the alloy if was intended to use as a neutron shielding material.

References

1. Suryanarayana, C. and A. Inoue, *Bulk metallic glasses*. 2010: CRC Press.
2. Klement, W., R.H. Willens, and P.O.L. Duwez, *Non-crystalline Structure in Solidified Gold-Silicon Alloys*. *Nature*, 1960. **187**(4740): p. 869-870.
3. Wang, W.H., *The elastic properties, elastic models and elastic perspectives of metallic glasses*. *Progress in Materials Science*, 2012. **57**(3): p. 487-656.
4. Davidson, M., et al., *Investigating amorphous metal composite architectures as spacecraft shielding*. *Advanced Engineering Materials*, 2013. **15**(1-2): p. 27-33.
5. Inoue, A. and A. Takeuchi, *Recent development and application products of bulk glassy alloys*. *Acta Materialia*, 2011. **59**(6): p. 2243-2267.
6. Greer, A.L., Y.Q. Cheng, and E. Ma, *Shear bands in metallic glasses*. *Materials Science and Engineering R: Reports*, 2013. **74**(4): p. 71-132.
7. Hofmann, D.C., et al., *Designing metallic glass matrix composites with high toughness and tensile ductility*. *Nature*, 2008. **451**(7182): p. 1085-1089.
8. Hays, C., C. Kim, and W.L. Johnson, *Microstructure controlled shear band pattern formation and enhanced plasticity of bulk metallic glasses containing in situ formed ductile phase dendrite dispersions*. *Physical Review Letters*, 2000. **84**(13): p. 2901.
9. Bouzaker, B., et al., *In situ characterization of a crack trajectory and shear bands interaction in metallic glasses*. *Journal of alloys and compounds*, 2007. **434**: p. 52-55.
10. Poulsen, H.F., et al., *Measuring strain distributions in amorphous materials*. *Nature Materials*, 2005. **4**(1): p. 33-36.
11. Huang, Y.J., et al., *In situ study of the evolution of atomic strain of bulk metallic glass and its effects on shear band formation*. *Scripta Materialia*, 2013. **69**(3): p. 207-210.
12. Huang, Y., et al., *The onset of plasticity of a Zr-based bulk metallic glass*. *International Journal of Plasticity*, 2014. **60**: p. 87-100.
13. Huang, Y., et al., *Understanding the deformation mechanism of individual phases of a ZrTi-based bulk metallic glass matrix composite using in situ diffraction and imaging methods*. *Applied Physics Letters*, 2014. **104**(3): p. 031912.
14. Barrett, C.S., *Structure of metals*. 1st ed. 1943, New York and London: McGraw-Hill.

15. Warren, B.E. and J. Biscoe, *The structure of silica glass by X-ray diffraction studies*. Journal of the American Ceramic Society, 1938. **21**(2): p. 49-54.
16. Duwez, P., R.H. Willens, and W. Klement, *Metastable Electron Compound in Ag-Ge Alloys*. Journal of Applied Physics, 1960. **31**(6): p. 1137-1137.
17. Chen, H.S., *Glassy metals*. Reports on Progress in Physics, 1980. **43**(4): p. 353.
18. Chen, H. and D. Turnbull, *Formation, stability and structure of palladium-silicon based alloy glasses*. Acta metallurgica, 1969. **17**(8): p. 1021-1031.
19. Pond, R. and R. Maddin, *Method of producing rapidly solidified filamentary castings*. Trans Met Soc AIME, 1969. **245**(11): p. 2475-2476.
20. Liebermann, H. and C. Graham Jr, *Production of amorphous alloy ribbons and effects of apparatus parameters on ribbon dimensions*. Magnetics, IEEE Transactions on, 1976. **12**(6): p. 921-923.
21. Drehman, A., A. Greer, and D. Turnbull, *Bulk formation of a metallic glass: Pd40Ni40P20*. Applied Physics Letters, 1982. **41**(8): p. 716-717.
22. Kui, H., A.L. Greer, and D. Turnbull, *Formation of bulk metallic glass by fluxing*. Applied Physics Letters, 1984. **45**(6): p. 615-616.
23. Inoue, A., *Stabilization of metallic supercooled liquid and bulk amorphous alloys*. Acta Materialia, 2000. **48**(1): p. 279-306.
24. Inoue, A., et al., *Al-La-Cu amorphous alloys with a wide supercooled liquid region*. Materials Transactions, JIM, 1990. **31**(2): p. 104-109.
25. Inoue, A., T. Zhang, and T. Masumoto, *Al-La-Ni amorphous alloys with a wide supercooled liquid region*. Materials Transactions, JIM, 1989. **30**(12): p. 965-972.
26. Axinte, E., *Metallic glasses from "alchemy" to pure science: present and future of design, processing and applications of glassy metals*. Materials & Design, 2012. **35**: p. 518-556.
27. Peker, A. and W.L. Johnson, *A highly processable metallic glass: Zr41. 2Ti13. 8Cu12. 5Ni10. 0Be22. 5*. Applied Physics Letters, 1993. **63**(17): p. 2342-2344.
28. Inoue, A., N. Nishiyama, and H. Kimura, *Preparation and thermal stability of bulk amorphous Pd 40Cu 30Ni 10P 20 alloy cylinder of 72 mm in diameter*. Materials Transactions, JIM, 1997. **38**(2): p. 179-183.
29. Lu, Z., et al., *Structural amorphous steels*. Physical Review Letters, 2004. **92**(24): p. 245503.

30. Byrne, C.J. and M. Eldrup, *Bulk Metallic Glasses*. Science, 2008. **321**(5888): p. 502-503.
31. Demetriou, M.D., et al., *A damage-tolerant glass*. Nature materials, 2011. **10**(2): p. 123-128.
32. Axinte, E., *Glasses as engineering materials: a review*. Materials & Design, 2011. **32**(4): p. 1717-1732.
33. Cheng, Y. and E. Ma, *Atomic-level structure and structure–property relationship in metallic glasses*. Progress in Materials Science, 2011. **56**(4): p. 379-473.
34. Dandliker, R., R. Conner, and W. Johnson, *Melt infiltration casting of bulk metallic-glass matrix composites*. Journal of materials research, 1998. **13**(10): p. 2896-2901.
35. Qiao, J., *In-situ dendrite/metallic glass matrix composites: a review*. Journal of Materials Science & Technology, 2013. **29**(8): p. 685-701.
36. Xue, Y., et al., *Strength-improved Zr-based metallic glass/porous tungsten phase composite by hydrostatic extrusion*. Applied physics letters, 2007. **90**(8): p. 081901.
37. Choi-Yim, H., S.-Y. Lee, and R.D. Conner, *Mechanical behavior of Mo and Ta wire-reinforced bulk metallic glass composites*. Scripta Materialia, 2008. **58**(9): p. 763-766.
38. Qiao, J.W., et al., *Tensile deformation micromechanisms for bulk metallic glass matrix composites: From work-hardening to softening*. Acta Materialia, 2011. **59**(10): p. 4126-4137.
39. Oh, Y.S., et al., *Microstructure and tensile properties of high-strength high-ductility Ti-based amorphous matrix composites containing ductile dendrites*. Acta Materialia, 2011. **59**(19): p. 7277-7286.
40. Szuecs, F., C.P. Kim, and W.L. Johnson, *Mechanical properties of Zr_{56.2}Ti_{13.8}Nb_{5.0}Cu_{6.9}Ni_{5.6}Be_{12.5} ductile phase reinforced bulk metallic glass composite*. Acta Materialia, 2001. **49**(9): p. 1507-1513.
41. Xue, Y.F., et al., *Deformation and failure behavior of a hydrostatically extruded Zr₃₈Ti₁₇Cu_{10.5}Co₁₂Be_{22.5} bulk metallic glass/porous tungsten phase composite under dynamic compression*. Composites Science and Technology, 2008. **68**(15–16): p. 3396-3400.
42. Son, C.-Y., et al., *Dynamic Compressive Properties of Zr-based Amorphous Matrix Composites Reinforced with Tungsten Continuous Fibers or Porous Foams*. Metallurgical and Materials Transactions A, 2012. **43**(6): p. 1911-1920.
43. Hirata, A., et al., *Direct observation of local atomic order in a metallic glass*. Nature materials, 2011. **10**(1): p. 28-33.

44. Egami, T., *Understanding the properties and structure of metallic glasses at the atomic level*. JOM, 2010. **62**(2): p. 70-75.
45. Elliott, S.R., *Physics of amorphous materials*. Longman Group, Longman House, Burnt Mill, Harlow, Essex CM 20 2 JE, England, 1983., 1983.
46. Sheng, H., et al., *Atomic packing and short-to-medium-range order in metallic glasses*. Nature, 2006. **439**(7075): p. 419-425.
47. Miracle, D.B., *A structural model for metallic glasses*. Nature materials, 2004. **3**(10): p. 697-702.
48. Jenkins, R., *X-Ray Techniques: Overview*. Encyclopedia of analytical chemistry, 2000.
49. Bilderback, D.H., P. Elleaume, and E. Weckert, *Review of third and next generation synchrotron light sources*. Journal of Physics B: Atomic, molecular and optical physics, 2005. **38**(9): p. S773.
50. Thompson, A., et al., *X-ray data booklet (2009)*. <http://xdb.lbl.gov>, 2009.
51. Science3d, *Basic principles of X-ray tomography - X-rays*. <https://www.science3d.org/content/basic-principles-x-ray-tomography-x-rays>, 2015.
52. Clarke, J.A., *The science and technology of undulators and wigglers*. 2004: OUP Oxford.
53. Synchrotron, A., *How is synchrotron light created?* <http://www.synchrotron.org.au/synchrotron-science/how-is-synchrotron-light-created>, 2015.
54. Dinnebier, R.E. and S.J. Billinge, *Powder diffraction: theory and practice*. 2008: Royal society of chemistry.
55. Egami, T. and S.J.L. Billinge, *Underneath the Bragg Peaks: Structural Analysis of Complex Materials*, 2003.
56. Chantler, C., *Detailed tabulation of atomic form factors, photoelectric absorption and scattering cross section, and mass attenuation coefficients in the vicinity of absorption edges in the soft X-ray ($Z=30-36$, $Z=60-89$, $E=0.1\text{ keV}-10\text{ keV}$), addressing convergence issues of earlier work*. Journal of Physical and Chemical Reference Data, 2000. **29**(4): p. 597-1056.
57. Hosokawa, S., et al., *Anomalous X-ray scattering studies on semiconducting and metallic glasses*. The European Physical Journal Special Topics, 2012. **208**(1): p. 291-304.
58. Hosokawa, S., et al. *A combination of anomalous x-ray scattering and neutron diffraction for structural characterizations of Zr₆₃Ni₂₅Al₁₂ metallic glass*. in *Journal of Physics: Conference Series*. 2014. IOP Publishing.

59. Bernal, J., *Geometry of the structure of monatomic liquids*. Nature, 1960. **185**: p. 68-70.
60. Bernal, J.D., *The Bakerian lecture, 1962. The structure of liquids*. Proceedings of the Royal Society of London. Series A, Mathematical and Physical Sciences, 1964. **280**(1382): p. 299-322.
61. Scott, G.D., *Packing of spheres: packing of equal spheres*. Nature, 1960. **188**(4754): p. 908-909.
62. Finney, J. *Random packings and the structure of simple liquids. I. The geometry of random close packing*. in *Proceedings of the Royal Society of London A: Mathematical, Physical and Engineering Sciences*. 1970. The Royal Society.
63. Finney, J. *Random packings and the structure of simple liquids. ii. the molecular geometry of simple liquids*. in *Proceedings of the Royal Society of London A: Mathematical, Physical and Engineering Sciences*. 1970. The Royal Society.
64. Mattern, N., et al., *Structural behavior of Cu_xZr_{100-x} metallic glass ($x=35-70$)*. Journal of Non-Crystalline Solids, 2008. **354**(10): p. 1054-1060.
65. Ma, D., et al., *Efficient local atomic packing in metallic glasses and its correlation with glass-forming ability*. Physical Review B, 2009. **80**(1): p. 014202.
66. Cheng, Y., E. Ma, and H. Sheng, *Atomic level structure in multicomponent bulk metallic glass*. Physical review letters, 2009. **102**(24): p. 245501.
67. Fujita, T., et al., *Atomic-scale heterogeneity of a multicomponent bulk metallic glass with excellent glass forming ability*. Physical review letters, 2009. **103**(7): p. 075502.
68. Ma, D., et al., *Nearest-neighbor coordination and chemical ordering in multicomponent bulk metallic glasses*. Applied physics letters, 2007. **90**(21): p. 211908.
69. Yamamoto, A., *Software package for structure analysis of quasicrystals*. Science and Technology of Advanced Materials, 2008. **9**(1): p. 013001.
70. Shechtman, D., et al., *Metallic phase with long-range orientational order and no translational symmetry*. Physical Review Letters, 1984. **53**(20): p. 1951.
71. Maciá, E., *The role of aperiodic order in science and technology*. Reports on progress in physics, 2006. **69**(2): p. 397.
72. Tsai, A.P., *Icosahedral clusters, icosahedral order and stability of quasicrystals-a view of metallurgy*. Sci. Technol. Adv. Mater, 2008. **9**(013008): p. 013008.

73. Unal, B., et al., *Nucleation and growth of Ag islands on fivefold Al-Pd-Mn quasicrystal surfaces: Dependence of island density on temperature and flux*. Physical Review B, 2007. **75**(6): p. 064205.
74. Sheng, H. and E. Ma, *Atomic packing of the inherent structure of simple liquids*. Physical Review E, 2004. **69**(6): p. 062202.
75. Anikeenko, A. and N. Medvedev, *Polytetrahedral nature of the dense disordered packings of hard spheres*. Physical review letters, 2007. **98**(23): p. 235504.
76. Anikeenko, A., N. Medvedev, and T. Aste, *Structural and entropic insights into the nature of the random-close-packing limit*. Physical Review E, 2008. **77**(3): p. 031101.
77. Gaskell, P., *A new structural model for transition metal-metalloid glasses*. Nature, 1978. **276**(5687): p. 484-485.
78. Miracle, D., *The efficient cluster packing model—an atomic structural model for metallic glasses*. Acta materialia, 2006. **54**(16): p. 4317-4336.
79. Inoue, A., et al., *Ti-based amorphous alloys with a wide supercooled liquid region*. Materials Letters, 1994. **19**(3): p. 131-135.
80. Senkov, O.N., *Correlation between fragility and glass-forming ability of metallic alloys*. Physical Review B, 2007. **76**(10): p. 104202.
81. Cai, A.-h., et al., *Progress of component design methods for bulk metallic glass*. Materials & design, 2007. **28**(10): p. 2694-2697.
82. Inoue, A., *Recent progress of Zr-based bulk amorphous alloys*. Science Reports of the Research Institutes Tohoku University Series A-Physics, 1996. **42**(1): p. 1-11.
83. Turnbull, D., *Under what conditions can a glass be formed?* Contemporary physics, 1969. **10**(5): p. 473-488.
84. Hrubý, A., *Evaluation of glass-forming tendency by means of DTA*. Czechoslovak Journal of Physics B, 1972. **22**(11): p. 1187-1193.
85. Inoue, A., *High strength bulk amorphous alloys with low critical cooling rates (overview)*. Materials Transactions, JIM, 1995. **36**(7): p. 866-875.
86. Lu, Z. and C. Liu, *A new glass-forming ability criterion for bulk metallic glasses*. Acta materialia, 2002. **50**(13): p. 3501-3512.
87. Lu, Z. and C. Liu, *Glass formation criterion for various glass-forming systems*. Physical review letters, 2003. **91**(11): p. 115505.
88. Mondal, K. and B. Murty, *On the parameters to assess the glass forming ability of liquids*. Journal of non-crystalline solids, 2005. **351**(16): p. 1366-1371.

89. Kim, J.-H., et al., *Heating and cooling rate dependence of the parameters representing the glass forming ability in bulk metallic glasses*. Journal of non-crystalline solids, 2005. **351**(16): p. 1433-1440.
90. Chen, Q., et al., *A new criterion for evaluating the glass-forming ability of bulk metallic glasses*. Materials Science and Engineering: A, 2006. **433**(1): p. 155-160.
91. Du, X., et al., *New criterion of glass forming ability for bulk metallic glasses*. Journal of applied physics, 2007. **101**(8): p. 086108.
92. Fan, G., H. Choo, and P. Liaw, *A new criterion for the glass-forming ability of liquids*. Journal of non-crystalline solids, 2007. **353**(1): p. 102-107.
93. Yuan, Z.-Z., et al., *A new criterion for evaluating the glass-forming ability of bulk glass forming alloys*. Journal of Alloys and Compounds, 2008. **459**(1): p. 251-260.
94. Long, Z., et al., *A new criterion for predicting the glass-forming ability of bulk metallic glasses*. Journal of alloys and compounds, 2009. **475**(1): p. 207-219.
95. Long, Z., et al., *On the new criterion to assess the glass-forming ability of metallic alloys*. Materials Science and Engineering: A, 2009. **509**(1): p. 23-30.
96. Suo, Z.Y., et al., *A new parameter to evaluate the glass-forming ability of bulk metallic glasses*. Materials Science and Engineering: A, 2010. **528**(1): p. 429-433.
97. Dong, B.-s., et al., *A new criterion for predicting glass forming ability of bulk metallic glasses and some critical discussions*. Progress in Natural Science: Materials International, 2011. **21**(2): p. 164-172.
98. Zhang, Y., et al., *Relationship between glass forming ability and thermal parameters of Zr based bulk metallic glasses*. Materials science and technology, 2003. **19**(7): p. 973-976.
99. Inoue, A., T. Zhang, and T. Masumoto, *Glass-forming ability of alloys*. Journal of non-crystalline solids, 1993. **156-158**: p. 473-480.
100. Nagel, S. and J. Tauc, *Nearly-free-electron approach to the theory of metallic glass alloys*. Physical Review Letters, 1975. **35**(6): p. 380.
101. Alamgir, F., et al., *Electronic structure of Pd-based bulk metallic glasses*. Journal of non-crystalline solids, 2000. **274**(1): p. 289-293.
102. Wang, X., M. Qi, and C. Dong, *Electronic structure models for the effect of Al addition on the glass forming ability of Zr-base amorphous alloys*. Acta Metallurgica Sinica-chinese edition, 2002. **38**(12): p. 1241-1245.

103. Zhang, G.-Y., Z.-Q. Hu, and H.-F. Zhang, *Electronic theory calculations of alloying effect to amorphous alloy forming ability*. Chinese Journal of Nonferrous Metals(China), 2003. **13**(1): p. 106-110.
104. Keong, K., W. Sha, and S. Malinov, *Artificial neural network modelling of crystallization temperatures of the Ni-P based amorphous alloys*. Materials Science and Engineering: A, 2004. **365**(1): p. 212-218.
105. Suryanarayana, C., *Rapid solidification*. Materials Science and Technology, 1991.
106. Jacobson, L.A. and J. McKittrick, *Rapid solidification processing*. Materials Science and Engineering: R: Reports, 1994. **11**(8): p. 355-408.
107. Goel, T., K. Chopra, and R. Budhani, *Melt-spinning technique for preparation of metallic glasses*. Bulletin of Materials Science, 1982. **4**(5): p. 549-561.
108. Chen, H.S., *Thermodynamic considerations on the formation and stability of metallic glasses*. Acta Metallurgica, 1974. **22**(12): p. 1505-1511.
109. Inoue, A., et al., *Mg-Cu-Y bulk amorphous alloys with high tensile strength produced by a high-pressure die casting method*. Materials Transactions, JIM, 1992. **33**(10): p. 937-945.
110. Inoue, A., et al., *Bulky La-Al-TM (TM= transition metal) amorphous alloys with high tensile strength produced by a high-pressure die casting method*. Materials Transactions, JIM, 1993. **34**(4): p. 351-358.
111. Nishiyama, N. and A. Inoue, *Glass-forming ability of bulk Pd 40 Ni 10 Cu 30 P 20 alloy*. Materials Transactions, JIM, 1996. **37**(10): p. 1531-1539.
112. Park, E. and D. Kim, *Formation of Ca-Mg-Zn bulk glassy alloy by casting into cone-shaped copper mold*. Journal of Materials Research, 2004. **19**(03): p. 685-688.
113. Inoue, A., et al., *Solidification Analyses of Bulky Zr 60 Al 10 Ni 10 Cu 15 Pd 5 Glass Produced by Casting into Wedge-Shape Copper Mold*. Materials Transactions, JIM, 1995. **36**(10): p. 1276-1281.
114. Yokoyama, Y., et al., *Production of Zr55Cu30Ni5Al10 glassy alloy rod of 30 mm in diameter by a cap-cast technique*. Materials transactions, 2007. **48**(12): p. 3190-3192.
115. Inoue, A. and T. Zhang, *Fabrication of bulky Zr-based glassy alloys by suction casting into copper mold*. Materials Transactions, JIM, 1995. **36**(9): p. 1184-1187.
116. Lynch, R., R. Olley, and P. Gallagher, *Squeeze casting of brass and bronze*. TRANS AFS, 1975. **83**: p. 561-568.

117. Kang, H.G., et al., *Fabrication of bulk Mg–Cu–Ag–Y glassy alloy by squeeze casting*. Materials Transactions, JIM, 2000. **41**(7): p. 846-849.
118. Zhang, T., et al., *Study on continuous casting of bulk metallic glass*. Materials Letters, 2011. **65**(14): p. 2257-2260.
119. Sharma, P., et al., *Nano-fabrication with metallic glass—an exotic material for nano-electromechanical systems*. Nanotechnology, 2007. **18**(3): p. 035302.
120. Saotome, Y., et al. *Superplastic nanoforging of Pt-based metallic glass with dies of Zr-BMG and glassy carbon fabricated by focused ion beam*. in *Materials science forum*. 2007. Trans Tech Publ.
121. Schroers, J., et al., *Thermoplastic blow molding of metals*. Materials Today, 2011. **14**(1): p. 14-19.
122. Qin, F., et al., *Corrosion behavior of a Ti-based bulk metallic glass and its crystalline alloys*. Materials transactions, 2007. **48**(7): p. 1855-1858.
123. Subramanian, B., *In vitro corrosion and biocompatibility screening of sputtered Ti 40 Cu 36 Pd 14 Zr 10 thin film metallic glasses on steels*. Materials Science and Engineering: C, 2015. **47**: p. 48-56.
124. Zberg, B., P.J. Uggowitzer, and J.F. Löffler, *MgZnCa glasses without clinically observable hydrogen evolution for biodegradable implants*. Nature Materials, 2009. **8**(11): p. 887-891.
125. Schroers, J., Q. Pham, and A. Desai, *Thermoplastic forming of bulk metallic glass—a technology for MEMS and microstructure fabrication*. Microelectromechanical Systems, Journal of, 2007. **16**(2): p. 240-247.
126. Gravier, S., et al., *Thermoplastic forming of bulk metallic glasses*. International Journal of Applied Glass Science, 2012. **3**(2): p. 180-187.
127. Kumar, G., H.X. Tang, and J. Schroers, *Nanomoulding with amorphous metals*. Nature, 2009. **457**(7231): p. 868-872.
128. Schroers, J., *The superplastic forming of bulk metallic glasses*. Jom, 2005. **57**(5): p. 35-39.
129. Duan, G., et al., *Bulk metallic glass with benchmark thermoplastic processability*. Advanced Materials, 2007. **19**(23): p. 4272-4275.
130. Yokoyama, Y., et al. *Cap casting and enveloped casting techniques for Zr₅₅Cu₃₀Ni₅Al₁₀ glassy alloy rod with 32 mm in diameter*. in *Journal of Physics: Conference Series*. 2009. IOP Publishing.
131. Okumura, K., et al. *Development of Fe-based metallic glass shot "AMO-beads" for peening with high strength and long life*. in *10th Int conf on shot peening (ICSP 10th)*, Tokyo, Japan. 2008.

132. Trexler, M.M. and N.N. Thadhani, *Mechanical properties of bulk metallic glasses*. Progress in Materials Science, 2010. **55**(8): p. 759-839.
133. Ashby, M.F. and A.L. Greer, *Metallic glasses as structural materials*. Scripta Materialia, 2006. **54**(3): p. 321-326.
134. Zhang, Z., J. Eckert, and L. Schultz, *Difference in compressive and tensile fracture mechanisms of Zr 59 Cu 20 Al 10 Ni 8 Ti 3 bulk metallic glass*. Acta Materialia, 2003. **51**(4): p. 1167-1179.
135. Schuh, C. and T. Nieh, *A survey of instrumented indentation studies on metallic glasses*. Journal of Materials Research, 2004. **19**(01): p. 46-57.
136. Oliver, W.C. and G.M. Pharr, *An improved technique for determining hardness and elastic modulus using load and displacement sensing indentation experiments*. Journal of materials research, 1992. **7**(06): p. 1564-1583.
137. Burgess, T. and M. Ferry, *Nanoindentation of metallic glasses*. Materials Today, 2009. **12**(1): p. 24-32.
138. Schuh, C.A. and T.G. Nieh, *A nanoindentation study of serrated flow in bulk metallic glasses*. Acta Materialia, 2003. **51**(1): p. 87-99.
139. Conner, R., et al., *Shear bands and cracking of metallic glass plates in bending*. Journal of applied physics, 2003. **94**(2): p. 904-911.
140. Conner, R., et al., *Shear band spacing under bending of Zr-based metallic glass plates*. Acta materialia, 2004. **52**(8): p. 2429-2434.
141. Spaepen, F., *A microscopic mechanism for steady state inhomogeneous flow in metallic glasses*. Acta Metallurgica, 1977. **25**(4): p. 407-415.
142. Argon, A.S., *Plastic deformation in metallic glasses*. Acta Metallurgica, 1979. **27**(1): p. 47-58.
143. Steif, P.S., F. Spaepen, and J.W. Hutchinson, *Strain localization in amorphous metals*. Acta Metallurgica, 1982. **30**(2): p. 447-455.
144. Wei, Q., et al., *Evolution and microstructure of shear bands in nanostructured Fe*. Applied physics letters, 2002. **81**(7): p. 1240-1242.
145. Leamy, H.J., T.T. Wang, and H.S. Chen, *Plastic flow and fracture of metallic glass*. Metallurgical Transactions, 1972. **3**(3): p. 699-708.
146. Yang, B., et al., *In-situ thermographic observation of mechanical damage in bulk-metallic glasses during fatigue and tensile experiments*. Intermetallics, 2004. **12**(10): p. 1265-1274.
147. Yang, B., et al., *Dynamic evolution of nanoscale shear bands in a bulk-metallic glass*. Applied Physics Letters, 2005. **86**(14): p. 141904.

148. Lewandowski, J.J. and A.L. Greer, *Temperature rise at shear bands in metallic glasses*. Nat Mater, 2006. **5**(1): p. 15-18.
149. Takeuchi, S. and K. Edagawa, *Atomistic simulation and modeling of localized shear deformation in metallic glasses*. Progress in Materials Science, 2011. **56**(6): p. 785-816.
150. Falk, M. and J. Langer, *Dynamics of viscoplastic deformation in amorphous solids*. Physical Review E, 1998. **57**(6): p. 7192.
151. Dragoi, D., et al., *Investigation of thermal residual stresses in tungsten-fiber/bulk metallic glass matrix composites*. Scripta Materialia, 2001. **45**(2): p. 245-252.
152. Balch, D.K., E. Üstündag, and D.C. Dunand, *Elasto-plastic load transfer in bulk metallic glass composites containing ductile particles*. Metallurgical and Materials Transactions A, 2003. **34**(9): p. 1787-1797.
153. Tabor, D., *The hardness of solids*. Review of physics in technology, 1970. **1**(3): p. 145.
154. Cahoon, J., W. Broughton, and A. Kutzak, *The determination of yield strength from hardness measurements*. Metallurgical Transactions, 1971. **2**(7): p. 1979-1983.
155. Chen, X.-Q., et al., *Modeling hardness of polycrystalline materials and bulk metallic glasses*. Intermetallics, 2011. **19**(9): p. 1275-1281.
156. Telford, M., *The case for bulk metallic glass*. Materials Today, 2004. **7**(3): p. 36-43.
157. Moreton, R. and J. Lancaster, *The friction and wear behaviour of various metallic glasses*. Journal of materials science letters, 1985. **4**(2): p. 133-137.
158. Miyoshi, K. and D.H. Buckley, *Friction and wear of some ferrous-base metallic glasses*. ASLE transactions, 1984. **27**(4): p. 295-304.
159. Girerd, G., P. Guiraldenq, and N. Du, *Surface fatigue during dry friction of a ferrous metallic glass Fe 40 Ni 40 P 14 B 6*. Wear, 1985. **102**(3): p. 233-240.
160. Prakash, B., *Abrasive wear behaviour of Fe, Co and Ni based metallic glasses*. Wear, 2005. **258**(1): p. 217-224.
161. Huang, Y., et al., *Mechanical performance of metallic glasses during nanoscratch tests*. Intermetallics, 2010. **18**(5): p. 1056-1061.
162. Blink, J., et al., *Applications in the nuclear industry for thermal spray amorphous metal and ceramic coatings*. Metallurgical and Materials Transactions A, 2009. **40**(6): p. 1344-1354.
163. Inoue, A., B. Shen, and C. Chang, *Super-high strength of over 4000 MPa for Fe-based bulk glassy alloys in [(Fe 1-x Co x) 0.75 B 0.2 Si 0.05] 96 Nb 4 system*. Acta Materialia, 2004. **52**(14): p. 4093-4099.

164. Matthews, D., V. Ocelik, and J.T.M. De Hosson, *Tribological and mechanical properties of high power laser surface-treated metallic glasses*. Materials Science and Engineering: A, 2007. **471**(1): p. 155-164.
165. Zhang, C., et al., *Wear behavior of HVOF-sprayed Fe-based amorphous coatings*. Intermetallics, 2012. **29**: p. 80-85.
166. Wang, Y., et al., *Slurry erosion–corrosion behaviour of high-velocity oxy-fuel (HVOF) sprayed Fe-based amorphous metallic coatings for marine pump in sand-containing NaCl solutions*. Corrosion science, 2011. **53**(10): p. 3177-3185.
167. Liu, X., et al., *Microstructure and properties of Fe-based amorphous metallic coating produced by high velocity axial plasma spraying*. Journal of Alloys and Compounds, 2009. **484**(1): p. 300-307.
168. Kobayashi, A., et al., *Mechanical property of Fe-base metallic glass coating formed by gas tunnel type plasma spraying*. Surface and Coatings Technology, 2008. **202**(12): p. 2513-2518.
169. Naka, M., K. Hashimoto, and T. Masumoto, *Corrosion resistivity of amorphous iron alloys containing chromium*. Nippon Kinzoku Gakkaishi/Journal of the Japan Institute of Metals, 1974. **38**(9): p. 835-841.
170. Naka, M., K. Hashimoto, and T. Masumoto, *High corrosion resistance of chromium-bearing amorphous iron alloys in neutral and acidic solutions containing chloride*. Corrosion, 1976. **32**(4): p. 146-152.
171. Masumoto, T. and K. Hashimoto, *Chemical properties of amorphous metals*. Annual Review of Materials Science, 1978. **8**(1): p. 215-233.
172. Luborsky, F., *Amorphous metallic alloys*. 1983, London, UK: Butterworth and Co.
173. Scully, J.R., A. Gebert, and J.H. Payer, *Corrosion and related mechanical properties of bulk metallic glasses*. Journal of Materials Research, 2007. **22**(02): p. 302-313.
174. Miller, M.K. and P. Liaw, *Bulk metallic glasses: an overview*. 2007: Springer Science & Business Media.
175. Pang, S., et al., *Bulk glassy Fe–Cr–Mo–C–B alloys with high corrosion resistance*. Corrosion Science, 2002. **44**(8): p. 1847-1856.
176. Pang, S., et al., *New Fe-Cr-Mo-(Nb, Ta)-CB Glassy Alloys with High Glass-Forming Ability and Good Corrosion Resistance*. Materials Transactions, 2001. **42**(2): p. 376-379.
177. Wang, Z., et al., *Susceptibility of minor alloying to corrosion behavior in yttrium-containing bulk amorphous steel*. Intermetallics, 2008. **16**(8): p. 1036-1039.

178. Jayaraj, J., et al., *Corrosion mechanism of N-containing Fe–Cr–Mo–Y–C–B bulk amorphous alloys in highly concentrated HCl solution*. Materials Science and Engineering: A, 2007. **449-451**: p. 517-520.
179. Farmer, J.C., et al., *Corrosion resistance of thermally sprayed high-boron iron-based amorphous-metal coatings: Fe_{49.7}Cr_{17.7}Mn_{1.9}Mo_{7.4}W_{1.6}B_{15.2}C_{3.8}Si_{2.4}*. Journal of Materials Research, 2007. **22**(8): p. 2297-2311.
180. Zhou, Z., et al., *Formation and corrosion behavior of Fe-based amorphous metallic coatings by HVOF thermal spraying*. Surface and Coatings Technology, 2009. **204**(5): p. 563-570.
181. Zois, D., A. Lekatou, and M. Vardavoulias, *Preparation and characterization of highly amorphous HVOF stainless steel coatings*. Journal of Alloys and Compounds, 2010. **504**(SUPPL. 1): p. S283-S287.
182. Zhang, C., et al., *Pitting initiation in Fe-based amorphous coatings*. Acta Materialia, 2012. **60**(10): p. 4152-4159.
183. Ni, H., et al., *High performance amorphous steel coating prepared by HVOF thermal spraying*. Journal of Alloys and Compounds, 2009. **467**(1): p. 163-167.
184. Agency, I.A.E., *The Net Enabled Waste Management Database*. IAEA, 2013.
185. Rebak, R.B., *Materials in nuclear waste disposition*. JOM, 2014. **66**(3): p. 455-460.
186. Farmer, J., et al., *Corrosion resistance of thermally sprayed high-boron iron-based amorphous-metal coatings: Fe 49.7 Cr 17.7 Mn 1.9 Mo 7.4 W 1.6 B 15.2 C 3.8 Si 2.4*. Journal of materials research, 2007. **22**(08): p. 2297-2311.
187. Rinard, P., *Neutron interactions with matter*. Passive Nondestructive Assay of Nuclear Materials, 1991: p. 357-377.
188. Nieh, T., et al., *Superplastic behavior of a Zr–10Al–5Ti–17.9 Cu–14.6 Ni metallic glass in the supercooled liquid region*. Scripta Materialia, 1999. **40**(9): p. 1021-1027.
189. Kawamura, Y., T. Nakamura, and A. Inoue, *Superplasticity in Pd 40 Ni 40 P 20 metallic glass*. Scripta Materialia, 1998. **39**(3): p. 301-306.
190. Kawamura, Y., et al., *Workability of the supercooled liquid in the Zr₆₅Al₁₀Ni₁₀Cu₁₅ bulk metallic glass*. Acta Materialia, 1998. **46**(1): p. 253-263.
191. Wang, G., et al., *Microstructure and properties of Zr₆₅Al₁₀ Ni₁₀Cu₁₅ amorphous plates rolled in the supercooled liquid region*. Materials Science and Engineering A, 2004. **373**(1-2): p. 217-220.

192. Lewandowski, J.J., M. Shazly, and A.S. Nouri, *Intrinsic and extrinsic toughening of metallic glasses*. Scripta Materialia, 2006. **54**(3): p. 337-341.
193. Matthews, D., et al., *An electron microscopy appraisal of tensile fracture in metallic glasses*. Acta Materialia, 2008. **56**(8): p. 1762-1773.
194. Kuzmin, O., Y. Pei, and J.T.M. De Hosson, *Size effects and ductility of Al-based metallic glass*. Scripta Materialia, 2012. **67**(4): p. 344-347.
195. Chen, C.Q., et al., *Intrinsic size effects in the mechanical response of taper-free nanopillars of metallic glass*. Physical Review B, 2011. **83**(18): p. 180201.
196. Greer, J.R. and J.T.M. De Hosson, *Plasticity in small-sized metallic systems: Intrinsic versus extrinsic size effect*. Progress in Materials Science, 2011. **56**(6): p. 654-724.
197. Yang, Y., et al., *Dual character of stable shear banding in bulk metallic glasses*. Intermetallics, 2011. **19**(7): p. 1005-1013.
198. Peters, W. and W. Ranson, *Digital imaging techniques in experimental stress analysis*. Optical engineering, 1982. **21**(3): p. 213427-213427-.
199. McCormick, N. and J. Lord, *Digital image correlation*. Materials today, 2010. **13**(12): p. 52-54.
200. Zhang, J., et al., *Complexity of shear localization in a Zr-based bulk metallic glass*. Scripta Materialia, 2009. **61**(12): p. 1145-1148.
201. Song, S., X.-L. Wang, and T. Nieh, *Capturing shear band propagation in a Zr-based metallic glass using a high-speed camera*. Scripta Materialia, 2010. **62**(11): p. 847-850.
202. Ott, R., et al., *Micromechanics of deformation of metallic-glass-matrix composites from in situ synchrotron strain measurements and finite element modeling*. Acta materialia, 2005. **53**(7): p. 1883-1893.
203. Wang, G., et al., *Atomic structure evolution in bulk metallic glass under compressive stress*. Applied Physics Letters, 2009. **95**(25): p. 251906.
204. Hemley, R.J. and N.W. Ashcroft, *The revealing role of pressure in the condensed matter sciences*. Physics Today, 2008. **51**(8): p. 26-32.
205. Sheng, H.W., et al., *Polyamorphism in a metallic glass*. Nature Materials, 2007. **6**(3): p. 192-197.
206. Mishima, O., L.D. Calvert, and E. Whalley, *An apparently first-order transition between two amorphous phases of ice induced by pressure*. Nature, 1985. **314**(6006): p. 76-78.

207. McMillan, P.F., et al., *A density-driven phase transition between semiconducting and metallic polyamorphs of silicon*. Nature Materials, 2005. **4**(9): p. 680-684.
208. Shick, A.B., W.E. Pickett, and A.I. Liechtenstein, *Ground and metastable states in γ -Ce from correlated band theory*. Journal of Electron Spectroscopy and Related Phenomena, 2001. **114-116**: p. 753-758.
209. Söderlind, P., *Theory of the crystal structures of cerium and the light actinides*. Advances in Physics, 1998. **47**(6): p. 959-998.
210. Zeng, Q.-s., et al., *Origin of pressure-induced polyamorphism in Ce 75 Al 25 metallic glass*. Physical review letters, 2010. **104**(10): p. 105702.
211. Zeng, Q., et al., *Properties of polyamorphous Ce 75 Al 25 metallic glasses*. Physical Review B, 2010. **82**(5): p. 054111.
212. Duarte, M., et al., *Polyamorphic transitions in Ce-based metallic glasses by synchrotron radiation*. Physical Review B, 2011. **84**(22): p. 224116.
213. Zeng, Q.S., et al., *Anomalous compression behavior in lanthanum/cerium-based metallic glass under high pressure*. Proceedings of the National Academy of Sciences of the United States of America, 2007. **104**(34): p. 13565-13568.
214. Li, G., et al., *Atomic configuration evaluation of Zr₆₀Ni₂₁Al₁₉ bulk metallic glass under high pressure*. Materials Chemistry and Physics, 2009. **113**(2-3): p. 937-940.
215. Wang, X.Y., et al., *Compression behaviour and micro-structure evaluation of Zr₅₇Nb₅Cu_{15.4}Ni_{12.6}Al₁₀ bulk metallic glass under high pressure*. Materials Letters, 2007. **61**(11-12): p. 2170-2172.
216. Ponnambalam, V., S.J. Poon, and G.J. Shiflet, *Fe-based bulk metallic glasses with diameter thickness larger than one centimeter*. Journal of Materials Research, 2004. **19**(05): p. 1320-1323.
217. Guo, F., et al., *Ductile titanium-based glassy alloy ingots*. Applied Physics Letters, 2005. **86**(9): p. 1907.
218. EN, B., *10002-1: 2001. Tensile testing of metallic materials. Method of test at ambient temperature*. British Standards Institution, 2001.
219. Willmott, P., *An introduction to synchrotron radiation: techniques and applications*. 2011: John Wiley & Sons.
220. Hammersley, A., S. Svensson, and A. Thompson, *Calibration and correction of spatial distortions in 2D detector systems*. Nuclear Instruments and Methods in Physics Research Section A: Accelerators, Spectrometers, Detectors and Associated Equipment, 1994. **346**(1): p. 312-321.

221. Schneider, C.A., W.S. Rasband, and K.W. Eliceiri, *NIH Image to ImageJ: 25 years of image analysis*. Nat Meth, 2012. **9**(7): p. 671-675.
222. Qiu, X., J.W. Thompson, and S.J. Billinge, *PDFgetX2: a GUI-driven program to obtain the pair distribution function from X-ray powder diffraction data*. Journal of Applied Crystallography, 2004. **37**(4): p. 678-678.
223. Zhang, H., et al., *Investigation of shear band evolution in amorphous alloys beneath a Vickers indentation*. Acta Materialia, 2005. **53**(14): p. 3849-3859.
224. Zhao, Y.-Y., et al., *Evolution of shear bands into cracks in metallic glasses*. Journal of Alloys and Compounds, 2015. **621**: p. 238-243.
225. Li, J., et al., *In situ SEM study of formation and growth of shear bands and microcracks in bulk metallic glasses*. Materials Science and Engineering: A, 2003. **354**(1): p. 337-343.
226. Song, S.X., X.L. Wang, and T.G. Nieh, *Capturing shear band propagation in a Zr-based metallic glass using a high-speed camera*. Scripta Materialia, 2010. **62**(11): p. 847-850.
227. Song, S.X. and T.G. Nieh, *Direct measurements of shear band propagation in metallic glasses - An overview*. Intermetallics, 2011. **19**(12): p. 1968-1977.
228. Kuzmin, O., et al., *Intrinsic and extrinsic size effects in the deformation of metallic glass nanopillars*. Acta Materialia, 2012. **60**(3): p. 889-898.
229. Spaepen, F., *Metallic glasses: Must shear bands be hot?* Nature Materials, 2006. **5**(1): p. 7-8.
230. Qiao, J.W., et al., *Micromechanisms of plastic deformation of a dendrite/Zr-based bulk-metallic-glass composite*. Scripta Materialia, 2009. **61**(11): p. 1087-1090.
231. Jayaraman, A., *Diamond anvil cell and high-pressure physical investigations*. Reviews of Modern Physics, 1983. **55**(1): p. 65.
232. Letoullec, R., J. Pinceaux, and P. Loubeyre, *The membrane diamond anvil cell: a new device for generating continuous pressure and temperature variations*. International Journal of High Pressure Research, 1988. **1**(1): p. 77-90.
233. Van Valkenburg, A., *Conference Internationale Sur-les-Hautes Pressions*. LeCreusot, Saone-et-Loire, France, 1965.
234. Piermarini, G., S. Block, and J. Barnett, *Hydrostatic limits in liquids and solids to 100 kbar*. Journal of Applied Physics, 1973. **44**(12): p. 5377-5382.

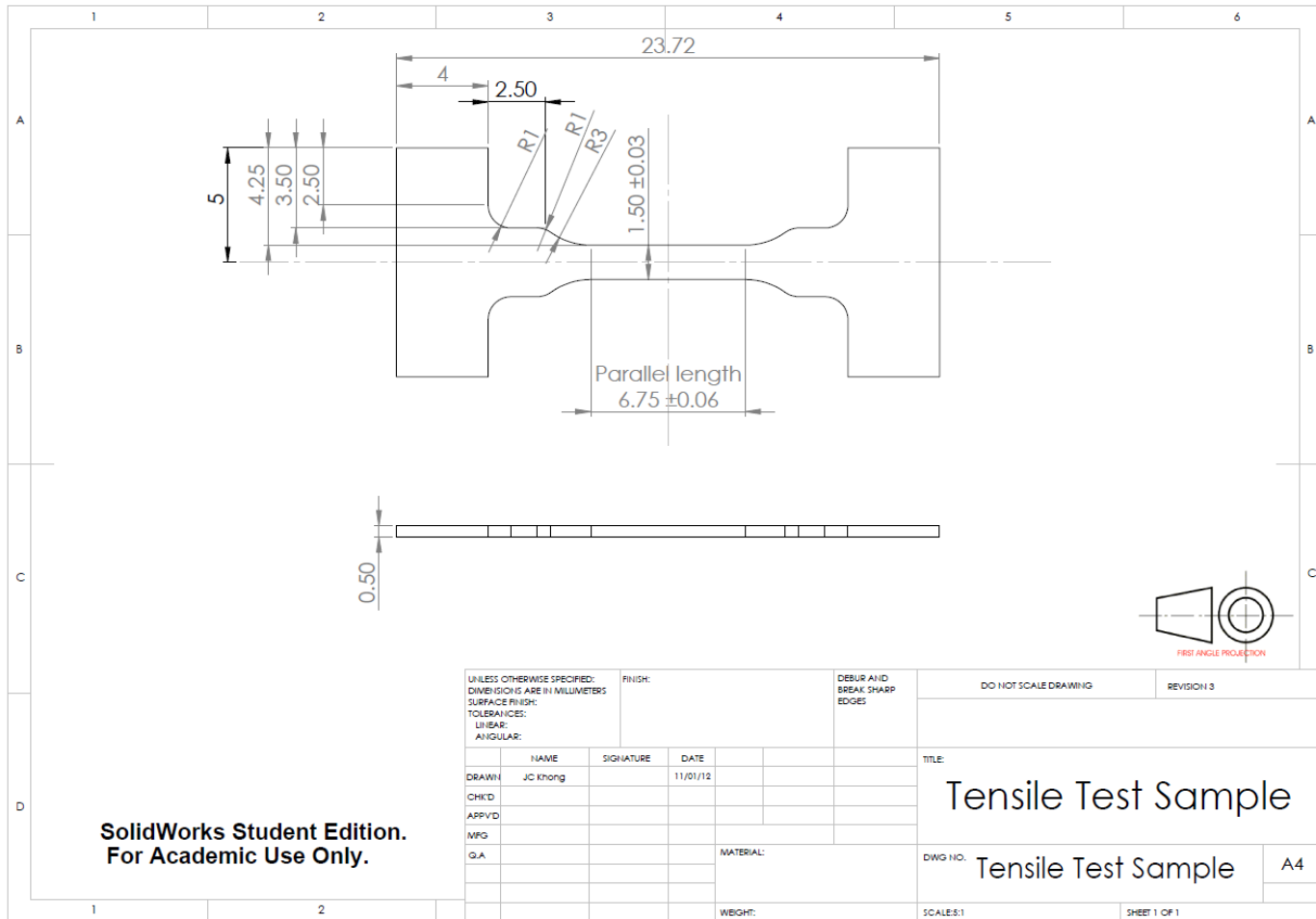
235. ESRF, *Diamond anvil cell, membrane driven*. <http://www.esrf.eu/home/UsersAndScience/Experiments/SciInfra/SampleEnvironment/high-pressure/sess-hp-loan-pool-dacs.html>, 2015.
236. Polsky, C.H. and E. Valkenburg, *The diamond anvil cell*. 2002: Wiley Online Library.
237. Barnett, J., S. Block, and G. Piermarini, *An Optical Fluorescence System for Quantitative Pressure Measurement in the Diamond-Anvil Cell*. Review of scientific instruments, 1973. **44**(1): p. 1-9.
238. DLS, *I15: High pressure P-measurement*. http://www.diamond.ac.uk/Beamlines/Engineering-and-Environment/I15/I15-Extreme/high_pressure.html, 2015.
239. Mao, H.K. and P.M. Bell, *High-pressure physics: The 1-megabar mark on the ruby R1 static pressure scale*. Science, 1976. **191**(4229): p. 851-852.
240. Liu, Z., Q. Cui, and G. Zou, *Disappearance of the ruby R-line fluorescence under quasihydrostatic pressure and valid pressure range of ruby gauge*. Physics Letters A, 1990. **143**(1-2): p. 79-82.
241. Syassen, K., *Ruby under pressure*. High Pressure Research, 2008. **28**(2): p. 75-126.
242. Shen, G., et al., *Structural investigation of amorphous materials at high pressures using the diamond anvil cell*. Review of scientific instruments, 2003. **74**(6): p. 3021-3026.
243. Saloman, E., J. Hubbell, and J. Scofield, *X-ray attenuation cross sections for energies 100 eV to 100 keV and elements Z= 1 to Z= 92*. Atomic Data and Nuclear Data Tables, 1988. **38**(1): p. 1-196.
244. Soignard, E., C.J. Benmore, and J.L. Yarger, *A perforated diamond anvil cell for high-energy X-ray diffraction of liquids and amorphous solids at high pressure*. Review of Scientific Instruments, 2010. **81**(3): p. 035110.
245. Besson, J.M. and J.P. Pinceaux, *Uniform stress conditions in the diamond anvil cell at 200 kilobars*. Review of Scientific Instruments, 1979. **50**(5): p. 541-543.
246. Eggert, J.H., et al., *Quantitative structure factor and density measurements of high-pressure fluids in diamond anvil cells by x-ray diffraction: Argon and water*. Physical Review B, 2002. **65**(17): p. 174105.
247. Kaplow, R., S. Strong, and B. Averbach, *Radial density functions for liquid mercury and lead*. Physical Review, 1965. **138**(5A): p. A1336.
248. Brennan, S. and P.L. Cowan, *A suite of programs for calculating x-ray absorption, reflection, and diffraction performance for a variety of materials at arbitrary wavelengths*. Review of Scientific Instruments, 1992. **63**(1): p. 850-853.

249. Fuoss, P., et al., *Application of differential anomalous x-ray scattering to structural studies of amorphous materials*. Physical Review Letters, 1981. **46**(23): p. 1537.
250. Faber, T. and J. Ziman, *A theory of the electrical properties of liquid metals: III. The resistivity of binary alloys*. Philosophical Magazine, 1965. **11**(109): p. 153-173.
251. Petkov, V., et al., *Local structure of In_{0.5}Ga_{0.5}As from joint high-resolution and differential pair distribution function analysis*. Journal of Applied Physics, 2000. **88**(2): p. 665-672.
252. Waasmaier, D. and A. Kirfel, *New analytical scattering-factor functions for free atoms and ions*. Acta Crystallographica Section A: Foundations of Crystallography, 1995. **51**(3): p. 416-431.
253. Sheng, H., et al., *Polyamorphism in a metallic glass*. Nature materials, 2007. **6**(3): p. 192-197.
254. Clementi, E.t. and D.-L. Raimondi, *Atomic screening constants from SCF functions*. The Journal of Chemical Physics, 1963. **38**(11): p. 2686-2689.
255. Suryanarayana, C. and A. Inoue, *Iron-based bulk metallic glasses*. International Materials Reviews, 2013. **58**(3): p. 131-166.
256. Pan, S.P., et al., *Origin of splitting of the second peak in the pair-distribution function for metallic glasses*. Physical Review B, 2011. **84**(9): p. 092201.
257. Inoue, A. and J.S. Gook, *Fe-based ferromagnetic glassy alloys with wide supercooled liquid region*. Materials Transactions, JIM, 1995. **36**(9): p. 1180-1183.
258. Stoica, M., et al., *New ternary Fe-based bulk metallic glass with high boron content*. Philosophical magazine letters, 2006. **86**(04): p. 267-275.
259. Ponnambalam, V., S.J. Poon, and G.J. Shiflet, *Fe-based bulk metallic glasses with diameter thickness larger than one centimeter*. Journal of Materials Research, 2004. **19**(5): p. 1320-1323.
260. Long, Z.L., et al., *Cr effects on magnetic and corrosion properties of Fe-Co-Si-B-Nb-Cr bulk glassy alloys with high glass-forming ability*. Intermetallics, 2007. **15**(11): p. 1453-1458.
261. Tan, M.W., et al., *The role of chromium and molybdenum in passivation of amorphous Fe-Cr-Mo-P-C alloys in de-aerated 1 M HCl*. Corrosion Science, 1996. **38**(12): p. 2137-2151.
262. Inoue, A. and X.M. Wang, *Bulk amorphous FC20 (Fe-C-Si) alloys with small amounts of B and their crystallized structure and mechanical properties*. Acta Materialia, 2000. **48**(6): p. 1383-1395.

263. Varley, F.S., *Neutron scattering lengths and cross sections*. Neutron News, 1992. **3**(3).
264. Rinard, P., G. Bosler, and J. Phillips, *Calculated neutron-source spectra from selected irradiated PWR fuel assemblies*. 1981, LANL Report No.: LA-9125-MS.
265. WNA, *World Nuclear Association: Radioactive waste management*. <http://www.world-nuclear.org/info/nuclear-fuel-cycle/nuclear-wastes/radioactive-waste-management/>, 2015.
266. Kockelmann, W.A., et al. *Application spectrum and data quality of the Time-to-Flight Neutron Diffractometer ROTAX at ISIS*. in *Materials Science Forum*. 2000. Trans Tech Publ.
267. Chadwick, M.B., et al., *ENDF/B-VII.1 Nuclear Data for Science and Technology: Cross Sections, Covariances, Fission Product Yields and Decay Data*. Nuclear Data Sheets, 2011. **112**(12): p. 2887-2996.
268. Sears, V.F., *Neutron scattering lengths and cross sections*. Neutron News, 1992. **3**(3): p. 26-37.
269. Carron, N.J., *An introduction to the passage of energetic particles through matter*. 2006: CRC Press.
270. Polk, D., *Structural model for amorphous metallic alloys*. Scripta Metallurgica, 1970. **4**(2): p. 117-122.
271. Tremsin, A.S., et al., *Optimization of Timepix count rate capabilities for the applications with a periodic input signal*. Journal of Instrumentation, 2014. **9**(5).
272. Liss, K.D., et al., *Directional atomic rearrangements during transformations between the α - and γ -phases in titanium aluminides*. Advanced Engineering Materials, 2008. **10**(4): p. 389-392.
273. Hildal, K., N. Sekido, and J. Perepezko, *Critical cooling rate for Fe₄₈Cr₁₅Mo₁₄Y₂C₁₅B₆ bulk metallic glass formation*. Intermetallics, 2006. **14**(8): p. 898-902.
274. Sheng, H.W., et al., *Atomic packing and short-to-medium-range order in metallic glasses*. Nature, 2006. **439**(7075): p. 419-425.
275. Toby, B. and T. Egami, *Accuracy of pair distribution function analysis applied to crystalline and non-crystalline materials*. Acta Crystallographica Section A: Foundations of Crystallography, 1992. **48**(3): p. 336-346.
276. Katagiri, H., et al., *An attempt at preparation of corrosion-resistant bulk amorphous Ni-Cr-Ta-Mo-P-B alloys*. Corrosion Science, 2001. **43**(1): p. 183-191.

Appendix

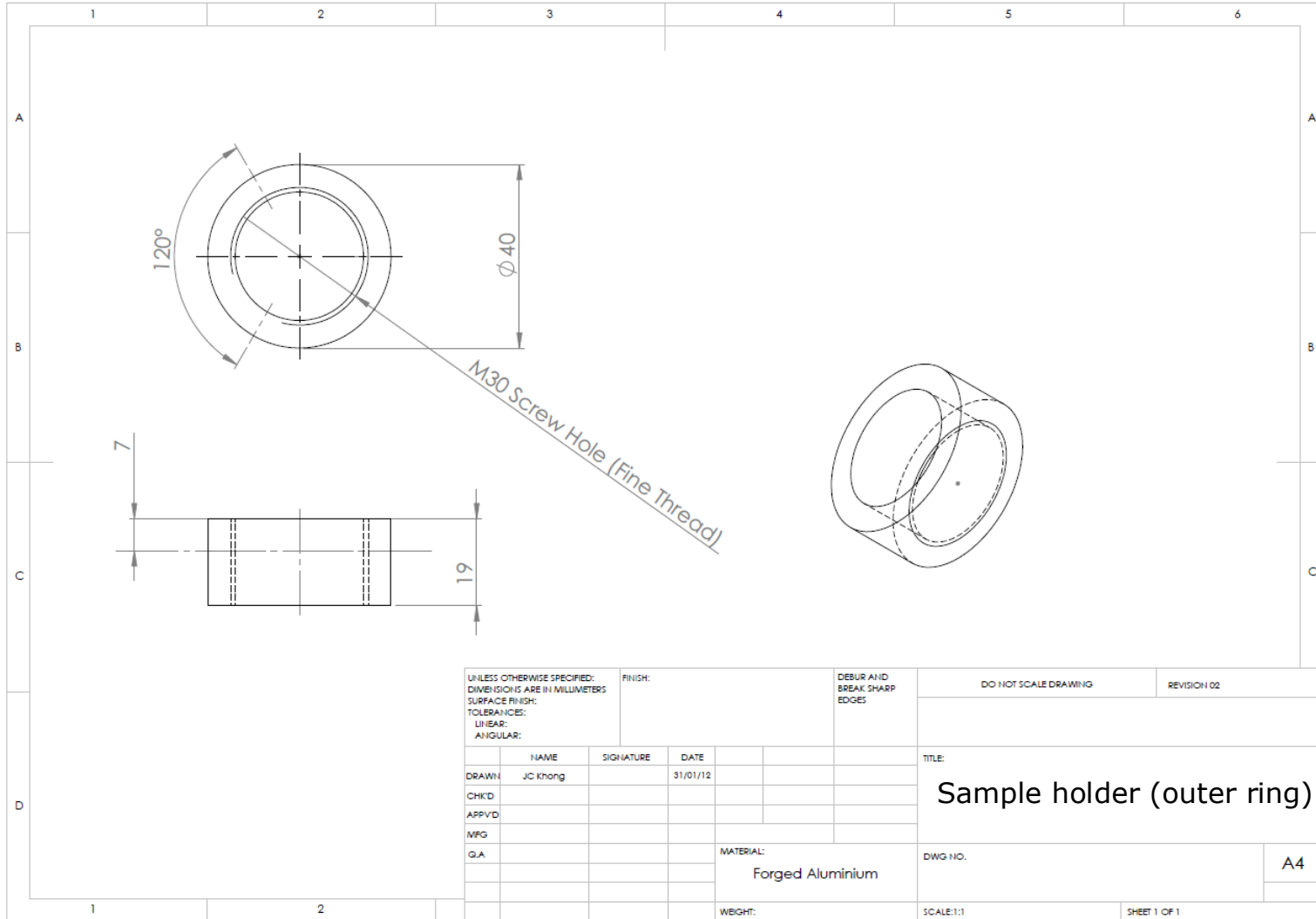
Appendix 1 Dog-bone sample



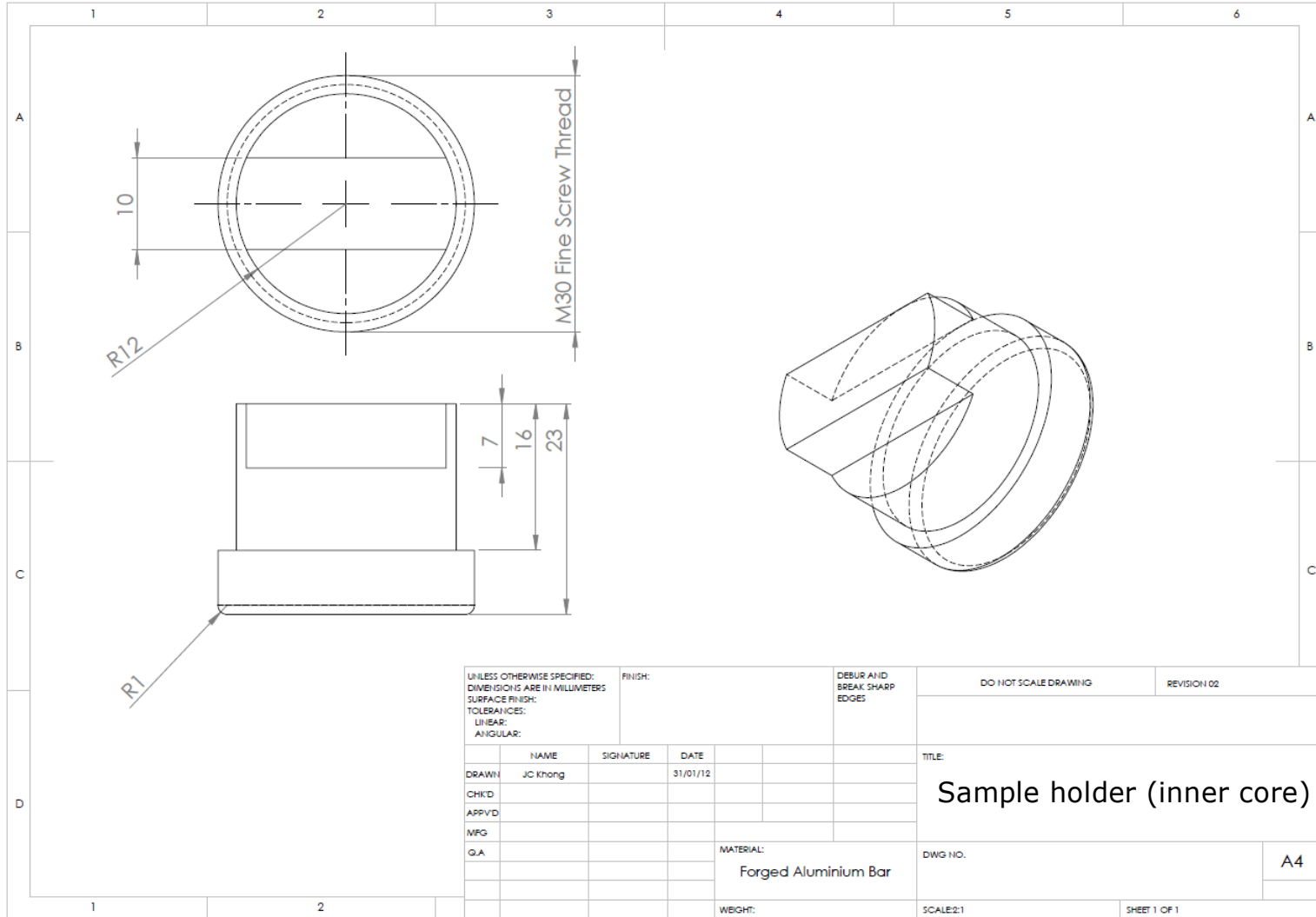
SolidWorks Student Edition.
For Academic Use Only.

UNLESS OTHERWISE SPECIFIED: DIMENSIONS ARE IN MILLIMETERS			FINISH:			DEBUR AND BREAK SHARP EDGES		
SURFACE FINISH:						DO NOT SCALE DRAWING		
TOLERANCES:						REVISION 3		
LINEAR:								
ANGULAR:								
	NAME	SIGNATURE	DATE			TITLE:		
DRAWN	JC khong		11/01/12			Tensile Test Sample		
CHE'K'D								
APP'VD								
MFG								
G.A.					MATERIAL:	DWG NO. Tensile Test Sample A4		
						SCALE: 1:1 SHEET 1 OF 1		

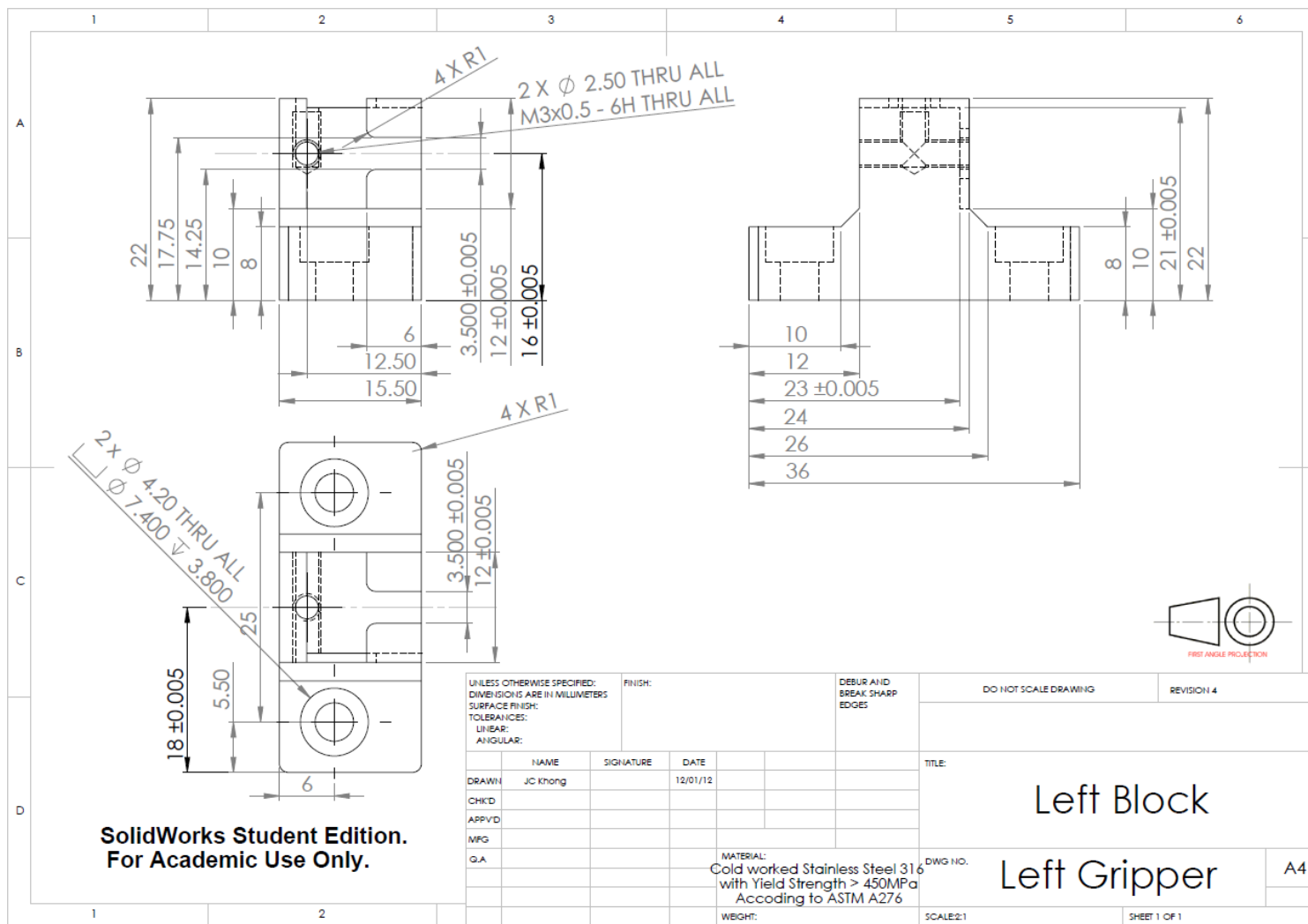
Appendix 2 Sample holder (outer ring)



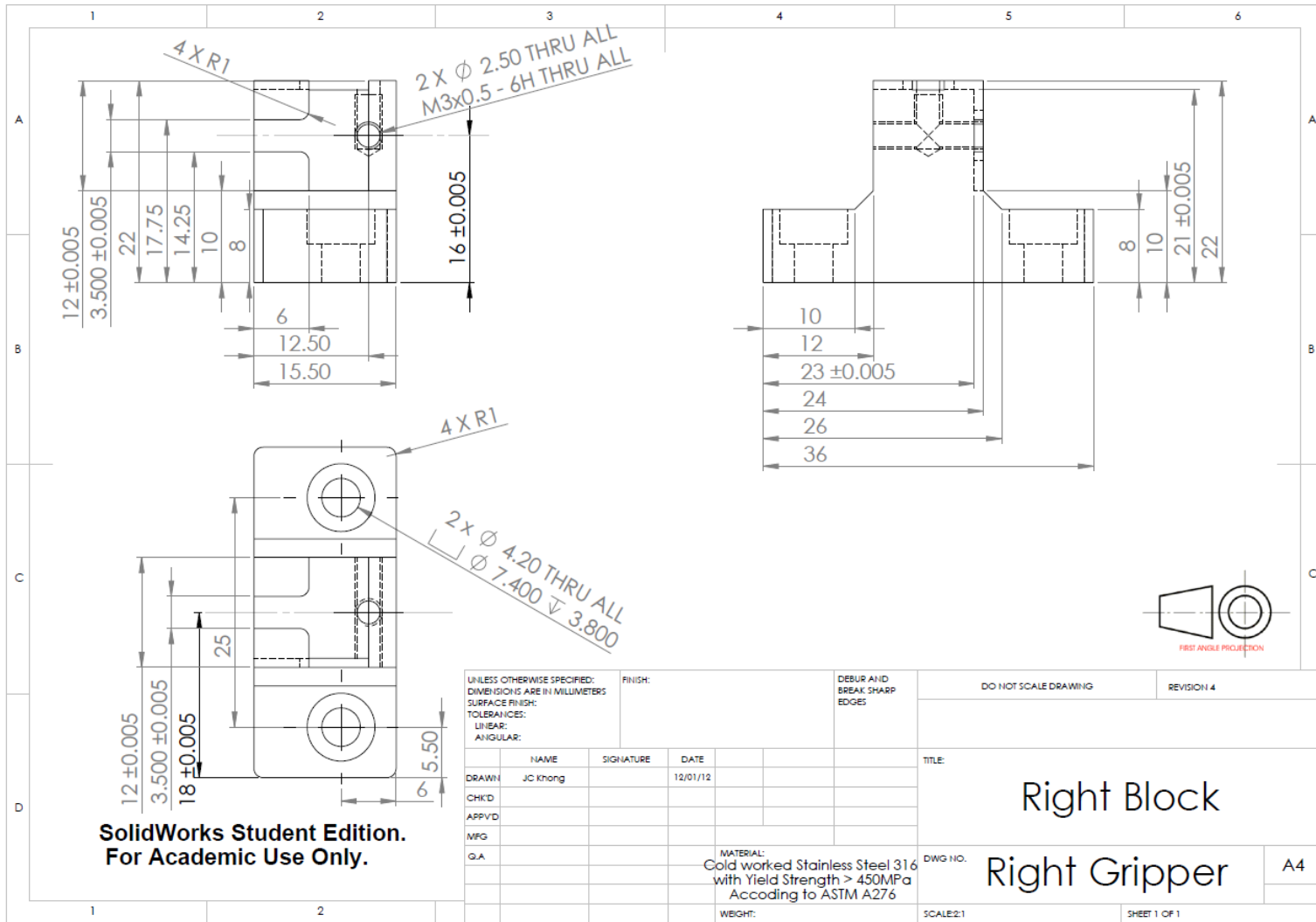
Appendix 3 Sample holder (inner ring)



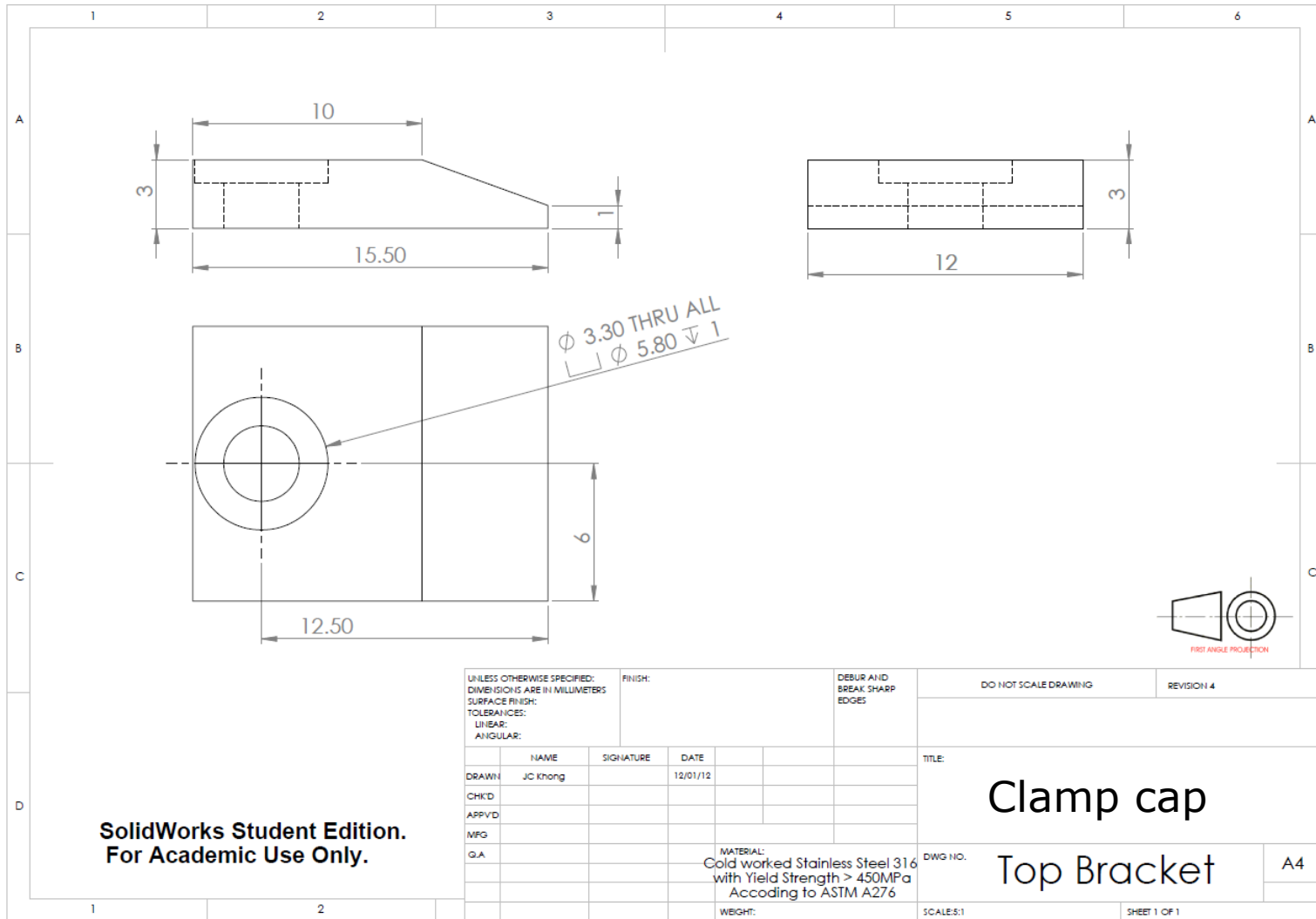
Appendix 4 Sample clamp (left block)



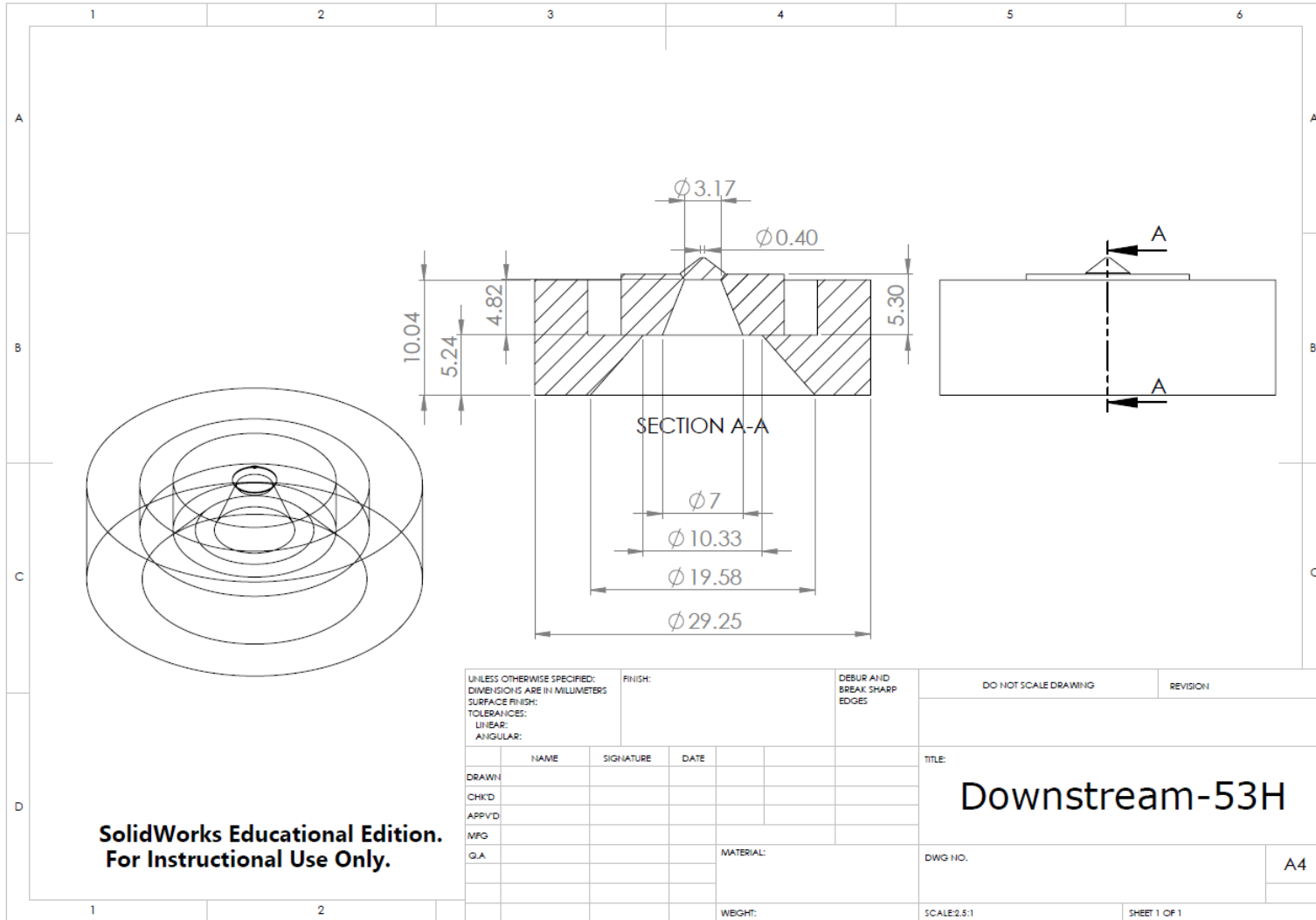
Appendix 5 Sample clamp (right block)



Appendix 6 Sample clamp (clamp cap X2)



Appendix 7 Downstream Diamond Anvil Cell (53H)



Appendix 9 Matlab code for calculating $T(2\theta)$

```

% must first import the 2 theta angle into the matlab workspace using
the
% 'import data' function. The name for the file put as 'data'
two_theta=data(:,1);
disp('Calculate the T(Q) for Diamond Anvil Cell')
prompt = 'Which Diamond Anvil Cell was used?\n 1. 2013 53H\n 2. 2014
53H(Cu50Zr50)\n 3. 2014 ST2(Fe60Nb15B25)\n Selection: ';
j = input(prompt);
if j==1
    disp('Calculate the T(Q) for 2013 53H Diamond Anvil Cell')
    img = imread('2013_53H.tif');
    imshow(img)
    %img = gpuArray(imread('2013_53H.tif'));
    %figure; imshow(img)
    prompt = 'Beam centre position (mm): \n (+) for shift away from the
backing plate \n (-) for shift toward the backing plate \nBeam centre
position: ';
    C = input(prompt);
    %Enter D1, D2, D3, D4, D5, D6, D7, M1 and M2 position
    prompt = 'Enter D1 value (mm)\D1=';
    D1 = input(prompt);
    prompt = 'Enter D2 value (mm)\D2=';
    D2 = input(prompt);
    prompt = 'Enter D3 value (mm)\D3=';
    D3 = input(prompt);
    prompt = 'Enter D4 value (mm)\D4=';
    D4 = input(prompt);
    prompt = 'Enter D5 value (mm)\D5=';
    D5 = input(prompt);
    prompt = 'Enter D6 value (mm)\D6=';
    D6 = input(prompt);
    prompt = 'Enter D7 value (mm)\D7=';
    D7 = input(prompt);
    prompt = 'Enter M1 value (degree)\M1=';
    M1 = input(prompt);
    prompt = 'Enter M2 value (degree)\M2=';
    M2 = input(prompt);
    D8=D4+C;
    D9=D5+C;
    D10=D6+C;
    D11=D7+C;
    i=1;
    for i=1:2880
        l1=tand(two_theta(i))*D1;
        l2=tand(two_theta(i))*D2;
        l3=tand(two_theta(i))*D3;
        k1(i)=D1/(cosd(two_theta(i)));

        if (l1 > D8 && l2 <= D9)
            k2(i)=((l1-D8)/(sind(90-M1-two_theta(i))))*sind(M1);
        elseif l2>D9
            k2(i)=(D2/cosd(two_theta(i)))-k1(i);
        else
            k2(i)=0;
        end
        if (l2>D10 && l3<=D11)
            k3(i)=((l2-D10)/sind(90-M2-two_theta(i)))*sind(M2);
        elseif l3>D11
            k3(i)=(D3/cosd(two_theta(i)))-k1(i)-k2(i);
        else
            k3(i)=0;
    end

```

```

end

%add in the attunuation of the WC and Diamond (attenuation are
%calculated in ##/mm, therefore the absorption is equals to
attunuation
%length * k distance

Total(i)=(k1(i)*0.057508)+(k2(i)*14.349)+(k3(i)*14.349);%attenuation
at 76keV and 0.163137A
T(i)=exp(-(Total(i)));
i=i+1;
%Plot a T(Q) graph
end
disp('Calculated T(Q) @76keV and 0.163137A wavelength')
plot(two_theta,T)
elseif j==2
disp('Calculate the T(Q) for 2014 53H(Cu50Zr50) Diamond Anvil
Cell')
img = imread('2014_53H_Cu50Zr50.tif');
imshow(img)
prompt = 'Beam centre position (mm): \n (+) for shift away from the
backing plate \n (-) for shift toward the backing plate \nBeam centre
position: ';
C = input(prompt);
%Enter D1, D2, D3, D4, D5, D6, D7, M1 and M2 position
prompt = 'Eneter D1 value (mm)\D1=';
D1 = input(prompt);
prompt = 'Eneter D2 value (mm)\D2=';
D2 = input(prompt);
prompt = 'Eneter D3 value (mm)\D3=';
D3 = input(prompt);
prompt = 'Eneter D4 value (mm)\D4=';
D4 = input(prompt);
prompt = 'Eneter D5 value (mm)\D5=';
D5 = input(prompt);
prompt = 'Eneter D6 value (mm)\D6=';
D6 = input(prompt);
prompt = 'Eneter D7 value (mm)\D7=';
D7 = input(prompt);
prompt = 'Eneter M1 value (degree)\M1=';
M1 = input(prompt);
prompt = 'Eneter M2 value (degree)\M2=';
M2 = input(prompt);
D8=D4+C;
D9=D5+C;
D10=D6+C;
D11=D7+C;
i=1;
for i=1:2880
l1=tand(two_theta(i))*D1;
l2=tand(two_theta(i))*D2;
l3=tand(two_theta(i))*D3;
k1(i)=D1/(cosd(two_theta(i)));

if l2 > D9
k2(i)=((l2-D9)/(sind(90-M1+two_theta(i))))*sind(M1);
else
k2(i)=0;
end
if (l2>D10 && l3<=D11)
k3(i)=((l2-D10)/sind(90-M2-two_theta(i)))*sind(M2);
elseif l3>D11
k3(i)=(D3/cosd(two_theta(i)))-((D1+D2)/cosd(two_theta(i)));

```

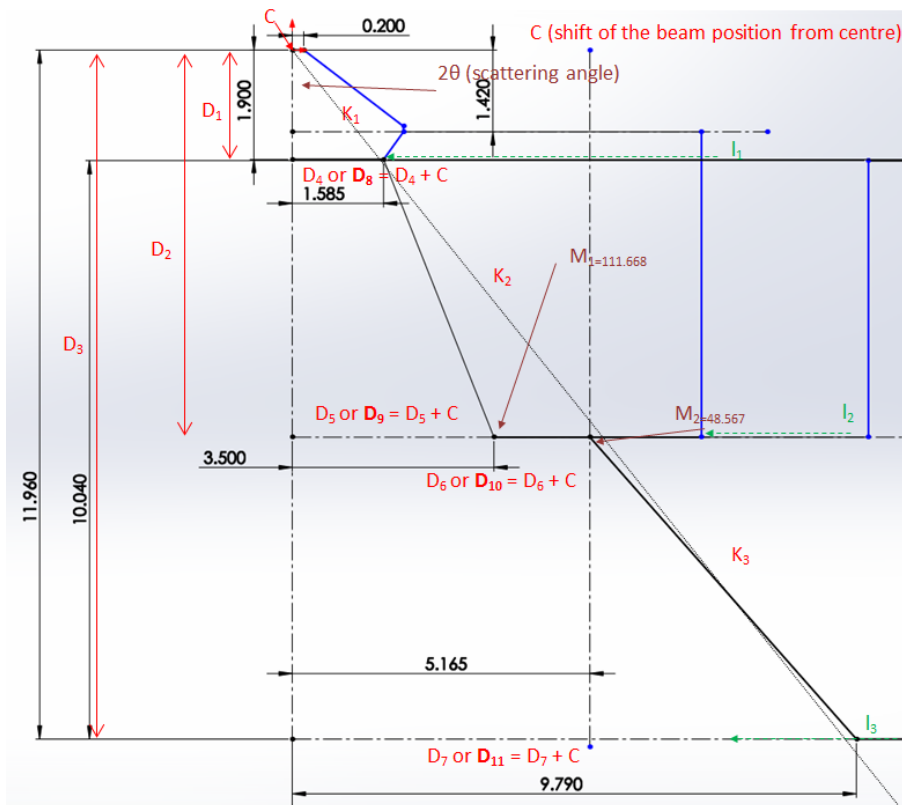
```

else
    k3(i)=0;
end
%add in the attenuation of the WC and Diamond (attenuation are
%calculated in ##/mm, therefore the absorption is equals to
attenuation
    %length * k distance

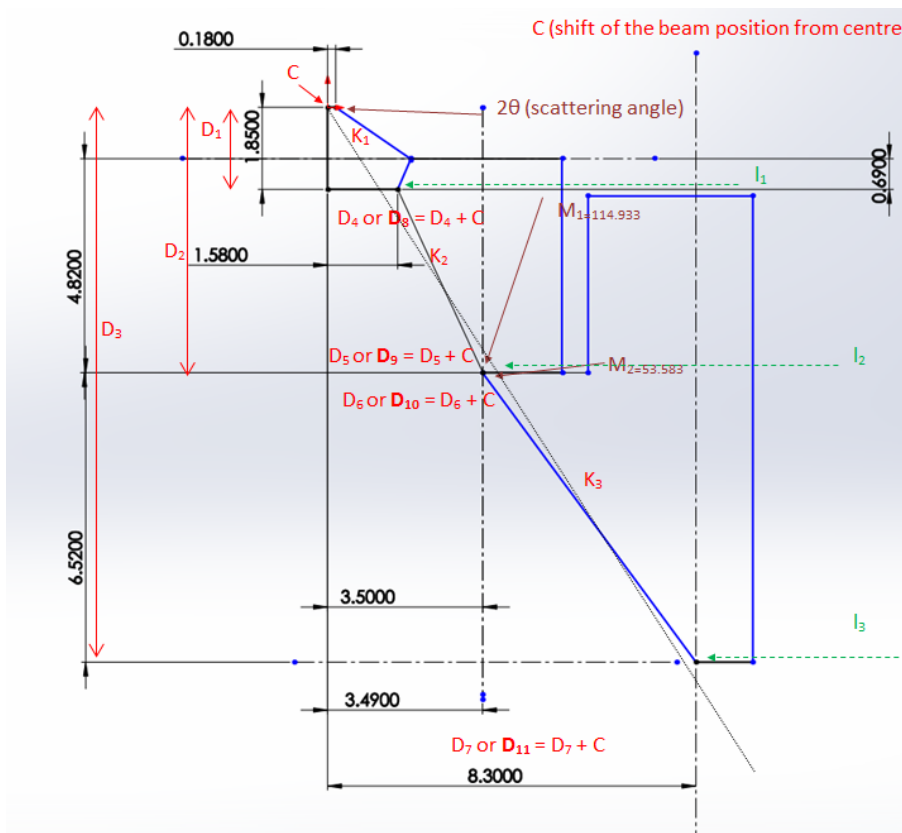
Total(i)=(k1(i)*0.057508)+(k2(i)*14.349)+(k3(i)*14.349);%attenuation
at 72keV and 0.1722A
T(i)=exp(-(Total(i)));
i=i+1;
%Plot a T(Q) graph
end
disp('Calculated T(Q) @72keV and 0.1722A wavelength')
plot(two_theta,T)
elseif j==3
    disp('Calculate the T(Q) for ST2(Fe60Nb15B25) Diamond Anvil Cell')
    img = imread('2014_ST2_Fe60Nb15B25.tif');
    imshow(img)
    prompt = 'Beam centre position (mm): \n (+) for shift away from the
backing plate \n (-) for shift toward the backing plate \nBeam centre
position: ';
    C = input(prompt);
    %Enter D1, D2, D3, D4, D5, D6, D7, M1 and M2 position
    prompt = 'Enter D1 value (mm)\D1=';
    D1 = input(prompt);
    prompt = 'Enter D2 value (mm)\D2=';
    D2 = input(prompt);
    prompt = 'Enter D3 value (mm)\D3=';
    D3 = input(prompt);
    prompt = 'Enter D4 value (mm)\D4=';
    D4 = input(prompt);
    prompt = 'Enter D5 value (mm)\D5=';
    D5 = input(prompt);
    prompt = 'Enter D6 value (mm)\D6=';
    D6 = input(prompt);
    prompt = 'Enter D7 value (mm)\D7=';
    D7 = input(prompt);
    prompt = 'Enter M1 value (degree)\M1=';
    M1 = input(prompt);
    prompt = 'Enter M2 value (degree)\M2=';
    M2 = input(prompt);
    D8=D4+C;
    D9=D5+C;
    D10=D6+C;
    D11=D7+C;
    i=1;
    for i=1:2880
        l1=tand(two_theta(i))*D1;
        l2=tand(two_theta(i))*D2;
        l3=tand(two_theta(i))*D3;
        k1(i)=D1/(cosd(two_theta(i)));

        if l2 > D9
            k2(i)=((l2-D9)/(sind(90-M1+two_theta(i))))*sind(M1);
        else
            k2(i)=0;
        end
        if (l2>D10 && l3<=D11)
            k3(i)=((l2-D10)/sind(90-M2-two_theta(i)))*sind(M2);
        elseif l3>D11
            k3(i)=(D3/cosd(two_theta(i)))-((D1+D2)/cosd(two_theta(i)));
        else

```

"2014_53H_Cu50Zr50.tif"



"2014_ST2_Fe60Nb15B25.tif"